Universidad del País Vasco
Euskal Herriko Unibertsitatea

Improving kesterite for its use in low-cost superstrate solar cells

David Payno Zarceño

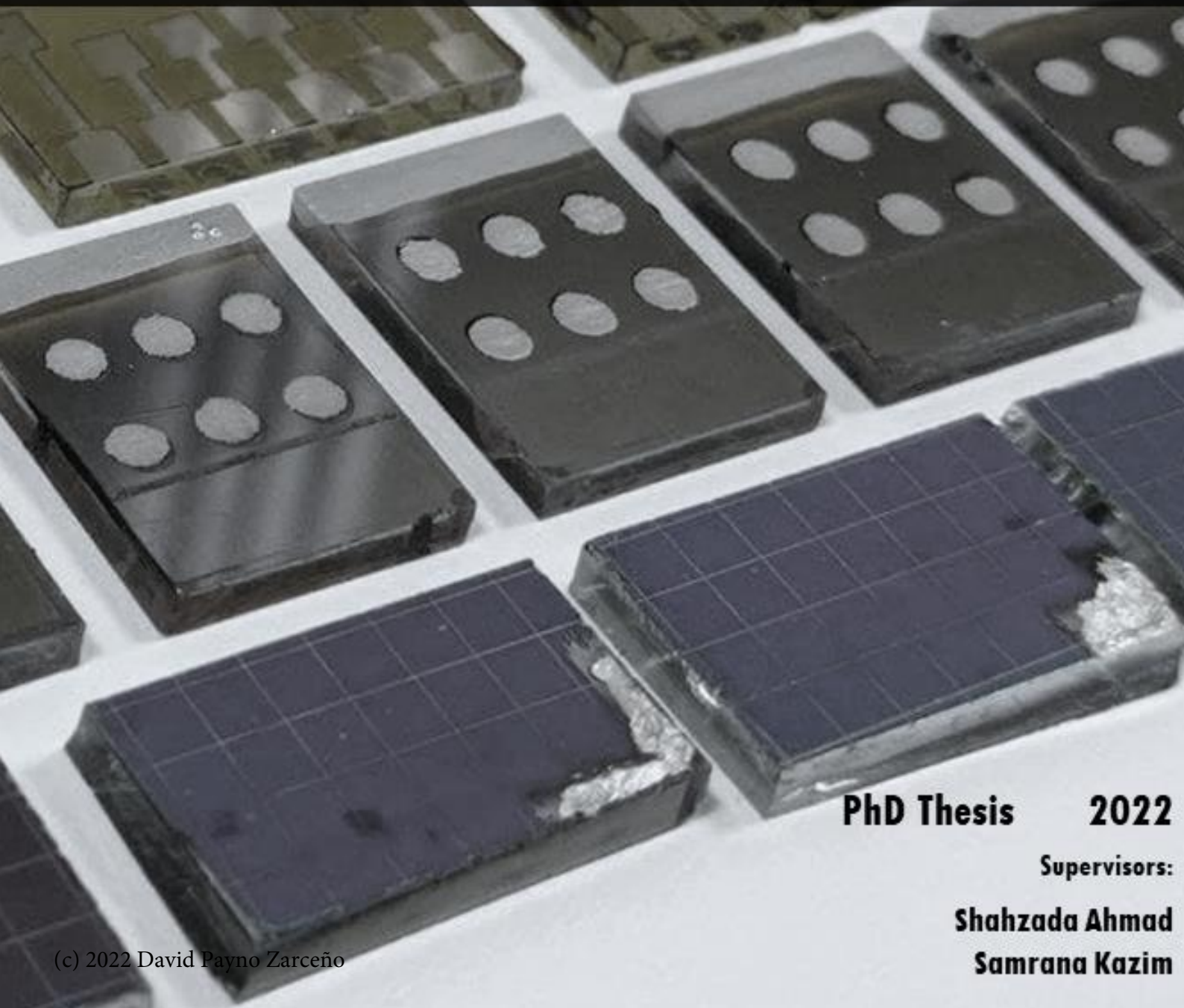

PhD Thesis **2022**

Supervisors:

Shahzada Ahmad

Samrana Kazim

Improving kesterite for its use in low-cost superstrate solar cells

Doctoral Thesis

Universidad del País Vasco / Euskal Herriko Unibertsitatea (UPV/EHU)

David Payno Zarceño

Supervisors: Shahzada Ahmad, Samrana Kazim

February 2022

This research work for PhD Degree by the University of the Basque Country (UPV/EHU) has been carried out at the Basque Center for Materials, Applications and Nanostructures (BCMaterials), and thanks to funding from the Basque Government and the Spanish Ministry of Science and Innovation.

Agradecimientos

Se acerca el final de esta ruta de poco más de tres años, y echando la vista atrás, veo a todas las personas que me han ayudado y acompañado en cada tramo. Habéis hecho que disfrute del camino y sé que sin vosotros no habría llegado a este punto, y por eso tengo que daros las gracias.

A mis padres, abuela y familia por creer en mí y tener siempre un hueco para mí en casa. A mis amigos que quedaron en Madrid, por hacerme sentir cada vez que vuelvo como si nunca me hubiera marchado, y a los de Bilbao, por acogerme y tratarme cómo si hubiera sido siempre de vuestra cuadrilla. A Juan y todos los que habéis pasado por Kukullu, no podría imaginar mejores compañeros de piso, me ayudasteis en los primeros baches y hemos disfrutado juntos de esta tierra, del mar, del monte y hasta del confinamiento. A Sofía, por acompañarme más que nadie y ayudarme con los detalles, tu marca queda reflejada. A mis directores por confiar y darme libertad para poner todas mis ideas en práctica. A mis compañeros de BCMaterials, por inspirarme cada día, y relajarnos juntos con una pachanguita o natxos después. A Manuel, por enseñarme y ayudarme tanto durante mis primeros pasos. A los que allanaron el camino hacia el doctorado antes que yo, sobre todo Paula y Ander por no dudar en aconsejarme, y a los que me seguirán, solo os puedo desear lo mejor y que disfrutéis del viaje.

Se abren ahora nuevos senderos algo inciertos, pero dónde lleven no me preocupa, porque sé que, en cualquier caso, todos seguiréis cerca.

RESUMEN

La tecnología fotovoltaica dominante en el mercado actual basada en el silicio ha demostrado ser una fuente de energía limpia y competitiva con las fuentes de energía tradicionales, ya que es una tecnología madura, robusta y de alta eficiencia. Esta tecnología se está acercando al mínimo coste que puede alcanzar. El constante crecimiento del mercado fotovoltaico junto a una alta competencia entre fabricantes son los principales motivos de la reducción de su precio, sin embargo, está limitado por los costosos procesos de obtención de materia prima, purificación y fabricación de obleas y celdas.

Cumplir los objetivos de cero emisiones en un futuro cercano sin afectar a la economía puede conseguirse solo si la energía fotovoltaica se propone objetivos más ambiciosos. Para ello, es necesario el estudio y desarrollo de nuevos materiales que superen las limitaciones de las tecnologías fotovoltaicas actuales. Sin embargo, la mayoría de tecnologías fotovoltaicas desarrolladas en los últimos años no han logrado llegar al mercado de forma notable, a pesar de aportar varias ventajas. Esto es debido a los fuertes requisitos exigidos: eficiencia competitiva, alta durabilidad, versatilidad, materias primas abundantes y procesos de fabricación de bajo coste.

En esta tesis se estudian los materiales y procesos de fabricación de células fotovoltaicas con potencial de cumplir los requisitos necesarios para competir con las tecnologías actuales, además de aportar múltiples ventajas. Los materiales estudiados están basados en calcogenuros de fase cuaternaria I_2-II-IV-VI_4, con estructura kesterita o estannita. Estos materiales son semiconductores con alta absorción de luz, energía de banda prohibida en rango ideal respecto al espectro solar, altamente estables y que pueden ser fabricados en forma de película delgadas mediante procesos de bajo coste.

Optimizar las propiedades de los materiales fabricados requiere familiarizarse con los procesos que ocurren durante el efecto fotovoltaico,

así como los métodos para caracterizar dichos procesos. Una revisión de los fundamentos, materiales y del estado del arte de la energía fotovoltaica se realiza en el primer capítulo de esta tesis.

Durante los últimos años, ha emergido un gran interés en torno al uso de $Cu_2ZnSn(S,Se)_4$, con estructura de kesterita, como material absorbedor de luz en células fotovoltaicas, ya que posee las propiedades necesarias y está compuesto por elementos abundantes. Existen varias limitaciones en la eficiencia de las células, que afectan principalmente al voltaje generado. Parte de estas limitaciones se encuentran en los materiales usados, principalmente CdS, para formar la unión *p-n* y las intercaras que forman con la kesterita. En el segundo capítulo, se estudia la modificación de las propiedades de la intercara mediante el uso de fullerenos en las células solares más avanzadas basadas en kesterita. Se observa como el uso de una delgada película de fullereno C_{60} entre la kesterita y el CdS pasiva la intercara y ralentiza los procesos de recombinación de carga, resultando en células fotovoltaicas que proporcionan un voltaje mayor. Además, se mejora la transparencia de las capas frontales, resultando en un ligero incremento en la corriente de la célula solar.

El tercer capítulo, se exploran métodos de depósito de películas delgadas de kesterita mediante métodos en base líquida. Estos métodos tienen un bajo coste debido al poco equipamiento que requieren, y mediante una disolución adecuada, son capaces de preparar películas delgadas de buena calidad manteniendo las propiedades de los materiales. Estos métodos se aplicarán posteriormente en la fabricación de células fotovoltaicas basadas en kesterita. Por otra parte, se explora una arquitectura alternativa de célula solar, con estructura superestrato. Esta estructura brinda varias ventajas respecto a la estructura substrato previamente utilizada, ya que comienza a fabricarse por el electrodo delantero transparente. Este tipo de electrodos, además de evitar el uso de elementos estratégicos, expande las aplicaciones a células solares semi-transparentes, bifaciales, su uso en tándem y el estudio de contactos traseros alternativos. Combinando un estudio del estado del arte

junto a ensayos preliminares, se pueden identificar los principales problemas que la kesterita ha tenido para llevarse a cabo en estructura superestrato.

El cuarto capítulo se enfoca en la optimización de los procesos de fabricación de células solares en arquitectura superestrato y desarrollo de estrategias para mejorar su eficiencia. La temperatura requerida para favorecer la cristalización de la kesterita se sitúa por encima de 530 ºC, ligeramente por encima de la temperatura a la que comienza a degradarse el contacto trasparente de fluor:dióxido de estaño (FTO). El uso de una capa intermedia de CdS es necesaria para favorecer el efecto fotovoltaico, sin embargo, se observa que la alta temperatura también favorece un intercambio de iones de cadmio y zinc en la unión CdS/Cu_2ZnSnS_4, lo que consume el CdS y forma una unión $(Cd,Zn)S/Cu_2(Cd,Zn)SnS_4$ mucho menos eficiente. Por otra parte, se explora también el uso de nanoestructuras mesoporosas mediante la aplicación de un film de nanopartículas de TiO_2. Un grosor de capa mesoporosa óptima de 150 nm resulta en una superficie que reduce la dispersión de luz, mejora la transmitancia, y favorece el posterior depósito de CdS mediante baño químico. La mayor superficie de contacto que ofrecen las nanoestructuras favorece la separación de pares electrón-hueco, resultando en células fotovoltaicas más eficientes.

En el quinto capítulo, se estudia cambios en la composición del absorbedor de luz. La sustitución de Zn por Cd resulta en la formación controlada de $Cu_2(Cd,Zn)SnS_4$. Una alta cantidad de Cd modifica la estructura cristalina de kesterita a estannita, mientras que valores intermedios forman una solución sólida de ambas fases. Se encuentra que una proporción de Cd alta mejora la cristalinidad del absorbedor, además de evitar la formación de (Cd,Zn)S. Las celdas fabricadas con proporciones de Cd/Cd+Zn entre el 75 y el 100 % muestran una eficiencia fotovoltaica mucho mayor. También se estudió la inclusión de Se en la composición, lo que resulta en un absorbedor $Cu_2CdSn(S,Se)_4$ con menor band-gap, y que muestra indicios de poseer una mejor conductividad debido a una considerable mejora en el factor de llenado y la eficiencia fotovoltaica.

LABURPENA

Silizioan oinarritutako egungo merkatuan nagusi den teknologia fotovoltaikoa energia-iturri garbia eta lehiakorra da energia-iturri tradizionalekin, teknologia heldua, sendoa eta eraginkortasun handikoa baita. Teknologia hori eduki dezakeen kosturik txikienera hurbiltzen ari da. Merkatu fotovoltaikoaren etengabeko hazkundea eta fabrikatzaileen arteko lehia dira prezioa murrizteko arrazoi nagusiak, baina lehengaia lortzeko, garbitzeko eta olatak zein gelaxkak fabrikatzeko prozesu garestiek mugatzen dute prezio jaitsiera.

Etorkizun hurbilean zero emisioko helburuak betetzea lortu nahi da, ekonomian eragin izan gabe. Energia fotovoltaikoak asmo handiagoko helburuak proposatzen baditu bakarrik lor daiteke. Horretarako, egungo teknologia fotovoltaikoen mugak gaindituko dituzten material berriak aztertu eta garatu behar dira. Hala ere, azken urteotan garatutako teknologia fotovoltaiko gehienek ez dute lortu merkatura modu nabarmenean iristea, nahiz eta hainbat abantaila desberdinak erakusten dituzten. Hori eskatzen diren baldintza gogorren ondorio da: lehiakortasun-eraginkortasuna, iraunkortasun handia, aldakortasuna, lehengai ugariak eta kostu txikiko fabrikazio-prozesuak.

Tesi honetan zelula fotovoltaikoak fabrikatzeko materialak eta prozesuak aztertzen dira, egungo teknologiekin lehiatzeko beharrezkoak diren baldintzak bete ditzaketenak, abantaila ugari emateaz gain. Ikertutako materialak fase kuaternarioko kalkogenuroetan oinarrituta daude (I_2-II-IV-VI_4), eta kesterita edo estannita egitura dute. Material horiek argi-xurgapen handiko erdieroaleak dira, eguzki-espektroarekiko maila idealean debekatutako banda-energia, oso egonkorrak eta kostu txikiko prozesuen bidez film mehe moduan fabrikatu daitezkeenak.

Fabrikatutako materialen propietateak optimizatzeko, efektu fotovoltaikoan gertatzen diren prozesuekin ohitu behar da, bai eta prozesu horiek ezaugarritzeko metodoekin ere. Tesi honen lehen kapituluan energia fotovoltaikoaren oinarriak, materialak eta artearen egoera berrikusten dira.

Azken urteotan, interes handia piztu da $Cu_2ZnSn(S,Se)_4$-ren erabileraren inguruan, kesterita egiturarekin, zelula fotovoltaikoetan argia xurgatzeko material gisa, beharrezko propietateak baititu eta elementu ugariz osatua baitago. Zelulen eraginkortasunean hainbat muga daude, batez ere sortutako tentsioari eragiten diotenak. Muga horietako batzuk erabilitako materialetan daude, batez ere CdS materialetan, kesteritarekin osatzen duten p-n lotura eta interaurpegiak osatzeko. Bigarren kapituluan, interaurpegiaren propietateen aldaketa aztertzen da, kesteritan oinarritutako eguzki-zelula aurreratuenetan fullerenoak erabiliz. Ikus daitekeenez, kesterita eta CdS pasiboaren artean C_{60} fullerenozko film mehe bat erabiltzeak interaurpegia eta karga birkonbinatzeko prozesuak moteltzen ditu, eta tentsio handiagoa ematen duten zelula fotovoltaikoak sortzen dira. Gainera, aurreko geruzen gardentasuna hobetzen da, eta eguzki-zelularen korronteak pixka bat gora egiten du.

Hirugarren kapituluan, oinarri likidoko metodoen bidez kesteritazko film meheak gordetzeko metodoak aztertzen dira. Metodo horiek kostu txikia dute, ekipamendu gutxi behar dutelako, eta disoluzio egoki baten bidez, kalitate oneko film meheak prestatzeko gai direlako, materialen propietateak mantenduz. Metodo horiek, ondoren, kesteritan oinarritutako zelula fotovoltaikoak fabrikatzeko erabiliko dira. Bestalde, superestratu egitura duen eguzki-zelularen arkitektura alternatiboa aztertzen da. Egitura horrek hainbat abantaila aurkezten ditu aurretik erabilitako substratu-egiturarekin alderatuta, aurreko elektrodo gardenak fabrikatzen hasten baitira. Elektrodo mota honek, elementu estrategikoen erabilera saihesteaz gain, aplikazioak eguzki-zelula erdi gardenetara, bi aurpegikoetara, tandemean erabiltzera eta atzeko kontaktu alternatiboen azterketara hedatzen ditu. Artearen egoeraren

azterketa eta aurretiazko saiakuntzak konbinatuz, kesteritak superestratu-egituran egiteko izan dituen arazo nagusiak identifika daitezke.

Laugarren kapituluak arkitektura superestratuan eguzki-zelulak fabrikatzeko prozesuak optimizatzea eta horien eraginkortasuna hobetzeko estrategiak garatzea du helburu. Kesterita kristalizatzeko behar den tenperatura 530 ºC-tik gorakoa da, fluorraren kontaktu gardena degradatzen hasten den tenperatura baino zertxobait handiagoa: eztainu dioxidoa (FTO). CdS tarteko geruza bat erabiltzea beharrezkoa da efektu fotovoltaikoa errazteko; hala ere, tenperatura altuak CdS/Cu_2ZnSnS_4 loturan kadmio- eta zink-ioien elkartrukea ere errazten du, eta horrek, CdS kontsumitzen du eta askoz eraginkorragoa den lotura bat eratzen du (Cd,Zn)S/Cu_2(Cd,Zn)SnS_4. Bestalde, nanoegitura mesoporosoen erabilera ere aztertzen da, TiO_2 nanopartikulaz osatutako film bat aplikatuz. 150 nm-ko geruza mesoporosoko lodiera optimoa argiaren dispertsioa murrizten duen gainazal batean gertatzen da, transmisantzia hobetzen du, eta ondoren, bainu kimiko bidez, CdS gordetzea errazten du. Nanoegiturek ukipen-azalera handiagoa dutenez, bikote elektronikoak eta hutsarteak bereizten dira, zelula fotovoltaikoak eraginkorragoak lortuz.

Bosgarren kapituluan, argi-xurgatzailearen konposizioan izandako aldaketak aztertzen dira. Zn, Cd-rekin ordezkatzea Cu_2(Cd,Zn)SnS_4 formazio kontrolatuan gertatzen da. Cd kantitate altu batek egitura kristalinoa kesteritatik estannitara aldatzen du, bitarteko balioek bi faseen soluzio sendoa osatzen duten bitartean. Cd altuaren proportzio batek xurgatzailearen kristaltasuna hobetzen du, eta, gainera, (Cd,Zn)S-ren eraketa saihesten du. Cd/Cd+Zn proportzioekin fabrikatutako gelaxkek % 75 eta % 100 artean eraginkortasun fotovoltaiko askoz handiagoa erakusten dute. Se konposizioan sartzea ere aztertu da, eta hori band-gap txikiagoa duen $Cu_2CdSn(S,Se)_4$ xurgatzaile batean gertatzen da, eroankortasun hobea izatearen zantzuak erakusten ditu, betetze-faktorea eta eraginkortasun fotovoltaikoa nabarmen hobetu direlako.

ABSTRACT

Today's market-dominant silicon-based photovoltaic technology has proven to be a clean and competitive energy source with traditional energy sources, as it is a mature, robust and highly efficient technology. This technology is approaching the minimum cost achievable. The steady growth of the photovoltaic market together with high competition among producers are the main reasons for its price reduction, however, it is limited by the costly processes of raw material extraction, purification and manufacturing of wafers and cells.

Meeting zero-emission targets in a near future without affecting the economy can only be achieved if photovoltaics set more ambitious goals. This requires the study and development of new materials to overcome the limitations of current photovoltaic technologies. However, most of the PV technologies developed in recent years have failed to reach the market in a significant way, despite providing several advantages. This is due to strong requirements: competitive efficiency, high durability, application versatility, abundant raw materials and low-cost manufacturing processes.

In this thesis, materials and manufacturing processes for photovoltaic cells with the potential to meet the requirements needed to compete with current technologies, as well as provide multiple advantages, are investigated. The materials studied are based on quaternary phase chalcogenides I_2-II-IV-VI_4, with kesterite or stannite structure. These materials are semiconductors with high light absorption, band gap energy in the ideal respect the solar spectrum, highly stable and can be fabricated as thin films by low-cost processes.

Optimising the properties of the fabricated materials requires familiarisation with the processes that occur during the photovoltaic effect, as well as methods to characterise these processes. A review of the fundamentals,

materials and state-of-the-art of photovoltaics is given in the first chapter of this thesis.

During the last few years, a great deal of interest has emerged in the use of $Cu_2ZnSn(S,Se)_4$, with a kesterite structure, as a light-absorber material in photovoltaic cells, as it possesses the necessary properties and is composed of abundant elements. There are several limitations to the efficiency of the cells, mainly affecting the voltage output. Part of these limitations are found in the materials used, mainly CdS, to form the p-n junction and the interlayer formed with the kesterite. In the second chapter, the modification of the interface properties by the use of fullerenes in the most advanced kesterite-based solar cells is studied. It is observed how the use of a thin C_{60} fullerene film between the kesterite and CdS passivates the interlayer and slows down charge recombination processes, resulting in photovoltaic cells that provide a higher voltage. In addition, the transparency of the front layers is improved, resulting in a slight increase in solar cell current.

In the third chapter, methods of depositing kesterite thin films by liquid-based methods are explored. These methods are inexpensive due to the minimal equipment required, and with proper dissolution, good quality thin films can be prepared, preserving the properties of the materials. These methods will be further applied in the fabrication of kesterite-based photovoltaic cells. Furthermore, an alternative solar cell architecture with a superstrate structure is studied. This structure offers several advantages over the previously used substrate structure, as it builds up from the transparent front electrode. This type of electrode, in addition to avoiding the use of strategic elements, expands the applications to semi-transparent, bifacial solar cells, their use in tandem and the study of alternative back contacts. Combining a survey of the state of the art with preliminary tests, the main problems that kesterite has encountered in realising a superstrate structure can be identified.

The fourth chapter focuses on the optimisation of the manufacturing processes of solar cells in superstrate architecture and the development of strategies to improve their efficiency. The temperature required to promote the crystallisation of kesterite is above 530°C, slightly above the temperature at which the fluorine-doped tin dioxide transparent contact (FTO) starts to degrade. The use of a CdS interlayer is necessary to favour the photovoltaic effect, however, it is observed that the high temperature also favours an exchange of cadmium and zinc ions at the CdS/$Cu_2ZnSnSnS_4$ junction, which consumes the CdS and forms a much less efficient (Cd,Zn)S/Cu_2(Cd,Zn)SnS_4 junction. On the other hand, the use of mesoporous nanostructures is also explored by applying a TiO_2 nanoparticle film. An optimal mesoporous layer thickness of 150 nm results in a surface that reduces light scattering, improves transmittance and favours the subsequent deposition of CdS by chemical bath. The larger contact surface offered by the nanostructures favours the separation of electron-hole pairs, resulting in more efficient photovoltaic cells.

In the fifth chapter, changes in the composition of the light absorber are studied. The substitution of Zn by Cd results in the controlled formation of Cu_2(Cd,Zn)SnS_4. A high amount of Cd changes the crystal structure from kesterite to stannite, while intermediate values form a solid solution of both phases. It is found that a high Cd ratio improves the crystallinity of the absorber, as well as prevents the formation of (Cd,Zn)S. Cells fabricated with Cd/Cd+Zn ratios between 75 and 100 % show a much higher photovoltaic efficiency. The inclusion of Se in the composition was also studied, resulting in a $Cu_2CdSn(S,Se)_4$ absorber with a lower band-gap, and suggesting a better conductivity due to a considerable improvement in the fill factor and photovoltaic efficiency.

Chapter 1: Introduction

Chapter 2: Partial substitution of CdS buffer layer by fullerenes in kesterite solar cells

Chapter 3: Solution-based CZTS thin films deposition and development of superstrate solar cells

Chapter 4: Temperature effects on the absorber, the device and the PV performance.

Chapter 5: Element substitution in all solution-processed superstrate solar cells

Chapter 6: General conclusions & future trends

1 Introduction

Photovoltaic energy is a topic with a long evolution that includes many old and new concepts. During the history of photovoltaics, it has gone from being an interesting effect that helped in the understanding of the properties of semiconductors and their quantum nature, to an indispensable tool for the generation of clean energy. This chapter is used as a review of the fundaments and the concepts required to understand the characterization techniques used, results, and conclusions obtained during this thesis. We also provide an introduction to the recent advances in materials and photovoltaic devices, giving a complete state-of-the-art framework, which will serve as a starting point for setting the research objectives in this thesis.

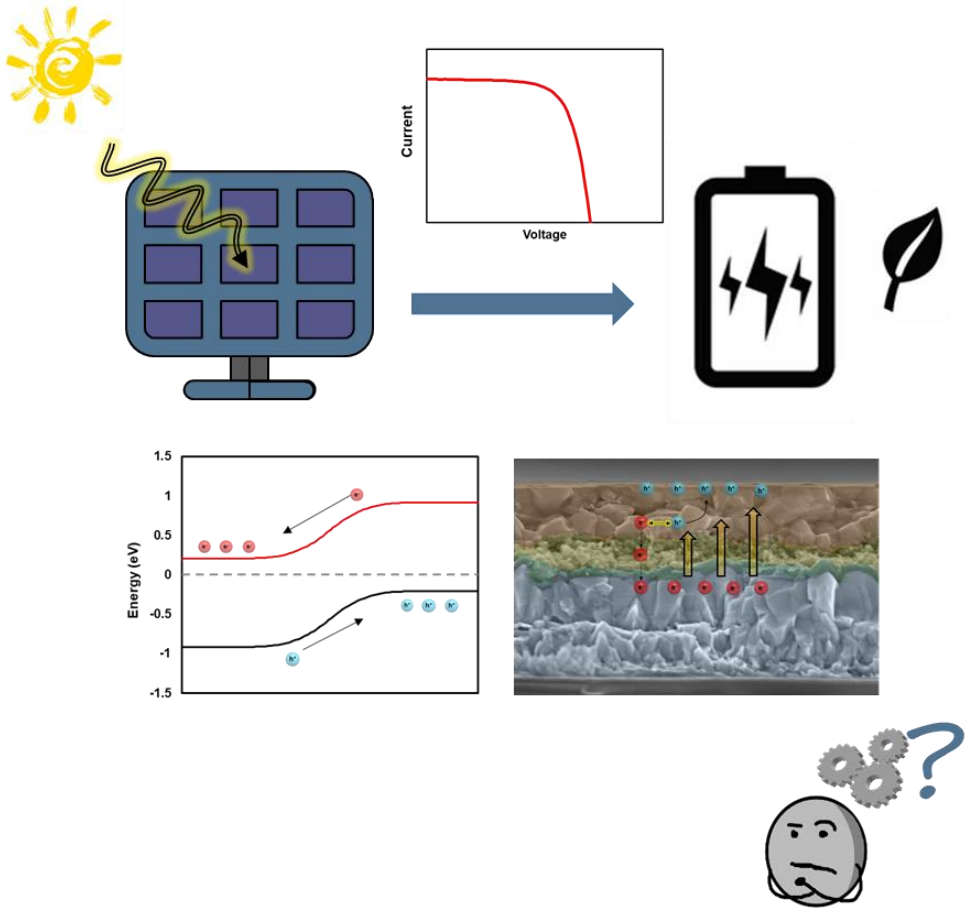

Contents:

1.1 Overview and motivation

The Paris Agreement, signed by 195 countries in 2015, sets the target for global warming below 1.5 ºC, recognizing the danger and risk of surpassing this limit for our planet. To achieve this objective, a reduction of the CO_2 and greenhouse gasses must be reached, with the objective of zero emissions set by the European Union in 2050. With the CO_2 emissions coming mainly from the burning of fossil fuels, used as large-scale energy sources in developed and developing countries, an intense shift in energy generation is required. With the current economic slowdown caused by the global pandemic, the world energy consumption will increase during the recovery, and so, the CO_2 emissions, putting under serious risk the objectives of the Paris Agreement. With the current trends, an increase of up to 3.9 ºC is estimated in the year 2100,[1] with devastating consequences. Consequently, a shift to renewable energy sources and decarbonization will be critical during the next decade to accomplish the global warming objectives.

Even during the crisis, installed renewable sources have experienced a higher growth rate, in particular, wind and photovoltaic (PV) energy.[2] Solar energy is by far the most abundant source of energy and PV technology is an efficient way to convert sunlight into electricity. PV is a relatively new renewable energy source with part of its potential still undeveloped, however, it is currently cost-competitive.[3] With the installed power capacity a reduction in PV energy cost can be seen, a signal that the learning curve is still in progress. This observation is represented by Swanson's law (**Figure 1.1**), an equivalent of Moore's law for the prediction of the PV cost. The dropping cost of a PV installation, suggests that PV will be the most important energy source in the next decades. But the main PV technology, based on silicon, is reaching theoretical and practical limits, and its cost reduction is mostly based on deflation due to market penetration.[4] The future validity of Swanson's law will depend on the capability for research and innovation in new concepts in all PV aspects (cells, modules, transport,

deploy, recycling …) to make it more polyvalent, attractive, and cost-effective.[4]

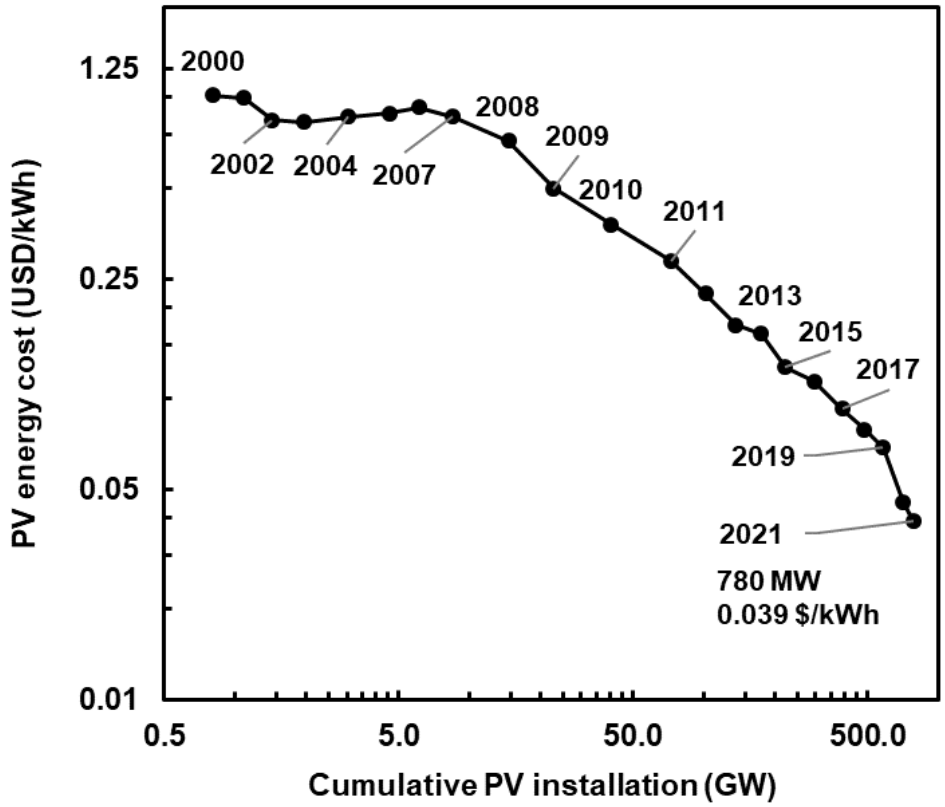

Figure 1.1. Evolution of the PV cost with the world installed power (data source: *ourworldindata*, *IRENA*)

1.2 Brief history of photovoltaic effect discovery

Interaction of light with matter has been one of the old intriguing questions for scientists. Edmond Becquerel first reported a kind of PV effect as early as 1839, noticing a flow of current under illumination when experimenting with the electrolytic cells.[5]

The journey starts in 1873, when Willoughby Smith used selenium bars as resistors in submarine wires and noticed changes in its conductivity under the Sun illumination. The observation is considered the photoconductivity discovery.[6] This led to another report in 1877 on the photoconductivity of selenium, which found that, upon illumination, a current was generated, demonstrating the first PV effect in a solid-state system.[7]

Charles Fritts presents the prototype of a modern version of a selenium photocell in 1883 with a film structure, inspiring the current design for PV cells. Different electrodes and multiple cells connected in series to form a module were tested. The rectification nature of the system was noted, however, it could not be explained at that time.[8] The PV effect was not stated in the original article, however, after sending the samples to Werner Siemens, they conclude that these cells could produce electric energy from the sunlight (**Figure 1.2**). Thus, it is considered the first practical solar cell.[9] These selenium cells further inspired Albert Einstein to explain the first insights on the nature of photoelectricity in 1905, for which he was awarded the Nobel Prize.[10]

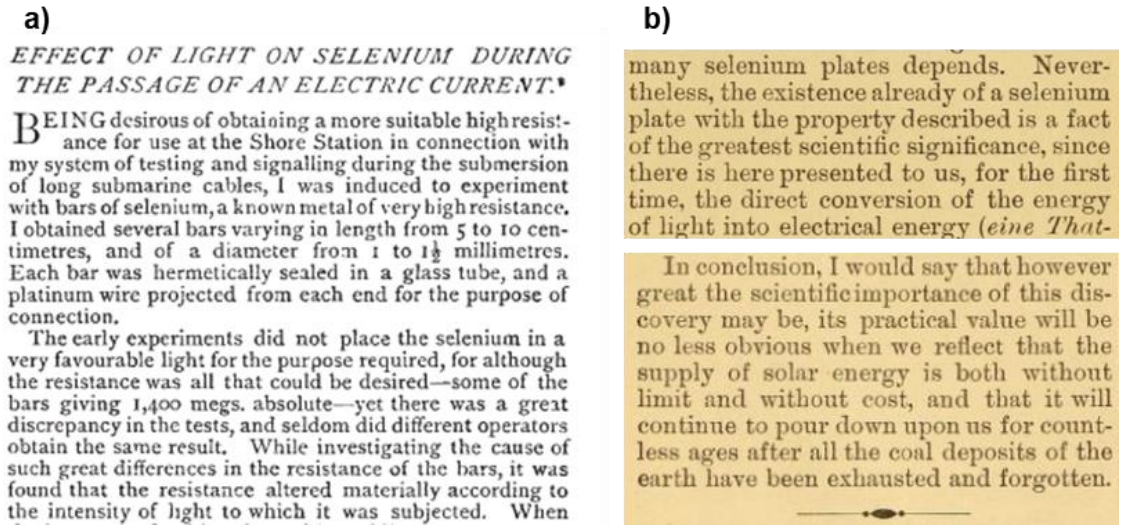
a)

EFFECT OF LIGHT ON SELENIUM DURING THE PASSAGE OF AN ELECTRIC CURRENT.

BEING desirous of obtaining a more suitable high resistance for use at the Shore Station in connection with my system of testing and signalling during the submersion of long submarine cables, I was induced to experiment with bars of selenium, a known metal of very high resistance. I obtained several bars varying in length from 5 to 10 centimetres, and of a diameter from 1 to 1½ millimetres. Each bar was hermetically sealed in a glass tube, and a platinum wire projected from each end for the purpose of connection.

The early experiments did not place the selenium in a very favourable light for the purpose required, for although the resistance was all that could be desired—some of the bars giving 1,400 megs. absolute—yet there was a great discrepancy in the tests, and seldom did different operators obtain the same result. While investigating the cause of such great differences in the resistance of the bars, it was found that the resistance altered materially according to the intensity of light to which it was subjected. When

b)

many selenium plates depends. Nevertheless, the existence already of a selenium plate with the property described is a fact of the greatest scientific significance, since there is here presented to us, for the first time, the direct conversion of the energy of light into electrical energy (*eine That-*

In conclusion, I would say that however great the scientific importance of this discovery may be, its practical value will be no less obvious when we reflect that the supply of solar energy is both without limit and without cost, and that it will continue to pour down upon us for countless ages after all the coal deposits of the earth have been exhausted and forgotten.

Figure 1.2. a) Extractions from Willoughby Smith communication,[6] and b) Werner Siemens article, with a conclusion by Charles Fritts regarding its use as renewable energy [9] (version of Van Nostrand's Engineering Magazine).

During the following years, progress was made on understanding the PV effect, and various improvements were made on the fabrication and reproducibility of these early solar cells. New materials were found to have similar properties to Se, with Cu_2O gaining more interest.[11] By that time, the working principle of these PV cells was not completely clear. These prototypes were based on a Schottky barrier, a rectifying effect produced on

the interface between a semiconductor and conductor that can produce a PV effect.

In parallel, the understanding of rectifying diodes was of interest for the development of electric AC/DC converters. The theory of a metal-semiconductor junction was developed in 1939 by Nevil Mott, improved by Walter H. Schottky, amended by Hans Bethe in 1942. Not by coincidence, large rectifier diodes were also based on Se and Cu_2O grown on metal substrates, but crystalline silicon (c-Si) with high purity was starting to become popular in the mid-1900s.

The similarities found between the rectifying and PV cells, led to the use of c-Si in a PV cell for the first time (1941) a *p*-*n* junction, in the Bell Laboratories.[12] Silicon-based PV cells gain attention after the physics of a *p*-*n* junction was explained by Shockley,[13] and an improved version of a solar cell was presented in 1954.[14] Further, the theoretical model for junctions between different materials (heterojunctions) was developed by Anderson in 1960.[15]

In 1964, Si solar cells were used for the first time in space, in the satellite Vanguard 1, however, its use on terrestrial applications was not possible due to birds damaging the costly modules. Nevertheless, after the first oil shock in 1973, research in PV noted a reduction of the cost and today is being widely deployed.

1.3 *p*-*n* junction and photovoltaic effect: qualitative fundaments

The main component of a PV system is the solar cell, the part capable of converting the incident light into electricity. Various processes can produce an electric current by illumination, but the PV effect is particularly referred to as the excitation of an electron from the valence band to the conduction band, on light illumination, followed by the separation of the electron-hole

pair generated. This was possible due to the intrinsic properties of semiconducting materials.

Semiconductors possess a band-gap, the energy that electrons need to move from the valence band to the conduction band. The band-gap is formed due to forbidden electron states due to Pauli's exclusion principle applied in a crystal lattice. Only light with an energy higher than the band-gap will be able to excite an electron. An excited electron will leave a hole in the valence band. This hole can be considered as a positive charge equivalent to an electron since it can freely move and participate in the conductivity of the material. The electron-hole pair remains linked as a pseudo-particle known as an exciton.

Excitons are metastable, so the electron will eventually recombine back with the hole, either by re-emitting a photon or by losing the energy in the form of heat. The second step in the PV effect is to avoid the recombination by the separation of the electron and hole. To do this, the effect of doping a semiconductor is exploited.

Doping of a semiconductor occurs by the substitution of a relatively low quantity of atoms with other elements. Introducing phosphor atoms (with 5 electrons in the last orbital) in a silicon lattice (4 electrons) implies adding unbounded electrons, which are already excited at room temperature, largely increasing the number of electrons in the conduction band. A semiconductor with a higher number of electrons than holes is *n*-type. A similar situation happens if boron (3 electrons) is added instead of phosphor, but the "missing" electron acts as a hole, which increases the number of holes in the valence band, producing a *p*-type material. Semiconductors other than silicon can be admitted as external dopants, but usually have a natural "doping" produced by the intrinsic defects in the lattice, and extrinsic doping is only used to improve particular properties.

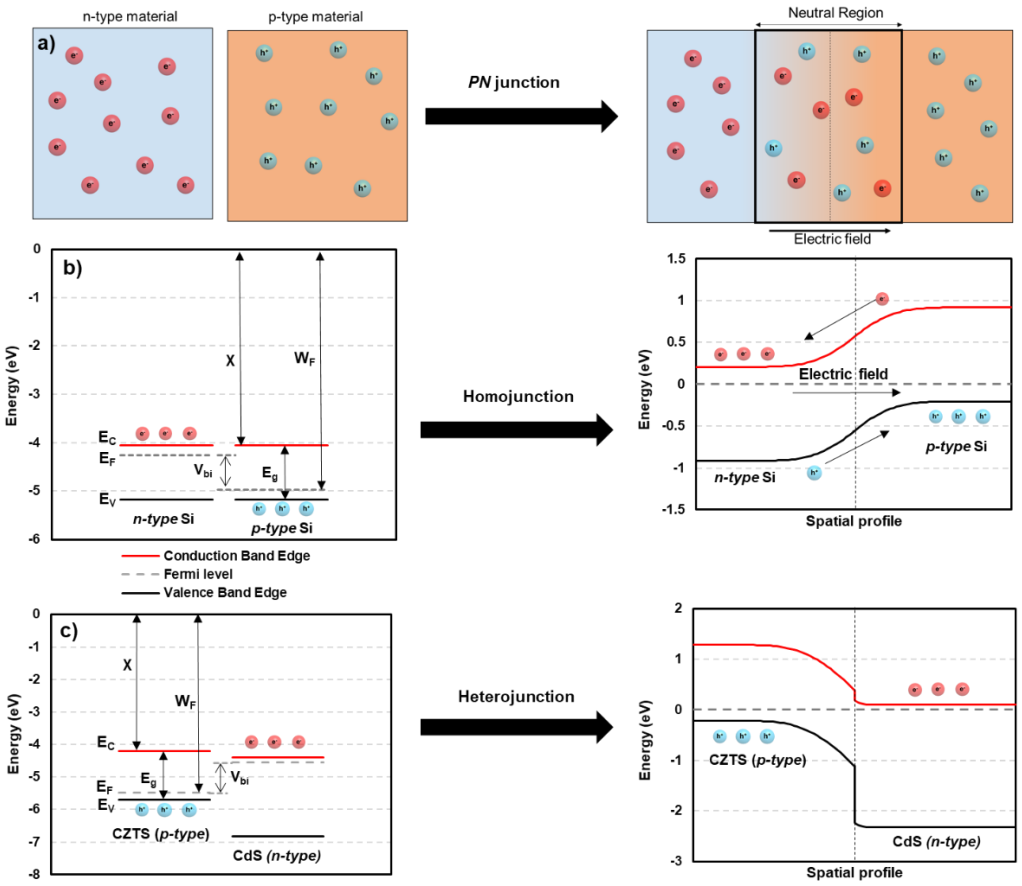

Figure 1.3. a) Schematic representation of the charge in a *p-n* junction, b) energy levels respect the vacuum of *p-type* and *n-type* silicon, and the homojunction they form, changing the reference to the fermi level. c) energy levels of materials with different chemistry and the heterojunction they form.

A *p-n* junction forms when a *p*-type and an *n*-type material are in contact. The difference in charge is compensated by electrostatic attraction resulting in an electric field along the interface. Some charges will be able to diffuse, forming a neutral region in the interface, as represented schematically in **Figure 1.3a**. The nature of the junction can be deducted from mainly three properties of the materials in contact.

- Band-gap (E_g): Energy that an electron needs to promote from the valence band (E_V) to the conduction band (E_C). This energy is provided by the photons. This property depends on the atomic structure of a solid and its composition, while has low sensitivity to doping.

- The Fermi level (E_F): It comes from the Fermi-Dirac statistics to help quantify the free carriers in a semiconductor. The statistics define it as a virtual energy level where an electron has a 50 % chance of getting excited spontaneously at any temperature. It can be also considered as the average energy of a solid. The Fermi energy is highly sensitive to doping and defects. The work function (W_F) is the energy required to extract an electron from the surface of a solid to the vacuum level, which is in average the energy difference between the vacuum and Fermi levels.
- Electron affinity (χ): Defined as the energy released when an electron is added from the vacuum to the surface of the material, which corresponds in semiconductors to the energy between the conduction band and the vacuum level. This property depends mostly on the chemistry and atom bounds in the surface, so the bulk doping usually does not have a significant impact.

Either the vacuum or Fermi level can be used as a *zero* reference to define the energy level of each property, but is the energy difference between the properties the critical point. **Figure 1.3b** represents the energy levels with respect to the vacuum of *n*-type and *p*-type silicon. They possess the same band-gap and electron affinity, but different work function. When a junction is formed, the reference used to represent the energy levels is the Fermi level, since is constant along the juntion. As result, the electric field emerges from the matched fermi levels, bending the conduction and valence bands. The difference in work function defines the built-in potential (V_{bi}), which is the electrostatic potential for the separation of the electron-hole pairs.

The model of Anderson can be used in case of having different materials with different band-gaps and work functions, as in the case of **Figure 1.3c**. Discontinuities in the bands are produced in the junction, which creates different barriers for holes and electrons. Engineering this effect can be used to selective block electrons or holes. However, this model does not take into

account possible defects created in the interface between different materials, and it can fail to predict the nature of the junction. These defects can modify both the Fermi energy and work function in the interface and must be taken into account in most cases.

Under illumination, electron-hole pairs are generated, breaking the equilibrium, and two pseudo-fermi levels are formed, one for electron and a second for holes. In the PV effect, the electric field formed by the *p*-*n* junction can separate the electron-hole pairs created by light illumination, maintaining electrons at the *n*-side and holes at the *p*-side (**Figure 1.4)**. Finally, the electrons and holes are extracted through contacts into an electric circuit in the form of an electric current able to generate work.

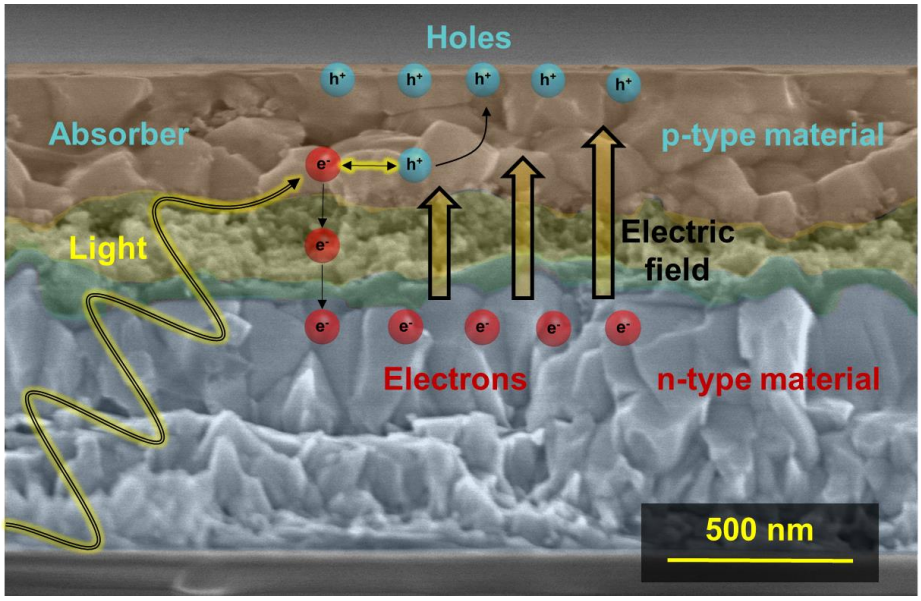

Figure 1.4. Scheme of the PV effect over a cross-section SEM image of a PV solar cell.

A similar effect can occur when a semiconductor is in contact with metal. In metals, the Fermi energy is not situated in a forbidden state of a bandgap, but in an allowed state inside a band, so electrons already participate in the conductivity. Between a metal and a semiconductor, the type of junction depends only on the difference between the work functions of the materials. This is known as a Schottky contact and should be taken into account to avoid the formation of barriers, or to improve the PV effect in the contacts.

1.4 PV physics and characterization

1.4.1 Characteristic parameters of a solar cell

The most significant characteristic of a solar cell is the current-voltage (*I-V*) or more commonly the current density-voltage curve (*J-V* curve). Both current and voltage vary depending on the charge applied. In the circuit shown in **Figure 1.5a**, a scan through different charge values reveals the characteristic *I-V* curve of the solar cell, (**Figure 1.5b**). By agreement, the current generated is considered positive. Under a short circuit, the photocurrent is maximum. This is the I_{SC} of the solar cell, which is, ideally, directly proportional to the illumination intensity, and becomes zero under dark conditions. The current decreases when the voltage starts to increase until the open circuit condition is reached, where the maximum photovoltage V_{OC} is obtained. Between the short and open circuits, we can extract useful power, since the power is the product $P = I \cdot V$. Consequently, the maximum power extracted from the PV cell is obtained at the point where the product is maximum. In the most ideal case, the maximum power extracted is $P_{MP}=I_{SC} \cdot V_{OC}$, but losses in current and voltage lead to a lower value of power extracted. The parameter accounting for these losses is the fill factor (*FF*), which is defined in *(Eq. 1.1)* by the difference between the real and ideal values, where V_{MP} and I_{MP} are the values of voltage and current measured at the maximum power point.

$$FF = \frac{V_{MP} \cdot I_{MP}}{V_{OC} \cdot J_{SC}}$$

(Eq. 1.1)

The relation of the output with the illumination power defines the maximum power conversion efficiency (η) of the solar cell defined by (*Eq. 1.2*).

$$\eta = \frac{V_{OC} \cdot I_{SC} \cdot FF}{P_{Ligth}}$$

(Eq. 1.2)

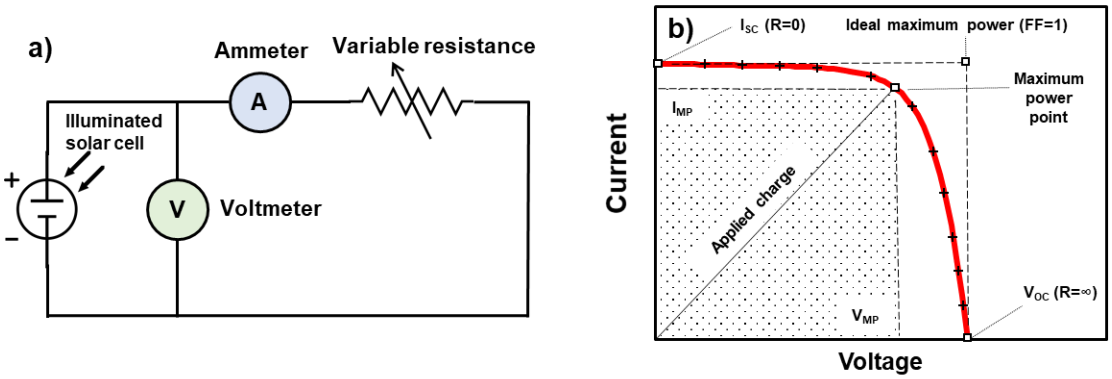

Figure 1.5. a) Circuit test for an *I-V* curve. b) Characteristic *I-V* curve of a solar cell.

For a deeper analysis of the PV properties, the *I-V* curve can be modelled with a characteristic circuit. Since a solar cell is equivalent to a diode, a basic circuit model can be modelled by a current source in parallel with a diode, where we impose the condition of $I(V=0)=I_{SC}$. Consequently, the *I-V* curve can be modeled by *(Eq. 1.3)*.

$$I(V) = I_{SC} - I_0\left(e^{(qV/nkT)} - 1\right)$$

(Eq. 1.3)

Where I_0 is the reverse saturation current of the diode, q is the electron charge, n is the diode ideality factor, which accounts for recombination processes, k is the Boltzmann constant and T is the temperature.

However, this model does not take into account the resistances that affect significantly solar cells. A series resistance (R_S) that agglomerates all the resistive components of a solar cell, and a shunt resistance (R_{SH}), which

represents any possible shunt path, will decrease the performance of the solar cell, have an impact mostly on the FF. The one diode model, represented in **Figure 1.6**, consists of a current source I_L with a diode and adds the series and shunt resistance. The *I-V* curve of this model can be calculated by *(Eq. 1.4)*. This model also defines the *I-V* curve in dark, which is the particular case when I_L=0. However, this model neglects the recombination in the junction by supposing a constant diode factor. The variation in the ideality factor can be modelled by adding a second diode. The first diode, with an ideality factor n_1 close to 1, represents the bulk recombination, while the second diode, with a less ideal n_2 value approaching 2, represents the recombination in the junction that dominates at low voltage or low irradiation level. The *I-V* curve of the double diode model is calculated by *(Eq. 1.5)*.

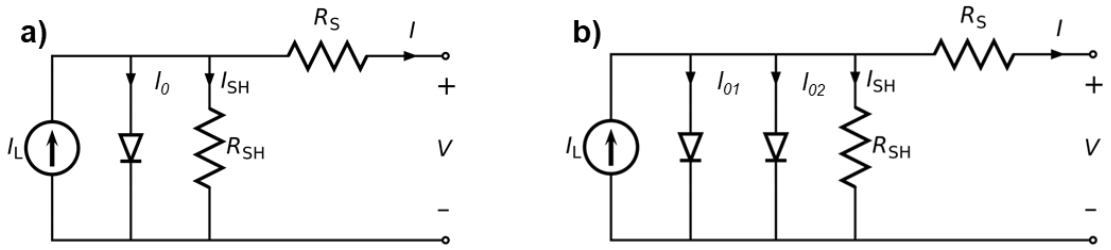

Figure 1.6. a) One diode and b) double circuit model for a solar cell.

$$I(V) = I_L - I_0\left(e^{(q(V-IR_S)/nkT)} - 1\right) - \frac{V - IR_S}{R_{SH}}$$

(Eq. 1.4)

$$I(V) = I_L - I_{01}\left(e^{(q(V-IR_S)/n_1kT)} - 1\right) - I_{02}\left(e^{(q(V-IR_S)/n_2kT)} - 1\right) - \frac{V - IR_S}{R_{SH}}$$

(Eq. 1.5)

As a drawback, these models do not have an analytical solution, and iteration methods are required to solve the equation in most cases. The double diode model usually requires more time, especially when more parameters (temperature, irradiation…) are taken into consideration.

1.4.2 Spectral response

The efficiency that photon is converted from electromagnetic to electric energy will highly depend on its wavelength. The spectral response of a solar cell can be evaluated by external quantum efficiency (EQE). EQE provides the efficiency of photon-to-electron conversion which depends on the photon wavelength, and provides information about the different loss mechanisms for the current. A scheme of the losses is shown in **Figure 1.7a**, explained by different mechanisms:

- As previously mentioned, the absorption of light depends on the band-gap of the absorber material used, and the materials are transparent to photons with lower energies than its band-gap. Naturally, non-absorbed photons are not converted and do not contribute to the current, as marked in red in **Figure 1.7a**.

- Small responses may be observed below the band-gap, marked in purple. This response is due to tail states, energy states that are close to the valence or conduction bands (in the order of kT), that can emerge from an excess of undesirable defects. The tail states strongly reduce the photo-voltage since they increase losses by charge thermalization.

- The green marked area represents the losses of photons with energy close to the band-gap. These photons are absorbed deeper in the material or close to the back surface. Consequently, deep excitons with insufficient lifetime are recombined before the charge separation.

Defects in the back surface increase the recombination in this region. An insufficient thickness of the absorber layer produces a low absorption in this range.

- The marked area in blue is the losses from the short wavelengths. The main loss comes from the absorptions of the photons by other materials rather than the absorber layer, such as a glass substrate, the TCO, or the buffer layer, which in general has a low capacity for separating the electron-hole pairs. Since these photons are absorbed close to the front surface, the surface defects also increase the exciton recombination.

- Grey area represents, the general current losses, such as light reflected, shunt paths, high resistance, or combination with the previous mechanism mentioned.

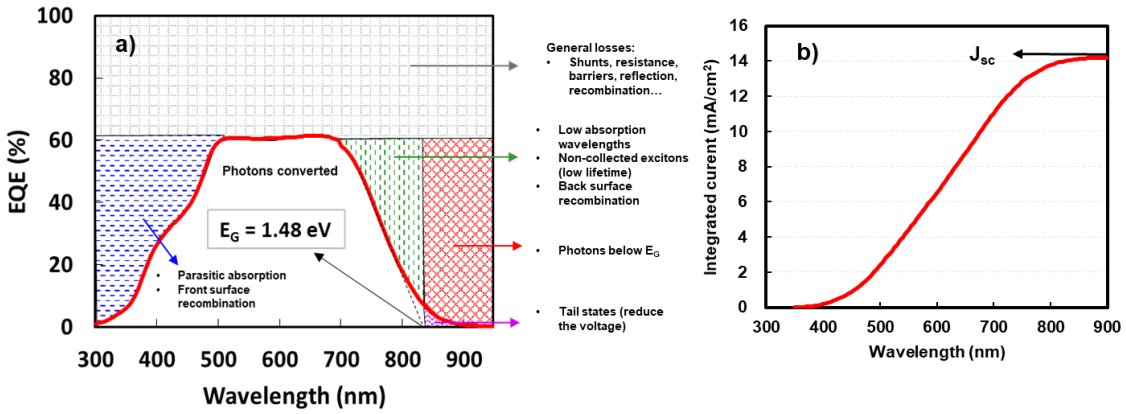

Figure 1.7. a) Example of an EQE spectrum from a CZTS solar cell, indicating the visible loss mechanisms and the band-gap, and b) integrated current calculated over the solar spectra.

This characterization can be made by measuring the generated current of the solar cell when is illuminated with a source of known wavelength and power. Typically, these measurements are made under short circuit conditions, but it can be done under other conditions to change the response of certain

mechanisms, such as the increase of collected excitons under reverse polarization.

An advantage of the EQE is that the current produced by a solar cell, under any kind of illumination, can be calculated using (*Eq. 1.6*) of integrated current.

$$J = \int J(\lambda)\, d\lambda \; = q \int \frac{G(\lambda)}{E_\lambda(\lambda)}\, EQE(\lambda)\; d\lambda = \frac{q}{hc} \int \lambda\, G(\lambda)\, EQE(\lambda)\; d\lambda$$

(Eq. 1.6)

Where $J(\lambda)$ is the wavelength-dependent current density, $G(\lambda)$ is the irradiance spectrum and $E_\lambda(\lambda)$ is the photon energy, q is the elementary charge, h is the Planck constant, and c is the speed of light.

If the integrated current is calculated for the solar spectrum, and the EQE is measured under a short circuit, the corresponding value of current is equivalent to the J_{SC} value measured in the *J-V* curve. An example of a calculated short circuit current by this method is shown in **Figure 1.7b**.

1.4.3 Shockley-Queisser limit

The main objective of PV cells is to convert sunlight into electricity, thus taking into account the solar spectra is of special interest. However, the solar irradiance significantly changes along the day, year period, and latitude. For the measurement of solar cells, a reference spectrum is used to properly compare. For terrestrial applications, the standard irradiance used is AM 1.5G, which is representative of an average sunny day with 1000 W/m^2. In the spectrum, the absorption from the atmosphere is considered to be 1.5 air mass (AM 1.5), and both direct and diffuse irradiance is considered as global (G). For a different application, when it is used in space, a different spectrum

has to be considered (AM0). Both these spectra are represented in **Figure 1.8a**.

In the previous section, we took into account the limitations for the photo-current depending on the band-gap of the absorber material. The photo-voltage is also limited by the built-in potential, which in turn cannot be higher than the lower band-gap, typically, the absorber band-gap. The energy of photons with higher energy than the band-gap is lost in form of heat by a fast decay (thermalization) of the exciton to the band edges. In addition, as shown by the model of *(Eq. 1.3)*, the temperature has an impact on the reduction of the voltage and *FF*.

Therefore, a compromise between the voltage and current, considering the solar spectrum, can be calculated as a function of the band-gap to find the best suitable values for terrestrial applications. The efficiency limitation is known as the Shockley-Queisser limit,[16] and can be used as a reference to find suitable absorber materials. The values of this limit for the basic PV parameters are shown in **Figure 1.8b**. The best band-gap values, with an efficiency limit higher than 30%, are in the range between 1−1.6 eV.

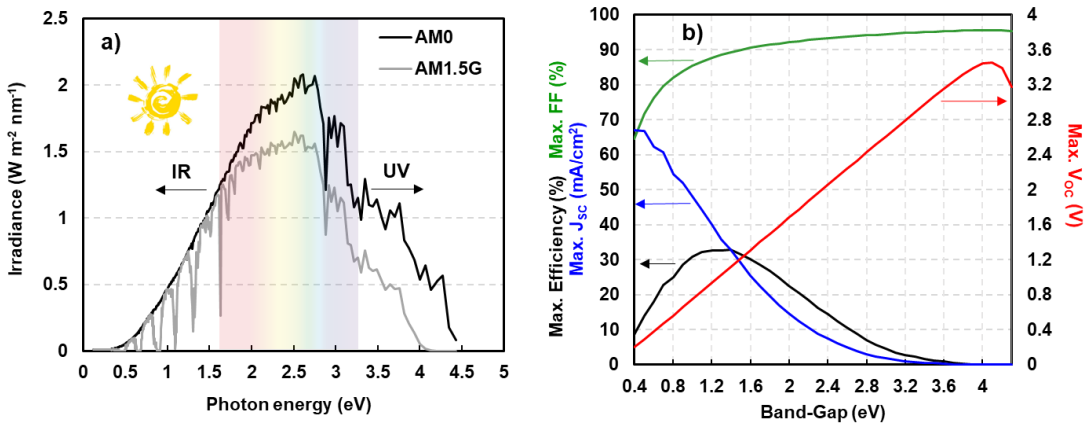

Figure 1.8. a) Spectral irradiance of the Sunlight, extra-terrestrial and under AM1.5G. (data source: *NREL*), and b) Shockley-Queisser limit of the PV parameters depending on the absorber band-gap.[16,17]

1.4.4 Stability and maximum power point tracker

Ideally, a PV cell should work mostly close to the maximum power point (MPP) to maximize the energy conversion. However, in realistic situations, the MPP fluctuates depending on various parameters (such illumination, dielectric polarization of the materials, temperature, emerging shunts, degradation…) and is not a static point. Evaluating the evolution of the MPP over time is of high importance for the development of new materials for PV application, and it can mark the difference between functional and practical materials.

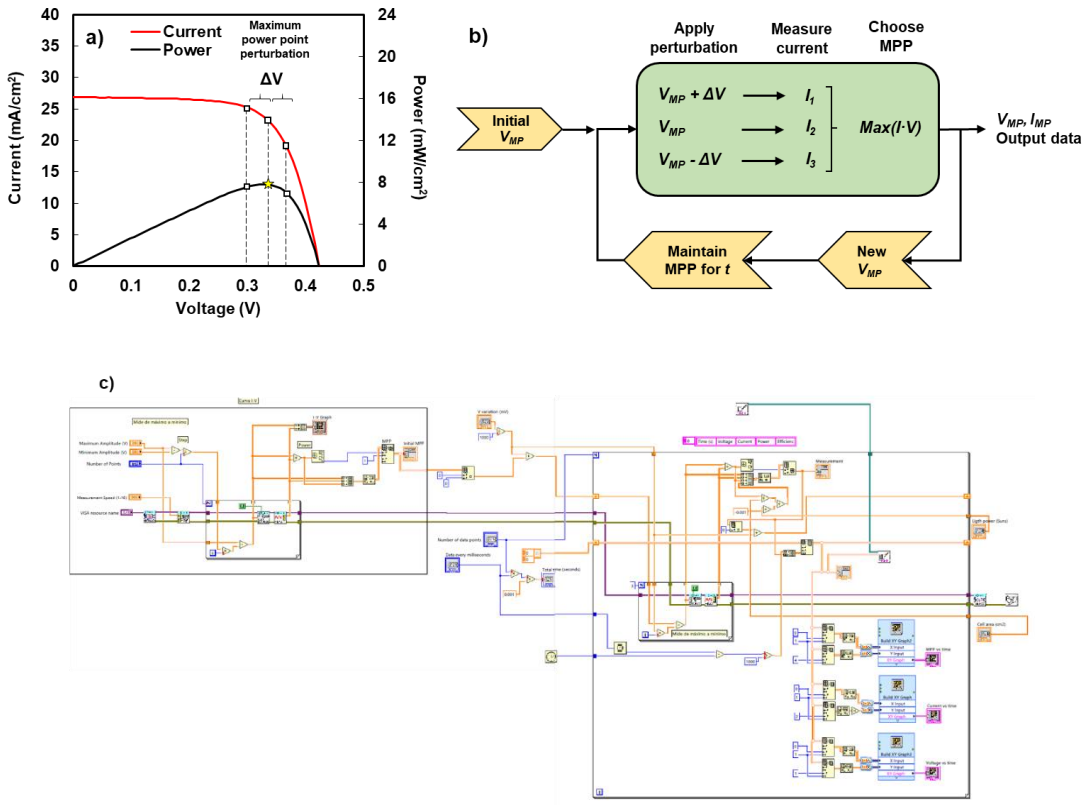

Figure 1.9. a) *J-V* and *P-V* curves of a solar cell, indicating the perturbation in the MPP, b) working flow scheme of the perturbation-observation method used, and c) block diagram used to prepare the MPP tracker on LABVIEW for a Keithley source meter.

During this thesis, a MPP tracker software was developed, mostly to evaluate the stability under constant working conditions or accelerated degradation test of solar cells by temperature and humidity. The method used for the

MPP tracking was the perturbation-observation.[18] Considering the same test circuit of **Figure 1.5a**, this simple method consists of applying small and periodical perturbations on charge (or the V_{MP} in the practice) to evaluate if the MPP has changed, as shown in **Figure 1.9a**. The new MPP can be used as feedback to repeat the process indefinitely, as shown in the flow scheme of **Figure 1.9b**. The LABVIEW block diagram of the developed software applying this method is shown in **Figure 1.9c**.

This method has the advantage over merely measuring the *I-V* curve periodically since the hysteresis effects are minimized. In addition, this method is already one of the most used in PV installations due to its simplicity, accuracy, and low-cost implementation. However, it has some limitations in comparison with other techniques, such as deviations from the MPP due to low-speed tracking in case of rapid changes of the conditions,[19] which is not significant in our case.

1.4.5 Impedance spectroscopy

Electrochemical impedance spectroscopy (EIS) is a non-destructive characterization tool used to study electronic devices. This characterization technique can be adapted to various applications depending on the type of device and its characteristics, and it is particularly effective in exploring chemical and electrical processes on interfaces.

The impedance has a resistive and a reactive component. The reactive component is only observed under an alternate signal, so it can be represented as the imaginary part of a complex number, while the resistive component is represented as the real part following the *(Eq. 1.7)*.

$$Z = Z_{Real} + i\, Z_{Im}$$

(Eq. 1.7)

The measurement of the impedance is based on the changes that the device incites an applied alternate signal, typically sinusoidal. A small voltage amplitude (typically from 10 to 50 mV) is chosen to ensure a linear response ($dQ \approx C dV$). As shown in **Figure 1.10a**, the current amplitude reduction will be due to the resistance component, while the phase shift will be due to the reactive one. The reactance can be modelled in electric circuits by capacitive and inductive elements, where usually the capacitance is defined as negative values and the inductive as positive.

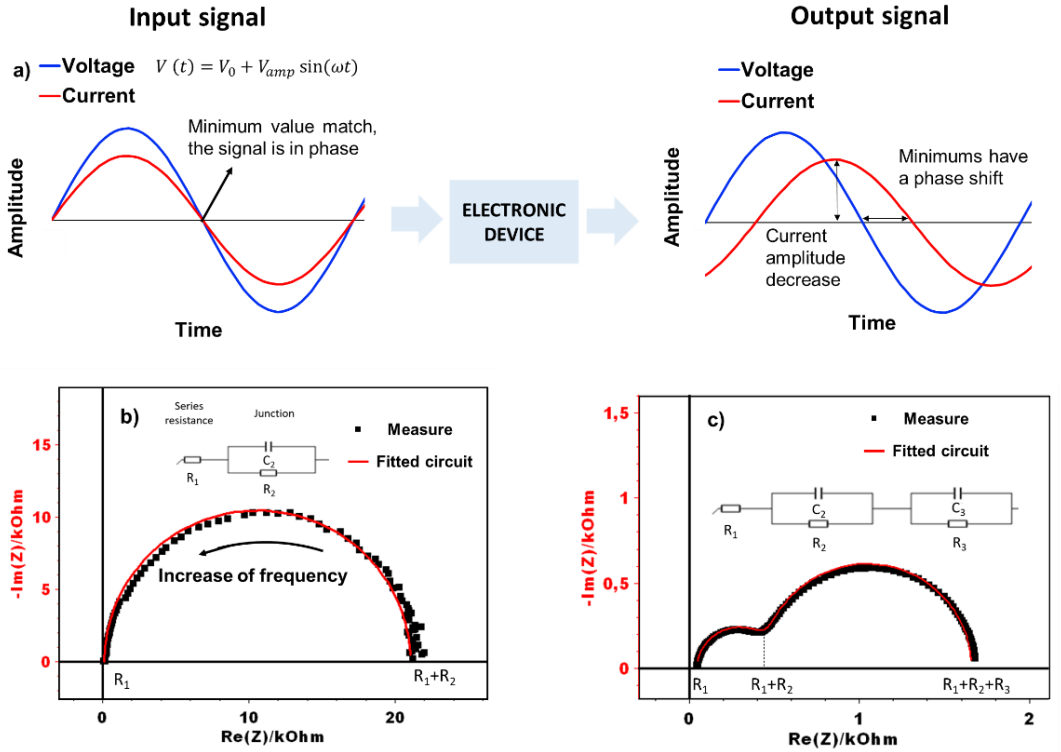

Figure 1.10. a) Scheme of how an impedance measurement is performed, b) Nyquist plot of a typical CZTSe solar cell, fitted with a junction circuit, and c) solar cell where two processes appear, fitted with a double-loop circuit.

The impedance is highly dependent on the frequency of the applied signal, since the physical process involved occurs at a particular time scale, and will be sensitive only to frequencies close to that time scale. A common and useful representation of the impedance is by the Nyquist diagram (also known as Cole-Cole plot), where the imaginary part is plotted in the y-axis, and the real in the x-axis. The representation of impedance points at different

frequencies results in curves that can be fitted in particular circuits to acquire useful information about the measured system if a physical correlation can be made for each element.

In solar cells, the most simple and useful circuit fit that works is a series resistance with a capacitor and a parallel resistance, as shown in **Figure 1.10b**. The capacitance behaviour appears in the *p-n* junction due to the potential difference between the materials, and separation between them by the depletion region, which acts as a dielectric. At high frequencies, only the series resistance of the materials remains, ideally 0, while the parallel resistance represents the reverse current through the junction, known as recombination resistance. High values of recombination resistance are desirable to avoid losses. However, more processes usually occur in a solar cell, which requires a complex circuit to explain them. Every non-ohmic interface will add a visible effect in the impedance spectra, adding new loops of capacitance and resistance,[20,21] as shown in **Figure 1.10c**. Other processes such as trap states, barriers, or ion diffusion can have an equivalent effect on the impedance, so this method is a good technique to detect these problems in solar cells, however, if many processes are involved, the association with a physical parameter can be ambiguous.

For every loop, a characteristic time τ can be calculated by $\tau = RC$, which represents the discharge time of the capacitor. In thin films, the large arc is associated with the charge recombination process in the *p-n* junction, which dominates at low frequency, and its characteristic time is associated with the charge lifetime or recombination time. At high frequency, a second and smaller arc is usually obtained, which represents a faster process, and is associated with the minority carrier diffusion. [22,23] The characteristic time of this arc represent the transit time τ_{tr}, and is associated then with the minority carrier diffusion coefficient D_n of the absorber layer by *(Eq. 1.8)*.[21,24]

$$D_n = \frac{L^2}{R_{tr}C_\mu} = \frac{L^2}{\tau_{tr}}$$

(Eq. 1.8)

Sometimes, a constant phase element (CPE) is used instead of a capacitor. A CPE is equivalent to a capacitor, but with a factor *a*, that aggregates the non-ideal resistances and capacitances. In these cases, the characteristic time can be calculated by the $\tau = (RQ)^a = RC$, where Q is the equivalent capacitance of the CPE.

1.4.6 Capacitance-Voltage

In the input signal, the constant voltage V_0 can be modified to explore the different properties of the solar cell. The measure of the capacitance at different voltages can be made by the method previously explained, fitting the curve in the Nyquist plot for every voltage, but is also popular to use a fixed frequency and measure the capacitance supposing a simple series or parallel RC circuit, both showed in **Figure 1.11a**. Calculating the capacitance in this way must be completed carefully, and only under certain conditions.

First, this approximation is only valid when the main contribution to the impedance is from the recombination in the *p-n* junction (only one arc dominates in the Nyquist plot). This limits the approximation to voltage values below the built-in potential. Above the built-in potential, the capacitance of the junction disappears and other processes, such as a diffusion capacitance, have a bigger impact. From the impedance equations of a R_SC circuit *(Eq. 1.9)*, a R_PC circuit *(Eq. 1.10)*, and R_SR_PC *(Eq. 1.11)* is demonstrated that for a frequency higher than $1/R_PC$, the capacitance calculation is equivalent to a RC series circuit in all cases. This is the most common way since a high-frequency measurement is faster, has higher precision, and is less sensitive to secondary processes, as can be noted in

Figure 1.11b. However, a low-frequency measurement can be used in some cases, where the capacitance calculation will be approximated to a parallel RC circuit (**Figure 1.11c**).

$$Z_{R_SC} = R_S + \frac{1}{i\omega C}, \qquad \boldsymbol{Im(Z_{R_SC}) = \frac{-1}{\omega C}}$$

(Eq. 1.9)

$$Z_{R_PC} = \frac{R_P}{1 + i\omega R_P C} = \frac{R_P}{1 + (\omega R_P C)^2} - i\frac{\omega C R_P^2}{1 + (\omega R_P C)^2},$$

$$For\ \omega \gg \frac{1}{R_P C} \rightarrow \boldsymbol{Im(Z_{R_PC}) \approx \frac{-1}{\omega C}};$$

$$For\ \omega \ll 1/R_P C \rightarrow \boldsymbol{Im(Z_{R_PC}) \approx -\omega C R_P^2}$$

(Eq. 1.10)

$$Z_{R_SR_PC} = R_S + \frac{R_P}{1 + i\omega R_P C},$$

$$For\ \omega \gg \frac{1}{R_P}\ C \rightarrow \boldsymbol{Im(Z_{R_PC}) \approx \frac{-1}{\omega C}};$$

$$For\ \omega \ll 1/R_P C\ and\ R_P \gg R_S \rightarrow \boldsymbol{Im(Z_{R_PC}) \approx -\omega C R_P^2}$$

(Eq. 1.11)

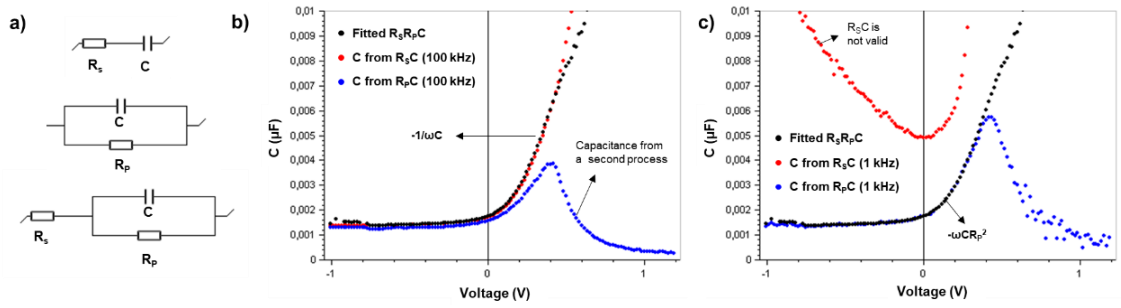

Figure 1.11. a) Scheme of a series RC circuit, a parallel RC circuit, and an R_SR_PC circuit. b) Capacitance-Voltage with the capacitance calculated from the three circuits at 100 kHz, and c) at 1 kHz.

In the case of using a CPE, or when other effects rather than the junction capacitance are not negligible, these approximations lose reliability and the

calculations may be complex. The only valid method is in cases, is the fit of a proper circuit in a Nyquist-Voltage map (**Figure 1.12a**).

The capacitance of the junction is presumed to follow the geometric capacitance of *(Eq. 1.12)*, so it can be directly related to the depletion width.

$$C = \varepsilon_0 \varepsilon_r \frac{A}{W}$$

(Eq. 1.12)

C is the capacitance, ε_0 is the vacuum permittivity, ε_r is the relative permittivity, A is the active area of the cell and W is the depletion width.

Physically, the change of the voltage modifies the carrier density in the borders of the device, and so the depletion region, following the *(Eq. 1.13)*. Typically, the buffer layer required a high-density carrier concentration $N_D \gg N_A$, so most of the depletion width falls in the absorber and the equation can be simplified as the *(Eq. 1.14)*.

$$W_{pvn} = \sqrt{\frac{2\varepsilon_0 \varepsilon_r}{q(N_D + N_A)} \frac{N_{DvA}}{N_{AvD}} (V_b - V)}$$

(Eq. 1.13)

$$W = W_p + W_n = \sqrt{\frac{2\varepsilon_0 \varepsilon_r}{q} \frac{N_D + N_A}{N_D N_A} (V_b - V)} \approx \sqrt{\frac{2\varepsilon_0 \varepsilon_r}{q N_A} (V_b - V)}$$

(Eq. 1.14)

W_p and W_n are the widths of the depletion region in the p and n sides, respectively, ε_r is the relative permittivity, N_D is the donor concentration of the n-type material, N_A is the acceptor concentration of the p-type material, and V_b is the built-in potential.

It can be noted that the depletion width can be ideally enlarged without limitation with the increased reverse voltage, but for working solar cells, in

particular thin films, this process can be limited by several factors such the thickness, shunts, or recombination, and the region where is valid have to be chosen carefully.

Combining the equations *(Eq. 1.12)* and *(Eq. 1.14)*, a relation between the capacitance and the acceptor concentration is obtained in (*Eq. 1.15*). This relation is only valid for $V<V_b$ to keep the meaning of the equation *(Eq. 1.14)*. The built-in potential can be also calculated by the Mott-Schottky plot. Plotting $1/C^2$ versus the voltage will follow a linear trend with the decrease of V and ideally become zero at the built-in potential. A stimulating procedure is to plot the acceptor concentration as a function of the depletion width, which gives an idea of the defects in the interface, as shown in **Figure 1.12b**.

$$N_A(W) = \frac{2C^2}{q\varepsilon_r\varepsilon_0 A^2}(V_b - V)$$

(Eq. 1.15)

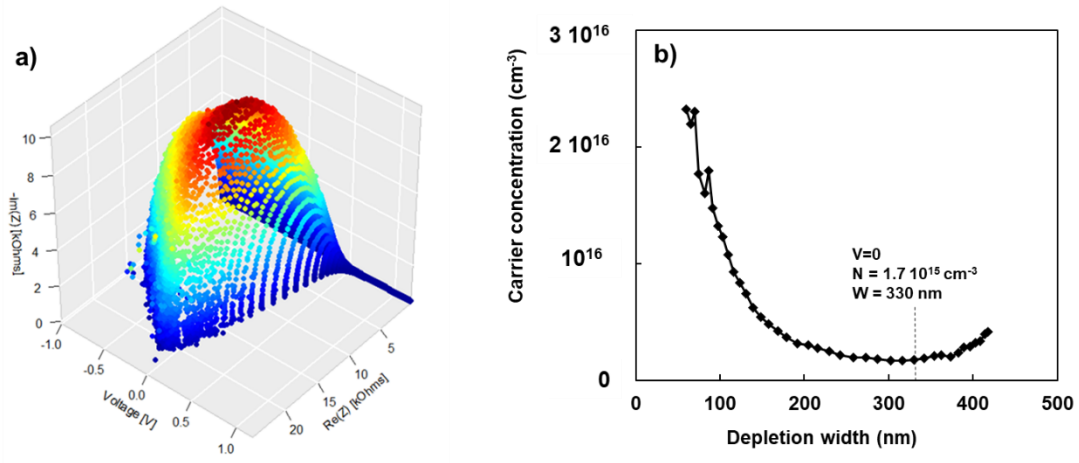

Figure 1.12. a) Nyquist-voltage map of a typical CZTSe solar cell. b) Carrier density profiling, indicating the values at open circuit voltage.

Additionally, is worth mentioning other common techniques derived from impedance reported in the literature. Temperature dependence impedance

can provide additional information about the interface traps. Analyzing the capacitance change due to freeze of the traps, the energy level and density of states of the traps can be obtained. On the other hand, drivel-level capacitance profiling (DLCP), is a variation of the *C-V* technique, where the voltage amplitude (V_{amp}) of the input signal is increased and varied (typically higher than 50 mV) to have a non-linear response of the capacitance.[25] Calculating the non-linear terms of the capacitance can be used as an alternative way to calculate the carrier density with higher sensitivity to deep defects. A combination of DCLP with temperature variations can bring also information about the activation of the defects, while another variation can be the effects of light soaking on the charge density.

1.5 PV materials and technologies

Materials with desirable properties to perform the role of the light absorber in a solar cell are limited. For new materials, several years of research are required for the optimization, which makes the current choices in the PV market quite limited. The light absorber material used defines the PV generation. Three generations of photovoltaic technologies exist.

1.5.1 First generation

The first generation of PV comprises those wafer-based technologies, which mostly refer to either mono or polycrystalline silicon.

Crystalline silicon-based PV was the first successful technology. It is fully commercial and dominates 95% of the market. One of the obvious advantages of these solar cells is they are composed only of one main element (Si), which facilitates the crystal growth processes. Si crystals are grown by melting and controlled cooling, producing polycrystalline bulk or a monocrystalline if the Czochralski method is used. Si is also highly abundant in the earth's crust, which ensures a shortage or cost variations of raw material very unlikely. Crystalline Si possesses a band-gap of 1.1 eV, which is in the range of values to get a good efficiency under sunlight

illumination, with a theoretical limit of 32%, and current records of 26.1 % and 23.3 % for mono and polycrystalline respectively in lab scale. Due to its unique properties, it will dominate the large-scale PV electric generation for coming years.

However, it has some limitations. Si demands a relatively high thickness, of hundreds of microns, for the wafer material to absorb enough light due to its indirect band-gap and low light absorption coefficient. Moreover, natural Si is found in form of SiO_2 with many impurities, and requires multiple purifications and synthesis processes with costly and dangerous chemicals and high temperatures, setting a strong limit for the cost production.

1.5.2 GaAs and III-V compounds

Between the first and second generations, we can find GaAs and other III-V compounds. This technology has not dominated the PV market significantly, but they are of interest in other aspects. Binary compounds were proposed to imitate and improve the properties of crystalline Si, by mixing elements close to Si in the periodic table. They are based on a mix of elements of columns III and V from the periodic table. GaAs was the first successful material with improved PV properties than Si, since it possesses a direct band-gap with a value of 1.44 eV and requires thinner thickness. GaAs holds currently the efficiency record of a single junction of 29.1% and 30.5% under light concentration. In multi-junction cells, a combination of various III-V materials can produce an impressive 47.1% of power conversion efficiency.

Despite the high efficiencies of this technology, the cost of fabrication of these solar cells is extremely high and impedes their large-scale commercialization. Its applications are limited to supply power in space exploration and small energy generation under light concentration.

1.5.3 Second generation

The second PV generation is focused on overcoming the Si limitations. It is based on materials with a higher absorption coefficient that allows its usage in thin films, in the order of a few μm or less, so the raw material usage can be largely reduced. The low thickness also allows the development of flexible and lightweight solar cells, creating new applications where the use of Si-based PV is difficult.

Thin-film PV is of significant interest since they have a high potential to meet the increasing energy demand.[26] Thin-film PV technologies have advantages in the manufacturing processes, offering fast deposition processes for large-scale PV production, less usage of raw elements, and low energy paybacks and carbon footprint.[27] Furthermore, they provide aesthetics in applications where lightweight, flexible, or semitransparency is required. These advantages are of special interest on the emerging energy applications, such as long-term powering of outdoors and indoors sensors, the internet of things, building integration PV, or small decentralized installations for self-consumption.[28]

This generation includes amorphous silicon (a-Si), CdTe, and Cu(In,Ga)Se_2 (CIGS), which were started to be developed in 1970 decade. All of them have a relative commercial success, entailing currently around 5 − 10 % of the PV market. CdTe in particular, commercialized by First Solar in 2002 with only a 10.4 % module efficiency, has been the most successful one and the efficiency has also increased. CdTe is considered the technology with a lower CO_2 print and faster energy payback. Despite the low use of raw material, its main disadvantage is found in the composition itself. As shown in **Figure 1.13**, Te is a very rare element and has a high risk of shortage, while in the case of CIGS, In is considered a strategic element due to its intensive use in ITO for touch screens and electronic devices, while Ga is expensive to purify. On the other hand, a-Si is the most environmentally friendly, since possessing the advantages of both being abundant and thin

film, however, it has a relatively high band-gap, of 1.75 eV, and high voltage loss, making its efficiency relatively low in comparison with other PV technologies. Also suffers from low stability under light (Stabler-Wronski Effect), which reduces the solar cell lifetime. These limitations raise doubts about their gigawatt-scale production.[29]

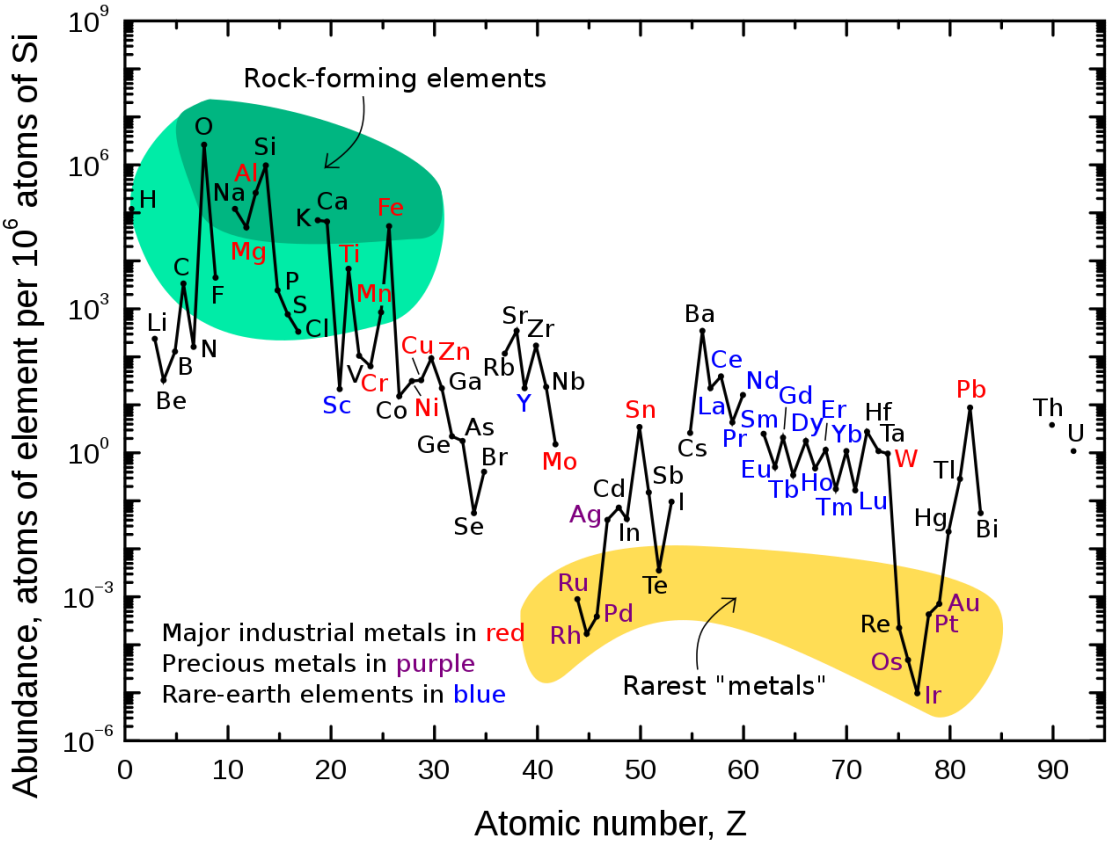

Figure 1.13. Element abundance in Earth crush. (source: Abundance of the chemical elements, Wikipedia, adapted from [30])

1.5.4 Third generation

The third generation of PV aims to find materials and new concepts with the potential to further reduce the cost, by using earth-abundant elements, low synthesis temperatures, or new applications such as semi-transparent solar cells. This generation encompasses a variety of PV technologies with the potential for commercialization. Dye-sensitized (DSSC), organic (OSC), quantum dots (QD), various types of inorganic materials, and perovskites

solar cells (PSC) are the most relevant technologies of the third generation. A summary of the properties for every PV technology can be found in **Table 1.1**.

Table 1.1 Characteristics of main PV technologies (single junction, November 2021).

Gen.	Technology	Thin film	Cost	Efficiency [31,32]	Stability	Comments
1º	Crystalline Si	No	High	26.7 %	Years	High purity and quantity of material required results in high cost.
N/A	GaAs, III-V	Yes*	Very high	29.1 %	Years	High-cost deposition methods. Attractive for multi-junction, space and concentration applications.
2º	Amorphous Silicon	Yes	Low	14 %	Months	Applications in low power devices and BIPV.
	CdTe	Yes	Medium	22.1 %	Years	Risk of Te shortage.
	CIGS	Yes	Medium	23.4 %	Years	Risk of In and Ga shortages.
3º	Inorganic (Kesterite)	Yes	Low	13 %	Years	Ideal candidate if the efficiency can be increased.
	Perovskite	Yes	Low	25.5 %	Weeks	Low stability and decomposition into soluble and toxic Pb compounds.
	Others (OSC, DSSC, QD)	Yes	Low	18.2 %+	Weeks - Months	OSC and DSSC suffer from fast degradation. QD has low scalability.

*A wafer is required for the III-V film growth.

+Based on perovskite QDs, other materials have significantly lower efficiency.

The research progress of the efficiency for most materials is represented in **Figure 1.14**. Among the third generation of solar cells, inorganic chalcogenides and perovskite-based solar cells stand out in research interest due to their particular characteristics.

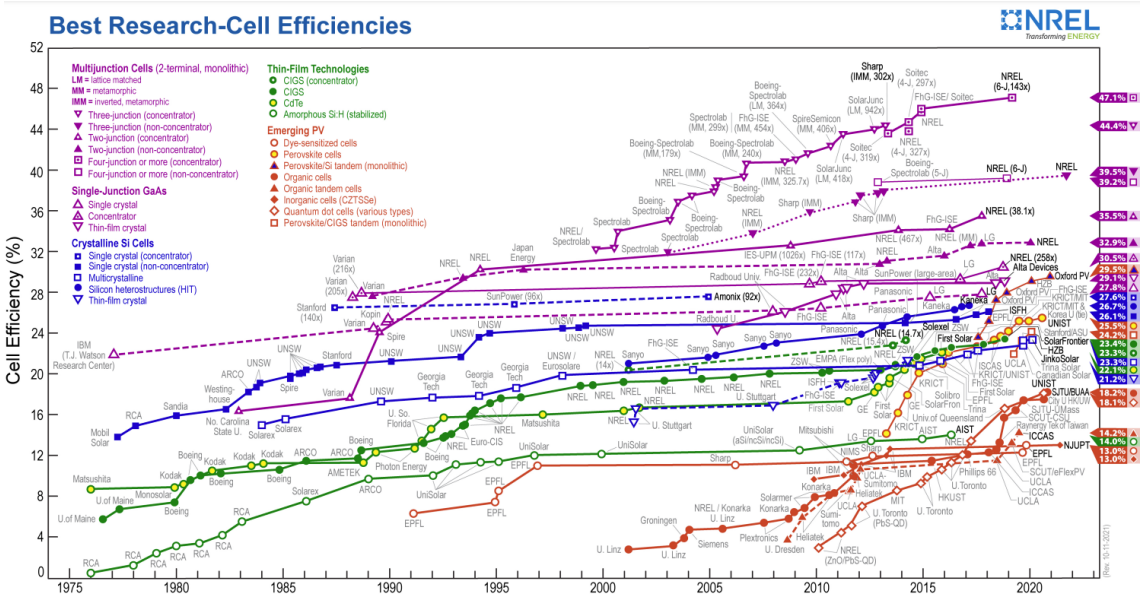

Figure 1.14. Best certified efficiency graph of solar cells classified by the absorber material.[32] (NREL, November 2021)

1.5.5 Inorganic and kesterite

Generally, inorganic materials possess an intrinsic high stability in comparison with organic or hybrid materials. Research in inorganic materials has been focused on chalcogenide compositions with abundant elements with suitable PV properties. A variety of inorganic materials with potential or interest ($Sb_2(S,Se)_3$, SnS, Bi_2S_3...[33]) can be found in the literature, with kesterite standing out due to its similarities with CIGS, but with a lower requirement of critical elements.

Kesterite is the stable structure of $Cu_2ZnSn(S,Se)_4$ (CZTSSe) compounds. Kesterite, just as CIGS or CdTe, belongs to the family of chalcogenides. These compounds are based on covalent bindings between metals and chalcogens elements. CZTSSe presents two main similar crystal phases, with the same lattice structure as chalcopyrite, but with a different atoms position. Stannite is present in samples prepared at low temperatures since it has slightly higher energy formation. Kesterite instead, has a lower energy formation and will be the predominant phase when it is prepared at sufficiently high temperatures.[34,35]

The high absorption coefficient of kesterite facilitates its application in thin films and flexible devices. Moreover, kesterite possesses a tuneable direct band-gap ranging from 1.0 −1.5 eV, suitable for single-junction solar cells, p-type conductivity, and exhibit robust stability in external conditions.[36] CZTSSe thin films can be deposited and synthesized at adequate temperatures, by various vacuum or wet chemistry thin film deposition methods:

- Vacuum deposition methods have the advantage of producing films with high purity, quality, and reproducibility. The most-reported vacuum techniques for kesterite are thermal vapour deposition and sputtering. Typically, the metal or binary precursors are vaporized and deposited in the substrate, forming a stack of layered precursors. The precursors are submitted to a 500 to 600 ºC temperature annealing under sulphur or selenium atmosphere to stimulate the reaction and crystallization of kesterite.[37]
- On the other hand, wet chemistry deposition methods are based on solutions or dispersions containing the precursor compounds. There is a variety of thin-film deposition methods starting from a precursor solution, each one with its advantages and disadvantages. Once the precursor film is formed, it also requires a sulfo-selenization treatment to crystallize and form a film with good quality. The potential of being solution processable makes it attractive for both small and large-scale manufacturing due to reduced investment and low capital cost.[38]

Sincere efforts have been laid to fabricate CZTSSe as an efficient PV material, however, its development has been halted in the last years and the best-reported cell efficiencies of 12.6% in 2012, and 13% in 2021 are still far from its Shockley-Queisser limit.[32,39] Kesterite-based absorbers still have many limitations in performance. These limitations are found in both the interfaces and intrinsic materials properties. Low charge carrier lifetime and interface barriers are sources of current loss,[40–42] while band-gap fluctuation,

non-ohmic contacts, grain boundaries, deep defects, band misalignment with the buffer, double layer formation, and recombination by point defects and long band tailing are identified as the reasons for a high voltage deficit.[36,43–47]

Most of the strategies to overcome these problems were focused on improvements of the absorber layer by alkali doping, alloying with isoelectronic elements, passivation of the interfaces, or controlling the microstructure. However, the advancement in kesterite-based absorber has been decelerated and less exploited during the last few years owing to its complexity, the difficulty of controlling its properties, and low power conversion efficiency as compared to the other thin-film emerging PV technologies.[48]

1.5.6 Perovskite

Perovskite-based solar cells attracted much attention due to their rapid development, reaching efficiency values close to their theoretical limit in less than a decade since it was first proposed as PV material,[49] making them the only 3º generation material with an efficiency comparable to Si-based solar cells. Perovskite successful and rapid progress is partially due to its easy and low-cost synthesis, facilitating the research on this topic. As represented in **Figure 1.15**, the number of publications on perovskite is currently much higher than in kesterite.

Perovskite is the structure adopted in compounds as ABX_3 with different element sizes, being A larger than X, and X larger than B, with A and B as cations, and X as the anion. Following this structure, $CH_3NH_3PbI_3$ ($MAPbI_3$) and some organolead-halide variants, have been found to possess extraordinary optoelectronic properties, high carrier mobility, and high absorption coefficients as well as long charge-carrier diffusion length and the possibility of tunning the optical bandgaps, the power conversion efficiency in the cell has improved from 3.8 % to over than 25.5 %. Thin

films of these perovskites are also prepared by low-cost and solution-based deposition methods, with a very low synthesis temperature of 60 −100 ºC.

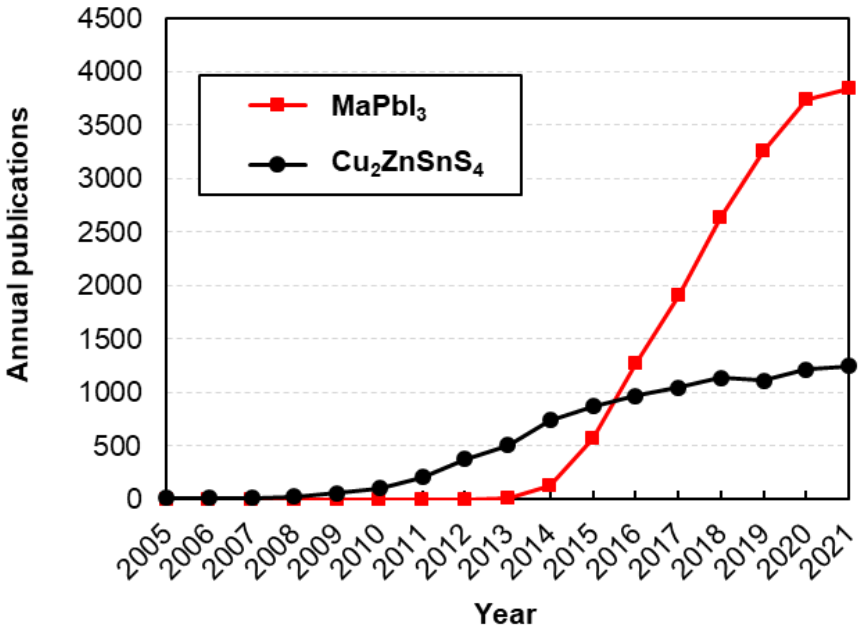

Figure 1.15. Annual publications containing $MAPbI_3$ (main perovskite compound used for solar cells) and Cu_2ZnSnS_4. (*Data source: dimensions.ai, November 2021*)

However, they have a critical drawback hindering their commercialization. Organolead-halide perovskites are intrinsically unstable due to the decomposition of their compounds under air, humidity, temperature, and light.[50] This decomposition reduces the lifespan of any device based on these classes of perovskite materials. Moreover, lead halide perovskite decomposes in hazardous lead salt compounds such as PbI_2, which is water-soluble, carcinogenic, and hazardous for the environment.[51] For these reasons, the research trends are focus currently on improving the stability of perovskite compounds and devices, together with strategies to substitute lead.

1.6 Conclusions and thesis scope

New PV materials have a huge potential of decreasing PV energy costs below what the current technologies can offer, offering simple methods for its fabrication with low capital investments. This opens the possibility to fight against energy deficiency, even in economically poor countries with low industrialization, with a green and renewable energy source. But these materials have some challenges to overcome before being ready for their large-scale commercialization.

The research of this thesis is focused on strategies to overcome some of the weak points described of the 3º generation PV materials:

- Chapter 2 is focused on improvements of the buffer material for kesterite solar cells in the classic substrate structure, by the application of different fullerene derivatives as interlayers.

- Chapter 3 various solution-based methods are compared for kesterite thin film deposition, to vouch its potential of up-scaling, and the change of solar cell architecture of kesterite from substrate to superstrate is introduced. We review the state-of-the-art, as well as the interest that the superstrate architecture have.

- Chapter 4 starts the development of a superstrate architecture using kesterite, to reveal the limitations of using kesterite on this architecture, along with various optimization processes proposed.

- Chapter 5 has the objective of overcoming the limitations found in chapter 4 by using different alloys as absorber material inspired on kesterite.

1.7 Chapter references

1. Climate Action Tracker. Climate summit momentum: Paris commitments improved warming estimate to 2.4°C. 0–12 (2021).
2. International Renewable Energy Agency (IRENA). *World energy transitions outlook: 1.5 °C pathway*. *Irena* (2021).
3. (EPIA) European Photovoltaic Industry Association. Global Market Outlook for Solar Power 2015-2019. *Glob. Mark. Outlook* 32 (2014).
4. Sivaram, V. & Kann, S. Solar power needs a more ambitious cost target. *Nat. Energy 2016 14* **1**, 1–3 (2016).
5. Becquerel, E. Mémoire sur les effets électriques produits sous l'influence des rayons solaires. *Comptes Rendus* **9**, 561–567 (1839).
6. Smith, W. Effect of light on selenium during the passage of an electric current. *Nature* **7**, 303 (1873).
7. G A, B. W. V. The action of light on selenium. *Proc. R. Soc. London* **25**, 113–117 (1877).
8. Fritts, C. E. On a new form of selenium cell, and some electrical discoveries made by its use. *Am. J. Sci.* **s3-26**, 465–472 (1883).
9. Siemens, W. On the electro motive action of illuminated selenium, discovered by Mr. Fritts, of New York. *J. Franklin Inst.* **119**, 514 (1885).
10. Einstein, A. Über einen die Erzeugung und Verwandlung des Lichtes betreffenden heuristischen Gesichtspunkt. *Ann. Phys.* **322**, 132–148 (1905).
11. Kennard, E. H. & Dieterich., E. O. An effect of light upon the contact potential of selenium and cuprous oxide. *Phys. Rev.* **9**, 58–63 (1917).
12. Ohl, R. S. Light-sensitive electric device. *United States Patent Office 2402662* 1–14 (1941).
13. Shockley, W. The Theory of p-n Junctions in Semiconductors and p-n Junction Transistors. *Bell Syst. Tech. J.* **28**, 435–489 (1949).
14. Chapin, D. M., Fuller, C. S. & Pearson, G. L. A new silicon p-n junction photocell for converting solar radiation into electrical power. *Journal of*

Applied Physics **25**, 676–677 (1954).

15. Anderson, R. L. Germanium-Gallium Arsenide Heterojunctions [Letter to the Editor]. *IBM J. Res. Dev.* **4**, 283–287 (2010).

16. Shockley, W. & Queisser, H. J. Detailed Balance Limit of Efficiency of p-n Junction Solar Cells. *J. Appl. Phys.* **32**, 510 (1961).

17. Rühle, S. Tabulated values of the Shockley-Queisser limit for single junction solar cells. *Sol. Energy* **130**, 139–147 (2016).

18. Enslin, J. H. R. & Snyman, D. B. Simplified feed-forward control of the maximum power point in PV installations. in 548–553 (Institute of Electrical and Electronics Engineers (IEEE), 2003). doi:10.1109/iecon.1992.254498

19. Subudhi, B. & Pradhan, R. A comparative study on maximum power point tracking techniques for photovoltaic power systems. *IEEE Trans. Sustain. Energy* **4**, 89–98 (2013).

20. Fernandes, P. A. *et al.* Effects of sulphurization time on Cu2ZnSnS4 absorbers and thin films solar cells obtained from metallic precursors. *Sol. Energy Mater. Sol. Cells* **115**, 157–165 (2013).

21. Gupta, G. K., Garg, A. & Dixit, A. Electrical and impedance spectroscopy analysis of sol-gel derived spin coated Cu2ZnSnS4 solar cell. *J. Appl. Phys.* **123**, (2018).

22. Bisquert, J. Theory of the impedance of electron diffusion and recombination in a thin layer. *J. Phys. Chem. B* **106**, 325–333 (2002).

23. Garcia-Belmonte, G. *et al.* Charge carrier mobility and lifetime of organic bulk heterojunctions analyzed by impedance spectroscopy. (2008). doi:10.1016/j.orgel.2008.06.007

24. Mora-Seró, I., Garcia-Belmonte, G., Boix, P. P., Vázquez, M. A. & Bisquert, J. Impedance spectroscopy characterisation of highly efficient silicon solar cells under different light illumination intensities. *Energy Environ. Sci.* **2**, 678–686 (2009).

25. Heath, J. T., Cohen, J. D. & Shafarman, W. N. Bulk and metastable defects in CuIn1-xGaxSe2 thin films using drive-level capacitance profiling. *J. Appl.*

Phys. **95**, 1000–1010 (2004).

26. Green, M. A. Consolidation of thin-film photovoltaic technology: The coming decade of opportunity. *Prog. Photovoltaics Res. Appl.* **14**, 383–392 (2006).

27. De Wild-Scholten, M. J. Energy payback time and carbon footprint of commercial photovoltaic systems. *Sol. Energy Mater. Sol. Cells* **119**, 296–305 (2013).

28. Pedrero, J., Hernández, P. & Martínez, Á. Economic evaluation of pv installations for self-consumption in industrial parks. *Energies* **14**, 728 (2021).

29. Wadia, C., Alivisatos, A. P. & Kammen, D. M. Materials availability expands the opportunity for large-scale photovoltaics deployment. *Environ. Sci. Technol.* **43**, 2072–2077 (2009).

30. USGS. Rare Earth Elements-Critical Resources for High Technology SUPPORTING SOUND MANAGEMENT OF OUR MINERAL RESOURCES. *USGS Fact Sheet 087-02* 1–4 (2002).

31. Green, M. A. *et al.* Solar cell efficiency tables (Version 58). *Prog. Photovoltaics Res. Appl.* **29**, 657–667 (2021).

32. NREL. Best efficiency chart Photovoltaic Research. *https://www.nrel.gov/pv/cell-efficiency.html* (2021). Available at: https://www.nrel.gov/pv/cell-efficiency.html. (Accessed: 13th October 2021)

33. Wong, L. H. *et al.* Emerging inorganic solar cell efficiency tables (Version 1). *J. Phys. Energy* **1**, 032001 (2019).

34. Das, S., Mandal, K. C. & Bhattacharya, R. N. Earth-Abundant Cu2ZnSn(S,Se)4 (CZTSSe) solar cells. in *Semiconductor Materials for Solar Photovoltaic Cells* 25–74 (Springer, Cham, 2015). doi:10.1007/978-3-319-20331-7_2

35. Rakitin, V. V. & Novikov, G. F. Third-generation solar cells based on quaternary copper compounds with the kesterite-type structure. *Russ. Chem. Rev.* **86**, 99–112 (2016).

36. Giraldo, S. *et al.* Progress and Perspectives of Thin Film Kesterite Photovoltaic Technology: A Critical Review. *Advanced Materials* **31**, 1806692 (2019).

37. Repins, I. *et al.* Co-evaporated Cu 2ZnSnSe 4 films and devices. *Sol. Energy Mater. Sol. Cells* **101**, 154–159 (2012).

38. Todorov, T. *et al.* Solution-based synthesis of kesterite thin film semiconductors. *JPhys Energy* **2**, 012003 (2020).

39. Wang, W. *et al.* Device Characteristics of CZTSSe Thin-Film Solar Cells with 12.6% Efficiency. *Adv. Energy Mater.* **4**, 1301465 (2014).

40. Hages, C. J. *et al.* Identifying the Real Minority Carrier Lifetime in Nonideal Semiconductors: A Case Study of Kesterite Materials. *Adv. Energy Mater.* **7**, 1700167 (2017).

41. Furuta, K. *et al.* Improvement of Cu2ZnSn(S,Se)4 solar cell efficiency by surface treatment. *Phys. Status Solidi Curr. Top. Solid State Phys.* **12**, 704–707 (2015).

42. Rey, G. *et al.* On the origin of band-tails in kesterite. *Sol. Energy Mater. Sol. Cells* **179**, 142–151 (2018).

43. Scragg, J. J. S. *et al.* Cu-Zn disorder and band gap fluctuations in $Cu_2ZnSn(S,Se)_4$: Theoretical and experimental investigations. *Phys. status solidi* **253**, 247–254 (2016).

44. Wu, S. H. *et al.* High-efficiency Cu2ZnSn(S,Se)4 solar cells fabricated through a low-cost solution process and a two-step heat treatment. *Prog. Photovoltaics Res. Appl.* **25**, 58–66 (2017).

45. Park, J. *et al.* Investigation of low intensity light performances of kesterite CZTSe, CZTSSe, and CZTS thin film solar cells for indoor applications. *J. Mater. Chem. A* **8**, 14538–14544 (2020).

46. Martinho, F. *et al.* Persistent Double-Layer Formation in Kesterite Solar Cells: A Critical Review. *ACS Appl. Mater. Interfaces* **12**, 39405–39424 (2020).

47. Gokmen, T., Gunawan, O., Todorov, T. K. & Mitzi, D. B. Band tailing and

efficiency limitation in kesterite solar cells. *Appl. Phys. Lett.* **103**, 103506 (2013).

48. Wong, L. H. *et al.* Emerging inorganic solar cell efficiency tables (Version 1). *J. Phys. Energy* **1**, 032001 (2019).

49. Jeong, M. *et al.* Stable perovskite solar cells with efficiency exceeding 24.8% and 0.3-V voltage loss. *Science (80-.).* **369**, (2020).

50. Niu, G., Guo, X. & Wang, L. Review of recent progress in chemical stability of perovskite solar cells. *J. Mater. Chem. A* **3**, 8970–8980 (2015).

51. Kwak, J. Il, Kim, L. & An, Y. J. Sublethal toxicity of PbI2 in perovskite solar cells to fish embryos (Danio rerio and Oryzias latipes): Deformity and growth inhibition. *Sci. Total Environ.* **771**, 145388 (2021).

2 Partial substitution of CdS buffer layer by fullerenes in kesterite solar cells

Over the last decades, significant progress has been made with inorganic materials to enable them as next-generation PV materials that can fulfil the demands of green energy. $Cu_2ZnSn(S,Se)_4$ stands out as a *p*-type absorber material due to exemption from scarce and strategic elements and its similarities with $Cu(In,Ga)Se_2$. Organic materials such as fullerenes and their derivatives are effective *n*-type semiconductors. In this chapter, we study the partial substitution of the CdS buffer layer with *n*-type C_{60} or C_{70} fullerenes for kesterite-based light absorbers in thin-film solar cells. Impedance measurements reveal that using C_{60} as an interlayer increases the recombination time and the depletion width thickness, suggesting a reduction in the interfacial recombination. This promotes charge conduction, resulting in an increased open-circuit voltage and thus device performance when the layers are properly positioned.

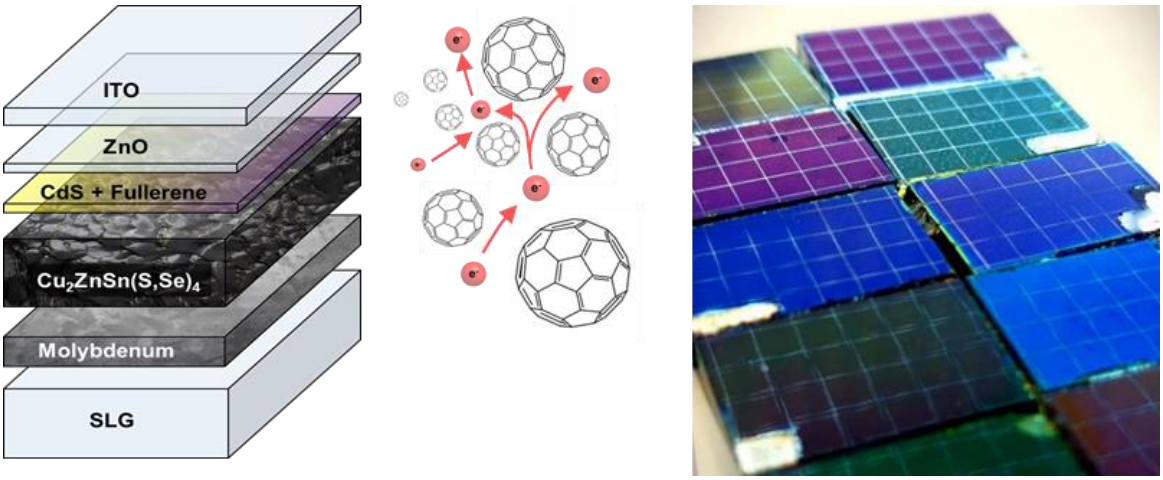

This chapter is mostly based on the article "Payno, D. et al. Partial substitution of the CdS buffer layer with interplay of fullerenes in kesterite solar cells. J. Mater. Chem. C ***8****, 12533–12542 (2020).".*[1] *This chapter contains some extra information and measurements later collected.*

Contents

2.1 Introduction to substrate architecture for kesterite solar cells

2.1.1 Front contact

To enable an efficient light collection, the front contact required high transparency and conductivity, as this is the last layer, it does not require stability as the back contact, therefore the popular options are Al:ZnO (AZO) or ITO, as TCOs. A high resistive material, typically un-doped ZnO, is used as an interlayer to avoid short circuits, however, it can not necessarily obtain efficiencies as high as 12 %.[2]

2.1.2 Buffer layer

One of the reasons for the lower performance lies in the formation of the heterojunction with the buffer layer.[3] Unfavourable band alignment (**Figure 2.1a)** can form an electron barrier, which promotes recombination. In addition, dipole formation and lattice mismatch create recombination paths that lower the open-circuit voltage. Further, buffer layers absorb part of the solar spectrum, which reduces the short-circuit current. CdS is the most studied *n*-type buffer layer for thin-film solar cells, inherited from the established technologies such as CdTe and $Cu_2InGaSe_4$ (CIGS), where it gave competitive PCE, owing to its high transparency, electrical properties, and ease of processing through chemical bath deposition (CBD).[3–5] Attempts to modify or substitute this buffer layer was limited to Zn(S,O),[6–8] In_2S_3,[9] (Zn,Sn)O,[10] (Cd,Zn)S,[11] or alloys with CdS.[11,12] However, little improvements in terms of reproducibility were obtained. In most cases, a second *n*-type material is required to improve the charge conduction and to minimize short circuits, typically ZnO as a window layer.

The influence of CdS thickness and the applied post-heat treatments (PHT) on solar cell performance have been widely studied. In the case of the selenium-containing absorber, the optimum CdS film thickness used is from

30 to 80 nm. Thinner films do not produce a sufficient depletion width thickness, and usually present a high risk of voids, decreasing the voltage and FF, while thicker layers increase the parasitic light absorption and increase the series resistance. PHT above 200 °C is usually performed. This treatment will induce a Cd^{2+} diffusion to the absorber, and exchanges between S and Se, reducing the interface recombination and thus improving the voltage and FF. This was reported for CIGS,[13] and is applied to CZTSe to deliver similar results.[14,15]

2.1.3 Substrate and back contact

The main characteristic of this architecture is that the substrate works also as back contact. The most common choice by far is a soda-lime glass (SLG) substrate with a thin film of 0.8 − 1 µm of molybdenum as the electrode. The Molybdenum (Mo) thickness is chosen to minimize the resistance while still allowing diffusion of Na from the SLG. Considering the required heat treatments for the kesterite synthesis are in the range of 500−600 ºC under sulfur or selenium atmosphere, other back contacts do not provide comparable results. Other possibilities to test are tungsten (W), with good stability, but with less conductivity. Noble metals such as gold (Au) suffer from aggregation and reduced adhesion.[16]

It can be noticed from **Figure 2.1b**, the junction between Mo and kesterite produces a Schottky contact that obstructs the hole collection. However, the use of Mo naturally produces an interlayer of $Mo(S,Se)_2$ (depending on the annealing atmosphere), which affects the contact between the absorber and the electrode. Since $Mo(S,Se)_2$ is a 2-dimensional layered material, its electrical properties change depending on the composition and orientation. It is presented as slightly *n-type* or *p-type*, with a high work function, that can form an *n-p* diode or an ohmic contact depending on the conditions.[3] Some examples of possible band alignments are presented in **Figure 2.1c** for CZTS and **Figure 2.1d** for CZTSe.

Typically, the substrate is coated with Mo by magnetron sputtering, which is a reliable method for metallic thin film preparation. To avoid an excess of $Mo(S,Se)_2$ formation, and obtain better reproducibility, in this work we use Mo tri-layer. The first one, with most of the thickness, provides a low resistivity. A second film is prepared by increasing oxygen partial pressure during the deposition, which generates film with higher chemical stability against sulfur and selenium, but with lower conductivity. The third one with about 40 nm, acts as sacrificial, and provides a controlled thickness for the $Mo(S,Se)_2$, improving the adhesion and hole extraction.[17] A variety of protective materials have been also reported in the literature, such as oxides,[18,19] nitrides, carbon,[20] or borides.[21]

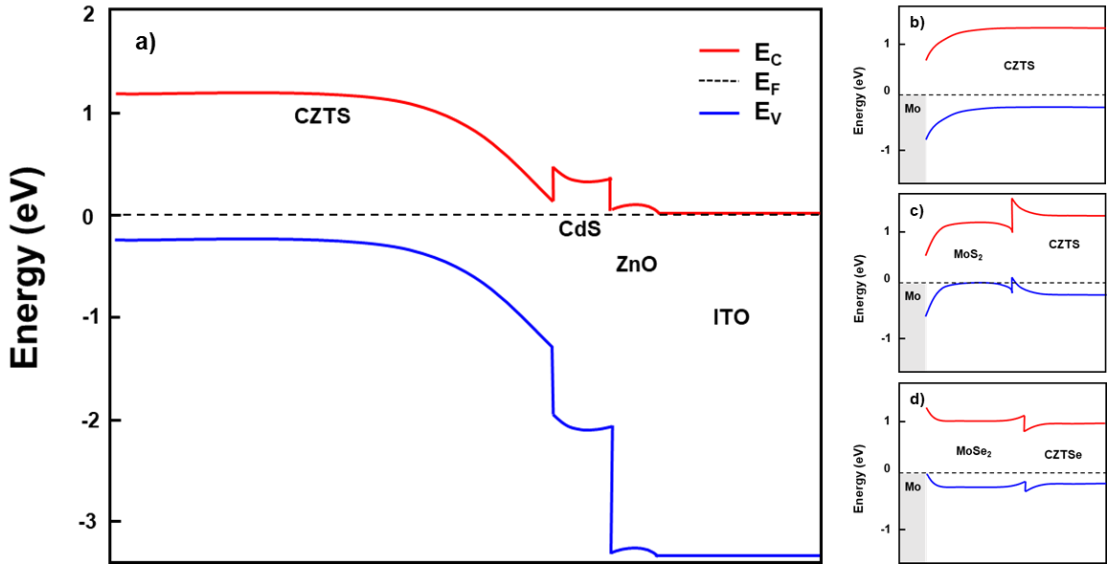

Figure 2.1. a) Front contact electronic structure of a CZTS solar cell in a substrate architecture. b) Back contact electronic structure for CZTS – Mo, c) with a MoS_2 interlayer and d) CZTSe with a $MoSe_2$ interlayer.[3,22]

Beyond opaque back contacts, transparent conductive oxide (TCO) contacts have been reported for bifacial solar cells. In_2O_3:SnO_2 (ITO) and F:SnO_2 (FTO) films provide good conductivity, transparency, chemical, and thermal stability, FTO has been the most stable and thus a popular choice for this role.[23,24] However, direct contact does not produce an ohmic contact, and

engineering with interlayers is required, along with an extrinsic Na doping source.[25]

2.1.4 Fullerenes as electron selective layer

Organic-based semiconductors have delivered significant results, due to the tuneable electro-optical properties that can be achieved by engineering the molecules. Fullerenes are being employed since 1985,[26] and their PV properties are studied.[27,28] Currently, fullerenes and their derivatives are widely used in organic and perovskite-based solar cells, as electron transport materials to substitute metal oxides.[29–31] They are environmentally friendly and stable, as they are composed of carbon atoms joined by covalent bonds. They can be further functionalized to increase their solubility, as in the case of [*6,6*]-phenyl-C_{61}-butyric acid methyl ester (PCBM).

However, reports dealing with fullerenes in kesterite solar cells are scarce and limited efforts were made of combining CZTSSe with organic materials. CZTSSe nanocrystals have been used for photodetectors or improvements in organic solar cells.[32–34] Among the reports, Saha *et al* attempted to create a planar superstrate device with CZTS nanoparticles and PCBM, with the limitation of having a non-ohmic contact between ITO and CZTS,[34] obtaining a 0.9 % PCE. Jang et al. introduced CZTS nanoparticles into a bulk heterojunction (P3HT:PCBM) to improve the absorption of the organic solar cell, thus increasing the generated photocurrent and yielding a PCE of 3.32 %.[33] Nevertheless, these attempts exhibited poor photovoltaic performances.

In this work, we designed an architect for both kesterite (CZTS and CZTSe) based absorbers, by the introduction of *n*-type C_{60} or C_{70} fullerenes as interlayer, reducing the CdS thickness. The reduction of CdS thickness was found to be advantageous by many groups, due to higher transparency in the short wavelength region and lower series resistance. On the contrary, reduced CdS thickness resulted in lower voltage and high risk of pinholes,[35,36] an effect that is more remarkable in CZTS than in CZTSe.[37]

We settled for the best possible configuration of a double-thin buffer layer by changing the deposition order and obtained promising results for both absorbers with C_{60}. The measured open-circuit voltage is notably high with both types of absorbers and gave a PCE of 8.37 % and 4.58 % with CZTSe and CZTS respectively, even with reduced CdS thickness. Additionally, an array of electrical measurements (impedance and *C-V*) were made for the CZTS samples to observe underlying phenomena. An increase in built-in potential (V_{bi}) and a reduction in the interface recombination was noted, allowing a significant improvement in the charge transport.

2.2 Experimental method

2.2.1 Solar cells fabrication

For the fabrication of CZTSe and CZTS solar cells, a cleaned soda-lime glass (SLG) was used as a substrate and Na source. 800 nm thick film of Molybdenum (Mo) was sputtered on the SLG as back contact, followed by the deposition of metallic precursors Sn, Cu, and Zn. This was then placed into a closed graphite box and then introduced inside a quartz tube furnace to perform the sulfurization or selenization. The annealing treatment was performed in two steps, in the first step, the low temperature was used to create the sulfides or selenides binary compounds, and in a second step high temperature to form the quaternary compound and to promote the grain growth.

Etching treatment was performed by dipping the samples on a 22 % diluted $(NH_4)_2S$ in H_2O, to remove the binary $Sn(S,Se)_x$ compounds formed at the surface. An extra air annealing treatment of 300 ºC was applied to the CZTS absorber to oxidize possible remaining binary compounds.

The following buffer layers were deposited on top of the absorber. CdS was grown by chemical bath deposition (CBD). $Cd(NO_3)_2$ was used as Cd precursor of CdS in the CBD, which allows for better growth control of the thickness as the formation is slower.[38] A standard deposition of a 60 nm film

in 40 minutes was required to achieve the best performance,[35,39] however, notably in this work, the process was reduced to 20 minutes to minimize the thickness, producing a thinner film of 30 nm of CdS. The fullerenes C_{60} and C_{70} thin films were prepared following the procedure reported elsewhere.[30] The fullerenes were dissolved with a concentration of 10 mg/mL on 1,2-dichlorobenzene and keeping it stirring overnight. The solution was filtered with a PTFE filter of 0.42 µm pore size and deposited by spin coating 50 µL at 1500 rpm for 60 seconds. After spin coating, it was transferred on a hotplate to dry at 80 ºC for 2 minutes. The devices were finished by sputtering 50 nm of ZnO as the window layer and 300 nm of ITO as the transparent conductive film at 200 °C. No further, top metallic contact nor anti-reflection coating was used in this work. The cells were then mechanically scribed in squares of 3x3 mm^2.

2.2.2 Characterization methods

SEM images were recorded with a Hitachi S-3400 electron microscope at 5 kV of acceleration potential. Absorption and transmittance spectra were recorded with the help of an Agilent Cary 60 UV-Vis spectrometer. For the device characterization, the current-voltage curves of the solar cells were measured on a class AAA Oriel solar simulator from Newport and a Keithley multimeter, by connecting the positive contact to the exposed molybdenum and the negative directly to the ITO. The external quantum efficiency was measured on a PVE300 Photovoltaic EQE (IPCE) system, consisting of a 150 W Xenon lamp and a 1/4m monochromator, in a range from 300 − 1100 nm. For the impedance measurements, a constant bias signal with 20 mV of perturbation was applied, in a frequency range from 5 GHz – 300 Hz, inside a Faradaic box to avoid interferences, with a Biologic impedance analyzer, and EC-LAB software was used to make the fitting of the data to extract the parameters of the equivalent circuit.

2.3 Results and discussion

2.3.1 Films characterization

A prerequisite for the buffer layer is high transmittance in a wide range of visible and near-infrared wavelengths, to allow maximum light absorption by the active material. The optical properties were acquired on the films deposited on glass (**Figure 2.2a**). The transmittance spectra of the CdS thin films with a thickness of 30 nm exhibit higher transparency within the 450−1000 nm wavelengths, while for a 60 nm thickness, a further reduction for wavelengths smaller than 500 nm is found, indicating an absorption dominated by a direct band-gap. In the case of C_{60}, a minute loss in transmittance occurs below 500 nm, while in the case of C_{70} it shows a loss in transparency up to 700 nm. The calculated optical band-gap values of these fullerenes through a linear fit of the Tauc plot (**Figure 2.2**b) are in agreement with the reported value in the literature for an amorphous fullerene film.[40] Thus, the high optical transparency of these organic materials suggests their usage as the buffer layer with an absorber material such as kesterite. However, parasitic absorption of these materials can slightly reduce the photocurrent which will be higher in the case of C_{70}.

Thermal treatments are usually applied to modify the interface properties on final solar cells. However, organic materials are susceptible to thermal treatments and can evaporate, carbonize or oxidize at high temperatures. Decomposition is not an issue for fullerenes as the covalent bonds of the carbon are stable,[41] but other effects can not be discarded. We explore the stability of the films under the required temperatures in **Figure 2.2c**. The transmittance of the C_{60} and C_{70} films after the deposition of the CdS thin film, and after annealing in air at 230 °C for 20 minutes, show a similar trend. A reduction of 5–10 % of the transmittance can be deducted after the organic material is covered with CdS, but no change was found in the transmittance after the heat treatment. The bandgap remains unchanged suggesting that the

amorphous nature of the fullerenes is conserved. Thermal sublimation of fullerenes film in the open air was reported to start at 350 °C, setting the limit for the temperature that we can apply in a post-process.

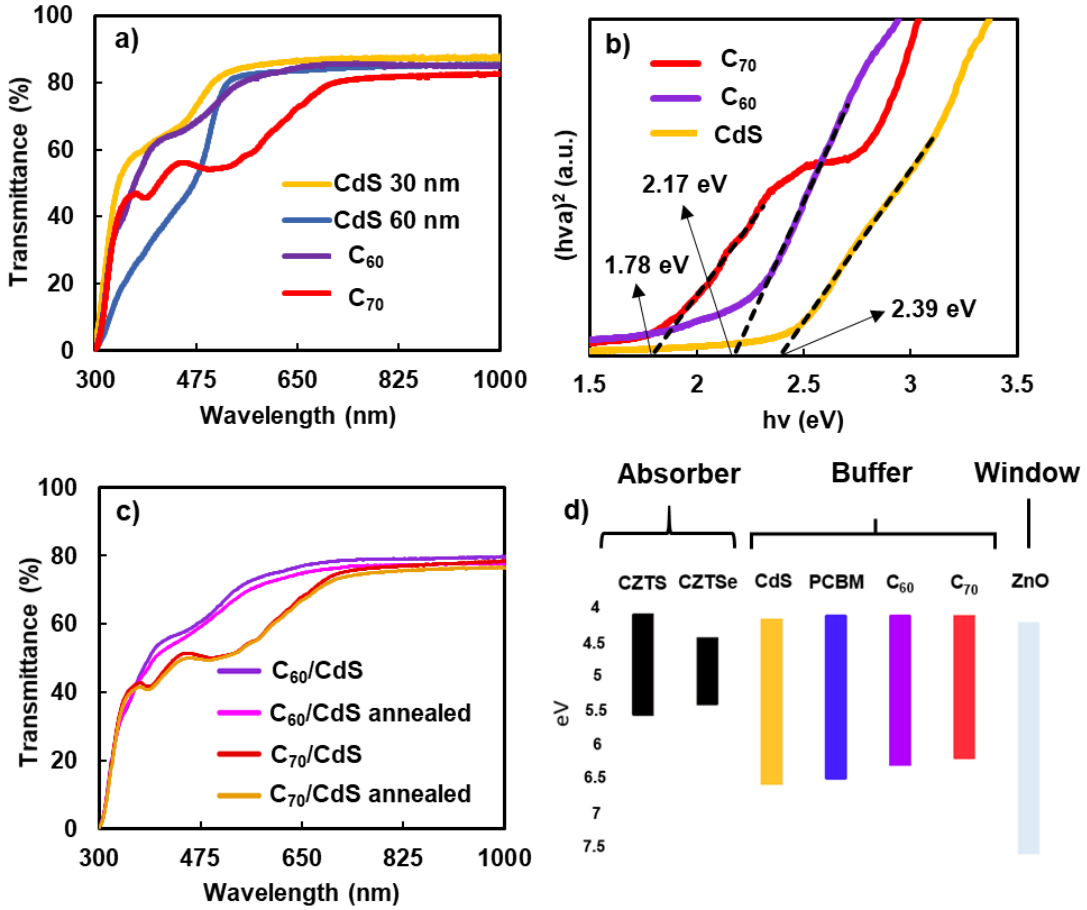

Figure 2.2. a) Transmittance spectra of thin films deposited on a glass of C_{60} and C_{70} (spin coating) and CdS (CBD), b) transmittance spectra of the double buffer layer before and after heat treatment of 230 °C for 20 minutes, c) Tauc plot and calculated band-gaps obtained from the absorption spectra, and d) energy level diagram of the used materials.

Figure 2.2d illustrates the energy levels diagram of the device with the employed materials. Despite different band-gaps of the materials, the energy level of the lowest unoccupied molecular orbital (LUMO) is close to the conduction band of the CZTS(e) in all cases, which facilitates the flow of electrons while the low energy level of the highest occupied molecular

orbital (HOMO) can block the holes effectively, making them good candidates as a buffer layer.

Different configurations were prepared, following the structure shown in **Figure 2.3a**. A cross-sectional view of the solar cell reveals the morphology of the microstructure. CZTSe absorber layer has a thickness of 1.5 µm, composed of compact and big grains up to 1 µm in size (**Figure 2.3b**). CZTS layer (**Figure 2.3c**) has the same thickness and is composed of compact big grains, however, some cavities can be noted in the Mo/CZTS interface. The formation of a $Mo(Se,S)_2$ interlayer can be noted in both cases in the interface, which seems slightly thinner in the sulfide case.

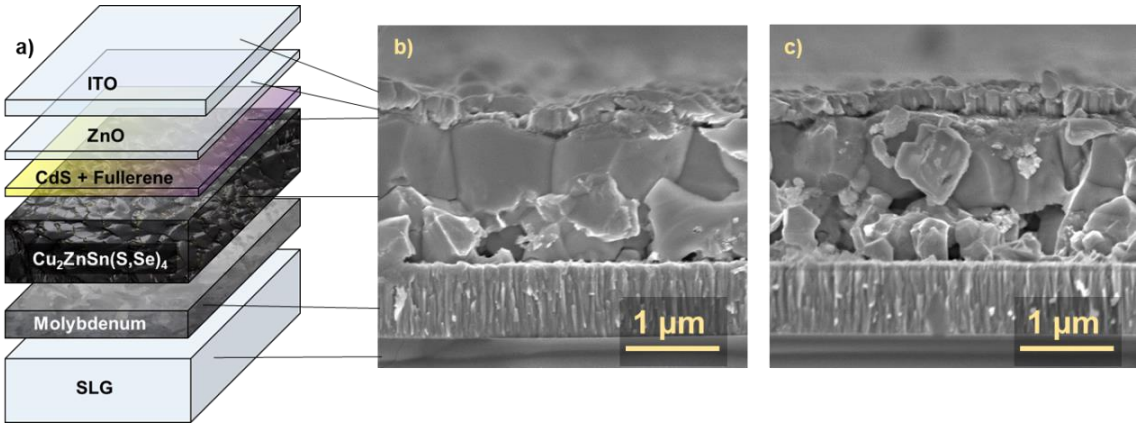

Figure 2.3. a) Architecture of the different configurations used for the solar cell fabrication, b) cross-sectional SEM image of a working solar cell using CZTSe, and c) CZTS.

2.3.2 Devices based on $Cu_2ZnSnSe_4$

Firstly, we analyze the optoelectrical properties of the solar cells with CZTSe as an absorber layer, with the samples denoted as the film deposition order. When a double buffer was used, the thickness of CdS was reduced and partially substituted by the fullerene with a double buffer layer. CdS/fullerene was intended to act as a thickness compensation with improved transparency, while C_{60}/CdS configuration was used as an interfacial agent, to test the possibility of minimizing the interface

recombination by fullerenes being deposited directly over the CZTSe absorber.

It is vital to evaluate the role of organic layers under the required treatments and the possible effects, which may impose on the fabricated solar cells. Optimization of the PHT temperature performed in air, on a hotplate, can be found on the supporting information. **Table S2.1** illustrates a detailed study of PHT and suggests that an optimum temperature of 225 °C. The open-circuit voltage can be further increased at higher temperatures, but the reduction of the current and fill factor (FF) will reduce the PCE. We can speculate that the use of an organic layer is compatible with the required post-heating treatment and will not hinder the element diffusion between CdS and CZTSe.

The final solar cells were characterized before and after an optimum PHT, of 225 °C for 20 minutes. The average parameters extracted from the *J-V* characterization of eight different solar cells are shown in **Table 2.1**. A similar trend was noted for all the devices. The V_{oc} and the FF showed an increased value after the heat treatment and gave an average PCE > 7 %.

The devices using C_{60} between CZTSe and CdS registered 20 mV higher V_{oc} and a competitive FF of 64% on average, which can indicate the surface passivation effect, and a small improvement in the photocurrent. The competitive FF of both CdS/C_{60} and C_{60}/CdS suggests rational energy level alignment between the conduction band of CdS and the LUMO level of C_{60}.

The *J–V* curves (**Figure 2.4a**) of the best solar cells with post-annealing yielded a value of 446 mV of V_{oc} without compromising other parameters, and a PCE of 8.37% was noted for the champion solar cell. CdS/C_{60} also showed a similar value and a PCE of 8.35 % was obtained, due to a slightly higher photocurrent, but a reduced voltage. The samples with complete substitution of CdS by C_{60} and PCBM, as well as partial substitution by C_{70} (**Figure S2.1, Figure S2.2, and Table S2.1**) were not able to deliver

competitive performance as compared to standard cell using only CdS or a bilayer buffer.

Table 2.1. Photovoltaic properties and standard deviation over eight cells before and after the post-heat treatment.

Sample	Heat treatment	V_{oc} (mV)	J_{sc} (mA cm^{-2})	FF (%)	PCE (%)
Reference	As prepared	339 ± 12	22.95 ± 0.79	45.2 ± 7.4	3.52 ± 1.0
	After PHT	**418 ± 2**	**24.81 ± 0.56**	**67.9 ± 0.9**	**7.04 ± 0.2**
C_{60}/CdS	As prepared	338 ± 34	24.24 ± 2.2	41.0 ± 5.6	3.45 ± 1.1
	After PHT	**443 ± 6**	**27.21 ± 0.57**	**64.0 ± 2.9**	**7.72 ± 0.4**
CdS/C_{60}	As prepared	404 ± 5	26.00 ± 0.80	49.2 ± 2.1	5.16 ± 0.3
	After PHT	**423 ± 8**	**27.91 ± 0.73**	**63.7 ± 3.5**	**7.54 ± 0.7**

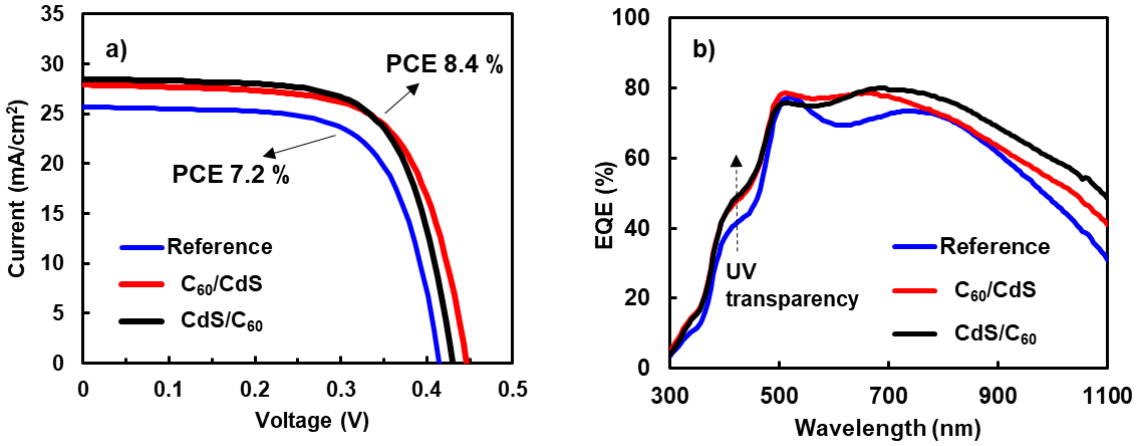

Figure 2.4. a) *J–V* curves under 1 Sun illumination for the CZTSe based solar cells. b) EQE spectra of the best devices after annealing.

The external quantum efficiency (EQE) spectra of the devices (**Figure 2.4b**) reveal a higher response in the violet and ultraviolet regions, which can be attributed to lower parasitic absorption of the double buffer layer in this region in comparison with that in the pure and thicker CdS buffer layer. On the other hand, a loss of response can be noticed in the infrared region for all

the samples, which we assigned to the absorber layer itself, rather than the buffer or the interfacial layers. The decrease in the infrared region is characteristic for CZTSe absorbers and can be attributed to bulk defects that cause recombination of the electron-hole pairs produced deep in the absorber.

From *J-V* in dark, in **Figure 2.5a**, the characteristic diode curve for the cells can be observed. It can be noticed that the cell with only CdS has a lower turn-on voltage, which may suggest higher interface recombination, and suffers from a higher shunt under reverse current, which also affects the performance. Both samples with C_{60} show a characteristic rectification shape, having the sample C_{60}/CdS slightly higher series resistance.

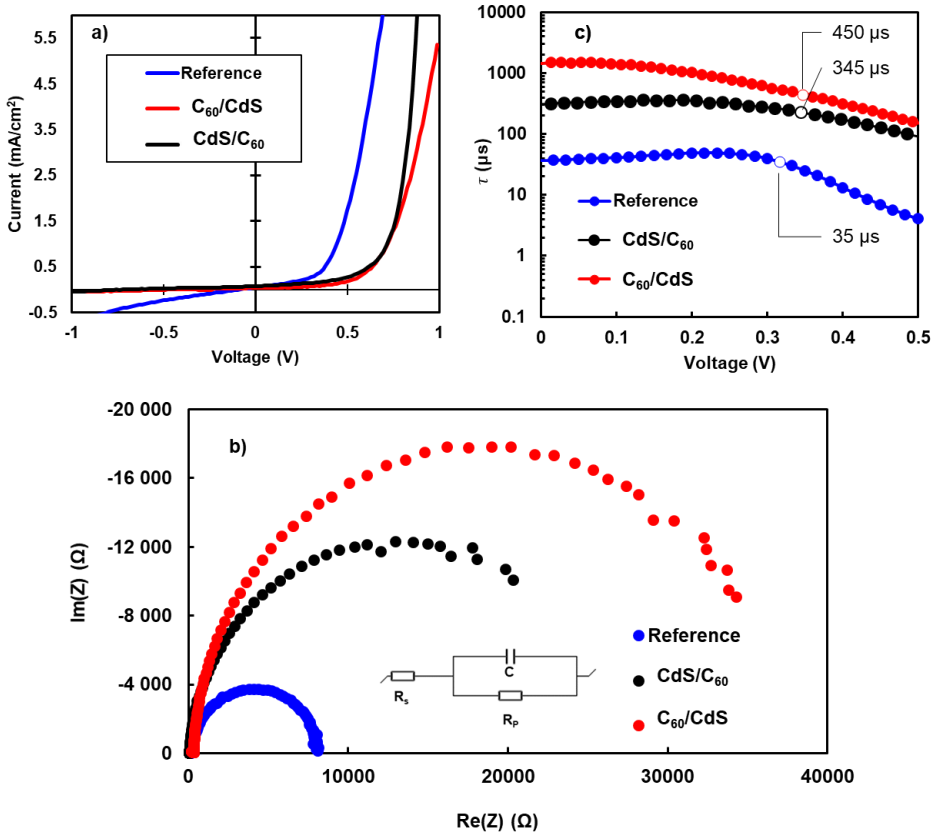

Figure 2.5. a) Dark J-V curve for the CZTSe solar cells. b) Nyquist plot of the impedance data obtained at the MPP voltage, in dark. c) Characteristic recombination time of the solar cells at low forward voltage, indicating the value at the MPP voltage.

Impedance measurements were performed on the devices to elucidate the properties of the junction. **Figure 2.5b** shows the Nyquist plot of the samples at the maximum power point (MPP) voltage. The shape of the semicircle indicates a much higher recombination resistance for the C_{60}/CdS sample, while for the CdS sample, the lower recombination resistance might have a high impact on the efficiency since the PV effect of the p-n junction is reduced. These curves fit well on the circuit shown in the inset, from where the recombination resistance and capacitance of the p-n junction can be obtained. The characteristic recombination time is obtained by the product of $R_P \cdot C$ and showed in **Figure 2.5c** for a range of low forward voltages. The recombination time close to the MPP is greatly increased when a double buffer layer is used, which may explain the improvement in the performance.

2.3.3 Devices based on Cu_2ZnSnS_4

Buffer layers based on fullerenes were also tested with a CZTS absorber, using the similar three configurations of CdS/C_{60}, CdS/C_{70}, and C_{60}/CdS. In this case, the surface passivation of the absorber is of significant interest, as the interface between CZTS and CdS presents several issues due to the valence band offset and secondary phases, which induce interface recombination. Usually, an etching treatment [42,43] or an oxide interlayer [44,45] is required for the passivation of interface defects.

Figure 2.6a shows the *J-V* curves of the best device for each condition under AM1.5 illumination, and the average values are shown in **Table 2.2** In the case where C_{60} was used as an interlayer between the CZTS absorber and CdS, the devices registered a significant increase in PCE from 1 % to 4.5 %, with a remarkable V_{oc} of 718 mV in the best solar cell. The best V_{oc} value reported in the literature for a pure CZTS was achieved with a high thermal annealing and a protective Al_2O_3 film in the back contact, of 730 mV.[46] In this case, no special treatment was applied on the back contact, so an excess

of MoS_2 formation during the sulfurization could increase the resistance and is responsible for the low FF in these solar cells.

Table 2.2. Averages of the extracted parameters for each configuration with the standard deviation.

Buffer	V_{oc} (mV)	J_{sc} (mA/cm^2)	FF (%)	PCE (%)
CdS/C_{60}	520 ± 8	7.5 ± 0.17	27.8 ± 0.6	1.09 ± 0.05
C_{60}/CdS	700 ± 32	12.6 ± 0.51	46.7 ± 2.9	4.16 ± 0.54
CdS/C_{70}	460 ± 47	5.3 ± 0.33	27.0 ± 1.0	0.65 ± 0.07

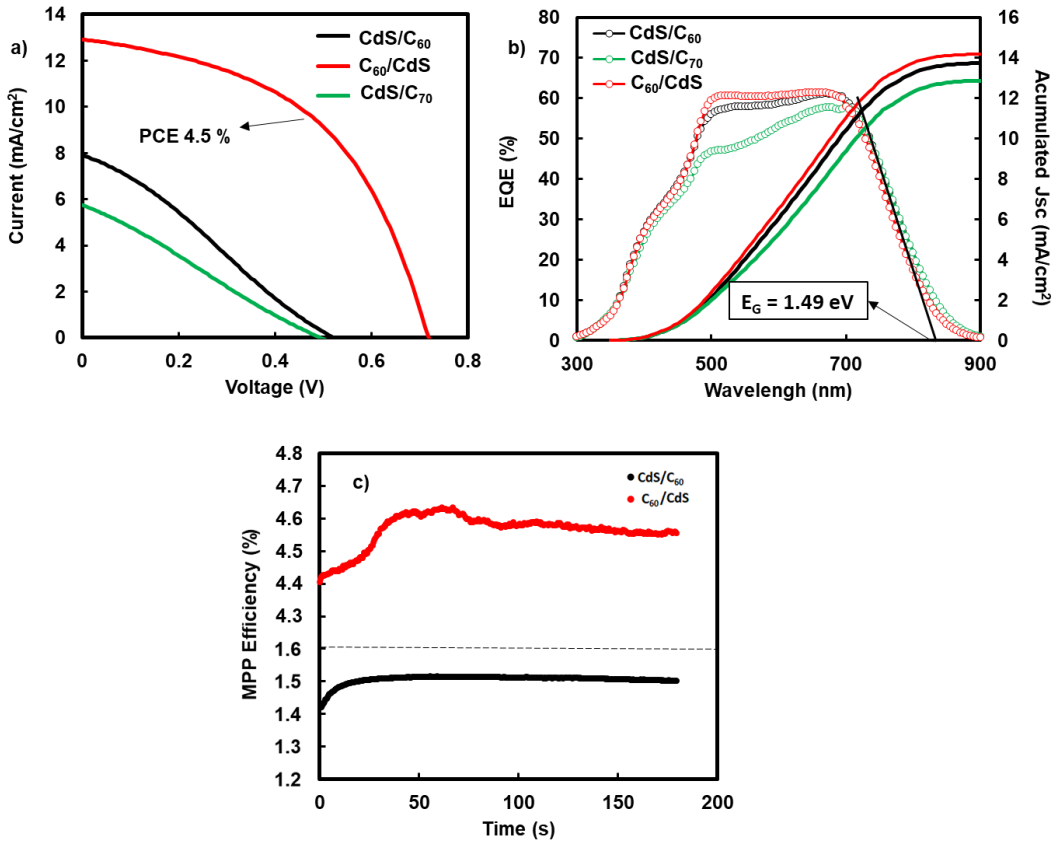

Figure 2.6. a) J-V curves under 1 Sun illumination. b) EQE (circles) and integrated current (lines) for CZTS based solar cells. A band-gap is calculated in the inset. c) Efficiency evolution at maximum power point for 180 seconds.

The EQE spectra were recorded, and the integrated photocurrent density is calculated to investigate the deficiency of the current in **Figure 2.6b**. No relevant changes in the band-gap of the absorber were noticed, having a value of 1.49 eV for all cases. The spectrum of the CdS/C_{70} sample is losing part of the signal in the 380 – 700 nm region, which can be associated with the absorption of C_{70} in this region. However, the differences between the samples are lesser than expected from the *J-V* and integrated photocurrent from the EQE.

The integrated current value usually matches with the J_{sc} value measured on the *J-V* curve, but a difference as high as 6.24 and 7.27 mA cm^{-2} is noted for the samples CdS/C_{60} and CdS/C_{70} respectively. This result reveals that there is a high loss of photocurrent when they are illuminated under AM1.5 conditions, less severe under low illumination and that this effect is less noticed in the C_{60}/CdS sample.

This suggests a change in the carrier concentration under light illumination and a possible high density of defects or secondary phases in the CZTS/CdS interface that aggravate the accumulation and recombination of the charge in the interface. CdS is known as a photo-resistance that increases its carrier concentration under illumination,[47] which can provoke a p-n^{+}-n barrier junction under short wavelengths. The photo-doping effect can be also noticed in the efficiency evolution under 1.5AM illumination in Figure 2.6c. The efficiency increases during the first 30 − 60 seconds and then get stabilizes. The increase in the carrier concentration in the CdS layer ensures a maximum depletion width thickness, and neutralizes deep acceptor traps, improving the electron-hole separation.[38]

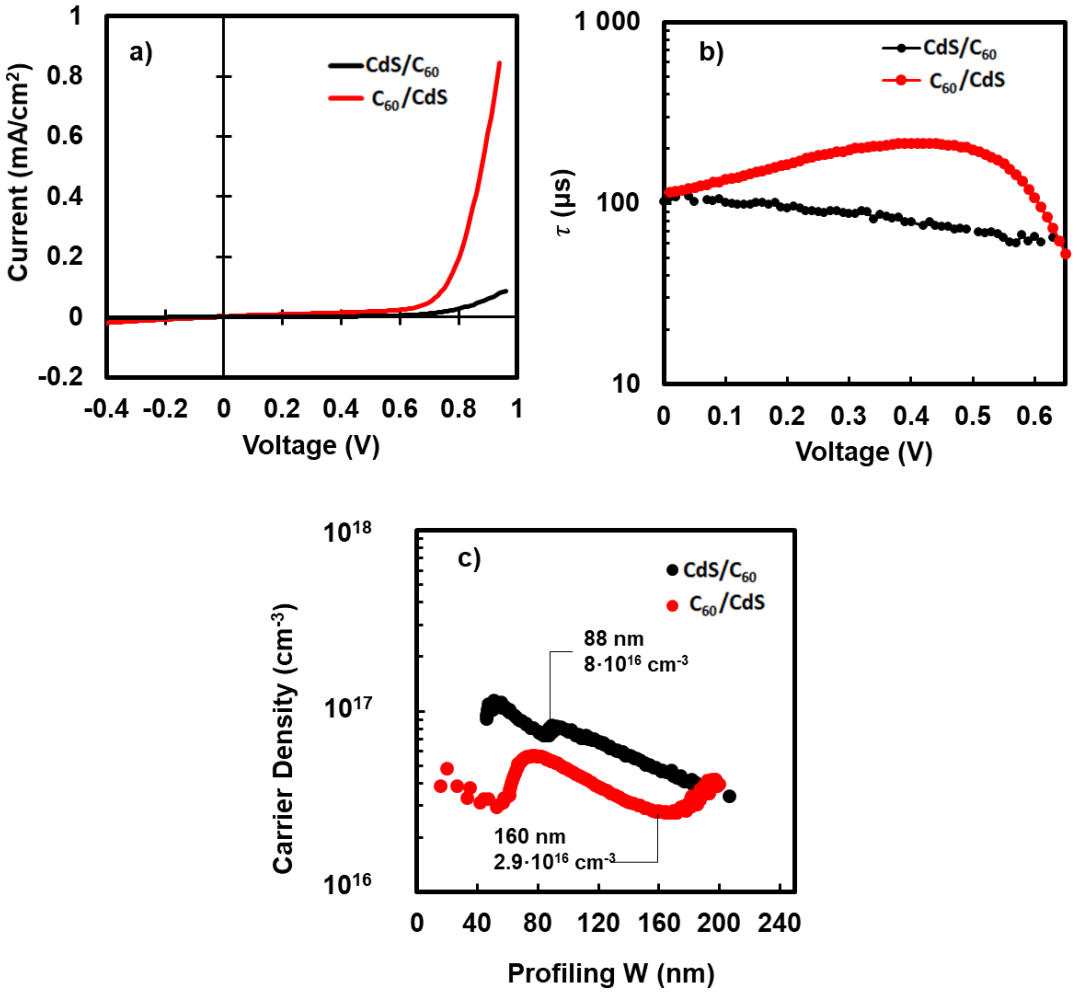

Figure 2.7. a) Dark *J-V* Curves, b) characteristic recombination time, and c) charrier density profiling obtained from capacitance-voltage fitting for CZTS based solar cells, indicating the values at *V*=0.

It will be unfair to attribute the reduction of the FF to the double buffer layer because, in the case of C_{60}, it works efficiently in the structure of CZTSe/CdS/C_{60}. The main barrier can be associated with the CZTS/CdS junction, however, the S and Se exchange and CdS recrystallization after the PHT in the CZTSe case can reduce the photo-doping effect in the buffer layer. In any case, when the C_{60} is placed between CZTS and CdS, a *p-n-n*$^+$ junction is formed, and electrons are transported efficiently through the buffer layer, avoiding interface recombination.

Focusing on the differences between samples with C_{60}, dark *J-V* curves (**Figure 2.7a**), shows a rectification curve for both samples, however, a

higher series resistance can be noticed for the CdS/C_{60} sample, corroborating the existence of a barrier for the charge injection caused probably by the reverse polarization of the CdS/C_{60} junction, while in the case of a CdS/C_{60}, the resistance is minimized.

To focus on the junction with CZTS, impedance spectroscopy measurements were performed, showed in **Figure S2.3**. Two recombination processes can be detected in the CdS/C_{60} sample, which already suggests the existence of a barrier due to an n^+-n junction. The characteristic recombination time of the *p-n* junction was extracted and represented in **Figure 2.7b**. As in the CZTSe case, an increment on the recombination time for voltages close to the MPP can be noted or the C_{60}/CdS, indicating that the CZTS/C_{60} interface has good properties for charge separation. These properties are further studied in **Figure 2.7c**, where the carrier density and depletion width is obtained from the fitted capacitance-voltage values of the junction. As expected, similar values of the hole concentration are obtained for both samples, in the order of 10^{16} to 10^{17} cm^{-3} for CZTS. The main difference is the value obtained at V=0 for the depletion width, of 160 nm for the C_{60}/CdS sample and 88 nm for CdS/C_{60}. A wider depletion width can have a high impact on CZTS solar cells since the photogenerated exciton has a low lifetime, reported in the order of ns, and the exciton recombination before the charge separation is one of the main limitations for this PV technology. The wider depletion width created by the C_{60}/CdS buffer layer avoids part of the exciton recombination by deeper charge separation since most light is absorbed close to the junction.

2.4 Conclusions

The partial substitution of CdS by organic charge transport materials is shown to be an effective method to reduce the loading of Cd-based materials, without harming the performance of the solar cells. We noted that reducing the thickness of CdS also induces an increase in the photocurrent in the violet and UV region of the spectra, where the absorption of CdS is parasitic. The

fullerene derivative used as an electron transport layer was noted to be stable at the required post-treatment temperature of 230 °C for the fabrication of CZTSe solar cells. Among the fullerene derivatives, C_{60} showed better electro-optical properties than C_{70} as a buffer layer in kesterite solar cells. The use of C_{60} as an interlayer between the absorber and the CdS allowed us to register remarkably high values of V_{oc}, of 446 mV for CZTSe, and 718 mV for CZTS, even with a significant reduction in CdS thickness. Both in CZTSe and CZTS absorbers, the recombination time is improved by a C_{60} interlayer, producing a high V_{oc}. Optimization of the process and the thickness of these films will be vital for further reducing the voltage deficit. One of the main barriers in inorganic solar cells is the limited choice of materials that can be used efficiently as buffer layers and is being typically dependent on cadmium or indium elements. We demonstrate that rational organic charge transport materials can be also a compatible choice. Our investigation paves the way for further optimization and exploration of using organic materials for kesterite-type solar cells to develop cost-effective and green photovoltaics.

2.5 Chapter Supporting Information

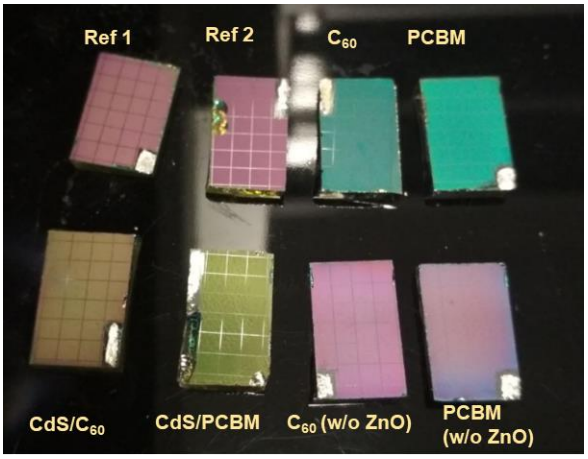

Figure S2.1. Image of the solar cell samples indicating the buffer used in each case.

Table S2.1. Devices parameters using CZTSe as the absorber, extracted from J-V characterization under 1 sun illumination (average over 8 cells).

Sample	PHT temperature	V_{oc} (mV)	J_{sc} (mA cm^{-2})	FF (%)	PCE (%)
Reference	As prepared	321.29	22.87	42.71	3.21
	200 ºC	366.38	27.17	53.22	5.49
	225 ºC	422,99	25,35	65,82	7,08
	250 ºC	451.03	23.84	60.89	6.55
CdS/PCBM	As prepared	399.07	22.79	52.71	4.80
	200 ºC	396.49	25.85	64.27	6.59
	225 ºC	409.29	24.97	69.39	7.09
	250 ºC	411.55	24.28	59.63	5.99
CdS/C_{70}	As prepared	404	19.62	31.7	2.52
	225 ºC	416	22.85	21.8	2.09
PCBM	As prepared	112.34	0.10	24.60	0.00
	200C	164.95	9.98	20.62	0.34
	225C	143.43	7.68	20.09	0.22
	250C	141.90	4.19	15.14	0.09
C_{60}	As prepared	54.38	0.13	28.79	0.00
	200C	194.13	14.21	26.96	0.74
	225C	142.06	8.68	28.75	0.35
	250C	113.08	7.44	30.67	0.26

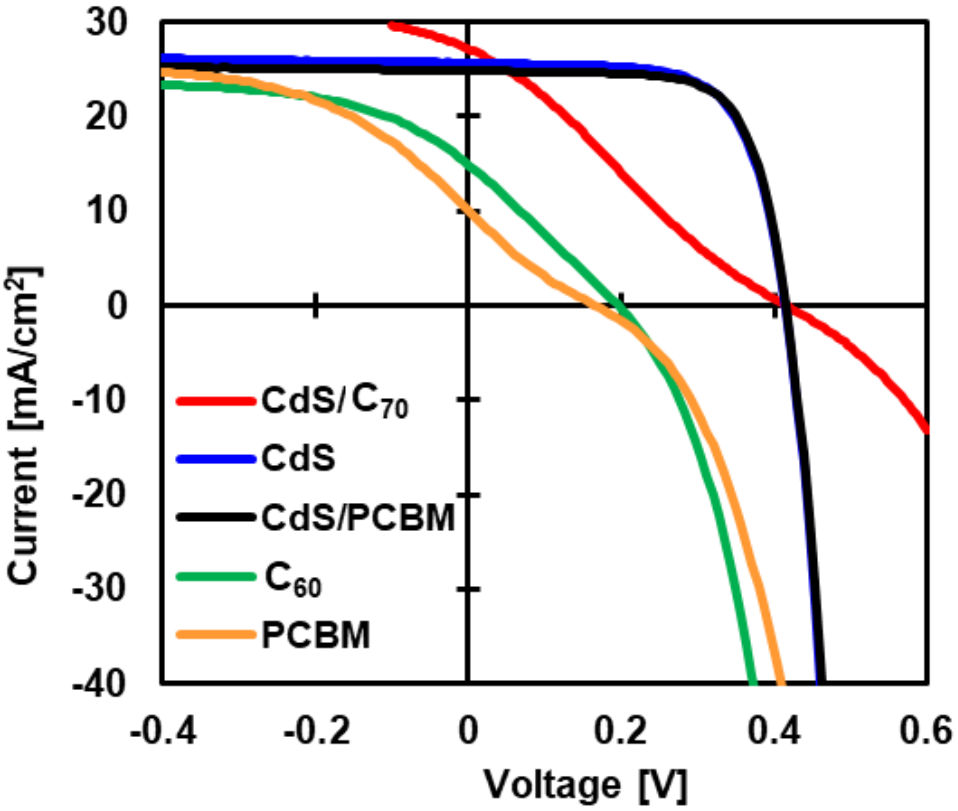

Figure S2.2. J-V curves under illumination for samples with different buffer layers, using CZTSe as the absorber. In the case of C_{70}, an improvement of the V_{oc} and J_{sc} can be noticed after the heat treatment, but the reduction in FF resulted in a drop in the final PCE. When comparing with C_{60}, the V_{oc} remains similar, but there is a decrease in the current value, as was expected from the transmittance and supported by the EQE. The signal is reduced for wavelengths shorter than the bandgap (1.79 eV). This behaviour is similar when using C_{70} as a buffer in other types of solar cells.[40]

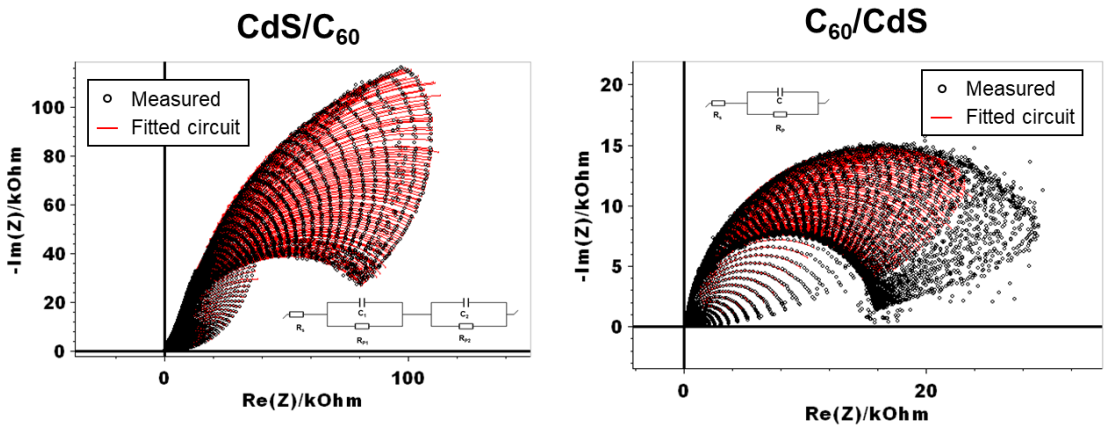

Figure S2.3. Impedance spectroscopy measurements and fitting for the solar cells using CZTS absorber. The circuit used for fitting is indicated in the inset. C_{60}/CdS sample only requires one loop of parallel resistance and capacitance for a good fitting, CdS/C_{60} require two loops, suggesting that two opposing junctions are present, associated with the p/n^+ and n^+/n junctions.

2.6 Chapter references

1. Payno, D. *et al.* Partial substitution of the CdS buffer layer with interplay of fullerenes in kesterite solar cells. *J. Mater. Chem. C* **8**, 12533–12542 (2020).
2. Su, Z. *et al.* Device Postannealing Enabling over 12% Efficient Solution-Processed Cu2ZnSnS4 Solar Cells with Cd2+ Substitution. *Adv. Mater.* **32**, 2000121 (2020).
3. Platzer-Björkman, C. *et al.* Back and front contacts in kesterite solar cells: State-of-the-art and open questions. *JPhys Energy* **1**, 044005 (2019).
4. Vigil-Galán, O. *et al.* Optimization of CBD-CdS physical properties for solar cell applications considering a MIS structure. *Mater. Des.* **99**, 254–261 (2016).
5. Neuschitzer, M. *et al.* Optimization of CdS buffer layer for high-performance Cu2ZnSnSe4 solar cells and the effects of light soaking: Elimination of crossover and red kink. *Prog. Photovoltaics Res. Appl.* **23**, 1660–1667 (2015).
6. Nguyen, M. *et al.* ZnS buffer layer for Cu2ZnSn(SSe)4 monograin layer solar cell. *Sol. Energy* **111**, 344–349 (2015).
7. Ghosh, A., Thangavel, R. & Gupta, A. Solution-processed Cd free kesterite Cu2ZnSnS4thin film solar cells with vertically aligned ZnO nanorod arrays.

J. Alloys Compd. **694**, 394–400 (2017).

8. Neuschitzer, M. *et al.* Towards high performance Cd-free CZTSe solar cells with a ZnS(O,OH) buffer layer: The influence of thiourea concentration on chemical bath deposition. *J. Phys. D. Appl. Phys.* **49**, 125602 (2016).
9. Barkhouse, D. A. R. *et al.* Cd-free buffer layer materials on Cu 2ZnSn(S xSe 1-x) 4: Band alignments with ZnO, ZnS, and In 2S 3. *Appl. Phys. Lett.* **100**, 193904 (2012).
10. Ericson, T. *et al.* Zinc-Tin-Oxide Buffer Layer and Low Temperature Post Annealing Resulting in a 9.0% Efficient Cd-Free Cu 2 ZnSnS 4 Solar Cell. *Sol. RRL* **1**, 1700001 (2017).
11. Sun, K. *et al.* Over 9% Efficient Kesterite Cu2ZnSnS4 Solar Cell Fabricated by Using Zn1–xCdxS Buffer Layer. *Adv. Energy Mater.* **6**, 1600046 (2016).
12. Hiroi, H. *et al.* Over 12% efficiency Cu2ZnSn(SeS)4 solar cell via hybrid buffer layer. in *2014 IEEE 40th Photovoltaic Specialist Conference, PVSC 2014* 30–32 (IEEE, 2014). doi:10.1109/PVSC.2014.6925044.
13. Contreras, M. A. *et al.* Optimization of CBD CdS process in high-efficiency Cu(In,Ga)Se2-based solar cells. in *Thin Solid Films* vols 403–404 204–211 (2002).
14. Teng, L. *et al.* Novel two-step CdS deposition strategy to improve the performance of Cu2ZnSn(S,Se)4 solar cell. *J. Energy Chem.* **42**, 77–82 (2020).
15. Chen, W.-C. *et al.* Interface engineering of CdS/CZTSSe heterojunctions for enhancing the Cu2ZnSn(S,Se)4 solar cell efficiency. *Mater. Today Energy* **13**, 256–266 (2019).
16. Altamura, G. *et al.* Alternative back contacts in kesterite Cu2ZnSn(S 1-xSex)4 thin film solar cells. in *Journal of Renewable and Sustainable Energy* vol. 6 011401 (2014).
17. Lopez-Marino, S. *et al.* The importance of back contact modification in Cu2ZnSnSe4 solar cells: The role of a thin MoO2 layer. *Nano Energy* **26**, 708–721 (2016).
18. López-Marino, S. *et al.* Inhibiting the absorber/Mo-back contact decomposition reaction in Cu2ZnSnSe4 solar cells: the role of a ZnO intermediate nanolayer. *J. Mater. Chem. A* **1**, 8338 (2013).
19. Liu, F. *et al.* Beyond 8% ultrathin kesterite Cu2ZnSnS4 solar cells by interface reaction route controlling and self-organized nanopattern at the back contact. *NPG Asia Mater.* **9**, e401 (2017).
20. Zhou, F. *et al.* Improvement of Jsc in a Cu2ZnSnS4 Solar Cell by Using a Thin Carbon Intermediate Layer at the Cu2ZnSnS4/Mo Interface. *ACS Appl. Mater. Interfaces* **7**, 22868–22873 (2015).
21. Liu, F. *et al.* Enhancing the Cu2ZnSnS4 solar cell efficiency by back contact modification: Inserting a thin TiB2 intermediate layer at Cu2ZnSnS4/Mo interface. *Appl. Phys. Lett.* **104**, 51105 (2014).
22. Saha, U. & Alam, M. K. Boosting the efficiency of single junction kesterite solar cell using Ag mixed Cu2ZnSnS4 active layer†. *RSC Adv.* **8**, 4905–4913

(2018).

23. Espindola-Rodriguez, M. *et al.* Bifacial Kesterite Solar Cells on FTO Substrates. *ACS Sustain. Chem. Eng.* **5**, 11516–11524 (2017).

24. Kim, J. S., Kang, J. K. & Hwang, D. K. High efficiency bifacial Cu2ZnSnSe4 thin-film solar cells on transparent conducting oxide glass substrates. *APL Mater.* **4**, 096101 (2016).

25. Becerril-Romero, I. *et al.* Transition-Metal Oxides for Kesterite Solar Cells Developed on Transparent Substrates. *ACS Appl. Mater. Interfaces* **12**, 33656–33669 (2020).

26. Kroto, H. W., Heath, J. R., O'Brien, S. C., Curl, R. F. & Smalley, R. E. C60: Buckminsterfullerene. *Nature* **318**, 162–163 (1985).

27. Sariciftci, N. S. *et al.* Semiconducting polymer-buckminsterfullerene heterojunctions: Diodes, photodiodes, and photovoltaic cells. *Appl. Phys. Lett.* **62**, 585–587 (1993).

28. Koltun, M. *et al.* Solar cells from Carbon. *Sol. Energy Mater. Sol. Cells* **44**, 485–491 (1996).

29. Chiang, C.-H. & Wu, C.-G. Bulk heterojunction perovskite–PCBM solar cells with high fill factor. *Nat. Photonics* **10**, 196–200 (2016).

30. Wojciechowski, K. *et al.* C60 as an efficient n-type compact layer in perovskite solar cells. *J. Phys. Chem. Lett.* **6**, 2399–2405 (2015).

31. Chen, C. *et al.* Effect of BCP buffer layer on eliminating charge accumulation for high performance of inverted perovskite solar cells. *RSC Adv.* **7**, 35819–35826 (2017).

32. Wang, J.-J., Hu, J.-S., Guo, Y.-G. & Wan, L.-J. Wurtzite Cu2ZnSnSe4 nanocrystals for high-performance organic–inorganic hybrid photodetectors. *NPG Asia Mater.* **4**, e2–e2 (2012).

33. Jang, S. J., Ho, N. T., Lee, M. H. & Kim, Y. S. Efficient hybrid solar cell with P3HT:PCBM and Cu2ZnSnS4 nanocrystals. in *Journal of Physics: Conference Series* vol. 864 012065 (IOP Publishing, 2017).

34. Saha, S. K., Guchhait, A. & Pal, A. J. Cu2ZnSnS4(CZTS) nanoparticle based nontoxic and earth-abundant hybrid pn-junction solar cells. *Phys. Chem. Chem. Phys.* **14**, 8090–8096 (2012).

35. Mokurala, K. *et al.* Combinatorial Chemical Bath Deposition of CdS Contacts for Chalcogenide Photovoltaics. *ACS Comb. Sci.* **18**, 583–589 (2016).

36. Tunuguntla, V. *et al.* Enhancement of charge collection at shorter wavelengths from alternative CdS deposition conditions for high efficiency CZTSSe solar cells. *Sol. Energy Mater. Sol. Cells* **149**, 49–54 (2016).

37. Ericson, T. *et al.* Zn(O, S) Buffer layers and thickness variations of CDS buffer for Cu 2ZnSnS4 solar cells. *IEEE J. Photovoltaics* **4**, 465–469 (2014).

38. Neuschitzer, M. *et al.* Optimization of CdS buffer layer for high-performance Cu2ZnSnSe4 solar cells and the effects of light soaking: Elimination of crossover and red kink. *Prog. Photovoltaics Res. Appl.* **23**,

1660–1667 (2015).

39. Lee, S. *et al.* Effect of annealing treatment on CdS/CIGS thin film solar cells depending on different CdS deposition temperatures. *Sol. Energy Mater. Sol. Cells* **141**, 299–308 (2015).

40. Lin, H. S. *et al.* Achieving High Efficiency in Solution-Processed Perovskite Solar Cells Using C60/C70 Mixed Fullerenes. *ACS Appl. Mater. Interfaces* **10**, 39590–39598 (2018).

41. Zubov, V. I., Tretiakov, N. P., Teixeira Rabelo, J. N. & Sanchez Ortiz, J. F. Calculations of the thermal expansion, cohesive energy and thermodynamic stability of a Van der Waals crystal - fullerene C60. *Phys. Lett. A* **194**, 223–227 (1994).

42. Bär, M. *et al.* Cliff-like conduction band offset and KCN-induced recombination barrier enhancement at the CdS/Cu2ZnSnS4 thin-film solar cell heterojunction. *Appl. Phys. Lett.* **99**, 222105 (2011).

43. Fairbrother, A. *et al.* Development of a selective chemical Etch to improve the conversion efficiency of Zn-rich Cu 2ZnSnS 4 solar cells. *J. Am. Chem. Soc.* **134**, 8018–8021 (2012).

44. Sun, H. *et al.* Efficiency Enhancement of Kesterite Cu2ZnSnS4 Solar Cells via Solution-Processed Ultrathin Tin Oxide Intermediate Layer at Absorber/Buffer Interface. *ACS Appl. Energy Mater.* **1**, 154–160 (2018).

45. Xie, H. *et al.* Enhanced Hetero-Junction Quality and Performance of Kesterite Solar Cells by Aluminum Hydroxide Nanolayers and Efficiency Limitation Revealed by Atomic-resolution Scanning Transmission Electron Microscopy. *Sol. RRL* **3**, 1800279 (2019).

46. Yan, C. *et al.* Cu2ZnSnS4 solar cells with over 10% power conversion efficiency enabled by heterojunction heat treatment. *Nat. Energy* **3**, 764–772 (2018).

47. Frerichs, R. The photo-conductivity of ‘incomplete phosphors’. *Phys. Rev.* **72**, 594–601 (1947).

3

Solution-based CZTS thin films deposition and development of superstrate solar cells

This chapter is used as a review of the state-of-the-art of various topics that will be experimentally studied in the following chapters. We first review some thin-film solution-based deposition methods for kesterite, considering the advantages and disadvantages of each one by preliminary tests. Spin-coating, ink-jet printing and spray pyrolysis are the solution-processed methods chosen for the present study and prepared the films later used for PV cells.

Second, we review the needed elements for the development of a kesterite-based solar cell in superstrate architecture, as well as a critical overview of the existing studies on this topic. Investigating this architecture, have been found viable, along with some new difficulties, however, it could be key for reach a better PV performance by using abundant elements, since it allows new ways of engineering in the fabrication of the solar cell.

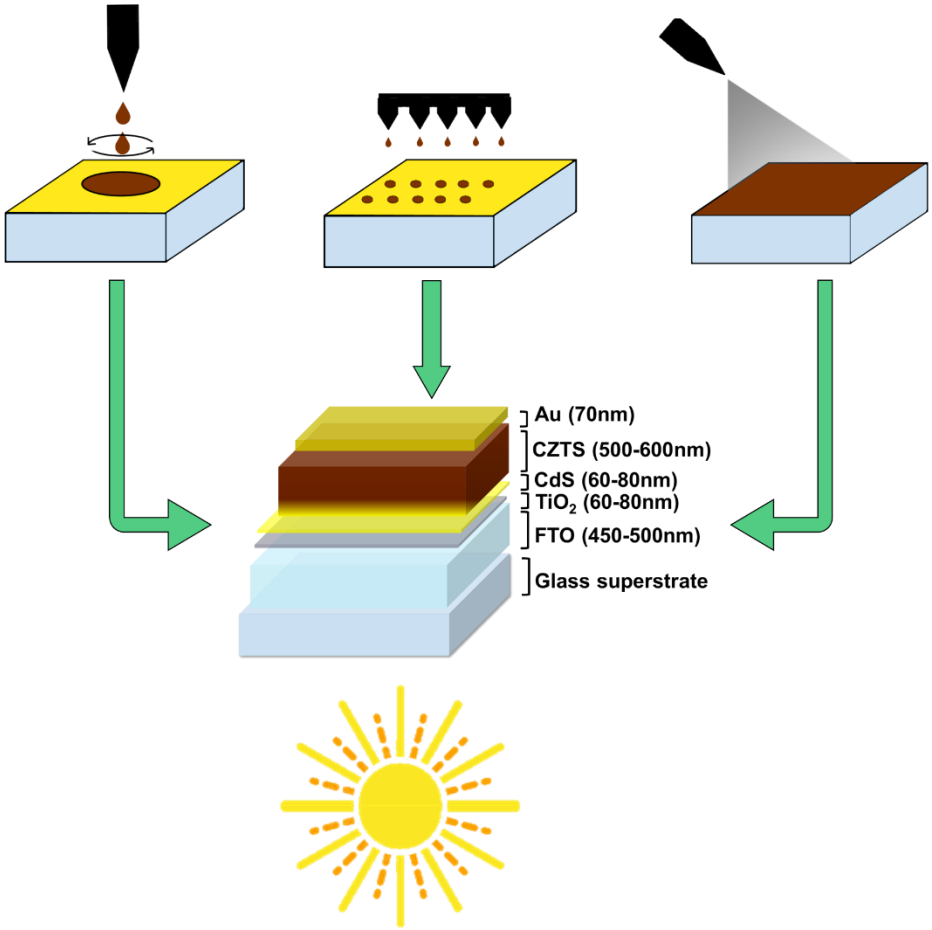

Contents

3.1 Introduction to solution-based deposition methods for chalcogenide thin-films

Since the emergence of interest in chalcopyrite films, a wide variety of solution-based methods have been developed for its synthesis, presented as low-cost methods in comparison with vacuum-based deposition methods. A Scheme of some relevant techniques is shown in **Figure 3.1a**. Many of them are compatible with roll-to-roll processes and can cover large areas at high speed, fundamental to ensure a low cost in the whole production process.[1] Metal oxides and sulphides of the functional layers can be also processed by wet chemistry methods, which allows the fabrication of all or most of the layers of the solar cell by wet chemistry methods.[2–4]

In particular, for CZTS, a simple but effective spray pyrolysis approach based on water and ethanol was first reported in 1995.[5] It was noted that films were considerable sulphur deficient and had a high temperature of 550 ºC in an H_2S atmosphere was needed to reach the stoichiometry and crystallization. This process has been adapted to many other thin-film deposition techniques,[6] either using molecular solutions or dispersion of the precursors. A scheme of the procedure for solution-coating techniques is shown in **Figure 3.1b**.

There is no universal solution, the solution properties have to be adapted to the liquid deposition technique intended to be used. Any technique will set limits for the viscosity of the solution used, which will depend on the solvent, the concentration and the additives used. Most techniques also have limitations in the thickness of the deposited layer, which is a crucial parameter for an absorber layer. To choose a proper liquid coating method, some variables must be taken into account, depending on the properties of the solution and the specific application. For the coating of an absorber layer, the quality, speed and good material usage must be prioritized. For other layers, such as contacts, coating techniques that facilitate patterning may be more interesting.

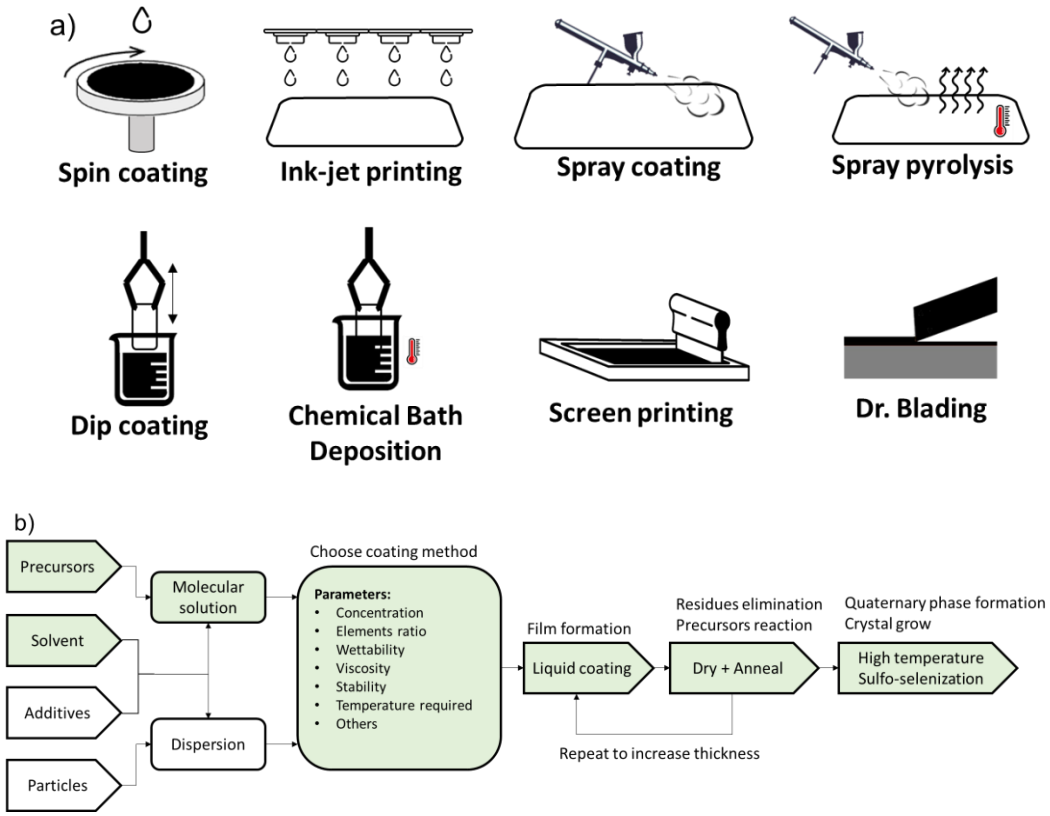

Figure 3.1. a) Scheme of some liquid coating methods compatible with solar cells preparation. b) Scheme of the process for a thin film formation of a quaternary chalcogenide. The route studied during this thesis is marked in green.

After the film formation, the coating requires drying of the solvent, elimination of the organic components and reaction of the precursors in case of sol-gel techniques. The resulting film is formed by secondary phases or compacted particles, compatible with further deposition layers to increase the thickness in most cases. Carbon and oxygen contamination produce films of low quality for PV cells. Due to this, it is preferable to avoid the use of additives in the solutions, which contains organic components and are hard to eliminate by temperature treatments.

The oxygen elimination, quaternary phase formation and crystal growth took place by second annealing at high temperature under an appropriate atmosphere of sulphur or selenium. Further post-heat treatments or etchings can be used to modify the surface properties, just as in the case of vacuum-based techniques.

In the next sections, a selection of methods is studied experimentally with the objective of being tested in the fabrication of CZTS-based photovoltaic cells.

3.1.1 Spin coating

Spin coating is based on the application of a centrifugation force on a wetted substrate that compensates the surface tensions, expulsing out the excess of the solution, accelerating the drying, and compacting or gelling the precursors.

Spin coating is able to form good quality films with thickness ranging from 10 to 500 nm, low roughness and good reproducibility. Due to these reasons, it is probably one of the most reported methods for thin-film fabrication on the laboratory scale, and is usually, the first method to be tested. PCE reached in CZTS solar cells prepared by spin coating have been always among the higher values, demonstrating that solution-based approaches are promising to obtain materials with quality for solar cells.

A route to prepare a molecular solution is shown as an example in **Figure 3.2a**. The metal precursors are typically salts such as chlorides, acetates, nitrates, etc. Chlorides are preferred in many cases since they reduce organic contamination. The solvent chosen will have an important impact on the film thickness. Solvents with a lower evaporation point produce thicker films by spin coating. Most reported solvents are dimethyl sulfoxide (DMSO), dimethylformamide (DMF) and 2-methoxyethanol, due to their ability to dissolve salt precursors in a stable solution.

The solutions for spin coating require a relatively high concentration to obtain decent thicknesses (> 0.5 M of metals concentration), low viscosity to avoid inhomogeneities and good substrate wettability. Good stability of the solution is required to avoid particle aggregation or precipitation, which have a high impact on the film quality due to the formation of comets and pinholes. Filtration may help to remove aggregation, but can also imply an uncontrollable change in the precursor's ratio, promoting the formation of secondary phases, as shown in **Figure 3.2b**.

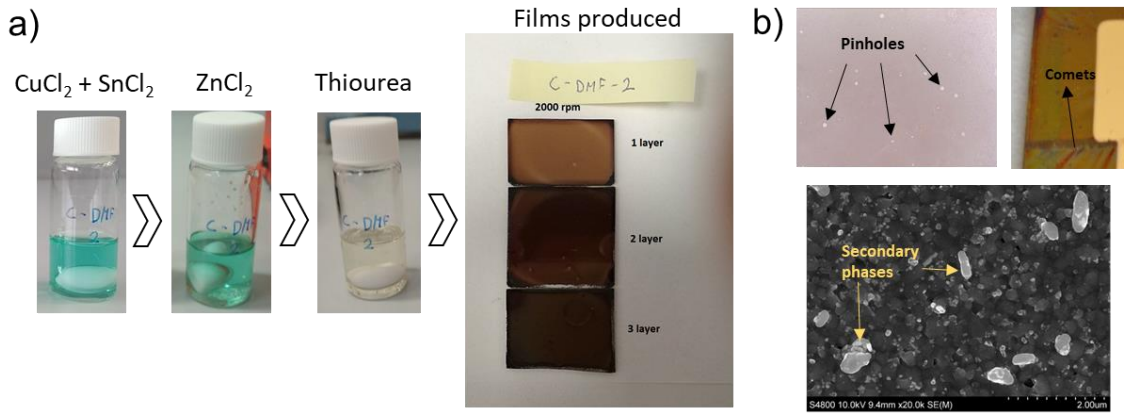

Figure 3.2. a) One of the prepared and tested solutions, used to prepare CZTS films on glass by spin coating. b) Typical film imperfections that can be visible under optical or electron microscopy.

However, it can have problems up to certain thicknesses. Cracks in the order of hundreds of microns to a few millimetres can appear in the films during the first annealing if the thickness of the deposited layer surpasses a certain value. This value will depend mostly on the mechanical properties of the formed complex after the dry of the solvent. During the first annealing step after the film deposition, a big weight loss is produced, creating internal tensions. When the thickness excess this limit and the tensions inside the film are too high, cracks at macro-scale will be easily produced,[7] which can be seen in most cases with the naked eye. Based on the solutions tested for CZTS, a film higher than 300 nm has a high risk of suffering this type of cracking, but this value will depend on the exact precursors and solvent used. Typically, films from 600 nm to 2 μm are required for using kesterite at absorber in solar cells, therefore, a multilayer approach is necessary to avoid the cracking.

In conclusion, the spin coating has the next advantages and disadvantages:

- ✓ Accepts a wide range of solutions.
- ✓ Simple and reproducible.
- ✓ Films with low roughness.
- ✓ Most reported method.
- × Requires concentrated solutions.
- × Low compatibility with green solvents.
- × High material waste.
- × Not suitable for scale-up.
- × High thicknesses produce low quality films.

3.1.2 Ink-jet printing

Ink-jet printing appears as an alternative technique that requires very similar solution properties like spin coating. In this sense, it is a good option to choose this method if the objective is to scale up or produce patterns of material from solutions that have been studied by spin-coating.

It consists of the ejection of a drop with pL volume onto a substrate, where the solvent rapidly evaporates. This method uses the amount of material required only where the cover is needed, so the usage of a material is much higher than in spin coating. The small droplet volume offers a high lateral resolution.[8] As a drawback, it is complicated to get films with low roughness as produced by spin coating.

The critical property for inks of ink-jet printing is viscosity. It requires a relatively high viscosity to prevent the ink from escaping through the nozzle, in the order of 10^{-2} Pa·s, but low enough to ensure that the drops fluid through the nozzle and are effectively ejected. The use of organic additives is usually needed to reach the ink properties required, which lead to films of lower quality.[8]

As a proof of concept for preparing chalcogenide films by ink-jet printing, films of Ag_2ZnSnS_4, were prepared from a molecular solution based on 2-methoxyethanol and metal salts. In **Figure 3.3a** it showed the used equipment, a Dimatix printer. The modified parameter to obtain a good coverage is the dot per inch (dpi), which is fundamentally equivalent to the density of drops used. As shown in **Figure 3.3b**, an insufficient density of drops does not produce a continuous film, since the drops are unable to join each other. The wettability of the substrate is another important parameter to account for, to improve the film continuity, which was improved by UV-Ozone cleaning.

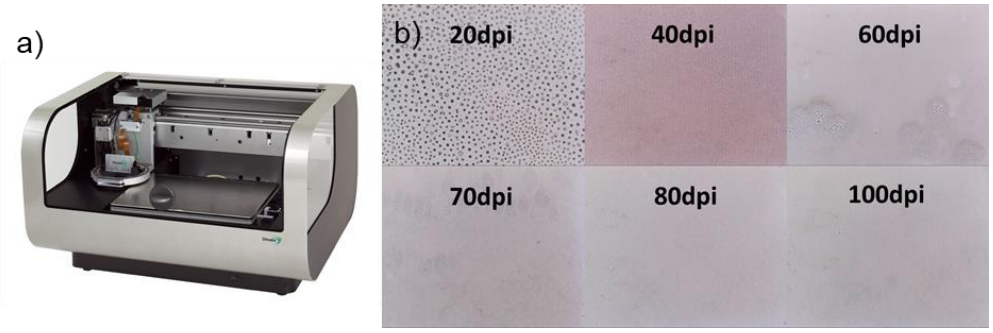

Figure 3.3. a) Image of a Dimatix ink-jet printer for materials. b) Microscope image of Ag_2ZnSnS_4 films produced with different drop densities.

For a solution of 0.5 M of metal salts concentration, the films produced were about 100 nm thick, which is thicker than single films deposited with the same solution by spin coating, but still not enough thick for the preparation of an absorber layer in a PV cell. A multilayer approach is in this case also necessary to obtain the required thicknesses. In conclusion, ink-jet printing possesses the next advantages:

✓	High material usage.	×	Requires highly concentrated solutions.
✓	Allows patterning.	×	Low compatibility with green solvents.
✓	Good coverage.	×	Low film thickness.

3.1.3 Spray pyrolysis

Spray pyrolysis consists of combining the spray coating, the drying, and the pre-annealing in a single step, by spraying a solution on a substrate at a high temperature. To reduce the number of steps favours the reduction of the cost of the process. Spraying is easily scalable and can be implemented into the roll-to-roll process. It also has a high material throughput and usage, making it very appropriate for covering large areas. Spray pyrolysis has demonstrated a high versatility to produce doping and alloys, since are easily implemented by engineering the precursors in the solution, resulting in devices with high PV performance.[9,10]

Spray coating solutions requires low viscosity, which usually means a low concentration of precursors. This brings the disadvantage of requiring a higher volume of solvent, however, it also opens the possibility of using greener and cheaper solvents where precursors have lower solubility, such as water or ethanol.[11,12] A low precursor concentration usually has the extra advantage of having better stability.

Creating patterns by spray coating techniques is not as direct as in the case of ink-jet printing. It is possible by using masks but usually losing the resolution and quality of the film. However, in PV applications, patterning is not a priority, and complete coverage of material is of higher interest.

During the spray pyrolysis, the substrate requires to be at sufficient temperature to make the precursors react at the moment of touching the surface. The sprayed solution flux control is an important parameter to ensure that the substrate temperature is maintained high enough to form a chalcogenide. The progressive formation of the film reduces the tensions created and reduces the risk of cracks, which virtually allows the deposition of any film thickness required.

The advantages described of spray pyrolysis motivate its deeper study in the fourth chapter as a technique to prepare the absorber material. As conclusions, the main advantages and disadvantages of this technique are:

- ✓ Low concentrated solutions.
- ✓ Green solvents.
- ✓ Good reproducibility.
- ✓ High throughput and material usage.
- ✓ Coating and reaction in one step.
- ✓ Can deposit high thickness films.
- × Requires a high solvent volume.
- × Patterning with low resolution.

3.2 Superstrate architecture for kesterite

Advances made on CZTS technology are mostly focused on the substrate architecture, adopted from its counterpart CIGS due to their composition similarities. Generally, this architecture stack follows Mo-CZTS-CdS-ZnO-ITO,

which presents the problems described in the previous chapter. Briefly, it presents a tricky back interface between molybdenum and CZTS, with voids, low crystallinity, carbon contamination and uncontrolled growth of a $Mo(S,Se)_2$ layer remains challenging; a non-ohmic contact formed on the back surface are usual problems reported in the back contact for this architecture, which tends to decrease the generated open-circuit voltage.[13,14] Moreover, this architecture is incompatible with semi-transparent or top-cell tandem applications. Limited efforts have been made to explore alternative configurations, which has been identified as one of the potential ways to overcome its limitations.[15]

Alternatively, these issues can be overcome by the superstrate architecture based on fluorine-doped tin oxide (FTO), which is thermally stable, and employ similar low-cost manufacturing with abundant elements. A superstrate architecture consists of inverting the fabrication process, by using the glass substrate as the front side, where the illumination proceed. This can positively affect the interfaces while simplifying the fabrication process and reducing its cost. A general process of superstrate solar cells is Glass → TCO → Solar cell → Back contact. Since the back contact is the last film, the limitations on the back interface are less, and the possibility of engineering it or using it in tandem is facilitated.

In this section, we review the components, materials and properties required to develop a superstrate architecture from the beginning, as well as precedents reported in the literature to have a clear picture of the state-of-the-art. In combination with some experimental data, we give a critical overview of the limitations and possibilities that the study of CZTS in a superstrate architecture can provide.

3.2.1 Front transparent contact

Superstrate structure based on fluorine tin oxide (FTO) coated glass is currently one of the most studied architectures due to its good thermal and chemical stability, preventing at the same time the use of scarce indium used in indium tin

oxide (ITO) as a transparent conductive layer. FTO can deliver excellent performance in PV when it is covered by a protective and electron blocking semiconducting layer of TiO_2, a methodology adopted in organic and perovskite solar cells using spin coating or spray pyrolysis. The fabrication of CZTS on an FTO-based superstrate architecture is in line with the motivation of reducing the use of scarce elements, while at the same time, it brings the possibility for new ways of improvements as absorber layer due to the sturdiness of the electrode.

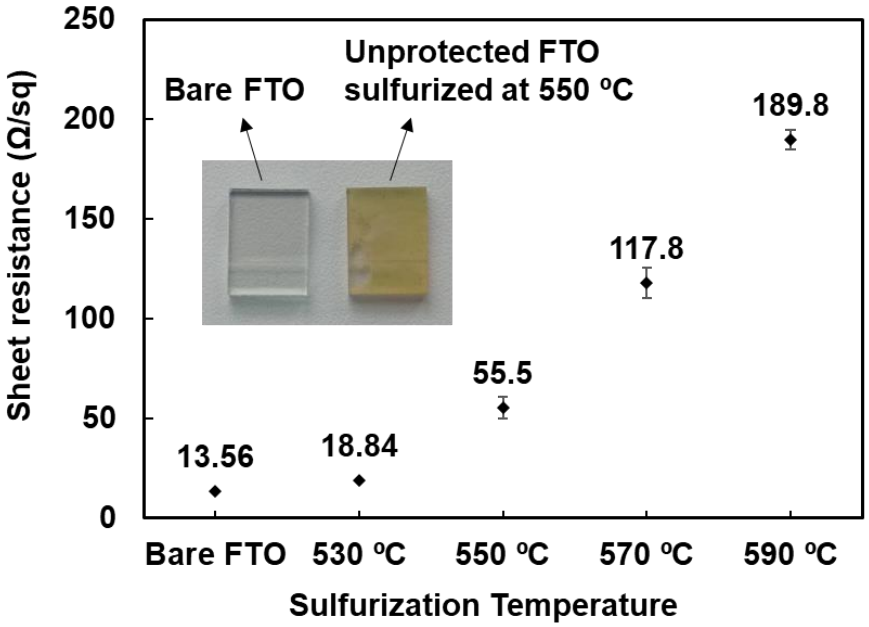

Figure 3.4. The sheet resistance of FTO (TEC-15) after sulfurization at different temperatures. Note that the FTO is conveniently covered by the blocking layer of TiO_2 and exposed with a piece of steel after sulfurization. A direct exposition of FTO to a sulphur atmosphere turns the FTO yellowish, shown in the inset, with a sheet resistance in the order of 1 - 100 kΩ/sq, probably due to formations of SnS_x phases.

As shown in **Figure 3.4**, it is also important to consider the influence of the temperature on the FTO film. To avoid a high degradation of the FTO under the sulfur atmosphere, all the FTO area was covered with the blocking layer of TiO_2, which acts conveniently as a protective layer against sulfur. The sheet resistance of protected FTO tends to increases with the increase of the annealing temperature when is higher than 530 ºC. At 550 ºC, a sheet resistance of 55.5

Ω/sq can be considered sufficient to achieve a good PV performance in our case, but at higher temperatures, the sheet resistance can limit the PCE. Therefore, the use of a temperature lower than 550 ºC is preferable to avoid an excessive reduction of the conductivity of the FTO.

3.2.2 Buffer layer

Poor compatibility has been found between a direct contact of FTO/TiO_2 and CZTS. Various reasons have been proposed for this poor compatibility, such as lower quality of the absorber layer, oxygen diffusion, oxides formation, or high defect density in the interface.[16–18] Just as in the case of the substrate architecture, superstrate also requires a buffer layer to maximize efficiency.

The buffer is the most problematic part of the superstrate structure due to its requirements. A common problem for all chalcogenide absorbers is a low hole-electron diffusion and carrier lifetime. Due to this, in CdTe, CIGS and CZTS solar cells the illumination from the *n-p* junction side is preferable rather than from the backside. This can be noticed in the attempts of preparing bifacial solar cells, where the efficiency when is illuminated from the backside is not as high as when it is illuminated from the front side, in particular for high absorber thicknesses.[19,20]

Having this in consideration, the buffer layer requires an n-type material, with good transparency, high electrical conductivity, stability under high temperature, with good affinity with the absorber, and that do not modify the synthesis path of the absorber layer later deposited. Unfortunately, a material that satisfies all these properties have not been found yet, and this is still the main bottleneck for the development of an efficient superstrate architecture for CZTS.

Nonetheless, the lack of the ideal buffer material should not be a hinder to attempt a superstrate structure. CdS or In_2S_3 can be used as a buffer if some of the mentioned properties are sacrificed. An option is the use of a thick buffer layer to maintain the properties after the CZTS annealing, which increases the resistance and the risk of forming intermediate phases in the interlayer.[21,22]

Another option is to use a lower final temperature annealing. Temperature up to 400 ºC can produce a fine-grain absorber layer, avoiding the reaction with the buffer layer. The electric properties of the absorber are the main limitation of this approach since the charge transport is reduced. A pure phase cannot be ensured, reducing the reproducibility, and its stability under ambient conditions.

A preliminary test comparing In_2S_3 and CdS as buffer layers were studied by SEM in **Figure 3.5**. When low-temperature annealing is used as in **Figure 3.5a**, the CdS can be observed as a dark interlayer between the FTO and the absorber by back-scattered electrons. However, a high-temperature treatment makes a thin film diffuse into the absorber, as in **Figure 3.5b** and **c**, likely forming alloys. This effect will be studied in deep in the next chapter.

The absorber layer shows an improvement in grain growth, when CdS is used in comparison with the sample that has an In_2S_3 interlayer. The final composition of the absorber and the existing phases of alloys will have a critical role in the grain growth of the absorber. A study of this process could be a key to get appropriate absorber properties for a superstrate architecture. Only samples prepared with a FTO/TiO_2/CdS structure shows the PV effect in our experiments.

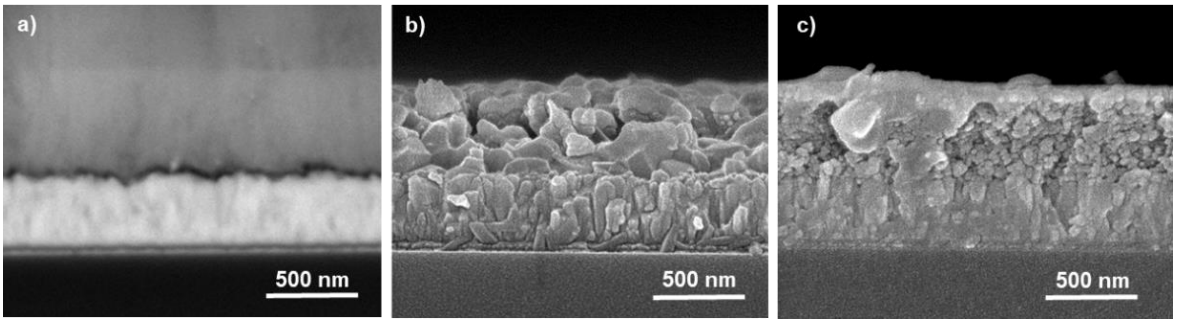

Figure 3.5. a) Cross-sectional back-scattered electrons SEM of a FTO/CdS/CZTS sample prepared at low (270 ºC) temperature, b) Secondary-electrons SEM image of samples prepared at high temperature (550 ºC) of a FTO/TiO_2/CdS/CZTS and c) FTO/TiO_2/In_2S_3/CZTS structures.

3.2.3 Nanostructured layer

In Silicon-based solar cells, engineering the surface using microstructures is a way of light management to reduce reflections. A similar concept was brought at nano-scale, which leads to the discovery of dye-sensitized solar cells [23] and was found beneficial in organic and perovskite solar cells, along with some attempts were made using chalcogenide materials such as $CuInS_2$.[24]

Nanostructures have the advantage of largely increasing the surface area of the junction. The electron-hole pairs will be generated always close to a junction, which reduces the necessity of having a long electron-hole pair lifetime to have an efficient electron-hole separation, thus, the charge recombination is reduced. This largely increases the range of materials that can be used as light absorbers. In addition, light can be managed depending on the type of structure used, such as porous, rods [16] and its different dimensions.

However, the use of nanostructures also comes with some drawbacks. It adds one or more steps in the device fabrication, since the formation of nanostructures requires the synthesis and film coating, or direct the growth, which can influence the final cost. There are limited options of materials compatible with CZTS to form nanostructures, typically TiO_2 and Al_2O_3. TiO_2 has slightly less transparency, but better conductivity than Al_2O_3, making it the usual choice as nanostructured material. In the next chapter, we will further study the effects of TiO_2 mesoporous structures on the PV properties.

3.2.4 Hole transport material and back contact

The layer stack in a superstrate architecture completes with the back contact, which provides room for research and engineering the properties of the backside. The direct advantage of using an interlayer between the contact and the absorber at the backside is that a second series diode creates a second electric field, known as a back surface field (BSF), which can help either with the charge separation at the backside and by applying and extra differential potential in the charges. Since an absorber layer is typically slightly *p-type*, the photo-voltage can be improved

by applying a p^+ layer in the back contact, followed by a metallic contact with an appropriated work function. An absorber with high doping provides a higher V_{bi} in the *n-p* junction due to a higher difference between fermi levels but sacrifices recombination time in exchange. A *n-p-p*$^+$ or *n-i-p* architecture partially solves the issue of choosing between an absorber with high doping or high carrier lifetime, since both junctions contribute to the total potential difference, and the absorber no longer requires high doping. In addition, engineering of the band alignments between the absorber and the interlayer can have a positive effect if a barrier for electrons is created without affecting the hole conduction if the valence bands are aligned, reducing the surface recombination. The materials used in this role are referred to as hole transport materials (HTM).

Every PV technology has required a specific HTM to reach its maximum potential. Highly doped a-Si has been the choice in Si-based solar cells,[25] ZnTe in commercial CdTe solar cells,[26,27] $MoSe_2$ is found acceptable in CIGS, while a wide variety of organic semiconducting materials such as P3HT, PEDOT:PSS or Spiro-OMeTAD are found playing as HTM role in organic, dye-sensitized, and perovskite solar cells.[28] However, currently, there are no studies of these materials as HTM in CZTS solar cells besides the effects of $Mo(S,Se)_2$. This is partially due to the low compatibility of materials in the substrate structure and less development of the superstrate architecture, where the focus has been put in the absorber layer or front interface rather than in the back contact.

Nevertheless, there are some suitable examples of materials used as HTM and metallic back contact for CZTS in the literature, most of them adopted from other technologies. Direct use of gold as back contact is typically the first approach at laboratory scale due to its chemically inert nature, high conductivity and high work function of about 4.5 to 5.1 eV.[29] Unfortunately, its high cost does not make it attractive for up-scaling. Molybdenum also possesses good stability, with good conductivity and a reduced cost, but its work function does not make ohmic contact.[30] Silver has been found as a low-cost option,[2] but it is less inert, especially in contact with chalcogenide species, which can lead to the formation

of an $Ag(S,Se)_2$ interlayer. A similar problem occurs with copper, which is very appropriate as contact due to its high conductivity and low cost. The use of an HTM interlayer can mitigate the reactivity problems on the metallic contact while reducing the barriers to create an ohmic contact. Some organic HTMs have been adapted from other PV technologies to CZTS, such as P3HT/Cu,[31] PEDOT:PSS/Au,[22] Spiro-OMeTAD/Ag,[32] or Spiro-OMeTAD/Au.[16] However, organic HTMs can have stability problems and may not be adequate for a long-term purposes. A variety of inorganic materials with properties suitable for its use as HTM are known,[33] such as NiO or MoO_3, which have better stability but have not been explored for CZTS.

A popular alternative is a graphite-based contact.[34–36] Graphite provides a stable and stiff coating, cost-effective contact prepared by simple drop casting or screen-printing methods, which is aligned with the objectives of this architecture. However, graphite has a higher resistance than typical contacts, so it is limited for small areas. Covering graphite with a second metallic contact is required to improve the in-plane conductivity in large-area devices.

In conclusion, the knowledge on back contact engineering is very limited for kesterite solar cells. A superstrate architecture opens the field for plenty of materials with the potential to passivate the back surface, select the charge, and create an ohmic contact, which may suppose a significant efficiency improvement, as happened in other PV technologies.

3.2.5 State-of-the-art of CZTS in superstrate architecture

We first take into account the Shockley-Queisser PV limitations for kesterite as absorber material, shown in **Table 3.1**. In these values, we include a minimum reduction of 10 % from optical losses that are difficult to avoid in a superstrate configuration due to reflections and parasitic absorption from the glass, the TCO and the buffer layers. For a pure CZTS absorber, a 1.5 eV bandgap strongly limits the current to 26 mA/cm^2 in favour of a higher V_{OC}. Kesterite compositions containing

selenium instead of sulphur reduce the band-gap to 1 eV, which increases the current generated due to better light absorption, losing some voltage due to thermal relaxation.

Table 3.1. Limits of PV parameters values for typical kesterite materials.

E_g (eV)	V_{oc} (V)	J_{sc} (mA/cm^2)*	FF (%)	η (%)*
1	0.75	43.40	85.40	27.74
1.1	0.84	39.81	86.60	29.01
1.2	0.94	35.99	87.70	29.47
1.3	1.03	32.24	88.50	29.31
1.4	1.12	29.59	89.30	29.62
1.5	1.22	26.07	89.90	28.48

** Considering 10 % of optical losses.*

With these limitations, we then turn the attention to the existing literature of kesterite-based solar cells prepared in a superstrate architecture.

The first report on CZTS used in a superstrate architecture was back in 2009,[37] with a modest efficiency of 0.23 % and using a classic window/buffer of ZnO/CdS structure. Since the absorber was based on nanocrystals, no annealing treatments were required and there were no incompatibilities between the layers. However, the use of nanocrystals implies an absorber with high surface recombination, and the following studies were focused on producing absorbers with better electric properties. During the last decade, a variety of configurations have been reported aiming to find the most suitable material stack to maximize PV efficiency. In **Table 3.2**, all the reported attempts of preparing solar cells using kesterite in a superstrate architecture, the PV parameters, and some important remarks are shown.

Most of the reported works use solutions process techniques to prepare the CZTS film, starting from more toxic (hydrazine, toluene, etc.) to more green solvents (DMSO, ethanol or water), following a similar trend to the literature of substrate architecture. The use of green solvents is one of the attractive points to be discussed during this thesis since it could represent a key point to ensure safe and low-cost solar cells.

Table 3.2. All relevant superstrate kesterite–based solar cells parameters reported, sorted by the year of publication.

Structure	Absorber dep. method (solvent)	V_{oc} (mV)	J_{sc} (mA/cm^2)	FF (%)	PCE (%)	Cell area (cm^2)	Anneal (temp., time)	Samples per condition	Characterization	Reference
ITO/ZnO/CdS/CZTS^{NC}/Au	Spray coating (Toluene)	321	1.95	37	0.23	n.m.	No	-	*JV*	[37]
FTO/TiO_2/In_2S_3/ CZTS^{p}/Graphite	Screen Printing (Ethylcellulose)	250	8.76	27	0.6	0.5	125 ºC 1 h	1	*JV*	[4]
FTO/TiO_2/TiO_2^{m}/CdS/ CZTS/Graphite	Spray pyrolysis (DMF)	502	2.85	36	0.51	n.m.	250 ºC 30 mins	1	*JV*	[38]
FTO/TiO_2/In_2S_3/CZTS^{p}/Mo	Doctor blade (Propylene glycol)	240	7.8	28	0.55	0.5	600 ºC 7 mins	1	*JV*	[39]
ITO/TiO_2/CdS/CZTSSe^{NC}/Au	Spin coating (Ethanol)	377	4.2	41	0.65	0.1	570 ºC 45 mins	1	*JV*	[29]
FTO/TiO_2/TiO_2^{m}/CdS/ CZTS/Graphite	Spray pyrolysis (DMF)	446	6.8	37	1.1	n.m.	300 ºC 30 mins	1	*JV*	[34]
ITO/ZnO^{NR}/CdS/CZTS/Au	Spin coating (Pyridine)	679	4.1	44	1.2	0.12	250 ºC 10 mins	-	*JV*	[40]
ITO/TiO_2/CdS/CZTSSe^{NC}/Au	Spin coating (Ethanol)	363	6.8	45	1.1	0.1	550 ºC 45 mins	1	*JV*	[41]
FTO/ZnO/ZnO^{NR}/CdS/ CZTS^{NP}/Spiro-OMeTAD/Au	Spin coating (Toluene)	540	11	47	2.8	0.45	350 ºC 10 min	-	*JV*	[42]
FTO/ZnO^{NR}/CdS/CZTS/Ag	Spin coating (DMSO)	589	7.1	54	2.27	0.09	250 ºC 40 mins	6	*JV, EIS*	[43]
ITO/CdS/CZTSe/Graphite	Spin coating (Hydrazine)	433	13.7	41	2.4	0.5	480 ºC 30 mins	1	*JV*	[35]
FTO/$Ag_2ZnSnSe_4$/MoO_3/ITO	Co-evaporation	504	21	48.7	5.2	0.45	470 ºC 2 mins	1	*JV, EQE*	[44]
FTO/TiO_2^{NR}/CdS/CZTS/ Spiro-OMeTAD/Au	Spin coating (Ethanol)	312	13.9	46	2	n.m.	600 ºC 30 mins	1	*JV, EQE*	[45]
ITO/ZnO^{NR}/ZnS/CZTS/Au	Spin coating (2-Methoxyethanol)	869	8.5	49	3.63	n.m.	250 ºC 10 mins	-	*JV*	[46]
FTO/TiO_2/TiO_2^{m}/In_2S_3/ CZTS/Graphite	Electrodeposition	615	13.9	41	3.5	0.023	580 ºC 90 mins	-	*JV, EQE*	[36]
FTO/TiO_2^{m}/ZnO/CdS/ CZTS/P3HT/Cu	Spin coating (DMF-Ethanol)	400	12.6	42	2.15	n.m.	550 ºC 60 min	1	*JV*	[31]
FTO/TiO_2/TiO_2^{m}/CdS/ CZTS/Au	Spray pyrolysis (Methanol)	474	5.1	44	1	0.09	350 ºC	-	*JV*	[47]
FTO/TiO_2^{NR}/Al_2O_3/CdS/ CZTS/Spiro-OMeTAD/Au	Spin coating (Ethanol)	470	17.1	53	4.2	0.13	580 ºC 10 mins	>1	*JV, EQE, EIS*	[16]
FTO/TiO_2^{NR}/Al_2O_3/CdS/ Li:CZTS/Spiro-OMeTAD/Au	Spin coating (Ethanol)	512	19	52	5.02	0.13	580 ºC 10 mins	>1	*JV, EQE, EIS*	[48]
ITO/TiO_2/In_2S_3/CZTS/Ag	Spin coating (Ethanol)	490	3.1	37	0.7	0.04	300 ºC 5 mins	-	*JV*	[2]

Structure	Absorber dep. method (solvent)	V_{oc} (mV)	J_{sc} (mA/cm^2)	FF (%)	PCE (%)	Cell area (cm^2)	Anneal (temp., time)	Samples per condition	Characterization	Reference
FTO/TiO_2^m/ZnO/CdS/ CZTS/Spiro-OMeTAD/Au	Spin coating (DMF-Ethanol)	380	27.3	40	3.92	n.m.	550 ºC 30 min	1	*JV, EQE, EIS*	[49]
FTO/TiO_2/CdS/CZTSSe/ Spiro-OMeTAD/Ag	Spray pyrolysis (DMF)	240	26.5	37	2.3*	0.1	540 ºC 20 mins	4	*JV, EQE*	[32]
FTO/TiO_2^{NR}/Al_2O_3/ CZTSSe/Au	Spin coating (Ethanol)	234	19.5	41	1.85	0.13	580 ºC 10 mins	1	*JV, EQE, EIS*	[50]
FTO/ZnO^{NR}/ZnS/CZTS/Au	Spin coating (2-Methoxyethanol)	454	5.65	41.6	1.07	n.m.	300 ºC, 1h	1	*JV*	[51]
FTO/TiO_2^{NR}/CdS/CZTS/Au	Spin coating (2-Methoxyethanol)	518	5.14	39*	1.04	0.24	250 ºC 1 h	-	*JV*	[3]
FTO/TiO_2/CdS/ CZTSSe/PEDOT:PSS/Au	Spray pyrolysis (DMF)	224	30.4	34	2.3*	0.1	540 ºC 20 mins	20	*JV, EQE*	[22]
FTO/TiO_2/In_2S_3/CZTS/Au	Spray pyrolysis (Water)	383	24.6	38	3.34	0.0425	380 ºC	1	*JV*	[52]
ITO/ZnO^{NR}/CdS/CZTS/Ag	Thermal evaporation	460	20.8	29.5	2.82	0.0314	400 ºC 30 mins	1	*JV*	[53]
FTO/TiO_2/$(Ag,Cu)_2ZnSnSe_4$ /PTB7/MoO_X/Au	Spin coating (DMF)	470	31.2	55	8.1	n.m.	490 ºC, 16 mins	>1	*JV, EQE, EIS*	[54]
FTO/TiO_2/CdS/CZTS/Au	Spin coating (2-Methoxyethanol)	258	7.6	27	0.52	0.55	550 ºC 1h	1	*JV, EQE, EIS*	Chapter 4
FTO/TiO_2/TiO_2^m/CdS/ $Cu_2(Cd,Zn)SnS_4$/Graphite	Spray pyrolysis (Water-Ethanol)	536	12.5	29	1.9	0.068	550 ºC 1h	12	*JV, EQE, EIS*	Chapter 5
FTO/TiO_2/TiO_2^m/CdS/ $Cu_2CdSnSe_4$/Graphite	Spray pyrolysis (Water-Ethanol)	397	14.7	46.1	2.7	0.068	550 ºC 1h	12	*JV, EQE*	Chapter 5
(Substrate) Mo/CZTS/CdS/ ZnO/ITO/MgF_2	Sputtering	731	21.7	69.3	11.0	0.23	560 ºC 3 mins	10	*JV, EQE*	[55]
(Substrate) Mo/CZTSSe/CdS/ ZnO/ITO/MgF_2	Spin coating (Hydrazine)	513	35.2	69.8	12.6	0.42	>500 ºC	1	*JV, EQE, EIS*	[56]

n.m. Not mention, ^{m} Mesoporous, ^{NC} Nano-crystals, ^{NR} Nano-rods, * Calculated from $\eta = \frac{V_{OC} \cdot J_{SC} \cdot FF}{1000}$, $^-$ only one solar cell is presented.

Many of them use low temperature or no sulfurization treatments to avoid element intermix and unwanted reactions, and the resulting crystallinity of the absorber layer is poor and thus an unavoidable limitation of the PV performance. On the other hand, the sulfurization treatments at high temperatures seem to be valid only under certain conditions.

As mentioned in sections 3.2.1 and 3.2.2, these treatments are used only with TiO_2 as a window layer, and an extra buffer layer of CdS or In_2S_3 is present. When a selenization treatment is used instead, the absorber seems to have better compatibility even if there is only one n-type layer.[35,50] This suggests that CZTS has low compatibility with TiO_2 while alloys of CZTSSe seems to have a better one.

Looking at the PV parameters reported, the V_{OC} values are considerable below the reported values for CZTS in a substrate architecture. When nanostructures are used, this difference is lower, suggesting that a barrier or a recombination process appears in the interface. An exception was reported with a value of 869 mV using ZnO nano-rod structure ,[46] but unfortunately, such value was not able to be reproduced in similar works.[43,51,53] The low FF, usually reported below 50 %, can be one of the responsible for lower V_{OC}. Excessive series resistance can impact significantly in both V_{OC} and FF. Direct shunts are not usually present in the dark *JV* curves reported, so further reduction of the FF is usually attributed to internal shunt paths, small grains size or interface recombination.

Turning the attention to the J_{SC} values reported, it is the parameter with the highest improvement, with values up to 27.3 mA/cm^2 for pure sulphide and of 30.4 mA/cm^2 for sulfo-selenide absorbers. Incoherence seems to appear, if we consider that the maximum short-circuit current value for a pure sulphide absorber with a band gap of 1.5 eV was 26.0 mA/cm^2, as shown in **Table 3.1**. In the cases where this occurs, it can be noticed that there is always a CdS or In_2S_3 layer was previously used, turning the final absorber layer into an alloy of $Cu_2(Cd,Zn)SnS_4$ or $CuInS_2$-CZTS respectively due to diffusion of Cd and In, both having band gaps below 1.5 eV. This effect may also explain the low reproducibility found between reported works since the degree of alloy and the final composition of both the absorber and the buffer will vary in terms of:

- The thickness of both buffer and absorber layer.
- The element ratio of the films.
- The annealing conditions used.

- Oxygen and carbon contamination.

A slight change in any of these parameters can lead to large changes in the electrical properties of the solar cells, hindering the understanding and development of these kinds of solar cells. This can be noticed in **Table 3.2**, where most of the articles only show one or few cells, and few of them are able to show statistics along with various samples. Therefore, controlling and studying the effect of these parameters is key for the further development of a superstrate architecture, and ensuring that the obtained knowledge is robust and reproducible.

The power conversion efficiency reported in a superstrate architecture are still below than in a substrate architecture, but on the other hand, there are fewer studies done on this topic (in the order of thousands for substrate, and around 30 for superstrate). However, the efficiency values are high enough for the latter, up to 5%, to encourage further research on this topic, and to find if the advantages of a superstrate architecture can be combined with element abundant absorber materials.

3.3 Chapter Conclusions

In this chapter, we have been studied and prepared experimental procedures of the materials and films for the development of superstrate solar cells in the next chapters. CZTS films have been prepared by various solution-processed methods, and the advantages and disadvantages of each method were considered. Spin-coating is the most reported method due to its simplicity and reproducibility at a lab scale, but it has bad scalability. Ink-jet printing is found to have better scalability, however, it requires concentrated solutions with lower stability or toxic solvents and its main advantage of patterning is not exploited in PV applications. Spray pyrolysis instead has good material usage, scalability and is compatible with green solvents, so it is probably the most interesting technique among the studied for PV applications.

Superstrate architecture for CZTS based photovoltaic cells is an attractive approach for large-scale PV if the present challenges can be overcome. It has the advantages of an exposed back contact, allows for a simple way to investigate hole transport materials, semi-transparent devices, or tandem PV.

Works from different groups have shown noticeable improvements in superstrate CZTS based devices, making it an attractive candidate for further study. Power conversion efficiency (PCE) of 2.3% is reached for CZTSSe when an optimized CdS thickness and selenization process is used. Opportunities of engineering the front surface have been explored using mesoporous TiO_2, achieving a 3.92% efficiency,[49] and in the case of modified TiO_2 nano-rods a PCE of 5% can be achieved,[16,48] with a considerable increment in the extracted photo-voltage. All of these have a common step of sulfurization or selenization at high temperature, where the crystallinity of the absorber material is enhanced and the change in composition occurs due to Cd diffusion from the buffer layer. The Cd diffusion is avoided in a Cd free cell,[54] where the kesterite is alloyed with Ag forming a $(Ag,Cu)_2ZnSnSe_4$ composition, reaching an outstanding efficiency of 8.1%.

The variety of materials and synthesis conditions used to prepare CZTS superstrate solar cells is remarkable, but the PCE values are considerably below the best values reported in a substrate architecture, in the order of 13%.

In the next chapters, we will try to study the reasons behind this and propose alternative solutions to overcome these problems.

3.4 Chapter references

1. Mitzi, D. B., Gunawan, O., Todorov, T. K., Wang, K. & Guha, S. The path towards a high-performance solution-processed kesterite solar cell. *Sol. Energy Mater. Sol. Cells* **95**, 1421–1436 (2011).
2. Tumbul, A., Aslan, F., Göktaş, A. & Mutlu, I. H. All solution processed superstrate type Cu2ZnSnS4 (CZTS) thin film solar cell: Effect of absorber layer thickness. *J. Alloys Compd.* **781**, 280–288 (2019).
3. Satale, V. V. & Bhat, S. V. Superstrate type CZTS solar cell with all solution processed functional layers at low temperature. *Sol. Energy* **208**, 220–226 (2020).

4. Chen, Q., Cheng, S., Zhuang, S. & Dou, X. Cu 2ZnSnS 4 solar cell prepared entirely by non-vacuum processes. *Thin Solid Films* **520**, 6256–6261 (2012).

5. Nakayama, N. & Ito, K. Sprayed films of stannite Cu2ZnSnS 4. *Appl. Surf. Sci.* **92**, 171–175 (1996).

6. Todorov, T. & Mitzi, D. B. Direct liquid coating of chalcopyrite light-absorbing layers for photovoltaic devices. *European Journal of Inorganic Chemistry* **2010**, 17–28 (2010).

7. Schwartz, R. W. & Narayanan, M. Chemical Solution Deposition-Basic Principles. in *Solution Processing of Inorganic Materials* 33–76 (John Wiley & Sons, Inc., 2008). doi:10.1002/9780470407790.ch2

8. Todorov, T. *et al.* Solution-based synthesis of kesterite thin film semiconductors. *JPhys Energy* **2**, 012003 (2020).

9. Collord, A. D. & Hillhouse, H. W. Germanium Alloyed Kesterite Solar Cells with Low Voltage Deficits. *Chem. Mater.* **28**, 2067–2073 (2016).

10. Sayed, M. H., Schoneberg, J., Parisi, J. & Gütay, L. Influence of silver incorporation on CZTSSe solar cells grown by spray pyrolysis. *Mater. Sci. Semicond. Process.* **76**, 31–36 (2018).

11. Enkhbat, T., Kim, S. & Kim, J. Device Characteristics of Band gap Tailored 10.04% Efficient CZTSSe Solar Cells Sprayed from Water-Based Solution. *ACS Appl. Mater. Interfaces* **11**, 36735–36741 (2019).

12. Larramona, G. *et al.* Fine-Tuning the Sn Content in CZTSSe Thin Films to Achieve 10.8% Solar Cell Efficiency from Spray-Deposited Water-Ethanol-Based Colloidal Inks. *Adv. Energy Mater.* **5**, 1501404 (2015).

13. Martinho, F. *et al.* Persistent Double-Layer Formation in Kesterite Solar Cells: A Critical Review. *ACS Appl. Mater. Interfaces* **12**, 39405–39424 (2020).

14. Wu, S. H. *et al.* High-efficiency Cu2ZnSn(S,Se)4 solar cells fabricated through a low-cost solution process and a two-step heat treatment. *Prog. Photovoltaics Res. Appl.* **25**, 58–66 (2017).

15. Wallace, S. K., Mitzi, D. B. & Walsh, A. The Steady Rise of Kesterite Solar Cells. *ACS Energy Lett.* **2**, 776–779 (2017).

16. Wang, Z., Brodusch, N., Gauvin, R. & Demopoulos, G. P. Nanoengineering of the Cu2ZnSnS4-TiO2 interface: Via atomic layer deposition of Al2O3 for high sensitivity photodetectors and solid state solar cells. *J. Mater. Chem. A* **6**, 11507–11520 (2018).

17. Houshmand, M., Esmaili, H., Hossein Zandi, M. & Gorji, N. E. Degradation and device physics modeling of TiO2/CZTS ultrathin film photovoltaics. *Mater. Lett.* **157**, 123–126 (2015).

18. Nisika *et al.* Engineering Cu2ZnSnS4grain boundaries for enhanced photovoltage generation at the Cu2ZnSnS4/TiO2heterojunction: A nanoscale investigation

using Kelvin probe force microscopy. *J. Appl. Phys.* **130**, 195301 (2021).

19. Larsen, J. K., Simchi, H., Xin, P., Kim, K. & Shafarman, W. N. Backwall superstrate configuration for ultrathin Cu(In,Ga)Se2 solar cells. *Appl. Phys. Lett.* **104**, 033901 (2014).

20. Espindola-Rodriguez, M. *et al.* Bifacial Kesterite Solar Cells on FTO Substrates. *ACS Sustain. Chem. Eng.* **5**, 11516–11524 (2017).

21. Lee, D. & Yang, J. Y. Investigation of Cu2ZnSnS4 solar cell buffer layer fabricated via spray pyrolysis. *Curr. Appl. Phys.* **21**, 184–191 (2021).

22. Pakštas, V. *et al.* Impact of CdS layer thickness on the composition, structure and photovoltaic performance of superstrate CZTSSe solar cells. *Sol. Energy* **207**, 1231–1239 (2020).

23. O'Regan, B. & Grätzel, M. A low-cost, high-efficiency solar cell based on dye-sensitized colloidal TiO2 films. *Nature* **353**, 737–740 (1991).

24. Nanu, M., Schoonman, J. & Goossens, A. Nanocomposite three-dimensional solar cells obtained by chemical spray deposition. *Nano Lett.* **5**, 1716–1719 (2005).

25. Yoshikawa, K. *et al.* Silicon heterojunction solar cell with interdigitated back contacts for a photoconversion efficiency over 26%. *Nat. Energy* **2**, 17032 (2017).

26. Series 6 | First Solar. Available at: https://www.firstsolar.com/Modules/Series-6. (Accessed: 25th November 2021)

27. Wolden, C. A. *et al.* The roles of ZnTe buffer layers on CdTe solar cell performance. *Sol. Energy Mater. Sol. Cells* **147**, 203–210 (2016).

28. Calió, L., Kazim, S., Grätzel, M. & Ahmad, S. Hole-Transport Materials for Perovskite Solar Cells. *Angewandte Chemie - International Edition* **55**, 14522–14545 (2016).

29. Wang, C. L., Wang, C. C., Reeja-Jayan, B. & Manthiram, A. Low-cost, Mo(S,Se)2-free superstrate-type solar cells fabricated with tunable band gap Cu2ZnSn(S1-xSex) 4 nanocrystal-based inks and the effect of sulfurization. *RSC Adv.* **3**, 19946–19951 (2013).

30. Saha, U. & Alam, M. K. Boosting the efficiency of single junction kesterite solar cell using Ag mixed Cu2ZnSnS4 active layer†. *RSC Adv.* **8**, 4905–4913 (2018).

31. Yan, R., Kang, L., Sun, Y. & Zhang, J. Solution-processed Cu2ZnSnS4 thin film with mixed solvent and its application in superstrate structure solar cells. *RSC Adv.* **8**, 11469–11477 (2018).

32. Franckevičius, M. *et al.* Efficiency improvement of superstrate CZTSSe solar cells processed by spray pyrolysis approach. *Sol. Energy* **185**, 283–289 (2019).

33. Rajeswari, R., Mrinalini, M., Prasanthkumar, S. & Giribabu, L. Emerging of Inorganic Hole Transporting Materials For Perovskite Solar Cells. *Chem. Rec.* **17**, 681–699 (2017).

34. Tanaka, K., Kurokawa, M., Moriya, K. & Uchiki, H. Surface morphology improvement of three-dimensional solar cell with Cu 2ZnSnS4 absorber. *J. Alloys Compd.* **571**, 98–102 (2013).

35. Zhang, Y., Sun, Y., Wang, H. & Yan, H. A facile non-vacuum-based Cu2ZnSnSe4 superstrate solar cell with 2.44% device efficiency. *Phys. Status Solidi Appl. Mater. Sci.* **213**, 1324–1328 (2016).

36. Berruet, M., Di Iorio, Y., Pereyra, C. J., Marotti, R. E. & Vázquez, M. Highly-efficient superstrate Cu2ZnSnS4 solar cell fabricated low-cost methods. *Physica Status Solidi - Rapid Research Letters* **11**, 1700144 (2017).

37. Steinhagen, C. *et al.* Synthesis of Cu2ZnSnS4 nanocrystals for use in low-cost photovoltaics. *J. Am. Chem. Soc.* **131**, 12554–12555 (2009).

38. Kurokawa, M., Tanaka, K., Moriya, K. & Uchiki, H. Fabrication of three-dimensional-structure solar cell with Cu 2ZnSnS 4. *Jpn. J. Appl. Phys.* **51**, 10NC33 (2012).

39. Chen, Q. M., Li, Z. Q., Ni, Y., Cheng, S. Y. & Dou, X. M. Doctor-bladed Cu 2ZnSnS 4 light absorption layer for low-cost solar cell application. *Chinese Phys. B* **21**, 038401 (2012).

40. Lee, D. & Yong, K. Solution-processed Cu2ZnSnS4 superstrate solar cell using vertically aligned ZnO nanorods. *Nanotechnology* **25**, 065401 (2014).

41. Wang, C. L. & Manthiram, A. Low-cost CZTSSe solar cells fabricated with low band gap CZTSe nanocrystals, environmentally friendly binder, and nonvacuum processes. *ACS Sustain. Chem. Eng.* **2**, 561–568 (2014).

42. Jiang, M., Wu, J., Di, G. & Li, G. Nanostructured solar cell based on solution processed Cu2ZnSnS4 nanoparticles and vertically aligned ZnO nanorod array. *Phys. Status Solidi - Rapid Res. Lett.* **8**, 971–975 (2014).

43. Chen, R. *et al.* Solution-Processed One-Dimensional ZnO@CdS Heterojunction toward Efficient Cu2ZnSnS4 Solar Cell with Inverted Structure. *Sci. Rep.* **6**, 35300 (2016).

44. Gershon, T. *et al.* Photovoltaic Device with over 5% Efficiency Based on an n-Type Ag2ZnSnSe4 Absorber. *Adv. Energy Mater.* **6**, 1601182 (2016).

45. Wang, Z., Gauvin, R. & Demopoulos, G. P. Nanostructural and photo-electrochemical properties of solution spin-coated Cu2ZnSnS4-TiO2 nanorod forest films with an improved photovoltaic performance. *Nanoscale* **9**, 7650–7665 (2017).

46. Ghosh, A., Thangavel, R. & Gupta, A. Solution-processed Cd free kesterite Cu2ZnSnS4thin film solar cells with vertically aligned ZnO nanorod arrays. *J. Alloys Compd.* **694**, 394–400 (2017).

47. Zhong, M., Liu, S., Li, H. & Li, C. Superstrate-type Cu2ZnSnS4 solar cells without sulfurization fabricated by spray pyrolysis. *Chalcogenide Lett.* **15**, 133–137 (2018).

48. Wang, Z., Brodusch, N., Gauvin, R. & Demopoulos, G. P. Lithium-doped Cu2ZnSnS4 superstrate solar cells with 5% efficiency – An alternative to thin film kesterite photovoltaics. *Nano Energy* **53**, 130–134 (2018).

49. Kang, L., Zhang, Z., Shi, J., Yan, R. & Zhang, J. Surface morphology control of Cu 2 ZnSnS 4 by addition of cellulose in solution process for high performance superstrate solar cell. *Mater. Res. Bull.* **113**, 31–37 (2019).

50. Wang, Z., Brodusch, N., Gauvin, R. & Demopoulos, G. P. New Insight into Sulfurized and Selenized Kesterite-Titania Nanostructures for CdS-free and HTM-free Photovoltaic and Voltage-Modulated Photodetecting Applications. *ACS Sustain. Chem. Eng.* **7**, 15093–15101 (2019).

51. Gayen, R. N. & Chakrabarti, T. Effect of series and shunt resistance on the photovoltaic properties of solution-processed zinc oxide nanowire based CZTS solar cell in superstrate configuration. *Mater. Sci. Semicond. Process.* **100**, 1–7 (2019).

52. Lee, D. & Yang, J. Y. Superstrate structured FTO/TiO2/In2S3/Cu2ZnSnS4 solar cells fabricated by a spray method with aqueous solutions. *Coatings* **10**, 548 (2020).

53. Peksu, E. & Karaagac, H. Preparation of CZTS thin films for the fabrication of ZnO nanorods based superstrate solar cells. *J. Alloys Compd.* **884**, 161124 (2021).

54. Wang, Z., Wang, Y. & Konstantatos, G. Highly efficient, ultrathin, Cd-free kesterite solar cells in superstrate configuration enabled by band level tuning via Ag incorporation. *Nano Energy* **94**, 106898 (2022).

55. Yan, C. *et al.* Cu2ZnSnS4 solar cells with over 10% power conversion efficiency enabled by heterojunction heat treatment. *Nat. Energy* **3**, 764–772 (2018).

56. Wang, W. *et al.* Device Characteristics of CZTSSe Thin-Film Solar Cells with 12.6% Efficiency. *Adv. Energy Mater.* **4**, 1301465 (2014).

4 Temperature effects on the absorber, the device and the PV performance

In this chapter, we begin the fabrication of a superstrate structure using CZTS as an absorber material. Solar cells are fabricated in a stack layer configuration of FTO-TiO_2-CdS-CZTS-Au. Except for the front (FTO) and back (Au) contacts, all the layers that composed the PV device are prepared by wet chemistry methods. First, we study the effect of the sulfurization temperature in CZTS thin films prepared by spin coating on a superstrate architecture. It is noted that the temperature affects the final composition of the absorber due to cadmium diffusion at 500 ºC from the CdS layer, while the temperature above 530 ºC is essential for a complete Zn incorporation into the crystal structure. The crystallinity is highly affected, and a temperature of 550 ºC is found to be favourable for the crystal growth, and the fabricated device gave an improved performance. Impedance spectroscopy measurements suggest the performance enhancement is due to the reduction of defects and an increase of the depletion width in the *p-n* junction. Second, we explore the use of a porous nanostructure in the window layer and the preparation of CZTS by spray pyrolysis. The use of a mesostructure improve the transmission of light and highly affects the deposition of CdS. A proper layer thickness is found to maintain a high transmittance in the front side along with the improvement in most of the photovoltaic properties due to a reduction of interface recombination and shunts. After considering all these factors, solar cells with a maximum PCE of 0.72 % was obtained, which is a significant value considering the cost-effective methods used. The challenges and possible improvements are considered for CZTS in a superstrate architecture.

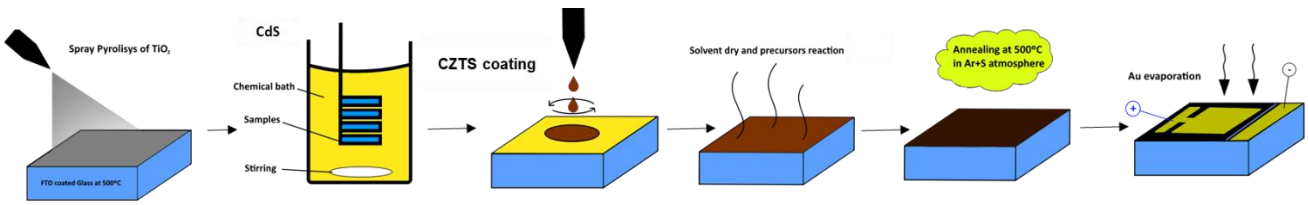

Section 4.1 is mostly based on the article Payno, D., Kazim, S., Salado, M. & Ahmad, S. Sulfurization temperature effects on crystallization and performance of superstrate CZTS solar cells. Sol. Energy ***224****, 1136–1143 (2021)*[1]

Content:

4.1 Effect of temperature on the absorber and the PV performance.

In this section, we turn attention to the temperature of synthesis required for a proper crystallization of CZTS as a starting point. For a photovoltaic cell, the crystallinity and grain size of the absorber layer are important factors to take into account, since the conductivity and inter-grain recombination are strong limiting factors. The range of temperature required for a pure phase of CZTS is at least 500 ºC,[2] and between 500 and 600 ºC for the grain growth. [3,4] Due to the limitation of the FTO, the range chosen to explore as a starting point is between 500 and 550 ºC. The first successfully films with good quality obtained were produced by spin-coating, following the 2-methoxyethanol route,[5] and this will be the first tested method to prepare solar cells.

The use of CdS is also tested. It is observed that the CdS layer is necessary to fabricate an efficient device, which may be related to the alloying of Cd with the absorber layer, and with a slight improvement of the crystallinity and the grain size. XRD and Raman analysis show that the sulfurization temperature influences the crystallinity and absorber composition, due to the reactivity of the CdS and the inclusion of Cd^{2+} into the lattice structure, which is dominating over Zn^{2+} at lower temperatures. Samples sulfurized at an adequate temperature can form layers with a bigger grain size to yield improved PCE. We noted a reduction of the defect density by impedance-voltage measurements, while an increase of the depletion layer helps to increase the photocurrent.

4.1.1 Substrate preparation

TEC-15 FTO coated glass was used after a sequential cleaning procedure. In short, the cleaning procedure includes a sequential ultra-sonication step for 10 minutes of the substrates immersed in Hellmanex-water solution, acetone, and isopropanol, respectively. After drying the substrates with compressed air, they were kept under UV light to remove any organic residue. A blocking layer of TiO_2 of c.a 60-80 nm was then deposited on FTO by spray pyrolysis. For that, a

solution containing titanium diisopropoxide bis(acetylacetonate) (Merck) in ethanol (Scharlab) with a volume ratio of 1:19 was sprayed at 500 ºC. After the deposition, the samples were maintained at 500 ºC for 30 minutes to ensure an anatase TiO_2 structure and that no organic residue remains.

4.1.2 Solar cells preparation

A thin film of c.a 60-80 nm of CdS was deposited by chemical bath deposition. The samples were immersed in a bath of 180 mL of deionized water at 65 ºC containing 56 mg of Cadmium sulphate (Alfa Aesar 98%). Then 18.2 mL of ammonia solution (30%, Alfa Aesar) were added, followed by 20 mL water solution with 100 mg of thiourea (99%, Alfa Aesar). The bath was maintained at 65 ºC and the samples were extracted 20 minutes later. CdS deposited on the glass side was removed with diluted HCl.

CZTS film was prepared on top of CdS by spin coating. The solution contains 0.88 M of anhydrous copper (II) chloride (98%, Alfa Aesar), 0.55 M zinc acetate dihydrate (98%, Fisher), 0.55 M tin(II) chloride dihydrate (98%) and 3 M of thiourea (99%, alfa aesar) dissolved on 2-methoxyethanol. The target was a Cu-poor (Cu/(Sn+Zn)=0.8) composition, with an excess of 50% sulfur, to prevent sulfur loss during the precursor film formation. The solution was stirred until all the salts were dissolved, obtaining a yellowish transparent colour. Then 50 µL of the CZTS precursor solution were spun coated at 1500 rpm for 30 s and dried at 270 ºC for 2 minutes on a hot plate in the air to form a CZTS precursor film of 450-500 nm.

Samples were then submitted to a sulfurization process at 500, 530, or 550 ºC for 45 minutes inside a close quartz tubular furnace containing 50 mg of sulfur powder (99.5%, Alfa Aesar) in an argon atmosphere. After cooling to room temperature, photovoltaic cells were completed by depositing 70 nm of Au as metallic contact by thermal evaporation, defining an active area of 0.55 cm^2 by a mask.

4.1.3 Measurements

XRD diffractograms were measured directly on the finished solar cells with a Cubix3 system from PANalytical with a Cu anode. Raman measurements were acquired with an inVia confocal Raman microscope using a 785 nm wavelength laser as excitation. SEM images were recorded with a Hitachi S-3400 electron microscope. The absorption spectrum was recorded with an Agilent Cary 60 UV-Vis spectrometer.

For the device characterization, *J-V* curves were measured with a 2400 Keithley multi-meter, and the illumination of the samples was performed with a class AAA Oriel solar simulator from Newport. The external quantum efficiency was measured on a PVE300 Bentham system, consisting of a 150 W Xenon lamp and a 1/4m monochromator, in a range from 300 to 1000 nm. Impedance measurements were performed inside a faraday box with a Biologic impedance analyser, by applying a 20 mV perturbation in a frequency range from 1 GHz to 100 Hz, and an applied constant voltage from -1 V to 1 V. EC-LAB software was used to fit the equivalent circuits.

4.1.4 Results and discussion

To understand the effect of the temperature on the CZTS crystal structure, XRD measurements were performed directly on the final devices. **Figure 4.1** shows the measured diffractogram for the samples sulfurized at 500 ºC, 530 ºC, and 550 ºC, and an additional CdS free, pure kesterite device at 550 ºC was used as a reference. An evolution of the phases can be distinguished when the temperature is increased. For the sample sulfurized at 500 ºC, the characteristic peaks of CdS are predominant, with a very small intensity of the peaks corresponding to the kesterite phase of CZTS. CdS peaks show a slight shift to a higher angle, which indicates a Zn alloying with CdS, forming a secondary phase of (Zn,Cd)S.[6] On the contrary, for higher temperatures, the peaks corresponding to CdS start to decrease, while the intensity of the kesterite peaks emerges. At 550 ºC, the highest peak intensity from kesterite can be observed, and peaks of CdS are not found,

indicating the enhanced crystallinity in kesterite, while there is a reduction of the CdS phase.

The peaks at [112] and [220] planes are indicated in **Figure S4.1a** and **Figure S4.1b** respectively. Shifting to lower angles can be observed for the sample prepared at 500 ºC, which can be attributed to a higher percentage of Cd in the crystal structure. This, along with the disappearing peaks of CdS aforementioned, is evidence of Cd incorporation into the kesterite crystal. Cd^{2+} can easily replace Zn^{2+}, forming an alloy of $Cu_2(Cd,Zn)SnS_4$ (CCZTS). The shift in the peaks is in agreement with works that intentionally includes Cd in the absorber structure.[7,8]

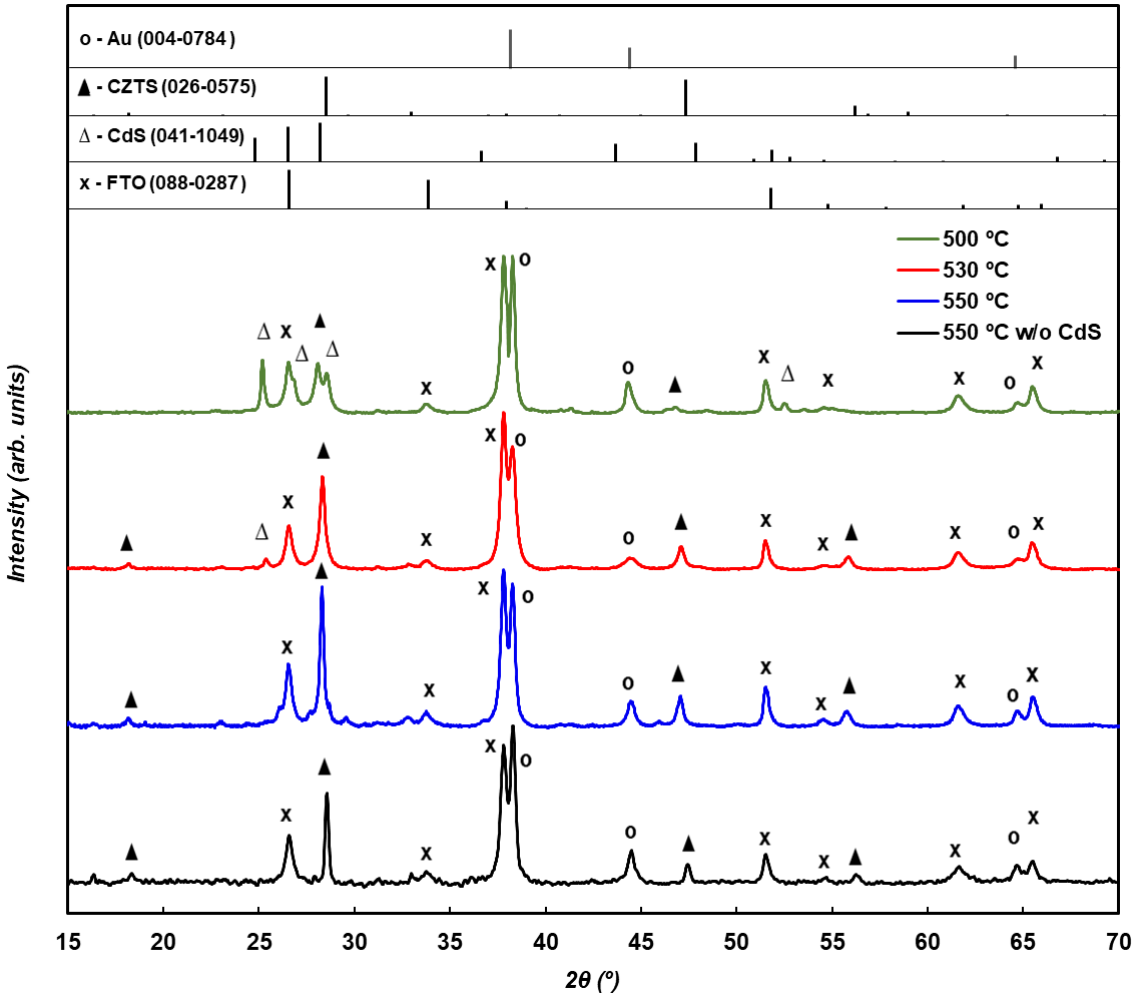

Figure 4.1. XRD spectra of samples with different sulfurization temperatures.

Table 4.1 shows the lattice parameters values calculated for every sample. As expected, the small size of Zn^{2+} reduces the unit cell volume, causing a shift to higher angles, which can be noticed in the reference sample (without CdS) and

pure CZTS is formed. When CdS is used, the maximum Cd incorporation is observed at 500 ºC, showing a larger cell volume. A stannite phase of Cu_2CdSnS_4 can be formed at temperatures of 460 ºC,[9] while a temperature higher than 500 ºC is necessary to promote the reaction of ZnS with Cu_2SnS_3 to form Cu_2ZnSnS_4,[2] and at least 550 ºC to eliminate the secondary phases.[3] In this case, the incorporation of Zn is not completed at 500 ºC, leading to a visible structure with high content of Cd.

Table 4.1. Calculated values for the lattice parameters.

Temperature	a (Å)	b (Å)	c (Å)	Cell volume (Å^3)	Crystalline size (nm)
500 ºC	5.485	5.485	11.048	332.4	21.2
530 ºC	5.453	5.453	10.902	324.2	24.1
550 ºC	5.458	5.458	10.909	325.0	40.1
550 ºC w/o CdS	5.414	5.414	10.799	316.6	37.4

At temperatures higher than 530 ºC, the cell volume is in intermediate values, suggesting that Zn starts to compete with Cd in the incorporation to the crystal structure. When the temperature is lower, the remaining Zn within the absorber material is expected to remain as it forms the highly stable phase of ZnS. According to literature, this phase will not contribute to the PV effect and its presence reduces the photocurrent, however, it does not shows a large effect in the big recombination impact due to its wide band-gap and high resistance.[10,11]

The Raman spectra of the samples are presented in **Figure 4.2** and the deconvolution of the peaks in the sample prepared without CdS shows four peaks that can be associated with a pure kesterite phase.[12] All the samples prepared with a CdS layer present a shift to a lower wavelength. A shift of the main peak has been reported for Cd-alloyed CZTS,[13] confirming that Cd is been incorporated into the absorber layer. The sample prepared at 500 ºC shows a higher shift with respect to the pure CZTS. This is in agreement with the XRD measurements that

show higher Cd incorporation. Also, the sample prepared at 500 ºC shows a tail corresponding to a peak at 400 cm^{-1}, which can match with a phase of (Zn, Cd)S.[14] The samples prepared at 530 ºC and 550 ºC does not show evident secondary phases by Raman spectroscopy.

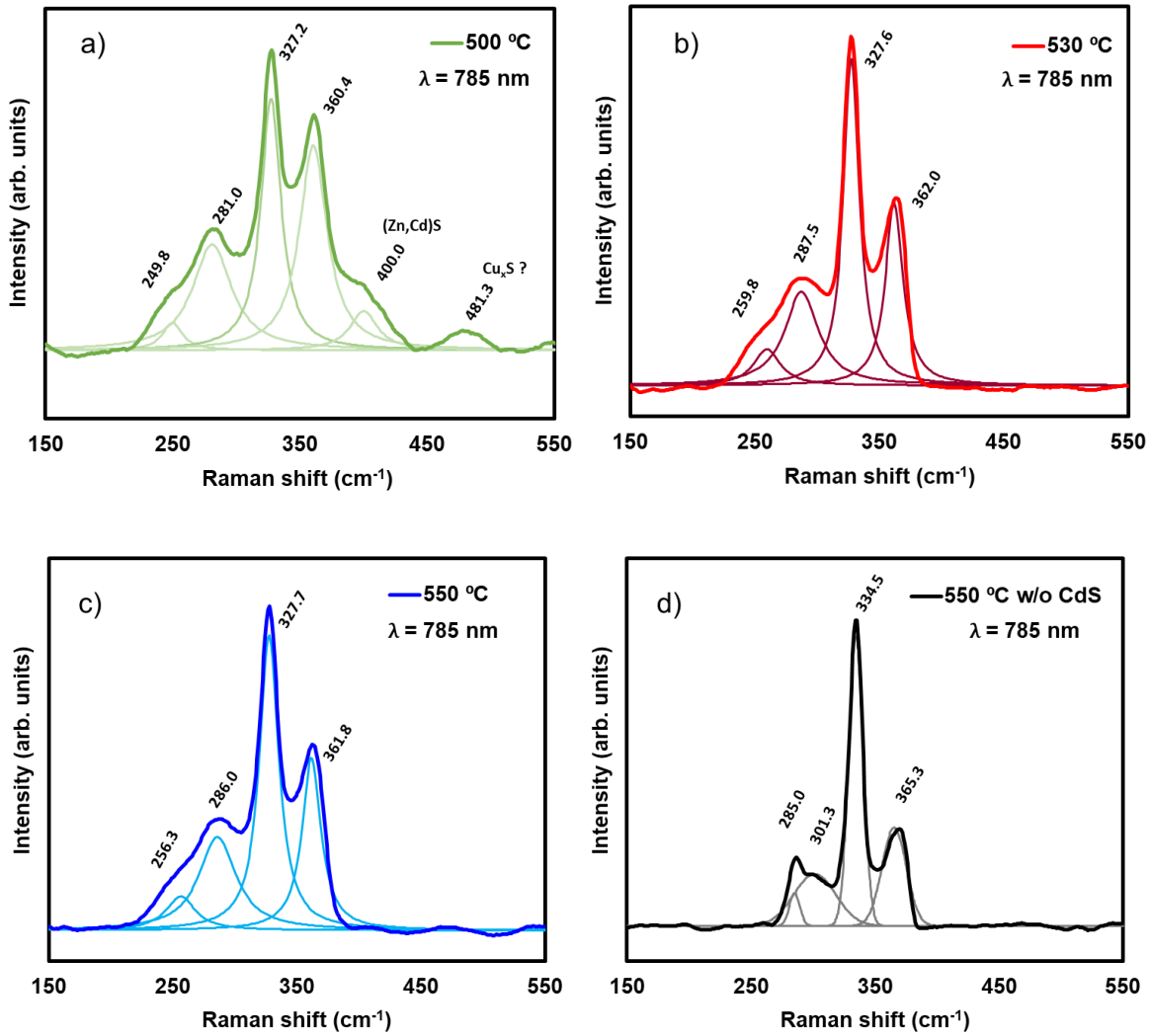

Figure 4.2. Raman shifts for the samples prepared at a) 500 ºC, b) 530 ºC, c) 550 ºC, and d) 550 ºC without CdS, with the values of the fitted peaks indicated.

PV performance is highly dependent on the crystallinity of the materials. The charge carrier conductivity is reduced when it travels across the inter-grains due to a higher density of defects that acts as recombination centres. This effect is particularly harmful in polycrystalline materials based on chalcogenides, so a crystal size equal to the film thickness is preferred to avoid recombination across the conductivity direction.

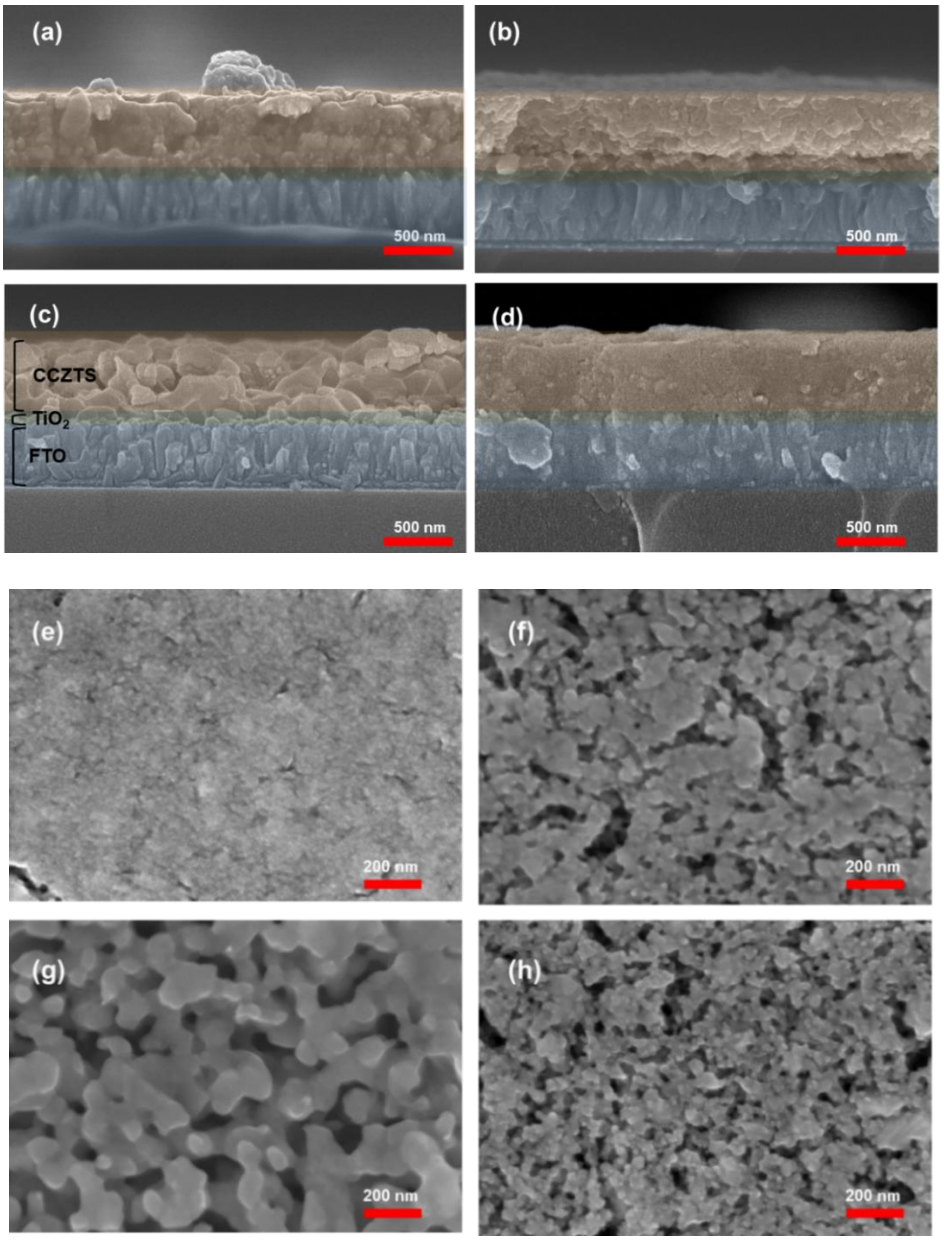

Figure 4.3. Cross-sectional and top view of solar cells samples sulfurization temperatures for a), e) 500 ºC, b), f) 530 ºC, c), g) 550 ºC, and d), h) 550 ºC without CdS interlayer.

To compare the effect of the temperature in the absorber crystal size, cross-section SEM images were performed (**Figure 4.3**). All of them present an absorber layer thickness of 450 – 500 nm, with no voids in the interface of the FTO/TiO_2 front contact. Samples sulfurized at 500 ºC and 530 ºC shows low crystallinity, making a layer of fine grains with less than 50 nm of diameter size.

On the other hand, the crystallinity drastically increases for the sample annealed at 550 ºC, showing large crystals of 100-200 nm.

It can be noticed in **Figure 4.3d** that the grain growth seems to be inhibited when no CdS interlayer is used, producing an absorber film of lower crystallinity. This is in agreement with the calculated crystallite size derived from the Scherrer equation (XRD measurements) represented in **Table 4.1**.

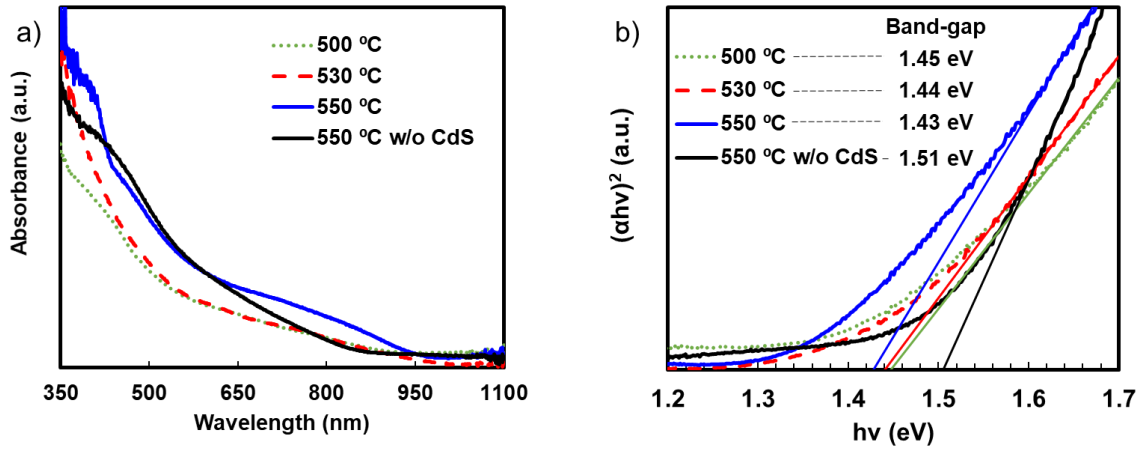

Figure 4.4. a) Absorbance spectra of the samples made at 500, 530, 550ºC and 550 ºC without CdS film. b) Tauc plot with calculated band-gap.

To explore the effect of temperature on the optical properties of the films, UV-Vis absorbance spectra were measured in **Figure 4.4a**. The optical bandgap for direct transitions is calculated in **Figure 4.4b** by a linear fitting in the Tauc plot $(\alpha h\nu)^2$ versus the photon energy $h\nu$. The absorption increases slightly for the samples prepared at 550 ºC in the UV-Vis range, which can be correlated with a higher phase purity. A similar optical bandgap was noted (1.43 eV to 1.45 eV) for the samples prepared with CdS, while a higher bandgap of 1.51 eV is found for the sample of pure CZTS. Since the incorporation of Cd into the kesterite structure decrease the bandgap, the lower bandgap observed suggest the formation of a $Cu_2(Zn,Cd)SnS_4$ alloy with a quantity of Cd of around 20 % to 30 %.[15] The presence of Cd itself in the final structure should not be considered necessarily as a drawback. Previous reports verified that alloys of $Cu_2(Zn,Cd)SnS_4$ with different quantities of Cd presented improved PV

performance by increasing the minority carrier lifetime [7,8,15,16] and reducing the interface recombination.[17]

A schematic of the kesterite-based solar cell is shown in **Figure 4.5a**, and the PV properties were evaluated by measuring the current-voltage (J-V) curve under 1 sun illumination intensity in **Figure 4.5b**, and the obtained characteristic parameters are shown in **Table 4.2**. Device prepared at lower temperature shows a lower performance due to the reduction in open-circuit voltage (V_{oc}) while maintaining a similar short circuit current (J_{sc}) and fill factor (FF) than the devices fabricated at intermediated temperature (530 ºC). For the sample annealed at 550 ºC, both the V_{oc} and the J_{sc} increases, resulting in a higher PCE, but compromising the FF.

Devices without CdS layers were shunted and gave a negligible PV response. A proper explanation is still unclear but we propose that CdS film could act as both dopant and crystallization seed for CZTS, while the contact with TiO_2 can promote oxidation of the secondary phases, such as SnO_2,[18] hindering the sulfur incorporation and so the CZTS crystallization.

Table 4.2. Characteristic parameters calculated from the photovoltaic performance. *J–V* measurements were performed at 100 $mV \cdot s^{-1}$ scan.

	V_{oc} (V)	J_{sc} (mA/cm^2)	Fill Factor (%)	PCE (%)	R_s (Ω cm^2)	R_{sh} (Ω cm^2)
500ºC	0.164	2.4	33.2	0.128	18.31	215.9
530ºC	0.220	2.5	38.9	0.216	19.53	282.2
550ºC	0.258	7.6	26.6	0.518	17.07	208.7

External Quantum Efficiency (EQE) was measured and represented in **Figure 4.5c**, all the samples showed a better photocurrent at shorter wavelengths, with a maximum between 400-500 nm, and a progressive reduction for longer wavelengths. Considering that the longer wavelengths are absorbed deeper in the material, the main collection of electron-hole pairs is for the ones generated closer

to the *p-n* junction, suggesting that the electron-hole pair lifetime is short enough to recombine before reaching the p-n junction, causing a high loss of current. A low minority lifetime of lower than 2 ns and electron diffusion length L_n less than 0.5 µm is usually reported even for high-performance devices, resulting in a low collection of current for absorber light far from the junction,[19,20] causing a noticeable decrease of the current collected when the depletion width is not sufficiently thick.

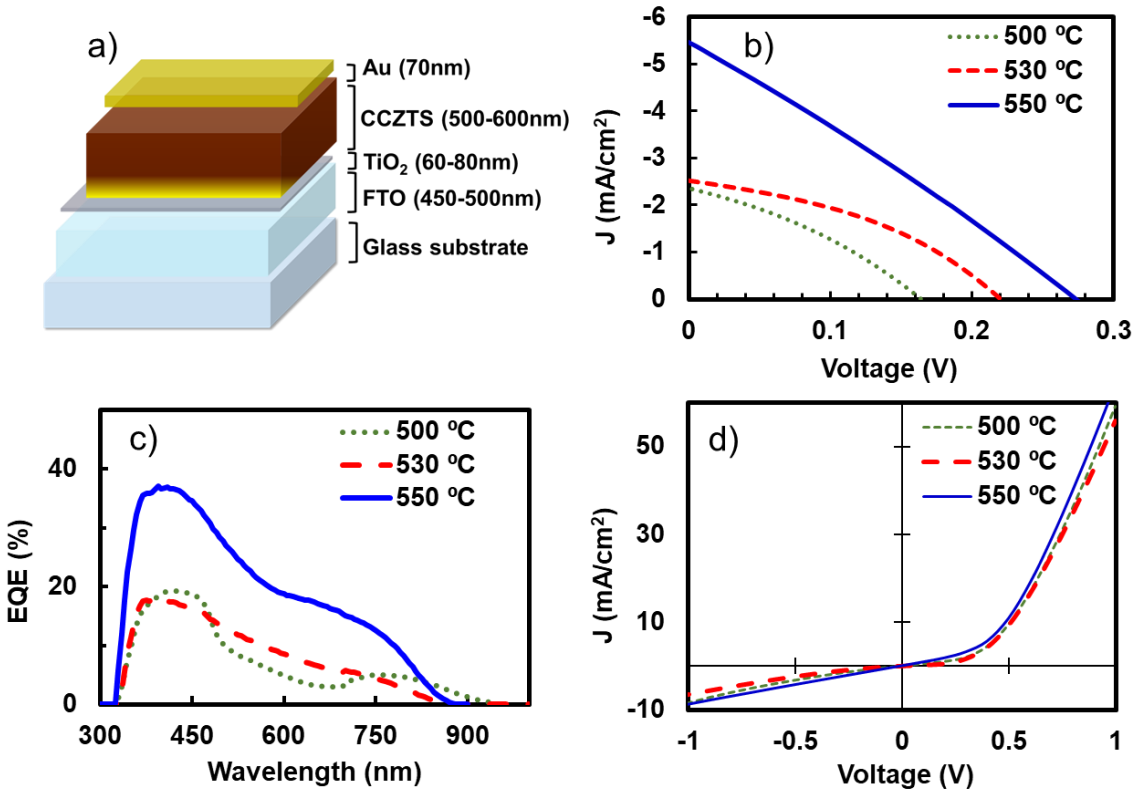

Figure 4.5. a) Scheme of the layer stack deposition, b) *J-V* curves under one sun illumination, c) EQE spectra, d) *J-V* curves in dark.

In particular, the sample annealed at 550 ºC showed an improved photon to current conversion throughout the whole visible wavelength region which can be attributed to the higher absorption in bigger crystal size, reducing inter-grain recombination. For wavelengths longer than 860 nm, corresponding with a 1.47 eV of photon energy, there is no photo-current generation, in agreement with the calculated bandgap from the tauc plot of 1.43 eV. The sample annealed at 500 ºC shows an extended range of wavelengths contributing to the EQE, until 900 nm,

which may be due to a higher Urbach absorption in the band tailings. Conversely, the sample annealed at 530 ºC has better photon conversion at intermediate wavelengths and shows a bandgap of 1.46 eV, similar to the calculated by the tauc plot (1.44 eV).

This supports the hypothesis shown by XRD, where the Zn incorporation to the kesterite lattice requires at least a temperature of 530 ºC. At lower temperatures, such as 500 ºC, the Zn incorporation is smaller, therefore, Zn could remain as a secondary amorphous phase of ZnS forming small grains as it was confirmed by SEM images.

Intrinsic instabilities and recombination processes can be evaluated by *J-V* curves measured in dark in **Figure 4.5d**. We suggest that a large leakage of the current at reverse polarization can be the plausible reason that affects the device performance, indicating the existence of shunts in the devices. These shunts can be attributed to a high quantity of conductive secondary phases in the absorber or due to a high surface porosity or crack defects that allows gold to infiltrate the pores between the crystals, increasing the possibilities of being in contact with the FTO.

To unravel the electrical properties of the samples, impedance spectroscopy (IS) was performed in an applied voltage range from -1 to 1 V under dark and illumination conditions. The used circuit to fit the impedance curves is shown in **Figure 4.6a**, it is composed of a series resistance (R_s) followed by an RC loop, which represents the recombination resistance R_{pn} and the capacitance of the *p-n* junction C_{PN}. The second loop consists of a non-ideal capacitor RC circuit, Q_d and R_d, which agglomerates other capacitive effects, such as secondary phases defects and metallic contacts interfaces. This circuit fits well with the measurements of **Figure S4.3** at every voltage. Under illumination, the recombination processes can be noticed. By using IS, a reduction of the semicircle is observed under illumination in **Figure 4.6b**, which represents the reduction in the recombination resistance R_{PN} due to an increase of the charge carrier density in the depletion region.[21]

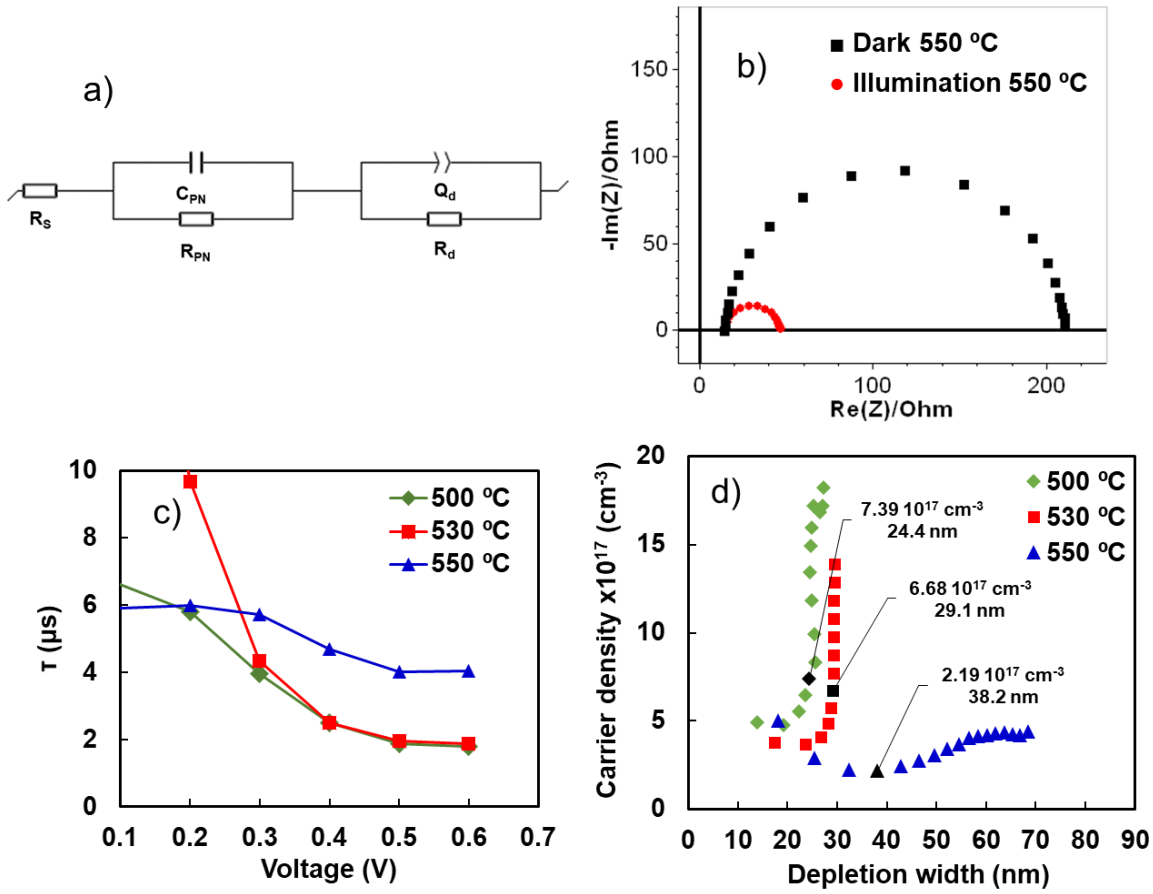

Figure 4.6. a) An equivalent circuit used to fit the impedance measurements, b) Nyquist plot at *V*=0 for the sample sulfurized at 550 ºC under dark and illumination, c) Carrier lifetime under illumination and d) carrier density profile calculated from the circuit values in dark, with the values at *V* = 0 indicated and marked in black.

The series resistance, mainly limited by the conductivity of the FTO/TiO_2 contact, did not change significantly, suggesting that the blocking layer of TiO_2 protects the FTO even at high temperatures and sulfur atmosphere. R_{PN} seems to increase with the processed temperature, reflecting the increase of the CZTS grain size and decrease of recombination centres. The capacitance of the junction decreases with the increasing temperature. The capacitance mainly depends on the depletion layer width and the drop in the capacitance value entails an increase of the depletion layer thickness.

The characteristic constant time (τ) of the RC circuit is calculated by multiplying R_{PN} and C_{PN} and is usually associated with the carrier lifetime, as it represents the

discharge time of the capacitor. τ gives a representative value when is measured on direct polarization under small applied voltage, and the recombination takes place mostly at the interface. This lifetime was extracted from the IS under illumination in **Figure 4.6c**, revealing that the electron lifetime is dramatically reduced with the voltage for the samples made at 500 ºC and 530 ºC. However, the sample sulfurized at 550 ºC retains a carrier lifetime of 4 µs at 0.6 V, which suggests that fast interface recombination is the main limitation for the current generation in the samples fabricated at 500 ºC and 530 ºC.

The carrier density and the depletion width close to the *p-n* junction can be extracted from the Mott-Schottky measurements of **Figure S4.2**, and are represented in **Figure 4.6d** using *(Eq. 1.15)*. The values for the constants used were 6.7 for the dielectric constant,[22] 0.55 cm^2 for the contact area, the calculated capacitance (C_P), and the built-in potential from **Figure S4.2**.

This method allows studying the electronic properties of the absorber layer, since the depletion width is extended mainly in the layer with lower carrier density, and the *n*-type carrier density is in the order of 10^{20} cm^{-3} due to the FTO contribution. Therefore, any possible impact from the remaining CdS will be small in comparison with the change of the properties of the absorber layer due to Cd alloying.

Samples annealed at 500 ºC and 530 ºC show a similar trend, with a very thin depletion width and an unusually high concentration of carrier density that drastically increase with the reverse voltage. A high carrier concentration can be due to the result of a high number of defects. According to previous studies, even a small quantity of secondary phases of CuS_x or SnS_x can have a huge effect on the electric properties.[10,11] These phases tend to accumulate in the inter-grains,[23] consequently, small grain size is expected to contain a higher amount of these secondary phases that acts also as recombination centres. The increase of the carrier concentration also produces a decrease of the depletion layer thickness, reducing the carrier concentration (electrons-hole pairs) that can be separated before reaching the *p-n* junction.

Sample annealed at 550 ºC shows a thicker depletion thickness and a lower carrier concentration of 2.19×10^{17} cm^{-3}, in accordance with typical values reported for CZTS.[24,25] This reduction of carrier concentration can be associated with the increase of the crystal grain size and a reduction of defects, resulting in an improved photo-voltage, while the thicker depletion layer gives a better carrier collection and a better photo-current. Even with the increase of the depletion width, this value is small compared with efficient PV devices. Attention has to turn into reducing the defects of the absorber material and increasing the depletion thickness to a value that allows the collection of most of the photocurrent.

The crystallinity of CZTS can be also stimulated at intermediate sulfurization temperatures for longer periods if a constant supply of sulfur is available.[23] In a superstrate architecture, a temperature of at least 530 ºC for a long time could promote the crystallization with better quality crystals, and ensure the inclusion of Zn atoms in the lattice over Cd, however, the diffusion of Cd seems hard to avoid due to the high temperature required. Nevertheless, an improve the quality of the absorber layer is still required to increase the charge diffusion and lifetime.

4.2 Impact of a mesoporous structures layer

In this section, we explore the impact of a TiO_2 mesoporous film with different thicknesses in the photovoltaic performance of prepared samples, and we establish the effects of that film in the subsequent layers. It is found that the benefits of using a mesoporous layer can be obtained using an appropriate thickness, improving the transmittance and reducing the recombination, however, beyond that thickness results in a detrimental efficiency due to parasitic absorption and increase of the resistance.

4.2.1 Solar cells preparation

Starting from the FTO/TiO_2 substrates described in section 4.1.1, a mesoporous film was prepared by spin coating at 2000 rpm a solution of TiO_2 paste (30NR-T

Dyesol) in ethanol at concentrations of 0.125 mg/ml and 0.25 mg/mL, to obtain a film of 150 nm and 300 nm respectively.

Cu_2ZnSnS_4 films were prepared by spray pyrolysis at 340 ºC from a solution of 0.1-0.4-0.5 ratio of water-ethanol-DMF. The precursors's concentration in the solution was 0.1 M of thiourea, 0.0534 M of $CuCl_2$, 0.0295 M of $ZnCl_2$ and 0.0369 M of $SnCl_2$. Following the treatment obtained, the samples were submitted to a sulfurization at 550 ºC for 1 hour in a close tubular furnace, in an argon atmosphere along with 50 mg of sulphur powder.

A PEDOT:PSS (AL4083, Clevios) layer was deposited on top as HTM by spin coating at 1500 rpm in this case, which provides a homogeneous top surface for the contact deposition. The cells were completed by the evaporation of a gold layer of 70 nm, defining the active area of 0.55 cm^2 by a mask.

4.2.2 Results and discussion

TiO_2 nanostructures were tested in form of a mesoporous film of 150 and 300 nm thickness, with TiO_2 particles of 32 nm size. In **Figure 4.7a** and **Figure 4.7b**, the layers of samples prepared with and without a mesoporous film can be compared. In the planar sample, small voids can be observed in the interlayer between TiO_2 and the absorber. When using a mesoporous layer, the voids move to the region between the planar and the mesoporous TiO_2. The mesostructure avoids the voids in the *p-n* interlayer, which are especially problematic since the recombination before charge separation is increased.

In **Figure 4.7c** the difference in transmittance between substrates with different TiO_2 layers can be seen. The light transmittance is increased when a mesoporous layer is added, in comparison with the case of using only a planar layer. A reduction of the reflections in the TiO_2 – air interface is due to a gradual change of the refractive index when a mesoporous layer is used, an effect that is maintained for the TiO_2/CdS interface, as can be observed in **Figure 4.7d**.

Another effect of using a mesoporous layer is that the subsequent CdS deposition is enhanced. In **Figure 4.7d,** the absorption associated with CdS, for wavelengths

below 500 nm, is increased for thicker TiO_2 mesoporous layers. Chemical bath deposition technique can infiltrate the pores and fill the mesostructure with CdS, resulting in an effective CdS thickness proportional to the mesoporous film.

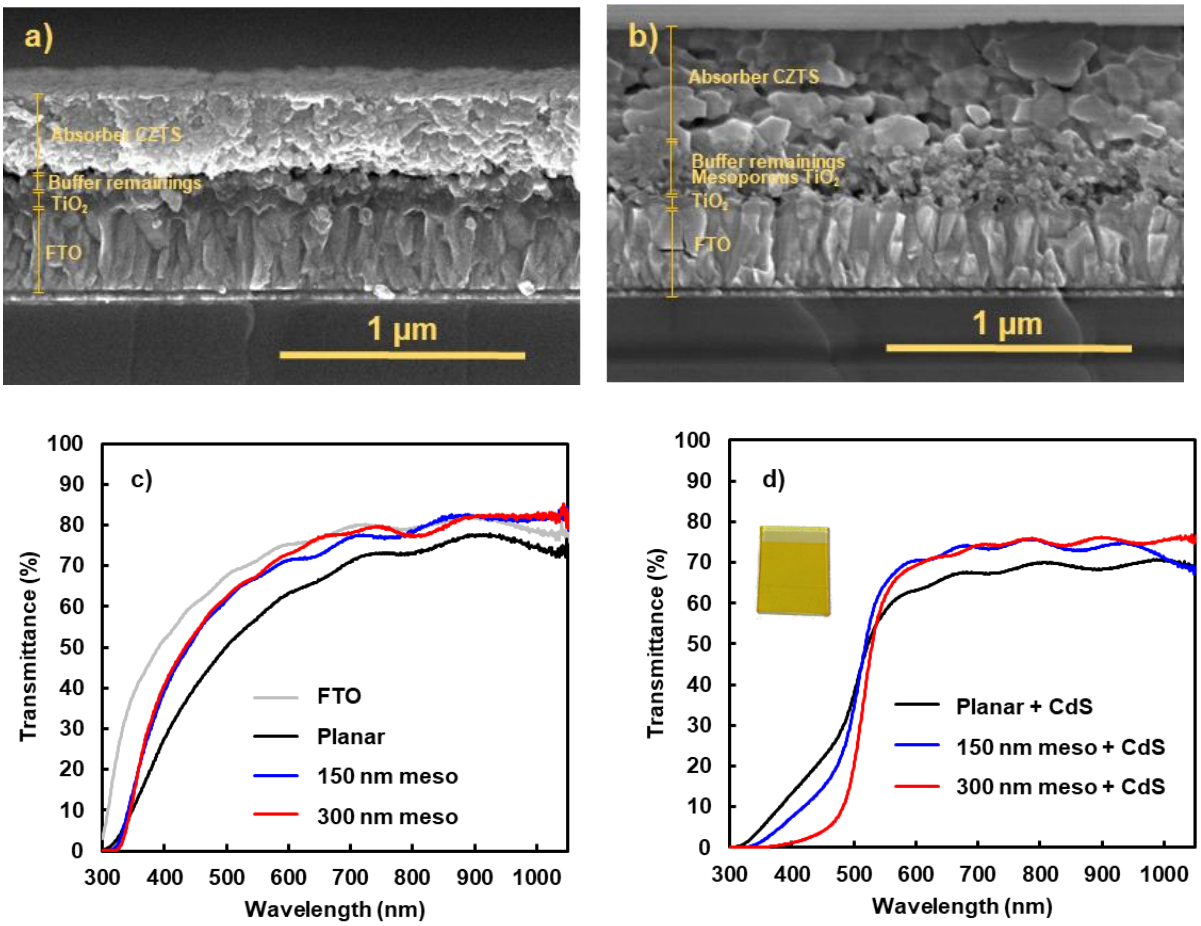

Figure 4.7. a) SEM cross-sectional images of superstrate PV cells without and b) with a 150 nm mesoporous TiO_2 layer. c) Transmittance spectra of the substrates with different nanostructures. d) Transmittance after depositing CdS. An image of a substrate with a mesoporous layer and CdS is shown in the inset.

The influence of the type of TiO_2 layer usage on the PV parameters was studied by fabricating the PV devices, adding an absorber CZTS layer and PEDOT:PSS/Au back contact. The characteristic PV parameters are shown in **Figure 4.8a** and **Figure 4.8b**, and the best sample for each condition is shown in **Table 4.3**. The V_{OC} is considerably increased for both samples using a mesoporous layer, suggesting a reduction in the recombination in the interface with TiO_2, and is probably due to the reduction of voids previously observed. J_{SC}

has an optimum value for the sample with a 150 nm thickness, and a lower value for the planar cell. The reasons behind this can be further studied by the EQE in **Figure 4.8c**. In the planar sample, the signal is only in the 300 to 500 nm wavelength region, while in the sample with a 300 nm of mesoporous layer, this signal in this range is lost. This can be associated with the decrease of the transparency in this region due to the increase of CdS previously observed. On the other hand, the signal is increased for longer wavelengths when a mesoporous layer is used, which may indicate a general improvement in the charge collection. For the sample with a 150 nm mesoporous layer thickness, the signal is conserved and improved at both short and long wavelengths. An optimum thickness is able to reduce the recombination without provoking parasitic absorptions.

The FF does not vary significantly, but for a slight reduction on the sample with higher TiO_2 thickness, which may be due to an increase of series resistance of the layer. The *JV* curve under dark, shown in **Figure 4.8d**, does not show shunts, and the series resistance of 10.4 Ω is observed, slightly high for a solar cell. The series resistance is not enough to explain the low FF under illumination, suggesting that the FF is dominated by recombination and insufficient charge collection.

A crossover between the illuminated and dark curves is also observed, with a strong effect that reduces the voltage up to 0.3 V under illumination with direct polarization. This indicates the existence of a photo-barrier. This barrier may come from the accumulation of holes in the interface, due to the large hole barrier that TiO_2 produce. A hole accumulation increases the p-type doping, and shifts the Fermi level of the absorber, increasing a barrier for electrons and a trap for holes close to the interface, increasing the recombination. Under dark, there are no photo-generated holes and Fermi level fluctuation disappears, reducing the barrier and increasing the apparent V_{BI}.[26]

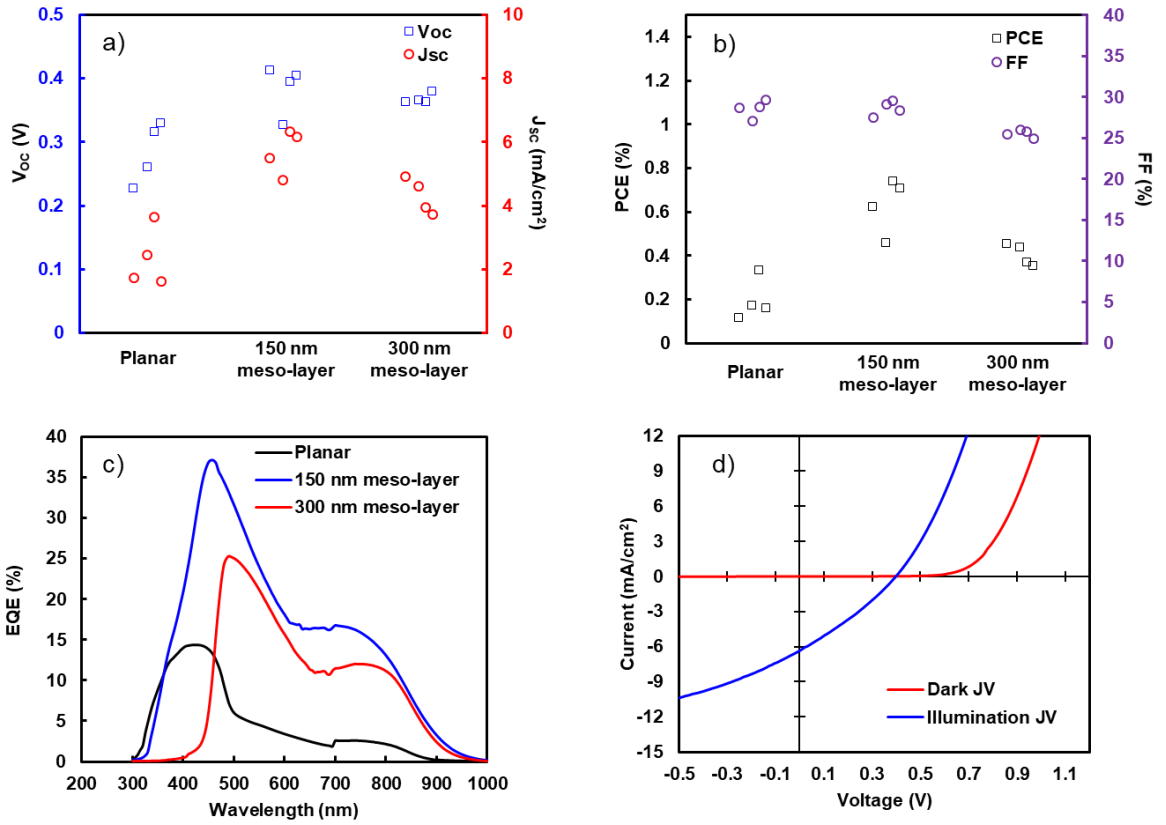

Figure 4.8. a) V_{OC}, J_{SC} and b) FF and PCE of PV cells prepared with different TiO_2 layers. c) EQE of the best solar cell of each TiO_2 layer condition. d) Dark and illuminated *JV* curve of the best sample with a mesoporous of 150 nm thick.

Table 4.3. Characteristic photovoltaic parameters measured at 1 Sun AM1.5.

	PCE (%)	V_{oc} (V)	J_{sc} (mA/cm^2)	Fill Factor (%)
Planar	0.33	0.315	3.65	28.8
150 nm	0.74	0.395	6.32	29.6
300 nm	0.45	0.363	4.91	25.5

Taking all into account, the efficiency with an optimum mesoporous layer is improved from 0.18 % to 0.62 % on average, with the best device obtaining a 0.72% efficiency of photon conversion, demonstrating that the use of nanostructures is a suitable and low-cost technique to boost the energy extracted from a solar cell.

4.3 Chapter Conclusions

Superstrate architecture for CZTS based photovoltaic cells is an attractive candidate if the current challenges can be overcome. This work reflects the importance of temperature sulfurization and its main effects on the morphological, electrical, and photovoltaic properties of absorber material. We noted the influence on the final composition and crystal structure when the annealing temperature was varied in the range from 500 ºC to 550 ºC. We noted, the crystal structure starts to form in a high quantity of Cd at a lower temperature, meanwhile, Zn incorporation in the structure is relevant at temperatures of 530 ºC. At this temperature, CdS is detected, while CZTS starts to show crystallization. Structural studies revealed crystallinity is enhanced at 550 ºC, however, most of the CdS layer is consumed at this temperature and incorporated into the kesterite structure. A larger crystal grain size is associated with a reduction of defects that acts as recombination centres, resulting in improved open-circuit voltage. Impedance measurements suggest an increase of the depletion width in the sample with higher crystallinity, improving efficient separation of electron and hole pairs, and thus increasing, the collected photocurrent in most of the wavelengths. A controlled composition with high crystallinity can allow a competitive use of CZTS on superstrate architecture.

Furthermore, mesostructures are tested on the FTO/TiO_2 contact. A TiO_2 mesoporous film of 150 nm is suitable to obtain clear advantages in the front surface recombination, improve the transmittance and reduce shunts, producing improvements in both the voltage and the current generated under illumination. The PCE improves from 0.33% when no mesoporous layer is used to 0.74% with an optimum layer, demonstrating the advantages of using a mesostructure. A crossover and a low FF are still the limiting factors for these samples, which may be related to a low exciton lifetime and carrier collection. The use of a suitable hole transport layer on the back contact still requires further study, considering that it can suppose an advantage due to better compatibility than in the substrate architecture to fabricate photovoltaic cells with earth-abundant materials.

4.4 Chapter supporting information

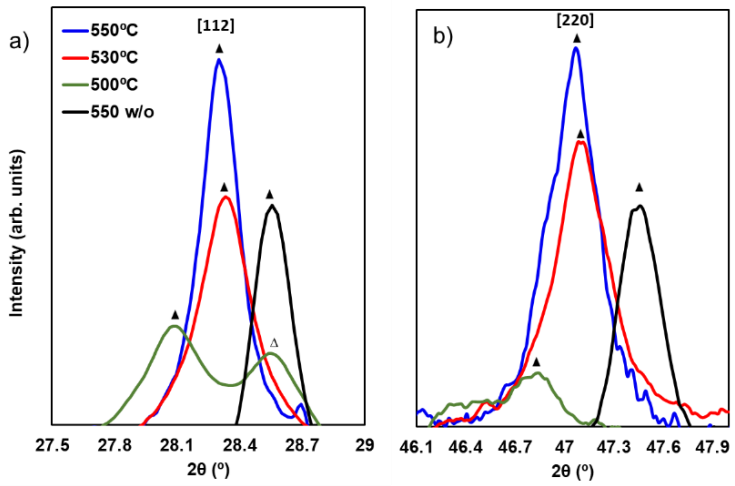

Figure S4.1. a) Zoom-in at [112], and b) [220] peaks from XRD in **Figure 4.1**.

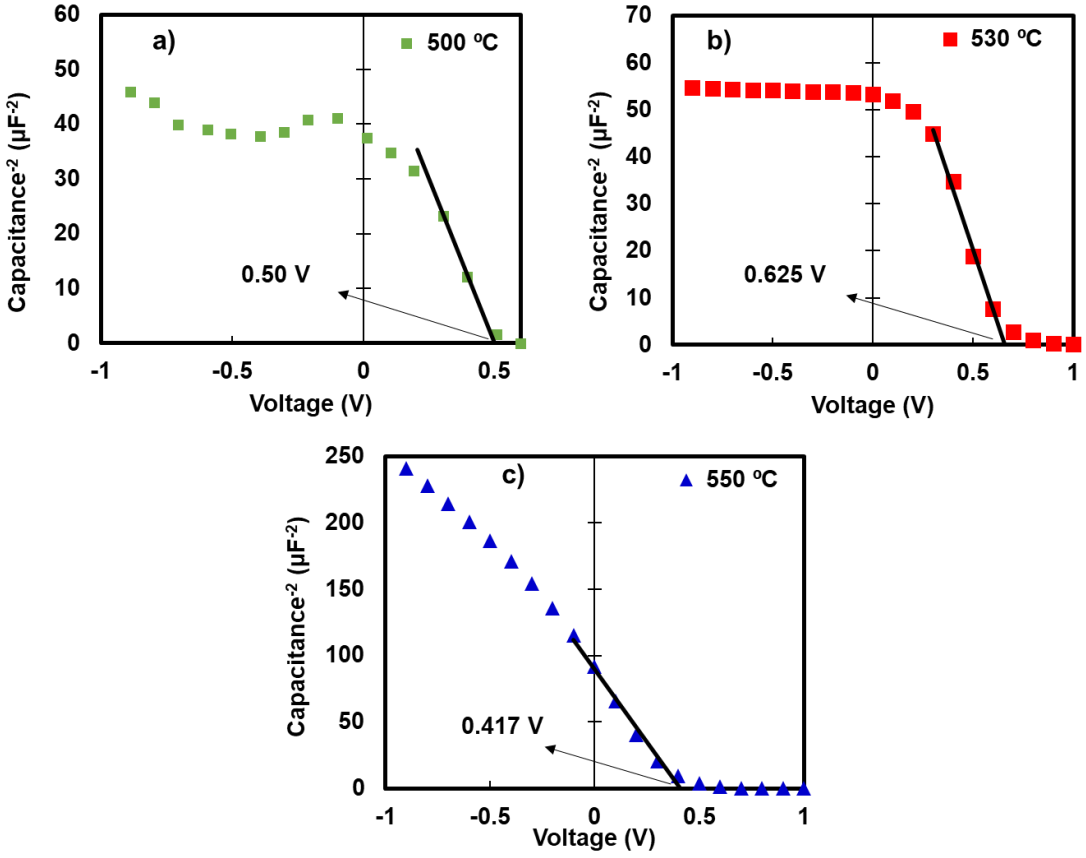

Figure S4.2. Mott-Schottky measurements for the samples prepared at a) 500 ºC, b) 530 ºC and c) 550 ºC. The linear decay at low direct polarization is used for the calculation of the V_{bi}, since the Mott-Schottky equation is valid for an applied voltage $V < V_{bi}$.

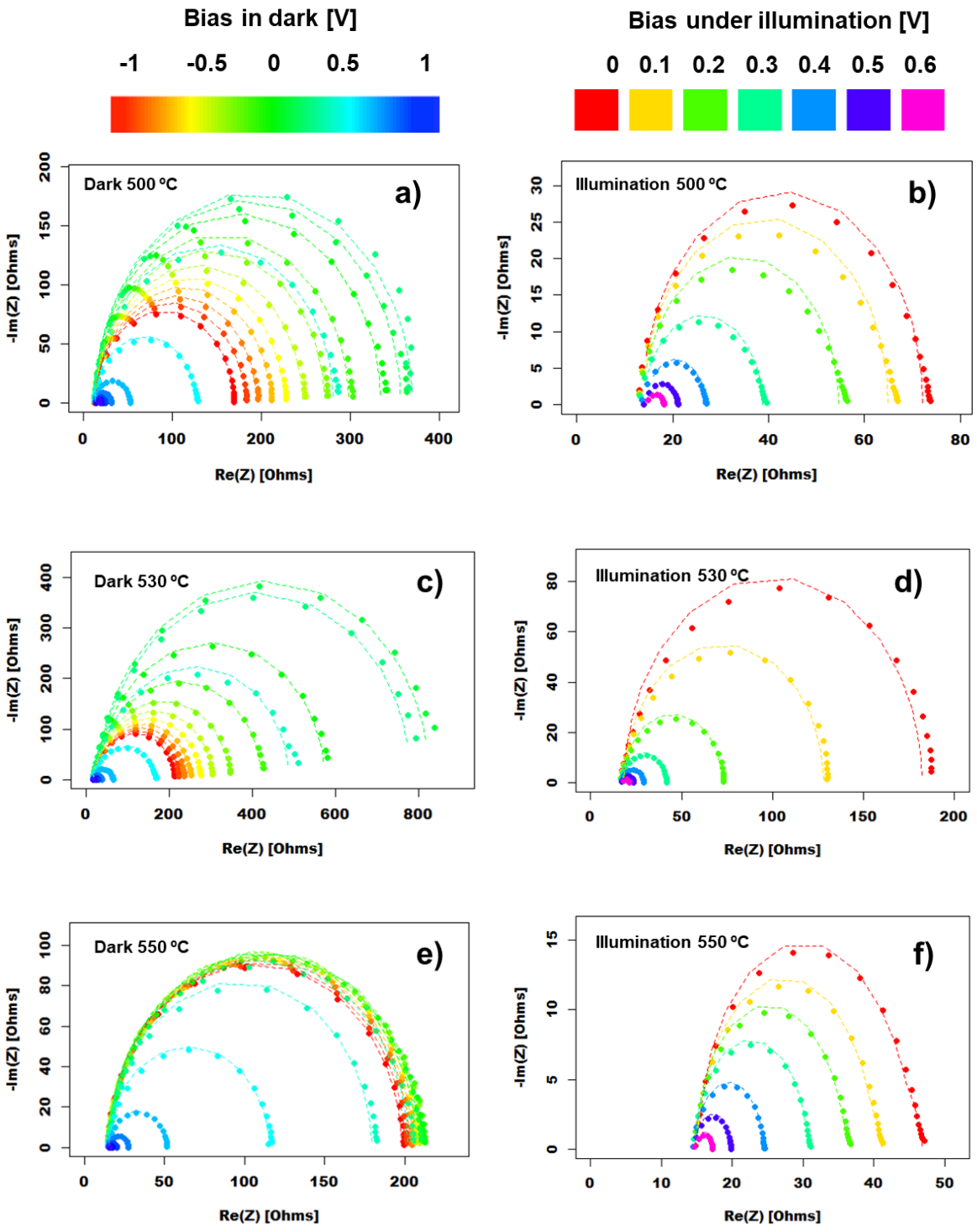

Figure S4.3. Nyquist spectra measurements (dots) and circuit fitting (lines) for the samples at 500, 530 and 550 ºC under dark a), c), e), and illumination b), d) and f) respectively. The bias was performed in 0.1 V steps, from -1 V to 1 V in dark and from 0 to 0.6 V under illumination, with every step represented with a different colour.

4.5 Chapter references

1. Payno, D., Kazim, S., Salado, M. & Ahmad, S. Sulfurization temperature effects on crystallization and performance of superstrate CZTS solar cells. *Sol. Energy* **224**, 1136–1143 (2021).
2. Gupta, I. & Mohanty, B. C. Eliminating secondary phases: Understanding kesterite phase evolution of Cu2ZnSnS4 thin films grown from ethanol based solutions with high photosensitivity. *Sol. Energy* **181**, 214–221 (2019).
3. Jung, H. R. *et al.* Phase evolution of Cu2ZnSnS4 (CZTS) kesterite thin films during the sulfurization process. *Ceram. Int.* **41**, 13006–13011 (2015).
4. Gong, Y. *et al.* Identifying the origin of the: Voc deficit of kesterite solar cells from the two grain growth mechanisms induced by Sn2+and Sn4+precursors in DMSO solution. *Energy and Environmental Science* vol. 14 2369–2380 (2021).
5. Dhanasekar, M. & Bhat, S. V. Facile synthesis of Cu 2 ZnSnS 4 absorber layer for thin film solar cells using a highly stable precursor solution. *Appl. Surf. Sci.* **418**, 194–198 (2017).
6. Datta, J. *et al.* Network analysis of semiconducting Zn 1-x Cd x S based photosensitive device using impedance spectroscopy and current-voltage measurement. *Appl. Surf. Sci.* **420**, 566–578 (2017).
7. Yan, C. *et al.* Beyond 11% Efficient Sulfide Kesterite Cu2ZnxCd1-xSnS4 Solar Cell: Effects of Cadmium Alloying. *ACS Energy Lett.* **2**, 930–936 (2017).
8. Hadke, S. *et al.* Suppressed Deep Traps and Bandgap Fluctuations in Cu2CdSnS4 Solar Cells with ≈8% Efficiency. *Adv. Energy Mater.* **9**, 1902509 (2019).
9. Zhang, Q. *et al.* Effects of sulfurization temperature on the structural and optical properties of Cu2CdSnS4 thin films prepared by direct liquid method. *Mater. Lett.* **193**, 206–209 (2017).
10. Kumar, M., Dubey, A., Adhikari, N., Venkatesan, S. & Qiao, Q. Strategic review of secondary phases, defects and defect-complexes in kesterite CZTS-Se solar cells. *Energy Environ. Sci.* **8**, 3134–3159 (2015).
11. Giraldo, S. *et al.* Progress and Perspectives of Thin Film Kesterite Photovoltaic Technology: A Critical Review. *Advanced Materials* vol. 31 1806692 (2019).

12. Moreno, R., Ramirez, E. A. & Gordillo Guzmán, G. Study of optical and structural properties of CZTS thin films grown by co-evaporation and spray pyrolysis. in *Journal of Physics: Conference Series* vol. 687 012041 (Institute of Physics Publishing, 2016).

13. Sun, R. *et al.* Beyond 11% efficient Cu2ZnSn(Se,S)4 thin film solar cells by cadmium alloying. *Sol. Energy Mater. Sol. Cells* (2018) doi:10.1016/j.solmat.2017.09.043.

14. Bakhsh, A. *et al.* Tailoring the structural and optical properties of CdZnS thin films by vacuum annealing. *Chalcogenide Lett.* **13**, 443–450 (2016).

15. Li, J., Wang, D., Li, X., Zeng, Y. & Zhang, Y. Cation Substitution in Earth-Abundant Kesterite Photovoltaic Materials. *Adv. Sci.* **5**, 1700744 (2018).

16. Su, Z. *et al.* Cation Substitution of Solution-Processed Cu2ZnSnS4 Thin Film Solar Cell with over 9% Efficiency. *Adv. Energy Mater.* **5**, 1500682 (2015).

17. Yan, C. *et al.* Cu2ZnSnS4 solar cells with over 10% power conversion efficiency enabled by heterojunction heat treatment. *Nat. Energy* **3**, 764–772 (2018).

18. Wang, Z., Brodusch, N., Gauvin, R. & Demopoulos, G. P. Nanoengineering of the Cu2ZnSnS4-TiO2 interface: Via atomic layer deposition of Al2O3 for high sensitivity photodetectors and solid state solar cells. *J. Mater. Chem. A* **6**, 11507–11520 (2018).

19. Repins, I. L. *et al.* Indications of short minority-carrier lifetime in kesterite solar cells. *J. Appl. Phys.* **114**, 084507 (2013).

20. Hages, C. J. *et al.* Identifying the Real Minority Carrier Lifetime in Nonideal Semiconductors: A Case Study of Kesterite Materials. *Adv. Energy Mater.* **7**, 1700167 (2017).

21. Mora-Seró, I., Garcia-Belmonte, G., Boix, P. P., Vázquez, M. A. & Bisquert, J. Impedance spectroscopy characterisation of highly efficient silicon solar cells under different light illumination intensities. *Energy Environ. Sci.* **2**, 678–686 (2009).

22. Persson, C. Electronic and optical properties of Cu2ZnSnS4 and Cu2ZnSnSe4. *J. Appl. Phys.* **107**, 053710 (2010).

23. Wu, S. H. *et al.* High-efficiency Cu2ZnSn(S,Se)4 solar cells fabricated through a low-cost solution process and a two-step heat treatment. *Prog. Photovoltaics Res. Appl.* **25**, 58–66 (2017).

24. Prabhakar, T. & Jampana, N. Effect of sodium diffusion on the structural and electrical properties of Cu2ZnSnS4 thin films. *Sol. Energy Mater. Sol. Cells* **95**, 1001–1004 (2011).

25. Payno, D. *et al.* Partial substitution of the CdS buffer layer with interplay of fullerenes in kesterite solar cells. *J. Mater. Chem. C* **8**, 12533–12542 (2020).

26. Moore, J. E., Dongaonkar, S., Chavali, R. V. K., Alam, M. A. & Lundstrom, M. S. Correlation of built-in potential and I-V crossover in thin-film solar cells. *IEEE J. Photovoltaics* **4**, 1138–1148 (2014).

5

Element substitution in all solution-processed superstrate solar cells

In this chapter, we demonstrate that a cation substitution of Zn by Cd improves the absorber compatibility on a superstrate architecture. Moreover, we employed all solution-processed using water and ethanol mixture as green solvents for thin-film deposition. An increase of the Cd amount in the absorber layer gave improved crystallinity and crystal size increment, bandgap decrement, and a change in crystal structure from kesterite to stannite. The composition of the buffer layer is controlled by the diffusion of Zn into CdS, forming (Cd,Zn)S with a relative Cd–Zn ratio. Solar cells prepared with high Cd showed a thicker depletion width and a reduction in the defect carrier density, leading to a significant increment in the power conversion efficiency up to 1.9 %. Furthermore, the fabricated solar cells show high stability on continuous light illumination of over 80 hours. The investigation of the electrical losses in Cu_2CdSnS_4 suggests ample opportunity to improve the solar cell performance in a superstrate architecture.

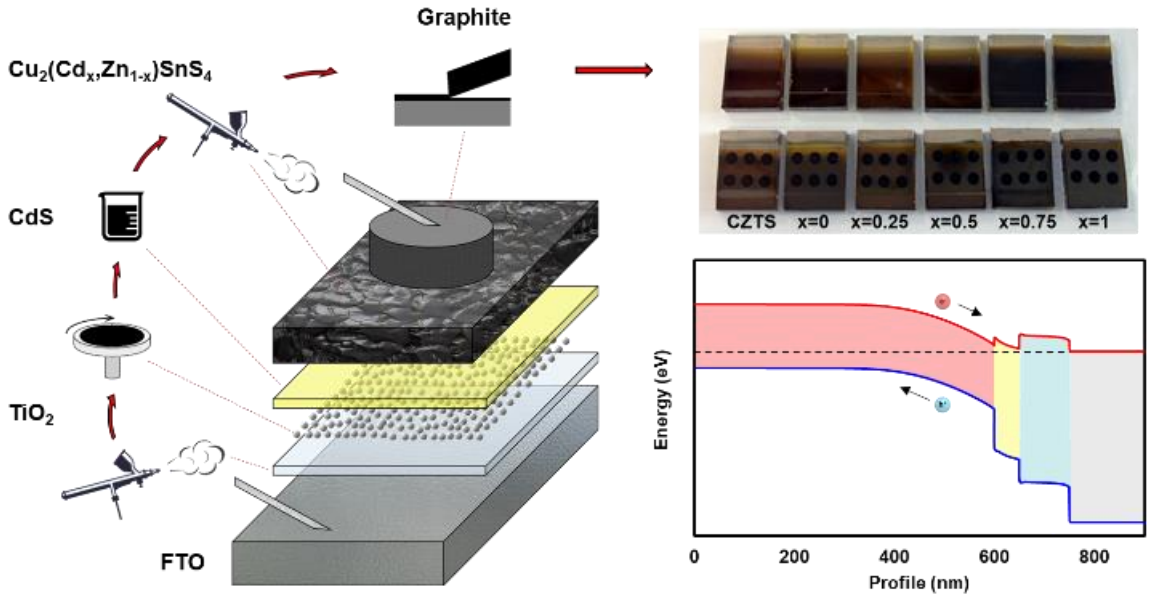

This section is based on the article "Payno Zarceño, D., Kazim, S. & Ahmad, S. Impact of cation substitution in all solution-processed $Cu_2(Cd,Zn)SnS_4$ superstrate solar cells. J. Mater. Chem. C (2021)." [1]

Contents:

5.1 Introduction to Cu_2CdSnS_4 and $Cu_2CdSnSe_4$

A promising approach to overcome the absorber limitations has been found in the cation substitution of Zn^{2+} by Cd^{2+}. The use of Cu_2CdSnS_4 (CCTS) compound as light absorber material in solar cells was demonstrated early in 1977, even before CZTS, with a CdS/Cu_2CdSnS_4 hetero-junction with a PCE of 1.6 % (under AM2) reported.[2] The electric properties of both CZTS and CCTS were estimated in 1988 to be 1.45 and 1.06 eV respectively,[3] with underestimation of the bandgap of CCTS that makes turn the focus into CZTS due to its more suitable value. Later reports found a band-gap for CCTS to be between 1.35 and 1.4 eV, values among the best for a light absorber material.[4] The interest in CCTS has increased in last years and is currently considered among the interesting emerging materials for photovoltaic.[5] Cd substitution leads to an absorber with enlarged grain size, reduced secondary phases, avoids Cu – Zn disorder defects, and increases minority lifetime, resulting in devices with improved PV performance and thicker depletion widths, which can lead to pure sulphide solar cells over 12 % efficiency.[6–9] The resulting compounds are compatible with wet-chemistry deposition methods and similar temperatures than CZTS for its synthesis.[10]

Just like in the case of CIGS and CdTe-based solar cells, the use of Cd raises concerns about their toxicity and uncertainty due to regulations of using toxic elements, although it has not been a problem or the commercialization of CdTe-based solar cells. Metallic, salts and other Cd-based compounds have limited large-scale applications due to their high toxicity and water solubility. Though Cd is not directly abundant in the earth's crust, it can be obtained as a by-product from Zn mining, resulting in a higher supply than demand, which makes it one of the cheapest metals.[11] A stimulating approach would be to develop applications for stable and insoluble Cd compounds with reduced toxicity, along with a lower processing cost, which can reduce Cd emission to the environment, avoiding its disposal as waste.[12] Despite the toxicity of Cd, the use of Cd containing chalcogenides has been found to have low Cd emissions to the environment, as they are stable and water-insoluble.[12] Moreover, CdS used in a

superstrate architecture, the Cd layer is sandwiched between TiO_2 and the absorber layer, thus reducing the possibilities of direct exposure to the environment.

In this work, we employ a sustainable (water-ethanol mixed) solvent to prepare the absorber thin films by spray pyrolysis, and we perform a cation substitution to evaluate the compatibility of $Cu_2(Cd_x,Zn_{1-x})SnS_4$ (CCZTS) compounds with a superstrate architecture. Moreover, all the solar cell layers were fabricated by wet-chemistry deposition methods with environmentally benign solvents to allow cost-effective manufacturing. We found that compounds with higher Cd content present a higher crystallinity and grain size, along with a low defects density, leading to an increase in the power conversion efficiency (PCE) from almost negligible to a maximum of 1.9 %. The Cd content of the absorber layer also affects the front contact by element diffusion of Zn into the CdS, forming an FTO/TiO_2/(Cd,Zn)S contact with a correlated Cd-Zn content to the absorber layer. In addition, we inspect the stability of the best PV cells under various conditions without any encapsulation. The PV cells are chemically and thermally stable, while the CCTS sample has the best stability under normal working conditions for more than 80 hours.

On the other hand, the introduction of different chalcogens in the composition is a usual practice in kesterite-based solar cells to obtain $Cu_2ZnSn(S,Se)_4$ (CZTSSe) solid solutions. As shown in chapter 2, kesterite with a selenium-rich composition possesses a lower band gap and produce homogeneous films with bigger grains and lower secondary phases, improving the carrier lifetime and leading to devices with a lower voltage deficit and an improved FF.[13–15] Similarly, it is known that materials based on $Cu_2CdSnSe_4$ possess a low band gap of 0.96 eV and p-type conductivity.[16] This material, with a Cu-rich composition, has drawn attention for its use in thermoelectricity.[17–19] However, it has not been widely explored for photovoltaic applications, despite having suitable properties for its use in thin films. A proof-of-concept of using $Cu_2CdSn(S,Se)_4$ (CCTSSe) as absorber layer in a substrate architecture lead to a device with a 3.1% efficiency,[20] which

confirms that this material has potential for its use in photovoltaics. Due to its similarities to CIGS and CZTSSe, we can expect that Se containing compositions of CCTSSe will have improved photovoltaic properties for an absorber than its pure sulphur counterpart, while the band gap can be tuned with the sulphur to selenium ratio.

The effects of including Se in a $Cu_2CdSn(S,Se)_4$ composition on superstrate solar cells are studied in this chapter for the first time, only by adding Se in the annealing step. Conversely to thermoelectrics, a Cu-poor and Cd-rich composition was maintained for a photovoltaic application, to reduce doping level, the recombination and the harmful CuS_x secondary phases. The prepared solar cells show an improved FF and a broader EQE in both short and long wavelengths, obtaining a maximum PCE of 2.7%. The band gap of the absorber can be tuned, from 1.4 eV to lower values depending on the Se. These results suggest that this material has a longer carrier lifetime, lower resistance, and possess suitable properties for superstrate solar cells.

5.2 Experimental

5.2.1 Solar cells fabrication

Commercial FTO (TEC-8) coated glass was used as substrate and front contact for the PV cells preparation. The FTO coated glass was subjected to a cleaning procedure consisting of a 10 minutes immersion under ultra-sonication in four different baths of 2% Hellmanex-water solution, distilled water, acetone, and isopropanol. After a fast dry with compressed air, the samples were exposed to a 15 minutes UV light to remove any organic residue.

The samples were preheated on a hotplate at 500 ºC in the open air, and a solution containing titanium(IV) diisopropoxide bis(acetylacetonate) (Merck) in ethanol (Scharlab) with a volume ratio of 1:19 was sprayed on the full area of the samples, producing a 60 nm TiO_2 compact layer. A small area of the sample will be left uncovered by the subsequent layers to be used as front contact. TiO_2 paste (18NR-T Dyesol) was dispersed in ethanol with a 125 mg/mL concentration. 50

µL of the dispersion was spin-coated at 2000 rpm on the FTO/TiO_2 substrates, followed by 30 minutes of air annealing at 500 ºC on a hotplate to produce a 150 nm TiO_2 mesoporous layer.

A CdS thin film was deposited by chemical bath deposition (CBD). The samples were immersed in a deionized water bath of 370 mL at 65 °C containing 75 mg of Cadmium sulphate (98%, Alfa Aesar). Then 18.2 mL of ammonia solution (30%, Alfa Aesar) were added, followed by 20 mL water solution with 200 mg of thiourea (99%, Alfa Aesar). The bath was maintained at 65 °C under constant stirring, and the samples were extracted after 10 minutes. CdS deposited on the glass side was removed with diluted HCl.

The absorber layer was prepared by spray pyrolysis from a water-ethanol molecular solution. Firstly, stock solutions were prepared by separately dissolving $Cd(NO_3)_2 \cdot 4H_2O$ (98%, Merck), $CuCl_2$, $ZnCl_2$, and $SnCl_2 \cdot 2H_2O$ (98%, Alfa Aesar) in ethanol with a 0.1 M concentration, and thiourea in deionized water at 1 M concentration. The precursor solution was prepared following the next steps. First, 3.56 mL of Cu solution was slowly added to 4 mL of thiourea solution to avoid gelling. Separately, a second solution was prepared by adding 1.976 mL of mixed Cd and Zn solutions, with variable percentage, to 2.47 mL of Sn solution, along with 300 µL of HCl (37%, Fisher) to increase the stability. Both solutions were then mixed, obtaining a clear and transparent solution, and 3.7 mL of deionized water was added to get a 1:1 mix of water-ethanol. As illustrated in **Figure 5.1a**, all the precursor solutions were sprayed using dry air as carrier gas on preheated samples, and clean glass substrates at the same time, on a hotplate at 340 ºC in open-air. The samples were then submitted to a sulfurization process at 550 °C for 1 hour inside a close quartz tubular furnace containing 50 mg of sulphur powder (99.5%, Alfa Aesar) in an argon atmosphere. For the $Cu_2CdSn(S,Se)_4$ samples, selenium powder was also introduced in the furnace.

Aligned with the objectives of this work, the PV cells were completed with a robust conductive graphite paste (GST 4500) of 0.2 mm thick as back contact

deposited by doctor-blade. Graphite possesses a deep work function of ~ 5 eV that provides an efficient hole extraction, having both material and the deposition method at a low cost. A vinyl mask was used to define the active area, measured in **Figure S5.1**, prepared with the help of a Roland GS-24 cutter. The FTO front contact area was exposed by scratching the TiO_2 protective layer and covered with Ag paint (RS Pro). Finally, all the samples were heated at 100 ºC for 10 minutes on a hotplate in the air to improve the graphite and Ag conductivity.

5.2.2 Characterizations

Electron-dispersive X-ray spectroscopy (EDX) was performed with a Quantax75 equipped in a TM4000 Series scanning electron microscope (SEM). X-ray diffractograms (XRD) were measured on the final device, without the graphite back contact, with a Cubix3 system from PANalytical with a Cu anode. SEM images were recorded with a Hitachi S-3400 electron microscope at 5 kV of acceleration potential. Transmittance spectra were recorded on the finished samples with an Agilent Cary 60 UV–Vis spectrometer.

The external quantum efficiency (EQE) was measured on a PVE300 Bentham system, consisting of a 150 W Xenon lamp and a 1/4m monochromator, in a range from 300 to 1000 nm in steps of 5 nm. Capacitance-voltage (*C-V*) measurements were performed inside a faraday box with a Biologic impedance analyser, applying steps of DC voltage between 1.5 to -1.5 V and 20 mV AC perturbation of 100 kHz. Current-voltage (J-V) curves were measured with a Keithley 2400 source meter. Characterization under illumination was performed with a class AAA Oriel solar simulator from Newport, calibrated to 1 Sun (AM 1.5) irradiance. For the light stability, a Motic-MLC-150C (~ 3000 K halogen lamp) was used as a light source. The measurements were made with a microampere-meter Keithley 6487, programmed using LabVIEW software. The program tracks the maximum power point (MPP) by the perturbation-observation method of the voltage and current, recording a measurement every second.

5.2.3 Material energy level bands and band bending.

The values of the energy levels and junction have been calculated from the material properties shown in **Table 5.1**. PC1D software was used to calculate the band structure of the materials separately, and the bending of the bands of the junctions under equilibrium conditions.

Table 5.1. Material properties used for the calculation of the bands.

	CZTS	CCTS	CdS	ZnS	TiO_2	FTO
Thickness (nm)	600	600	50	50	150	150
Dielectric constant ($\varepsilon_0/\varepsilon$)	7	7	10	9	30	9
E_G (eV)	1.5	1.4	2.42	3.6	3.2	3.8
Electron affinity (eV)	4.2	4.47	4.4	3.5	4	4.1
N_c/N_v	0.0255	0.0255	0.0112	0.044	50	1.2
n_i (cm^{-3})	$1.8\ 10^{6}$	$2.3\ 10^{9}$	0.182	0.01	$1.44\ 10^{-5}$	$3.6\ 10^{-13}$
Doping concentration (cm^{-3})	10^{16}-10^{18}	10^{16}	10^{17}	10^{18}	10^{17}	$2\ 10^{19}$
References	21–23	21	21,23,24	23,24	25	25

5.3 Cation substitution: $Cu_2(Cd,Zn)SnS_4$

We prepared the samples with different cation content by changing the ratio of Cd and Zn in the precursor solution. The ratio of Cd/(Cd+Zn) content in the precursor solution was used to denoted the samples, as x = 0, x = 0.25, x = 0.5, x = 0.75 and x = 1. Previously, we noted that most of the Cd from the CdS layer will be diffused into the absorber layer,[26] therefore, an extra substrate without CdS with the x = 0 solutions was sprayed to be used as a reference of pure Cu_2ZnSnS_4, denoted as CZTS. The composition of the sulfurized films was measured by EDX in both glass and prepared substrates and we measured the ratio of Zn to Cd, shown in **Figure 5.1b**.

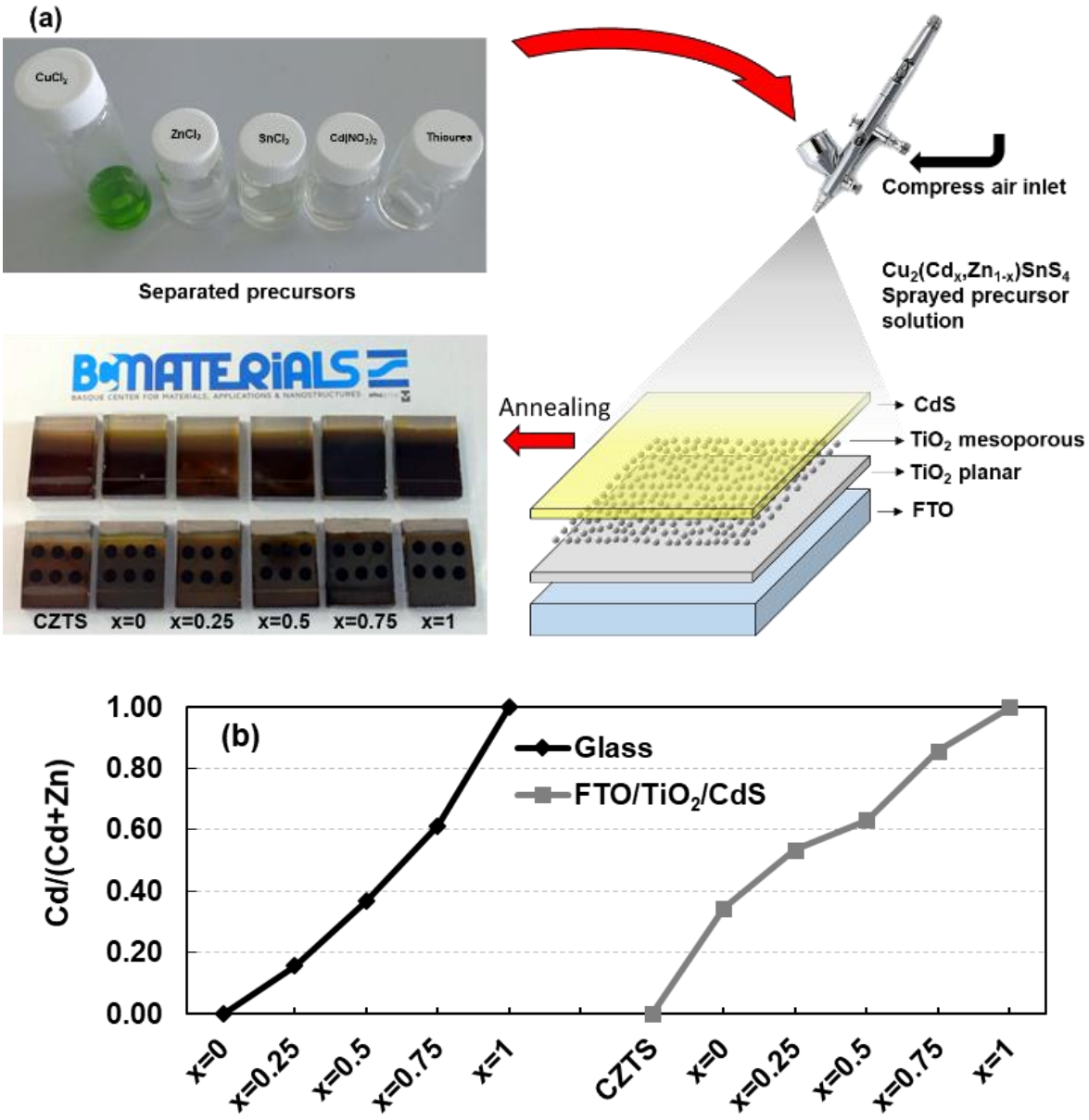

Figure 5.1. a) Scheme of the architecture of the sample, with images of the precursor solutions and the final samples, and b) Cd and Zn ratio measured by EDX from the sprayed solutions on FTO/TiO_2/CdS substrate and bare glass.

Table 5.2. Compositional ratios of CCZTS thin films.

	Cd/(Cd+Zn)	Cu/(Cd+Zn+Sn)	(Cd+Zn)/Sn	S/Metals
Stoichiometry	-	1	1	1
Precursor solution	x	0.8	0.8	5
CZTS	0.00	0.79	1.24	0.91
x=0	0.35	0.64	1.98	1.00
x=0.25	0.53	0.64	2.02	1.07
x=0.5	0.63	0.63	2.00	1.03
x=0.75	0.82	0.78	1.94	1.07
x=1	1.00	0.75	1.57	1.04

The measured compositional ratios are shown in **Table 5.2**. In this case, all the samples show a copper-deficient stoichiometry, slightly below the selected ratio of the precursor solution, likely due to the contribution of the Cd from the CdS film. The Cu-deficient ratio from 0.6 − 0.9 is typically considered as a competitive value for the performance, owing to the reduction in the formation of highly harmful CuS_x secondary phases, which causes shunts and recombination due to its high conductivity and high *p*-type doping.[27]

On the other hand, the Sn ratio is highly different from the precursor solution to the final composition. Even if a metal^{2+} rich composition is required to get an efficient CZTS absorber, a metal^{2+} poor ratio of (Cd+Zn)/Sn of 0.8 was deliberately used. Due to the higher volatility of Sn compounds, a high loss of Sn is usually reported during the synthesis of CZTS thin films, especially during the precursor decomposition in wet chemistry methods.[28,29] To compensate for the Sn loss, our precursor solution contains a 25 % extra Sn than the stoichiometry. A final metal^{2+} rich composition was obtained in all cases in the final layers, even in the CZTS sample without CdS, showing that this is an effective technique to control the Sn ratio. Arguably, in the samples, where a CdS layer is used, the metal^{2+} ratio is higher due to the Cd contribution from the CdS. The sulphur source used in the precursor was thiourea, in a ratio 5 times higher than the

stoichiometric. During the thiourea decomposition, the excess of sulphur vaporizes, creating a local area where the formation of metal-oxide secondary phases is avoided and the formation of a sulphur-rich film is favoured.[30] Sulphur rich films favour the formation of quaternary phases and, during the sulfurization step, promote better crystal growth.

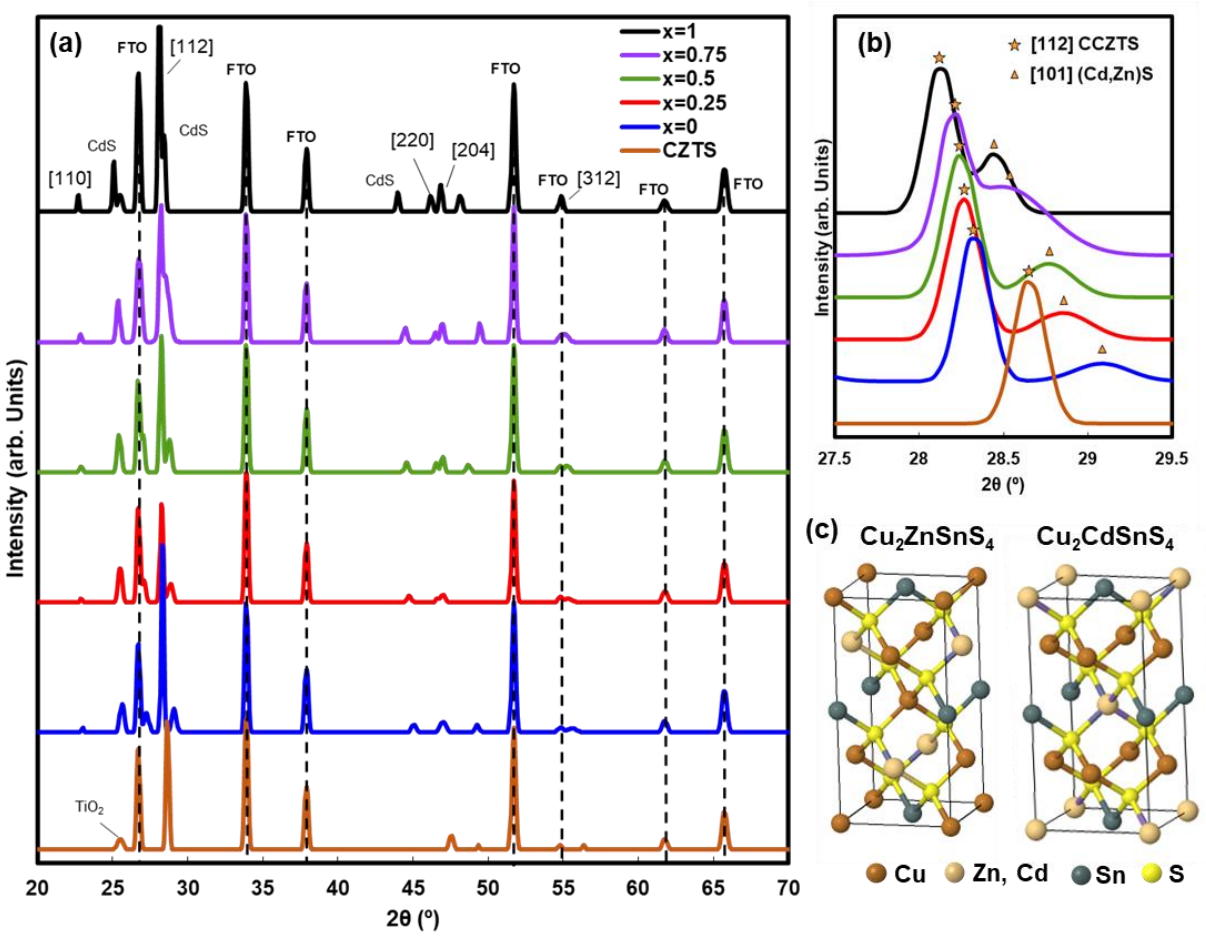

Figure 5.2. a) XRD pattern of the prepared samples, where the peaks associated with CCTS are indicated with the corresponding plane (ICDD reference 04-003-8937 for CCTS and 00-026-0575 for CZTS). The peaks associated with pure CdS are indicated in the x = 1 sample (reference 00-041-1049), while the peaks corresponding to FTO match with the spectrum of SnO_2 in all the samples (reference 01-088-0287). b) Close look to the shift of the [112] plane of CCZTS and [101] of (Cd,Zn)S. c) Representation of the atomic structure of Kesterite (CZTS) and Cernyite (CCTS).

Table 5.3. Properties derived from the XRD pattern.

Sample	a (Å)	c (Å)	Cell volume (Å^3)	c/2a	Crystallite size (nm)
CZTS	5.415	10.692	313.5	0.987	36.38
x=0	5.487	10.773	324.4	0.982	38.23
x=0.25	5.519	10.720	326.6	0.971	34.78
x=0.5	5.522	10.730	327.2	0.972	35.82
x=0.75	5.536	10.733	328.9	0.969	43.97
x=1	5.566	10.699	331.4	0.961	35.82

The structural differences produced by the cation substitution were studied by X-ray diffractograms in **Figure 5.2a**, a gradual transition from Cu_2ZnSnS_4 to Cu_2CdSnS_4 (CCTS) is observed with the increase of Cd to Zn ratio in the precursor, producing $Cu_2(Cd,Zn)SnS_4$ (CCZTS). The [112] peak situated at 28.65 ° gradually shift to a lower angle until 28.13 ° for CCTS (**Figure 5.2b**). The shift in the angle corresponds with a crystal lattice expansion due to the larger size of Cd than Zn and expanding the cell volume from 313.5 Å^3 to 331.4 Å^3 (**Table 5.3**) using Bragg's law. The change of crystal symmetry from kesterite to stannite is observed in the [220] peak, where the peak starts to divide into two peaks corresponding to [220] and [204] at x = 0.25, which corresponds with the samples where the Cd content is higher than Zn.[4] The structure changes with high Cd content, represented in **Figure 5.2c**, consists of a stannite-like structure, first reported in a mineral as Cernyite,[31] where Cd and Cu are layered, in contrast with the kesterite structure. This effect can be also noticed in the c/2a value from Table 1, where lower values are associated with stannite-like structures, and values close to 1 are more characteristic of kesterite.[32] The crystallite size is estimated using the Scherrer equation from the [112] peaks and the samples showed a similar crystallite size, except for x = 0.75 which gave a higher value.

While the CZTS sample shows peaks corresponding to a pure phase, in the CCZTS samples, several peaks corresponding to $(Cd_x,Zn_{1-x})S$ secondary phase can be also deduced. Considering the excess of metal^{2+} previously detected, these

peaks reveals that part of the Cd is preserved, most likely as the original CdS layer, but forming an alloy with the Zn from the precursor solution, which gradually shifts the CdS peaks to a higher angle when the Zn content in the solution is higher. This is in agreement with reported observations of Zn accumulation at the interface after high-temperature treatment.[33] The final $(Cd_x,Zn_{1-x})S$ alloy formation may play an important role in the fabricated solar cells and will impact electrical properties, producing a CCZTS/$(Cd_x,Zn_{1-x})S$ junction, rather than a CCZTS/TiO_2. High conductivity is preferred for this phase to act as an upright electron transport material and properties, where CdS is superior to ZnS. As shown in **Figure 5.3**, the conduction band alignment of ZnS is less favourable, producing an extra barrier for electron extraction. Therefore we can expect that Cd-rich samples have improved behaviour than Cd-deficient ones.

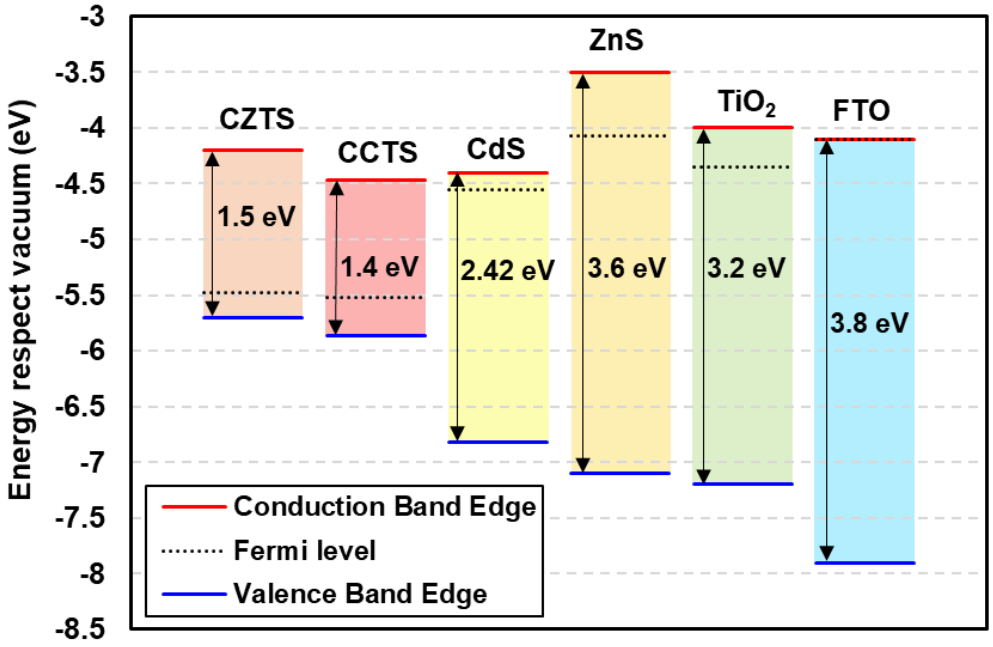

Figure 5.3. Band structure of the materials involved in the solar cells. The Fermi level is marked and used as a reference.

To investigate the impact of the composition on the microstructure of the absorber layer, we recorded the top-view SEM image of the samples in **Figure 5.4**. An increase of the crystal size can be noticed for the samples with a higher Cd content, indicating that Cd facilitates the crystallization in a similar way that

happens in substrate architecture.[34] A larger crystal size along the horizontal direction has clear advantages. The area between grains has a high number of defects and unbound atoms, which reduces the conductivity and increases charge recombination. Moreover, the diffusion of unwanted elements is favoured in the inter-grains, which can result in faster degradation due to composition changes.

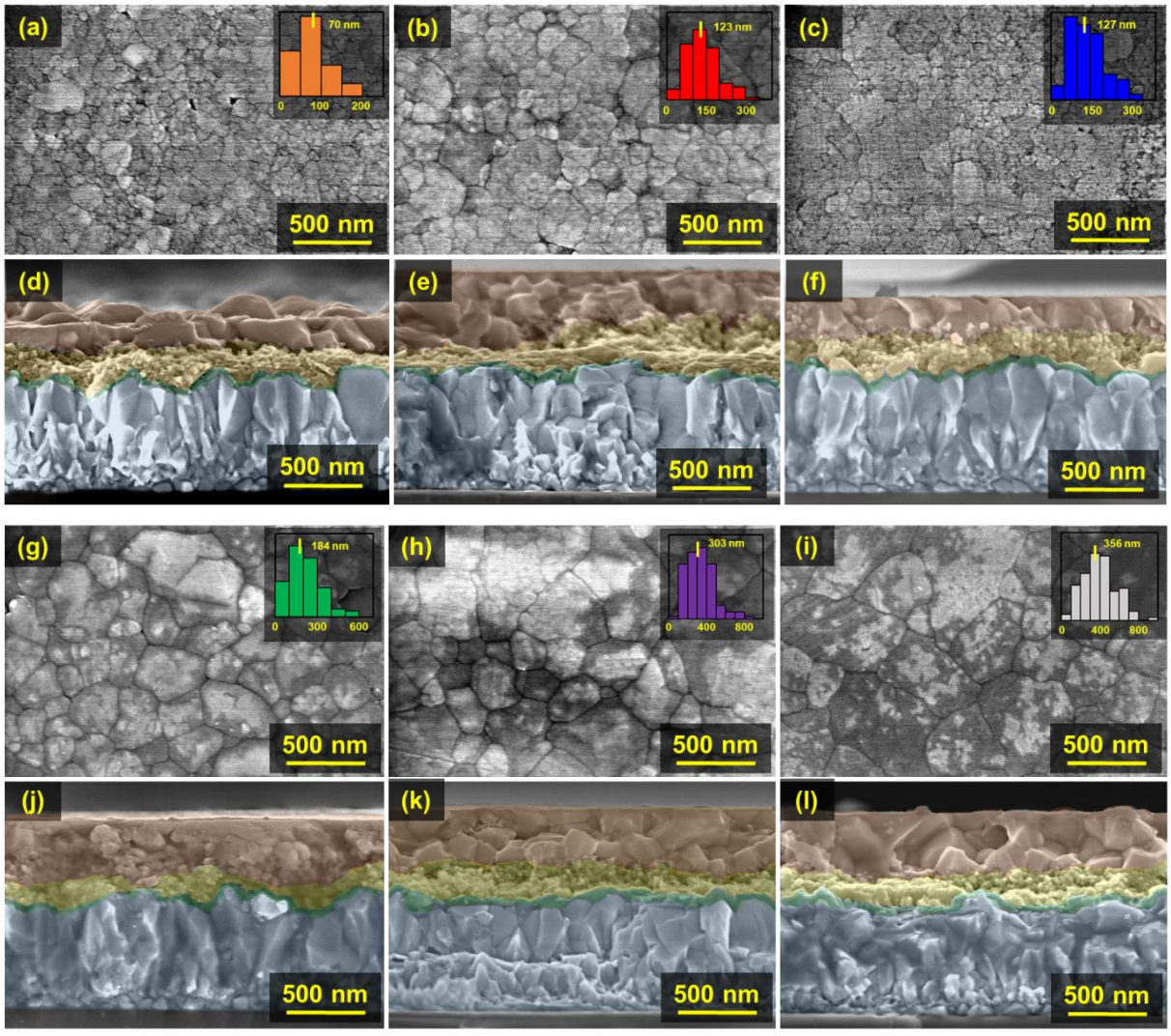

Figure 5.4. SEM top view and cross-sectional view of the samples CZTS (a, d), x=0 (b, e), x=0.25 (c, f), x = 0.5 (g, j), x = 0.75 (h, k) and x = 1 (i, l) respectively. Inset depicts the histogram distribution and average grain size. The films are marked as blue (FTO), green (planar TiO_2), yellow (mesoporous TiO_2 + (Cd,Zn)S) and red (CCZTS).

The size distribution of the grains shows a progressive increase of the grain size, particularly notable in x = 0.75 and x = 1 samples, where the average grain size

is close to the film thickness, and therefore there are fewer impediments and inter-grain recombination through the current flow direction.

A cross-sectional SEM of the samples shown in **Figure 5.4** reveals the layer structure and thickness of the samples. Most samples have a compact layer formation without visible voids. The layer stack consists of a 600 – 700 nm thick FTO, a compact TiO_2 layer of 30 − 40 nm, a fine grain mesoporous layer of TiO_2 of 140 – 160 nm, and an active layer formed of bigger crystals of 300 − 500 nm thick. Since CZTS and x = 0 samples were prepared in the same batch, the difference in the thickness can be attributed to the lack of the CdS, suggesting the significant contribution of CdS to the absorber layer. The advantage of using a mesoporous TiO_2 layer is to improve the adhesion and to increase the contact area between absorber and the buffer layers, which in combination with the high pore penetration of the CdS deposited by CBD, ensures to minimize cavities at the interface. However, the CZTS sample seems to have small voids at the interface due to the CdS layer absence. Cavities are not desirable since they can block part of the current and reduce the electron-hole separation in the interface.

The optical properties of the samples were studied by measuring transmittance in the UV-Vis region (**Figure 5.5a**). The samples show a high transmittance up to 65% in the near-IR region higher than 950 nm, while the transmittance sharply decreases for shorter wavelengths, which denotes a high absorption coefficient due to bandgap absorption for all the materials, an indispensable requirement for a thin-film solar cell. Since the thickness of the absorber films was only 300 − 500 nm, the light is not completely absorbed, and mild variation in the thickness are the plausible reason for the differences in the transmittance at short wavelengths, in particular for thinner samples CZTS and x = 0.25. The impact of the thickness on the transmittance can be found in **Figure S5.2**. Nevertheless, the thickness of the absorber layer did not largely impact the PV properties due to limitations in the electrical properties.

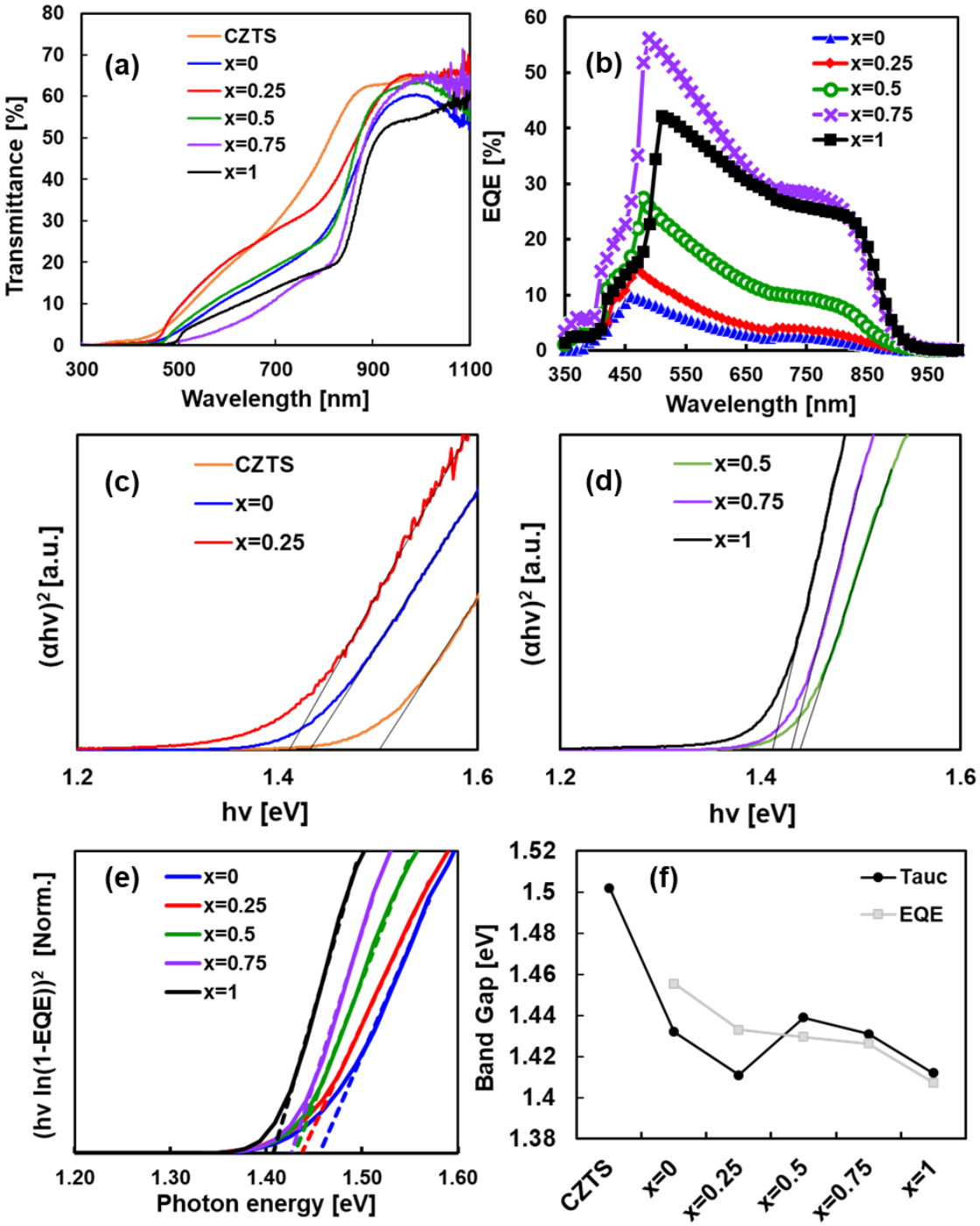

Figure 5.5. a) Transmittance spectra in the UV-Visible region of the samples. b) EQE spectra of the functional solar cells. c) Band-gap calculation by Tauc plot, extracted from the absorption of the samples CZTS, x = 0 and x = 0.25 and d) x = 0.5, x = 0.75 and x = 1. e) Band-gap calculation derived from the EQE edge. f) Band-gap comparison derived from the two methods.

The solar cells were completed by the deposition of a conductive graphite electrode on top of the device to measure the EQE spectra and study the wavelength response (**Figure 5.5b**). We noted a significant increase in the photon-to-electron conversion across the wavelengths for the devices with a higher quantity of Cd. The CZTS samples did not have gave sufficient signal and were discarded for the electro-optical measurements. Since the light absorption was similar, the electrical properties of the absorber material and/or better compatibility with the FTO/TiO_2 front contact are the plausible reason. The shape of the EQE spectra provides insight into the interface. A small shoulder in the region below 450 nm indicates losses in the front contact due to parasitic absorption of the FTO and TiO_2 layers. A thickness optimization of these layers could increase the short-wavelength light that reaches the absorber material and thus can improve the photon to electron conversion efficiency in this region. A maximum EQE is found in all the devices in the range of 450-500 nm, followed by a progressive decay of the quantum efficiency at longer wavelengths. The decrease in absorption at longer wavelengths is not sufficient to explain the loss in efficiency, we ascribed it to the carrier diffusion length since photons absorbed deeper in the absorber layer produce electron-hole pairs that have to diffuse longer to reach the p-n junction where the electron-hole separation occurs.

We calculated the band gap (**Figure 5.5e**) by the linear extrapolation of the $hv\ ln(1\text{-}EQE)^2$. For comparison, the bandgap of the different absorbers is extracted from the Tauc plot (**Figure 5.5c** and **Figure 5.5d**). The calculated results (**Figure 5.5f**), showed a maximum difference between both values of 0.023 eV. A value of 1.5 eV was obtained for the pure CZTS sample, while all the other samples with Cd in the composition showed a reduction in the bandgap, with a minimum value obtained of 1.41 eV for the x = 1 sample. However, the bandgap values for this family of compounds are among the ideal values considering the Shockley-Queisser limit.

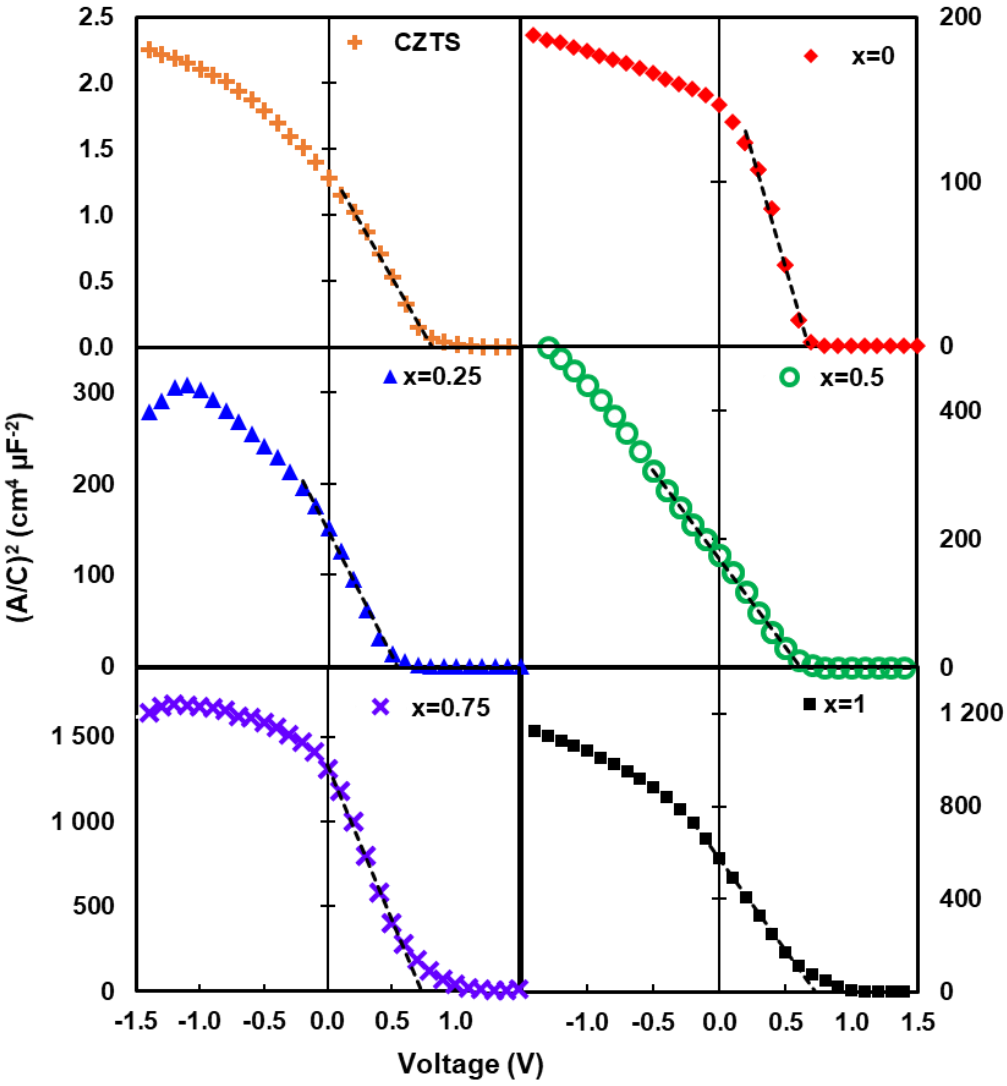

Figure 5.6. Mott-Schottky plots with a linear regression were used to calculate the built-in potential. The measurements were obtained under dark, using a 20 mV AC at 100 kHz.

The electrical properties of the sample were studied by capacitance-voltage measurements, from where the Mott-Schottky plot was used to calculate the built-in potential (V_{bi}) of the junction (**Figure 5.6**). The built-in potential indicates the voltage produced at the *p-n* interface, setting an upper limit for the voltage that can be extracted. Interestingly, intermediate values of Cd-Zn in the composition result in lower built-in potential, while this value increases for pure Zn sample CZTS and high values of Cd. However, this value alone needs to be complemented with other junction properties to have a comprehensive model. Assuming the capacitor model of the *p-n* junction, the depletion width is inversely

proportional to the capacitance, following *(Eq. 1.12)*. The depletion width, and therefore the capacitance, can be modified if an external voltage is applied and, at the same time, the density of free carriers N_D in the absorber layer can be calculated with *(Eq. 1.15)*.

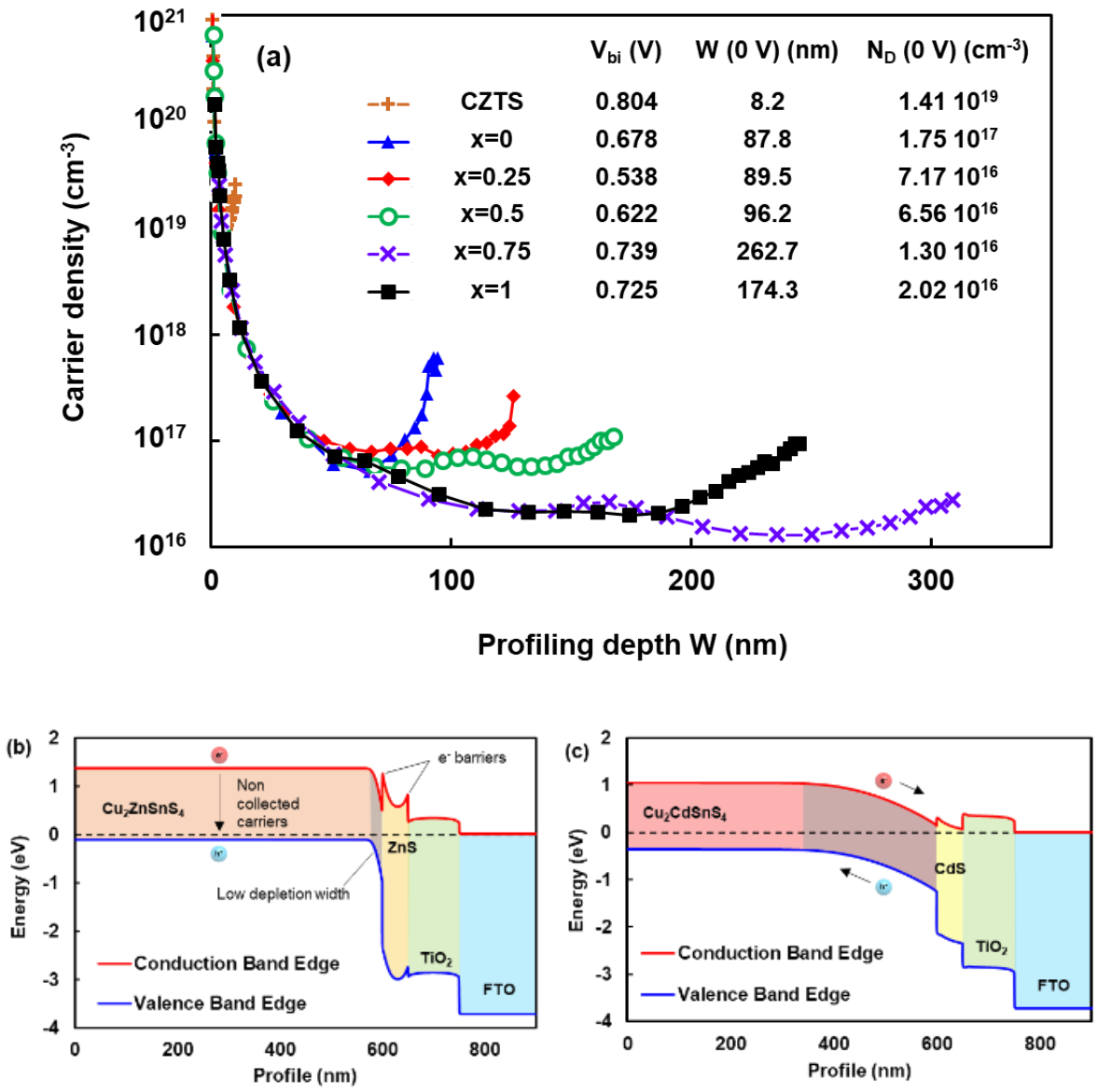

Figure 5.7. a) Carrier density profile calculated from the C-V measurements, with the values of built-in potential, depletion width, and carrier density at short circuit condition. b) Steady-state band bending simulation of a CZTS device with high doping (10^{18} cm^{-3}) and a ZnS interlayer, indicating the major problems. c) Band bending of CCTS with low doping (10^{16} cm^{-3}) and a CdS interlayer.

The results and values at 0 V are represented in **Figure 5.7a**. For samples with low or no Cd content, a carrier density of 10^{17} to 10^{19} cm^{-3} is obtained, which is higher than the reported values obtained for CZTS prepared in a substrate structure, of 10^{16} cm^{-3}.[35] We associate this high carrier concentration with a higher number of inter-grain defects in samples with lower grain size and defects produced in the *p-n* interface.

A progressive increase of the depletion width and a reduction of N_D with the increase of Cd can be deduced, which correlates with the values of the EQE. This reveals that the main current limitation for the samples with a low Cd ratio is a small depletion width, drastically reducing the electron-hole pair collection, along with a high density of carriers associated with trap states that decrease the diffusion length. The increase of V_{bi} while the carrier density decrease, suggests that carriers are dominated by trap states in samples with intermediate Cd-Zn content. A high Cd ratio is found to overcome this limitation while increasing the built-in potential, which results in a higher charge collection with a higher potential separation.

The obtained values are used to simulate the band bending on the two extreme cases of CZTS/ZnS/TiO_2 in **Figure 5.7b** and CCTS/CdS/TiO_2 in **Figure 5.7c**. These results further support that there is a metal^{2+} accumulation in the interface, inhibiting a direct junction between TiO_2 and the absorber layer, shown in **Figure S5.3**. In agreement with the C-V measurements, we can notice that the bending is produced in a much smaller region when the doping is increased. ZnS-like interfaces produce a barrier for the carrier collection, stimulating the interface recombination.

The dark I-V curve was measured and represented in **Figure 5.8a** and all the samples present a rectification shape, with no leakage under reverse current. The samples with a higher Cd ratio present an increase of the turn-on voltage, which suggests the existence of a barrier affecting the output voltage is low in Cd samples since the built-in potential follows a different trend. These barriers are likely produced at the *p-n* interface due to band bending, caused by a high charge

density in the p-type absorber. In addition, barriers can be also produced in the grain boundaries of the polycrystalline absorber, thus the samples with higher crystallinity can mitigate this problem.

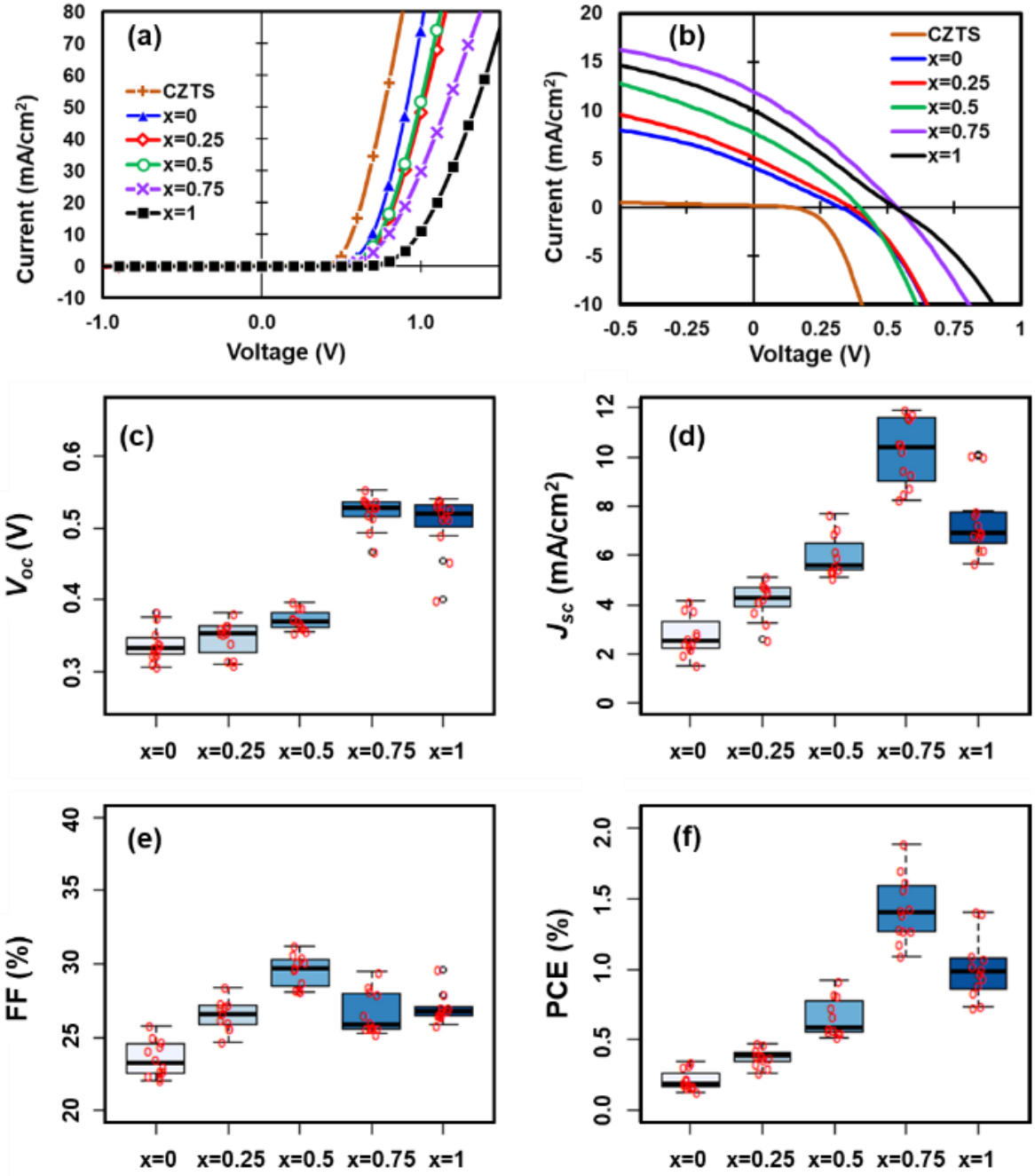

Figure 5.8. a) Dark *J-V* curves, b) *J-V* curves of the efficient device of each condition under 1 Sun illumination, c) V_{OC}, d) J_{SC}, e) FF, and f) PCE statistical (boxes) and values (red dots) extracted from the *J-V* curves under 1 Sun illumination.

The characteristic *J-V* curve under 1 Sun (AM 1.5) illumination is represented in **Figure 5.8b**, with the parameters shown in **Table 5.4**. The statistical distribution of the PV properties, over 10 individual devices for each condition (except for the CZTS sample due to low values), is shown in **Figure 5.8c − f**.

The open-circuit voltage (V_{OC}) has an increasing trend for the samples with higher Cd content, especially for the samples x = 0.75 and x = 1, where it reaches a value of 540 mV, while the best value of sample x = 0.5 is just 402 mV. This increment seems to be highly correlated with the increase in the built-in potential, which allows an efficient charge separation, and the reduction of defects density, reducing the traps states and recombination, allowing the separated charges to retain a higher potential. The remaining (Cd,Zn)S as secondary phase found in the XRD plays an important role in the V_{OC} increment. CdS are well-known buffer material, with low resistance and high *n*-type doping, while ZnS usually present high resistance and low *n*-type doping, producing barriers that difficult charge separation. However, it has been reported that (Cd,Zn)S can reduce the interface recombination and produce solar cells with better performance.[36,37] The short circuit current (J_{SC}) values naturally follow a similar trend as in the EQE and the thickness of the depletion width. In this case, sample x = 0.75 stands out with better values, followed by the x = 1 sample. High Cd content improves the charge collection, however, the short-circuit current values are still below the ideal values that can be attained with these materials (up to 34 mA/cm^2 for a 1.4 eV band-gap according to the Shockley-Queisser limit). The low fill factor is of concern (between 25 and 30 % in most cases). Direct shunts are not observed under dark, but internal shunts seem to produce a low shunt resistance under illumination. We attribute this to an insufficient exciton lifetime along with the reduction of the depletion width with the voltage, producing an apparent shunt. Also, a slight S shape can be noted in some samples, which suggest the presence of a barrier for the carrier collection, and the existence of parasitic resistances, most likely due to non-optimized front and back contacts. Improvements on the interfaces and absorber layer properties are necessary to increase the FF.

Table 5.4. PV parameters of the best cell of every condition.

Condition	V_{OC} (V)	J_{SC} (mA/cm^2)	Fill Factor (%)	Efficiency (%)
x=0	0.323	4.14	25.8	0.34
x=0.25	0.364	5.13	25.6	0.48
x=0.5	0.397	7.69	30.1	0.92
x=0.75	0.537	11.90	29.5	1.89
x=1	0.531	10.00	26.5	1.41

Comparing devices with the same composition, but with different absorber thicknesses, (**Figure S5.4**), we noted a change in the initial PV performance. Moreover, a reduction of the PV parameters for the absorber thicker than 500 nm corroborates a strong limitation existing in the diffusion length and conductivity within the bulk material.

Taking into account, the overall power conversion efficiency (PCE) is found to have a clear improvement for the device with the higher Cd content, with a remarkable record value of 1.9 % for x = 0.75 and 1.4 % for x = 1. Considering that is the first time, under our knowledge, that CCTS is reported to be used in a superstrate architecture, these PCE values are promising. Moreover, the results gave good reproducibility, with a maximum dispersion of 30 % among different samples.

While the PCE extracted from the *J-V* curve is the standard parameter to compare with other PV technologies, it is not an important parameter to evaluate the potential of a PV technology to substitute the current PV technologies. Reliability is a critical factor when a new PV technology has to compete with established technologies. Thus, we have focussed on the three main stability aspects: chemical, thermal, and light stability. In the context of chemical stability, we noted that the samples have low or unnoticeable changes when exposed to common solvents (water, acetone, isopropanol, and ethanol), or even highly basic and acid environments, such as NH_3 vapours typically used in the CBD process, or concentrated HCl, in agreement with other reports for this type of solar cells.[38]

The high chemical stability will not only be beneficial to keep a constant PCE over time but also to ensure that the potentially dangerous elements such as Cd are not released to the environment.

We then investigated thermal stability by applying a heat treatment to the samples of 150 ºC for 10 minutes on a hot plate, (**Figure S5.4**). The device PV parameters decrease after heat treatment, which affects mainly the V_{OC} and J_{SC}. However, after keeping the samples under dark for two weeks, all the PV parameters recovered to their original values. This temporal behaviour suggests that the effect of the temperature in these samples is not due to chemical reactions, such as oxidation or decomposition, but rather a trap state activation in the *p-n* junction. Proper control of the trap states, by an appropriate dopant, for example, can mitigate this and increase the temperature stability.

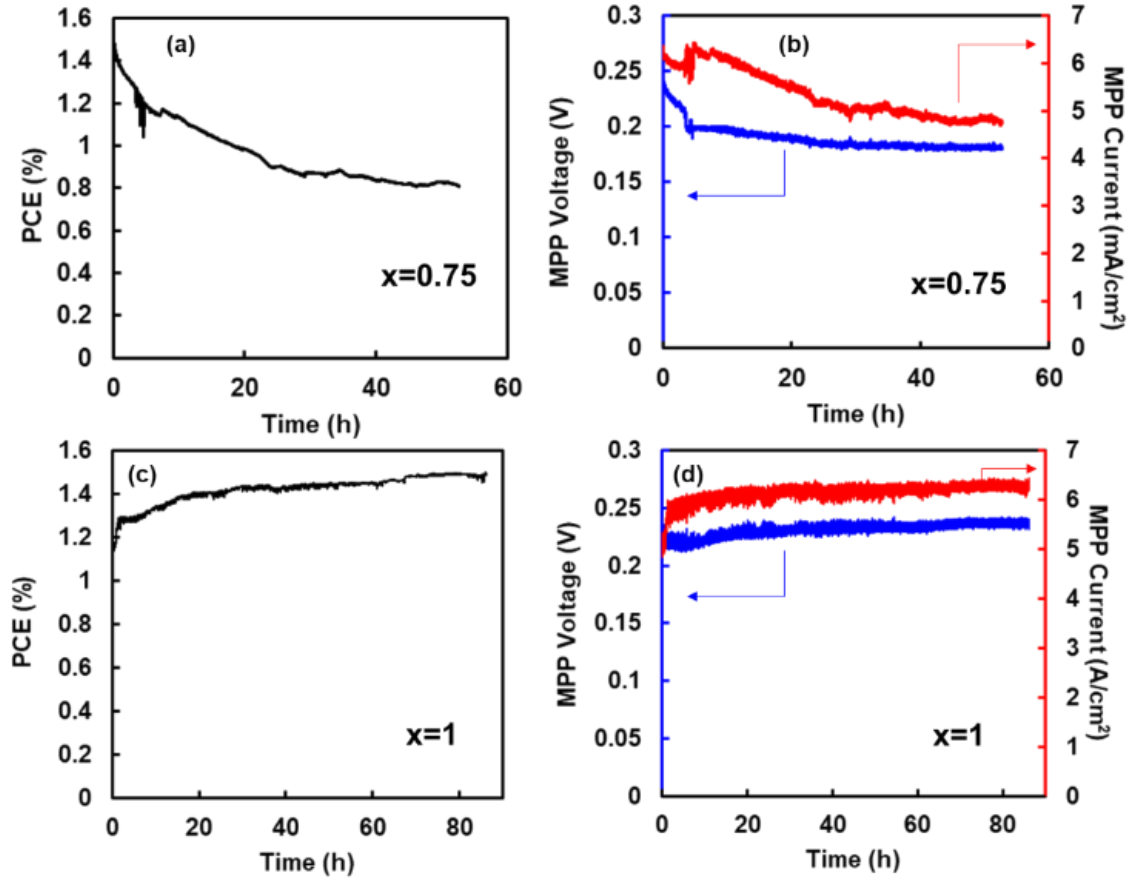

Figure 5.9. a) PCE evolution under continuous illumination for the sample, x = 0.75, and c) x = 1, b) values of voltage and current measured at the tracked maximum power point for the sample x = 0.75, and d) for x =1.

Subsequently, the light stability was probed by monitoring the maximum power point (MPP) under continuous illumination for several hours, (**Figure 5.9**). Since the illumination was provided with a halogen lamp, the intensity was calibrated with reference cells, by adjusting the initial J_{SC} to the value measured under one Sun. The comparison of the *J-V* curves at one Sun (**Figure S5.5**) was made to put the samples close to a real application scenario. We compared the conditions, of x = 0.75 and x = 1, and noted different behaviours. The sample x = 0.75 has a decreasing trend of the MPP voltage during the first 5 hours, followed by a drop of the voltage that elevates the current. This behaviour could be caused by the creation of shunt paths due to micro dielectric breakdowns. At this point, the voltage is almost kept constant, while the photocurrent shows a decrement until and is stabilised after 40 hours. As previously seen, the short-circuit current was mostly dependent on the depletion width, which suggests that this current reduction is caused by the slow activation of traps that increases the density of free carriers in the absorber, reducing the depletion width and therefore the collected charges. For the sample x = 1, we found a progressive increase of the MPP during the first 20 hours, and then, a stabilized behaviour in the investigated window of 60 hours. The difference between the samples indicates that the small quantity of Zn in the sample x = 0.75 has an impact on light stability. CdS are known to exhibit high photoconductivity under visible illumination,[39] lowering the resistance and improving its properties as a buffer layer, which causes an increase of the PCE. However, this effect is much lower or even disappears, in a (Cd,Zn)S solid solution,[40] explaining why only the x = 1 sample, that contains pure CdS, presents an increase of the PCE under continuous illumination.

These findings postulate CCTS as an attractive absorber material for the development of a new generation of stable, thin-film, and cost-effective PV technology based on a superstrate architecture, while CCZTS could be also a candidate if the light stability issues can be addressed. We identified the limiting factors that can be addressed to improve the PCE. The main limitation was found in the charge collection, affecting the short-circuit current and FF. A charge collection dependence on the depletion width instead of the absorber thickness

indicates that the limitation comes from a low diffusion length of the photo-generated electron-hole pairs. Good control of the composition and grow mechanism of the absorber layer could be key to further improving the exciton lifetime and avoiding the formation of deep defects in the surface.[41] Strategies such as doping, alloying, or nanostructures can also help to address such limitations. Additionally, optimization of both the front and back contacts could reduce the series resistance and improve the FF.

5.4 Chalcogen substitution: $Cu_2CdSn(S,Se)_4$

To study the effects of including selenium in a $Cu_2CdSn(S_{4-y}Se_y)$ composition, the as-deposited absorber layers were submitted to a sulfo-selenization treatment, by adding 25 mg or 50 mg of selenium powder into the tubular furnace, while maintaining 50 mg of S in all cases. The resulting layer composition is shown in **Table 5.5**. The ratio of selenium to sulphur changes to 0.15 and 0.3 for the samples annealed with 25 mg and 50 mg of selenium respectively. To label the samples, the value of y=4(Se/S+Se) is used. The composition of the films was maintained Cu-poor and Cd-rich, however, a higher than expected chalcogen ratio was obtained. This can be due to chalcogen rich secondary phases, or condensation on the surface during the cooling step. Nevertheless, a chalcogen rich composition is preferable to a poor one, since the defects and secondary phases associated has a lower impact on the PV performance.

Table 5.5. Compositional ratios of CCTSSe thin films.

	$Cu_2CdSn(S_{4-y}Se_y)$	Se/S+Se	Cu/Cd+Sn	Cd/Sn	VI/Metal
0 mg Se	Cu_2CdSnS_4	0	0.82	1.23	1.17
25 mg Se	$Cu_2CdSn(S_{3.4}Se_{0.6})$	0.15	0.86	1.20	1.30
50 mg Se	$Cu_2CdSn(S_{2.8}Se_{1.2})$	0.3	0.76	1.09	1.50

The EQE was measured in the PV cells prepared with these films, showed in **Figure 5.10a**. There are several effects that can be noticed when the spectrum of

the different samples is compared. First, there is a slight increase of the signal for wavelengths near 450 nm, while the peak of efficiency is progressively shifted to longer wavelengths with the Se ratio increasing. The peak depends on the balance of light reaching the absorber and light absorbed by the buffer layer, which presumably is composed of Cd(S,Se) with a similar ratio of Se to S than the absorber. Since the Se ratio reduces the band gap of the buffer, it can absorb light with a longer wavelength, shifting the peak observed in the *EQE*. The slight increase of the signal at 450 nm can be also associated with Cd(S,Se), however, this increase does not compensate for the loss produced by its absorption and therefore, a reduction or elimination of this layer could be necessary to maximize the *EQE* in this type of solar cells.

On the other hand, a broader spectrum is obtained in long wavelengths with the increasing Se ratio, associated with the reduction of the absorber band gap. This shift is used to calculate the band gap in **Figure 5.10b**, obtaining values of 1.356 and 1.285 eV for the samples y=0.6 and y=1.2 respectively, and maintaining a 1.42 eV for the pure sulphur sample.

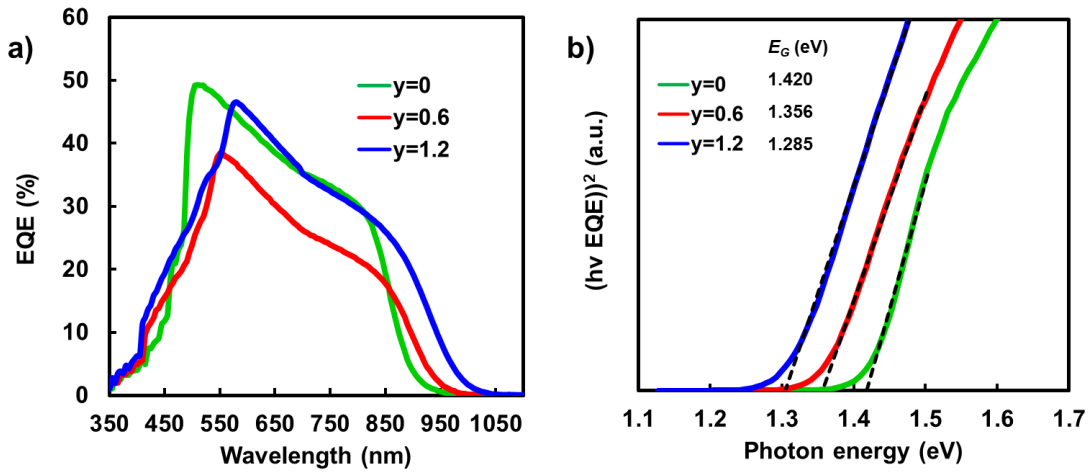

Figure 5.10. a) *EQE* and b) band gap calculation from the *EQE*.

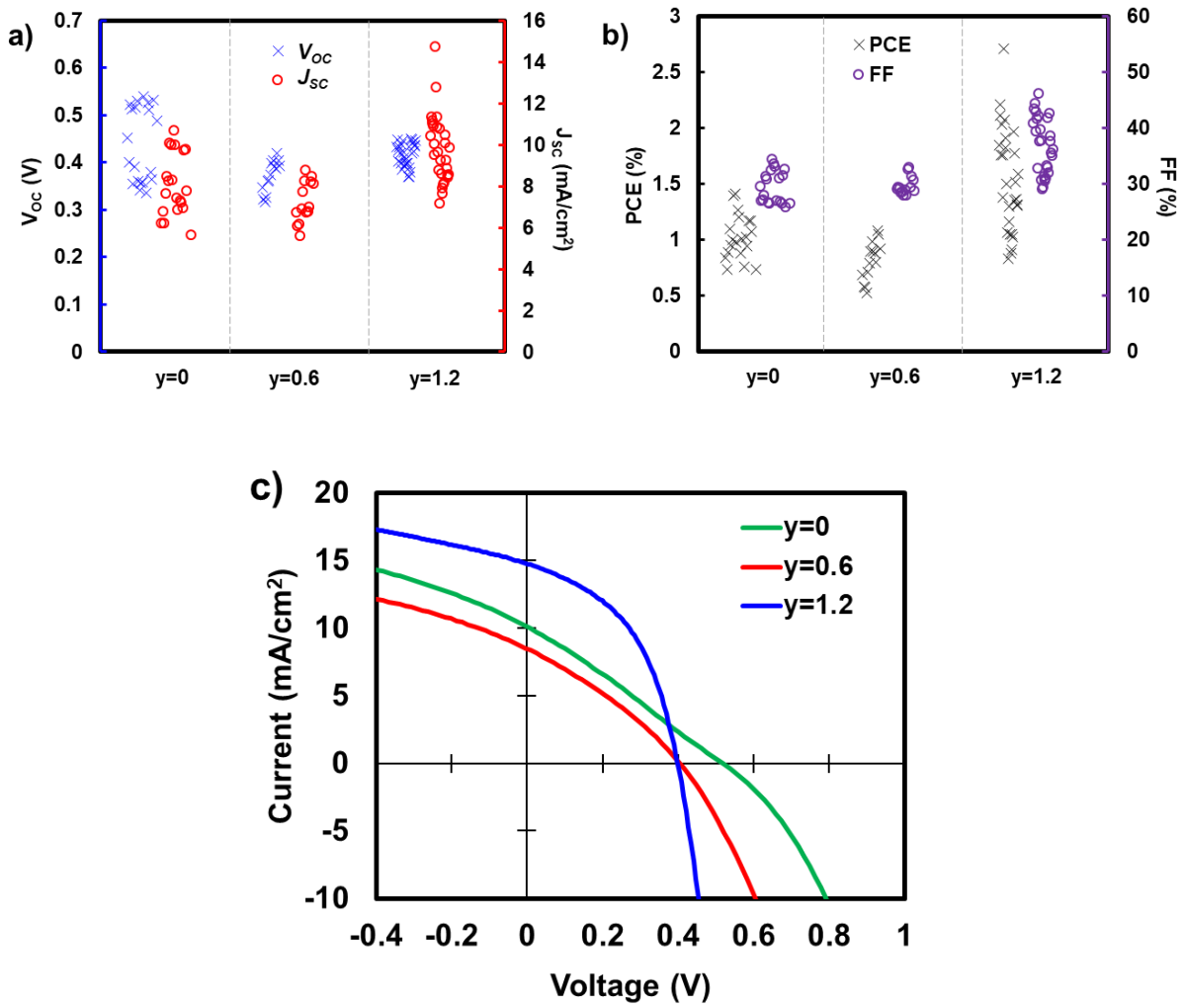

Figure 5.11. a) V_{OC}, J_{SC}, b) PCE and FF of the samples prepared with different content of Se. c) *J-V* curves and d) dark *J-V* curves of the most efficient device of each condition under 1 Sun illumination.

A comparison of the PV parameters of the solar cells prepared are shown in **Figure 5.11a** and **Figure 5.11b**, and the particular values of the best devices and averages are shown in **Table 5.6**, corresponding to the *JV* curves under illumination of **Figure 5.11c**. The open-circuit voltage is higher in the pure sulphur cells, but taking into account the reduction of the band gap, the loss of voltage with respect to the ideal value remains nearly the same for the y=1.2 samples, suggesting that a limiting factor for the voltage is not highly dependent on the Se ratio. Similarly, the increase of current due to a higher absorption is proportional to the decrease of the band gap.

Table 5.6. PV parameters of the best cells for every condition, with the averages under brackets.

	V_{OC} (mV)	J_{SC} (mA/cm^2)	FF (%)	PCE (%)	V_{OC} loss (mV)	Rs (Ω cm^2)
y=0	517 (432)	10.09 (7.95)	26.7 (29.3)	1.39 (1.01)	613	11.2
y=0.6	419 (371)	8.20 (7.20)	31.3 (29.6)	1.08 (0.79)	651	5.1
y=1.2	398 (416)	14.73 (9.68)	46.1(36.4)	2.70 (1.47)	612	2.3

On the other hand, it can be noticed that the most affected parameter is the FF, with a significant increase for the samples containing more Se. One of the factors affecting the FF is the series resistance. An improvement of the series resistance can be noticed in the dark *JV* curve of **Figure 5.12a**, which is reduced from 11.2 to 2.3 Ω cm^2. However, the reduced series resistance seems insufficient to completely explain the FF improvement.

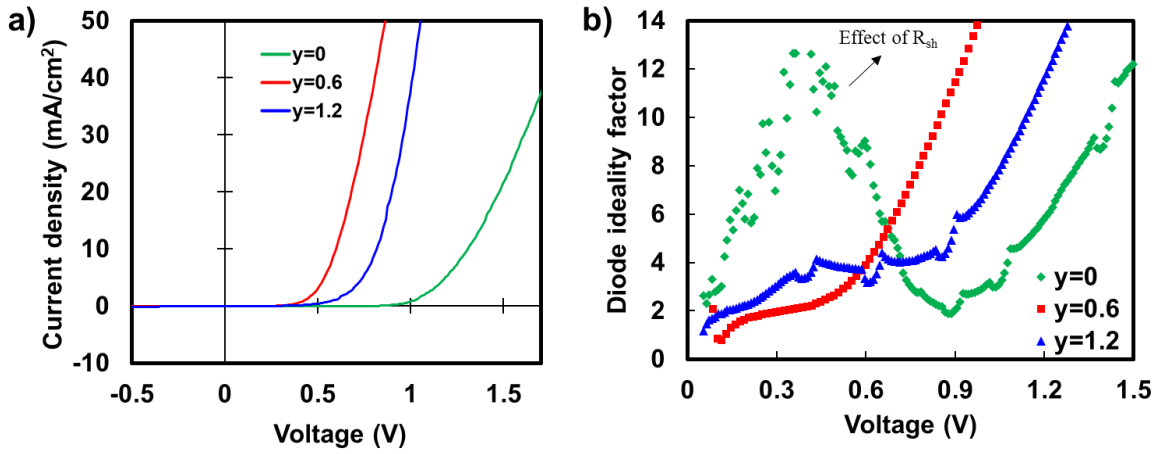

Figure 5.12. a) Dark *J-V* curves and b) calculation of the local ideality factor.

The local diode factor was calculated from the dark *JV* curves in **Figure 5.12b.** The bump obtained in the low voltage region indicates that the shunt resistance has also an important impact on the FF for the CCTS cells, which is mostly eliminated in the Se containing cells. In these cells, the ideality factor shows a plateau slightly higher than 2 at voltages from 0 to 0.6 V. A value close to 2 indicates that the recombination in the junction dominates, which is common in

thin-film solar cells, while the values above suggest an increase of the bulk trap density, due to recombination in the grain boundaries.[42] This also helps to explain part of the V_{OC} deficit and the crosslink between the dark and illuminated *JV* curves. Strategies for passivation of the grain boundaries as well as increment in the grain size will likely mitigate these problems and reduce the V_{OC} deficit. Nevertheless, the improved FF suggest improved mobility of the photo-generated carriers in the bulk of the absorber, which facilitates the carriers to reach the *p-n* junction.

Even with the mentioned limitations, it has been shown that the inclusion of Se into the composition of the absorber mitigates the harmful processes that reduce the FF in superstrate solar cells. Superstrate solar cells using an absorber with a $Cu_2CdSn(S_{2.8}Se_{1.2})$ composition, prepared by spray pyrolysis from a water-ethanol based solution, present a maximum PCE of 2.7 %, which is fairly comparable with the best result reported using similar absorber compositions in a substrate architecture.[20]

5.5 Chapter Conclusions

Water-ethanol spray pyrolysis deposition was used as a benign media to prepare $Cu_2(Cd_x,Zn_{1-x})SnS_4$ films and used as absorber material in all-solution-processed superstrate-type solar cells. The Zn-Cd ratio impacts the electro-optical properties. A high Cd content improves the crystal growth and avoids the formation of $(Cd_x,Zn_{1-x})S$ in the interface, largely increasing the depletion width of the *p-n* junction and thus photo-generated charge collection. Both the V_{OC} and J_{SC} increase significantly, leading to PCE values from 0.3 % for low Cd content to 1.9 % for higher ones. The fabricated solar cells also showed chemical, thermal and light stability, suggesting their suitability for large-scale applications. The main limitations for the light conversion efficiency are found to be a low exciton diffusion, impeding a complete charge collection, and the low FF.

In a preliminary test, the introduction of Se in the compositions shows a huge impact in the FF thanks to improved series resistance. However, the limiting

processes for the V_{OC} and the J_{SC} that affect the cells based on Cu_2CdSnS_4 are still present in the $Cu_2CdSn(S,Se)_4$ cells. Nevertheless, the FF is almost doubled only by introducing a Se/S+Se of 0.3, which lead to a maximum PCE of 2.7 %, in the range of best values reported for quaternary materials in a superstrate architecture, and comparable with similar materials used in a substrate architecture. Overcoming the limitations could promote this type of solar cell as a green and cost-effective alternative to the current PV technologies and, simultaneously, avoid the use of critical or scarce elements.

5.6 Chapter supporting information

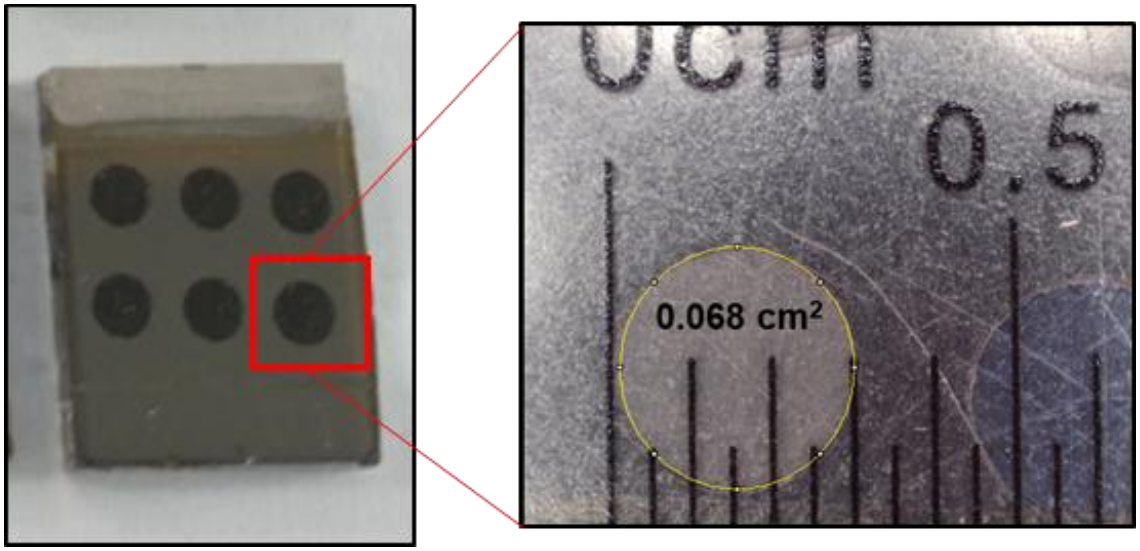

Figure S5.1. A microscope image of a carbon dot electrode, which defines the cell area.

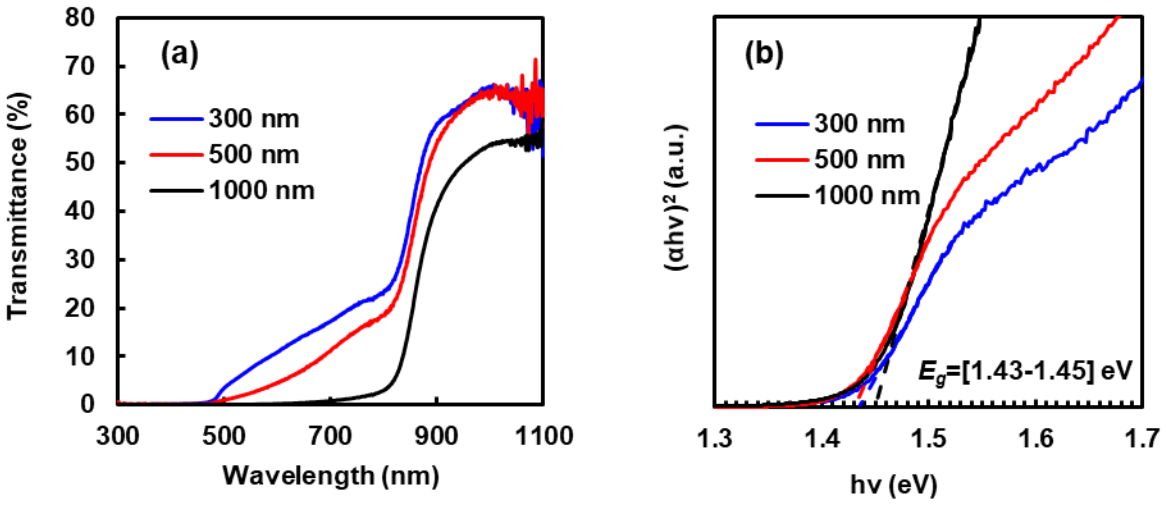

Figure S5.2. a) Transmittance spectrum and b) Tauc plot with bandgap calculation of samples with different absorber thickness, all prepared with an x=0.75 solution.

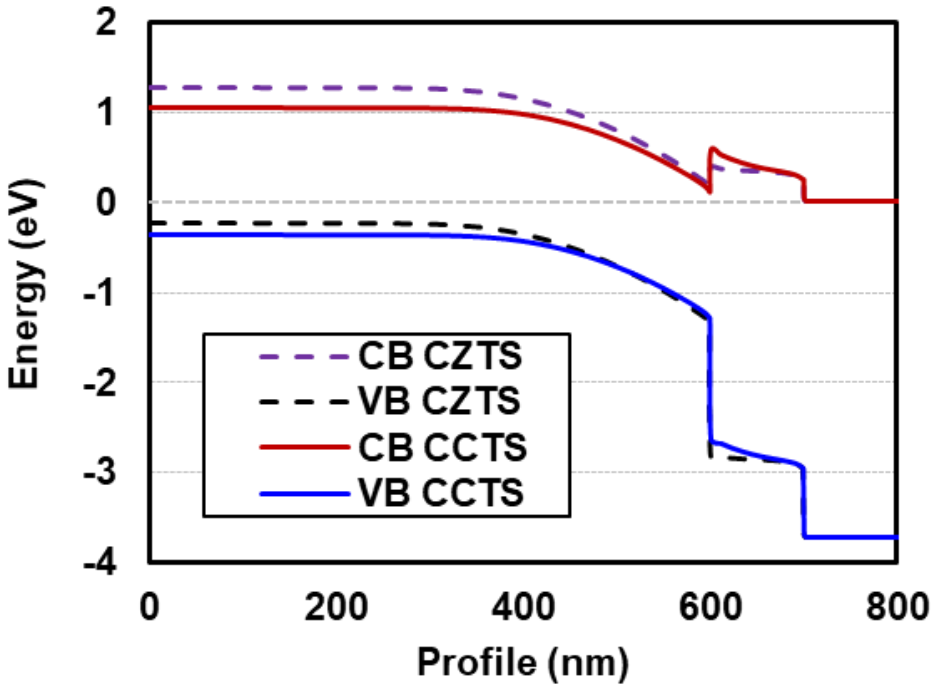

Figure S5.3. Junction formed between the absorber layer and TiO_2. It consists of a spike-like junction, with a small barrier for CZTS than CCTS (both with doping of 10^{16} cm^{-3}).

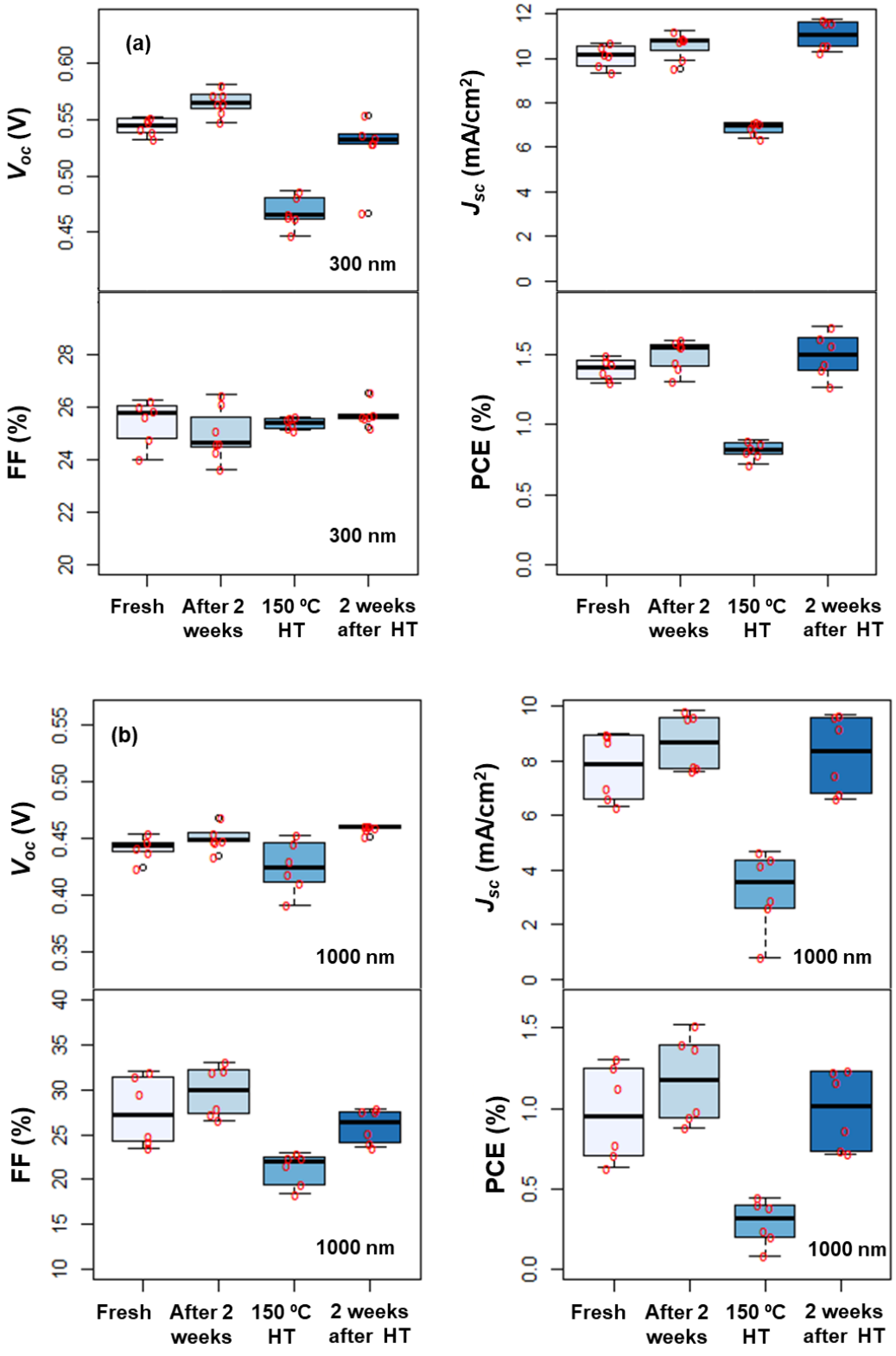

Figure S5.4. PV parameters extracted from the *J-V* curve under the illumination of the sequence were prepared to test the temperature stability. The samples were prepared with the x=0.75 solution, with an absorber thickness of a) 300 nm and b) 1000 nm.

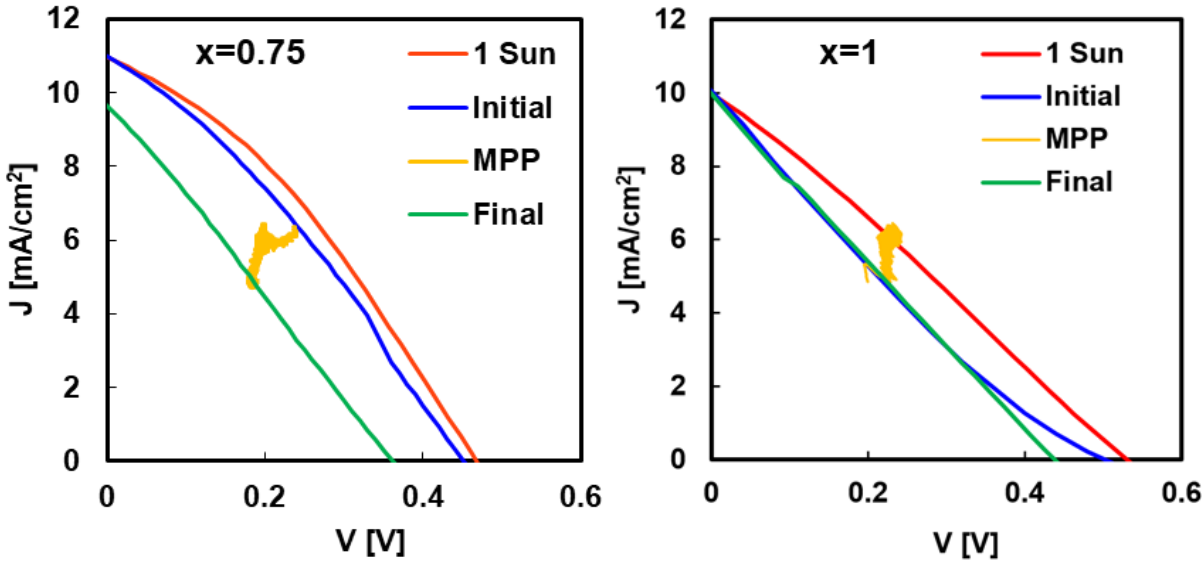

Figure S5.5. *J-V* curves of the tested samples, used for calibration of the halogen lamp under 1 Sun, under halogen illumination, and after the light stability test. The *J-V* points measured during the stability test are also marked. The slight variations between the curve at 1 Sun and the curve used for calibration, are associated with the different light spectrum, with a higher intensity of the infrared in the halogen lamp.

5.7 Chapter references

1. Payno Zarceño, D., Kazim, S. & Ahmad, S. Impact of cation substitution in all solution-processed Cu2(Cd,Zn)SnS4 superstrate solar cells. *J. Mater. Chem. C* (2021). doi:10.1039/d1tc04527j

2. Wagner, S. & Bridenbaugh, P. M. Multicomponent tetrahedral compounds for solar cells. *J. Cryst. Growth* **39**, 151–159 (1977).

3. Ito, K. & Nakazawa, T. Electrical and Optical Properties of Stannite-Type Quaternary Semiconductor Thin Films. *Jpn. J. Appl. Phys.* **27**, 2094–2097 (1988).

4. Pilvet, M. *et al.* Compositionally tunable structure and optical properties of Cu1.85(CdxZn1 - X)1.1SnS4.1(0 ≤ x ≤ 1) monograin powders. in *Thin Solid Films* **582**, 180–183 (Elsevier, 2015).

5. Hadke, S. *et al.* Emerging Chalcogenide Thin Films for Solar Energy Harvesting Devices. *Chem. Rev.* acs.chemrev.1c00301 (2021). doi:10.1021/ACS.CHEMREV.1C00301

6. Su, Z. *et al.* Cation Substitution of Solution-Processed Cu2ZnSnS4 Thin Film Solar Cell with over 9% Efficiency. *Adv. Energy Mater.* **5**, 1500682 (2015).

7. Yan, C. *et al.* Beyond 11% Efficient Sulfide Kesterite Cu2ZnxCd1-xSnS4 Solar Cell: Effects of Cadmium Alloying. *ACS Energy Lett.* **2**, 930–936 (2017).

8. Hadke, S. *et al.* Suppressed Deep Traps and Bandgap Fluctuations in Cu2CdSnS4 Solar Cells with ≈8% Efficiency. *Adv. Energy Mater.* **9**, 1902509 (2019).

9. Su, Z. *et al.* Device Postannealing Enabling over 12% Efficient Solution-Processed Cu2ZnSnS4 Solar Cells with Cd2+ Substitution. *Adv. Mater.* **32**, 2000121 (2020).

10. Zhang, Q. *et al.* Effects of sulfurization temperature on the structural and optical properties of Cu2CdSnS4 thin films prepared by direct liquid method. *Mater. Lett.* **193**, 206–209 (2017).

11. Fthenakis, V. M. Life cycle impact analysis of cadmium in CdTe PV production. *Renew. Sustain. Energy Rev.* **8**, 303–334 (2004).

12. Fthenakis, V. M. & Kim, H. C. CdTe photovoltaics: Life cycle environmental profile and comparisons. *Thin Solid Films* **515**, 5961–5963 (2007).

13. Dimitrievska, M. *et al.* Role of S and Se atoms on the microstructural properties of kesterite Cu 2 ZnSn(S x Se 1−x) 4 thin film solar cells. *Phys. Chem. Chem. Phys.* **18**, 8692–8700 (2016).

14. Wei, Y. *et al.* Effects of selenium atmosphere on grain growth for CZTSe absorbers fabricated by selenization of as-sputtered precursors. *J. Alloys Compd.* **755**, 224–230 (2018).

15. Temgoua, S., Bodeux, R. & Naghavi, N. Influence of the annealing atmosphere and precursor's thickness on the properties of CZTSSe based solar cells. *Sol. Energy Mater. Sol. Cells* **191**, 123–132 (2019).

16. Matsushita, H., Maeda, T., Katsui, A. & Takizawa, T. Thermal analysis and synthesis from the melts of Cu-based quaternary compounds Cu–III–IV–VI4 and Cu2–II–IV–VI4 (II=Zn, Cd; III=Ga, In; IV=Ge, Sn; VI=Se). *J. Cryst. Growth* **208**, 416–422 (2000).

17. Liu, M. L., Chen, I. W., Huang, F. Q. & Chen, L. D. Improved thermoelectric properties of cu-doped quaternary chalcogenides of Cu2CdSnSe4. *Adv. Mater.* **21**, 3808–3812 (2009).

18. Fan, F. J. *et al.* Colloidal synthesis of Cu2CdSnSe4 nanocrystals and hot-pressing to enhance the thermoelectric figure-of-merit. *J. Am. Chem. Soc.* **133**, 15910–15913 (2011).

19. Ibáñez, M. *et al.* Composition Control and Thermoelectric Properties of Quaternary Chalcogenide Nanocrystals: The Case of Stannite Cu2CdSnSe4. *Chem. Mater.* **24**, 562–570 (2012).

20. Zhao, W. *et al.* Solution-processed Cu2CdSn(S,Se)4 thin film solar cells. *Sol. Energy Mater. Sol. Cells* **133**, 15–20 (2015).

21. Yuan, Z. K. *et al.* Engineering Solar Cell Absorbers by Exploring the Band Alignment and Defect Disparity: The Case of Cu- and Ag-Based Kesterite Compounds. *Adv. Funct. Mater.* **25**, 6733–6743 (2015).

22. Nisika *et al.* Energy level alignment and nanoscale investigation of a-TiO2/Cu-Zn-Sn-S interface for alternative electron transport layer in earth abundant Cu-Zn-Sn-S solar cells. *J. Appl. Phys.* **126**, 193104 (2019).

23. Saha, U. & Alam, M. K. Boosting the efficiency of single junction kesterite solar cell using Ag mixed Cu2ZnSnS4 active layer†. *RSC Adv.* **8**, 4905–4913 (2018).

24. Kabulov, R. R. Features of a ZnxCd1 – xS Buffer Layer for Use in Thin-Film Solar Cells in the Context of a Literature Review. *Appl. Sol. Energy (English Transl. Geliotekhnika)* **56**, 383–387 (2020).

25. Haidari, G. One-dimensional modeling for optoelectrical simulation of a mesoporous perovskite solar cell. *Appl. Opt.* **58**, 7006 (2019).

26. Payno, D., Kazim, S., Salado, M. & Ahmad, S. Sulfurization temperature effects on crystallization and performance of superstrate CZTS solar cells. *Sol. Energy* **224**, 1136–1143 (2021).

27. Kumar, M., Dubey, A., Adhikari, N., Venkatesan, S. & Qiao, Q. Strategic review of secondary phases, defects and defect-complexes in kesterite CZTS-Se solar cells. *Energy Environ. Sci.* **8**, 3134–3159 (2015).

28. Wu, S. H. *et al.* High-efficiency Cu2ZnSn(S,Se)4 solar cells fabricated through a low-cost solution process and a two-step heat treatment. *Prog. Photovoltaics Res. Appl.* **25**, 58–66 (2017).

29. Nguyen, T. H. *et al.* Cu2ZnSnS4 thin film solar cells with 5.8% conversion efficiency obtained by a facile spray pyrolysis technique. *RSC Adv.* **5**, 77565–77571 (2015).

30. Su, Z. *et al.* Fabrication of Cu2ZnSnS4 solar cells with 5.1% efficiency via thermal decomposition and reaction using a non-toxic sol-gel route. *J. Mater. Chem. A* **2**, 500–509 (2014).

31. Szymanski, J. T. The crystal structure of Cernyite, Cu2CdSnS4, a cadmium analogue of stannite. *Can. Mineral.* **16**, 147–151 (1978).

32. Schorr, S., Hoebler, H.-J. & Tovar, M. A neutron diffraction study of the stannite-kesterite solid solution series. *Eur. J. Mineral.* **19**, 65–73 (2007).

33. Franckevičius, M. *et al.* Efficiency improvement of superstrate CZTSSe solar cells processed by spray pyrolysis approach. *Sol. Energy* **185**, 283–289 (2019).

34. Su, Z. *et al.* Cation Substitution of Solution-Processed Cu2ZnSnS4 Thin Film Solar Cell with over 9% Efficiency. *Adv. Energy Mater.* **5**, 1500682 (2015).

35. Payno, D. *et al.* Partial substitution of the CdS buffer layer with interplay of fullerenes in kesterite solar cells. *J. Mater. Chem. C* **8**, 12533–12542 (2020).

36. Yan, C. *et al.* Cu2ZnSnS4 solar cells with over 10% power conversion efficiency enabled by heterojunction heat treatment. *Nat. Energy* **3**, 764–772 (2018).

37. Kaiwen Sun *et al.* Beyond 10% efficiency Cu 2 ZnSnS 4 solar cells enabled by modifying the heterojunction interface chemistry. *J. Mater. Chem. A* **7**, 27289–27296 (2019).

38. Wang, Z., Gauvin, R. & Demopoulos, G. P. Nanostructural and photo-electrochemical properties of solution spin-coated Cu2ZnSnS4-TiO2 nanorod forest films with an improved photovoltaic performance. *Nanoscale* **9**, 7650–7665 (2017).

39. Fraser, D. B. & Melchior, H. Sputter-deposited CdS films with high photoconductivity through film thickness. *J. Appl. Phys.* **43**, 3120–3127 (1972).

40. Gordillo, G. Photoluminescence and photoconductivity studies on ZnxCd1-xS thin films. *Sol. Energy Mater. Sol. Cells* **25**, 41–49 (1992).

41. Gong, Y. *et al.* Identifying the origin of the: Voc deficit of kesterite solar cells from the two grain growth mechanisms induced by Sn2+and Sn4+precursors in DMSO solution. *Energy and Environmental Science* **14**, 2369–2380 (2021).

42. Sozzi, G., Mosca, R., Calicchio, M. & Menozzi, R. Anomalous dark current ideality factor (n > 2) in thin-film solar cells: The role of grain-boundary defects. in *2014 IEEE 40th Photovoltaic Specialist Conference, PVSC 2014* 1718–1721 (Institute of Electrical and Electronics Engineers Inc., 2014). doi:10.1109/PVSC.2014.6925252

6 General conclusions & future trends

Contents:

6.1 Highlights from this thesis

Throughout this thesis, we have studied quaternary chalcogenide materials, mostly kesterite based, for PV applications, proposing innovations to increase its attractiveness for its use on large scale. The feasibility and potential of using thin films of these materials as light absorbers in PV cells have been demonstrated. From the reviewed literature, along with the results obtained on the first part of the thesis, we highlight the following conclusions:

- Cu_2ZnSnS_4 and $Cu_2ZnSnSe_4$ are promising materials for a large scale PV production, composed of abundant elements with low toxicity, a high absorption coefficient and a band-gap among the ideal range for the solar spectrum, however, the solar cells based on those materials have limitations that yet impedes a competitive performance in comparison with other PV technologies.
- The conversion from light to electricity of kesterite based solar cells is limited by several factors. The main bottleneck is in the output voltage, with values 40% below the expected for its bandgap. The voltage losses are partially associated with bulk defects, and partially with interface recombination and barriers in the front and back contacts, as well as an insufficient built-in potential.
- In the case of $Cu_2ZnSnSe_4$ or kesterite with a high content of Se, the bulk defects are less critical than in Cu_2ZnSnS_4, reducing the V_{OC} deficit, but limiting the band-gap to low values, close to 1 eV.
- Using an ultrathin interlayer of C_{60} between kesterite and the CdS buffer was found beneficial to avoid interface recombination, enhancing the voltage in solar cells based on both Cu_2ZnSnS_4 and $Cu_2ZnSnSe_4$.
- Using an ultrathin layer of C_{60} allows a reduction of the CdS buffer thickness, improving transparency and allowing more light to reach the absorber, resulting in an increase of the current.

- A C_{60} film alone did not produce enough charge separation to completely substitute CdS but provides a simple and inexpensive method of surface passivation.
- Due to the high-temperature requirements for the crystallization of kesterite, an architecture based on glass/Mo provides a robust substrate and back contact for the kesterite deposition. The quality of the absorber and back contact obtained in this architecture is high, resulting in solar cells with the best efficiency obtained to date, but presenting some limitations in the performance and the possible applications that these solar cells can have.

In the second part of this thesis, kesterite films have been prepared by liquid deposition methods and tested in solar cells using an alternative superstrate structure of glass/FTO/TiO_2/CdS. From this section, we can highlight the following points:

- Kesterite thin films of PV quality can be prepared by liquid deposition methods from simple molecular precursor's solutions. The solutions are compatible with a variety of deposition methods, such as spin coating, ink-jet printing or spray coating. Spray pyrolysis is found to be interesting for PV applications since provides a high throughput, low material usage, and compatibility with green solvents such as water and ethanol.
- A superstrate structure is of interest to produce different classes of solar cells, such as bifacial, ultra-thin, semi-transparent, or tandem solar cells, which can unlock its use in new applications. It also allows the use of different back-contacts, avoiding the problem of having non-ohmic contacts and improving the hole extraction.
- Solar cells prepared on a superstrate structure are compatible with liquid deposition methods and thus avoid the use of strategic or costly elements and types of equipment. This increases its attractiveness for large-scale

fabrication and can make them competitive, even if its efficiency is below other PV technologies existing.

- A thin film of TiO_2 provides FTO with good resistance to high temperatures and protect it from chemical changes under sulfurization or selenization treatments. At the same time, it acts as a transparent n-type material, transporting electrons and blocking holes to the negative contact.
- Using Cu_2ZnSnS_4 in a superstrate structure manifest some glitches that limit its PV efficiency. The use of a CdS layer was found crucial to ensure good interface properties. Direct contact between Cu_2ZnSnS_4 and TiO_2 produce a highly defective interface with a very small depletion region, unsuitable for an efficient electron-hole collection and separation.
- A TiO_2 mesoporous layer was found beneficial in various aspects. It provides a porous surface that allows a better CdS deposition, reducing the voids and increasing the interface area while the shunts are reduced. An optimum thickness maintains good transparency, resistance, and improves the electron-hole separation, increasing the open-circuit voltage and short circuit current.
- The temperature required for crystallization and grain growth of kesterite triggers the exchange of Cd and Zn from the CdS buffer and the absorber layers, resulting in an accumulation of Zn rich (Cd,Zn)S phases in the interface. These phases produce a barrier in the interface, reducing the open-circuit voltage, and increasing the defect density in the interface, reducing the depletion region and consequently the collection of electron-hole pairs. CdS also modify the final composition of the absorber, producing an alloy of $Cu_2(Cd,Zn)SnS_4$ with better crystallinity and PV properties.
- Carbon was found to be a stimulating back contact. Thin-films of this green and low-cost material can be prepared by a doctor blade or screen printing. It possesses good hole extraction due to its high work function.

However, its conductivity is not sufficient enough for a large scale application without a second layer of a conducting metal. It also lacks reflectivity. Ultrathin absorbers (300-600 nm) in combination with highly reflective back contact can provide as much current as a thicker absorber, but with fewer losses by bulk recombination.

In the third part of the thesis, strategies were performed to overcome the critical problems found, focusing on modifications in the absorber composition.

- The substitution of the problematic elements can mitigate the problems of Cu_2ZnSnS_4. Partial substitution of Zn by Cd in the absorber layer reduces the formation of Zn-rich phases, producing an interface with better properties for charge separation, better band alignment with fewer barriers for the electron extraction, and an increase of the built-in potential.
- In addition, $Cu_2(Cd,Zn)SnS_4$ compounds show better properties as light absorber layers when the content of Cd/Cd+Zn is higher than 0.75. The band-gap is reduced to 1.4 eV, while the crystallinity and grain size is improved. This results in absorber layers with lower defects in the interface, increasing the depletion region, and so the charge collection.
- The stability was exceptionally good for the Cu_2CdSnS_4 solar cells. After storing them in dark for several months, or under working conditions for several hours, no changes or small improvements were observed in its PV properties.
- $Cu_2(Cd,Zn)SnS_4$ solar cells still show a low fill factor, and their efficiency is lower at longer wavelengths. These problems can be attributed to a low exciton diffusion length and high bulk and back surface recombination.
- In an early attempt of finding a material to overcome Cu_2CdSnS_4 limitations, alloys of $Cu_2CdSn(S,Se)_4$ were tested with promising results. A reduced band-gap allows an increase of the absorption range in

exchange for a V_{oc} reduction, but with an improved FF, which we speculatively associate with an improvement of the carrier lifetime.

As a final remark, we conclude that there is a high potential in the study of chalcogenide materials for their use in solar cells following a superstrate architecture. A historical of the best PV efficiency of the solar cells prepared during this thesis are shown in **Figure 6.1**. If the trend in efficiency improvements is maintained, this new class of PV cells could be susceptible to become promptly competitive, thanks to its advantages and reduced cost.

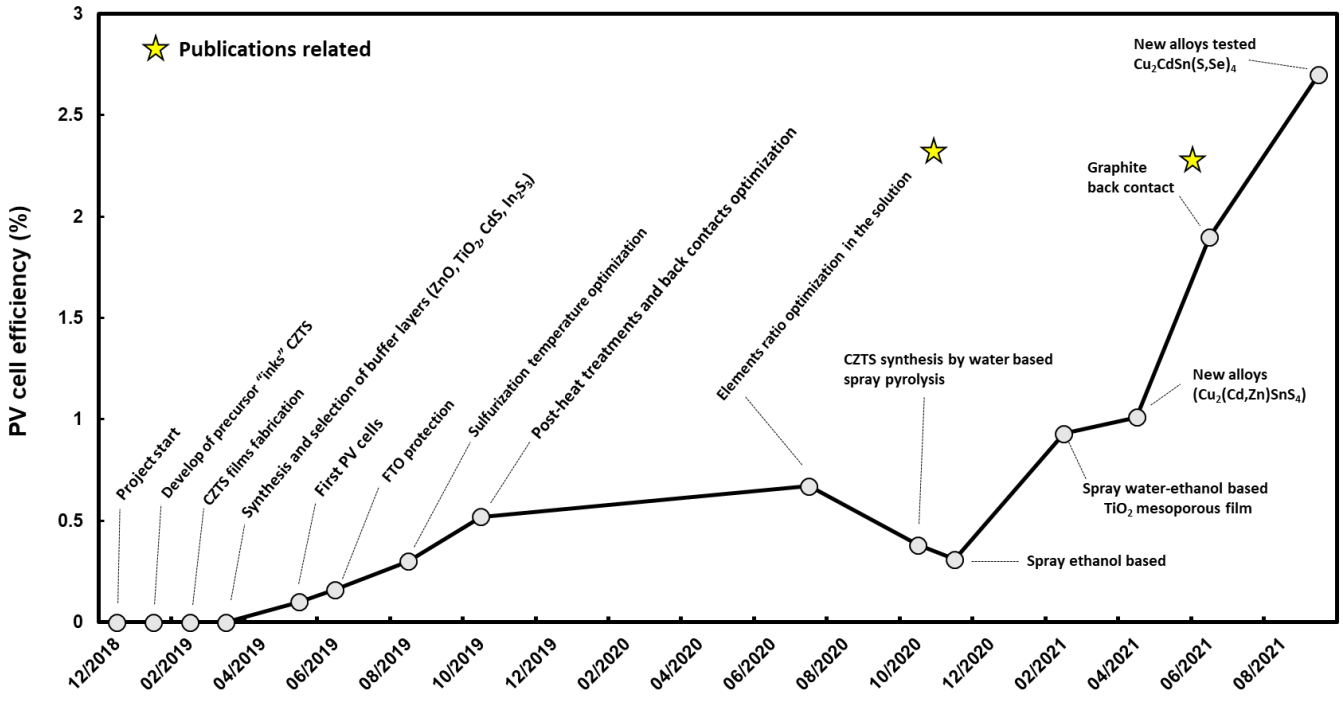

Figure 6.1. Progress of the PV efficiency milestones of solar cells in a superstrate architecture prepared during this thesis.

6.2 Current trends and future possibilities

For kesterite and similar critical elements free materials, there are still several issues that must be addressed in future work to make these classes of solar cells competitive enough to reach the market and have an important impact. A sufficient efficiency increase along with improved reliability and scale-up techniques are the next challenges that these technologies have to evolve.

Focusing on the efficiency improvements, the substrate structure is predominant. Improvements in the properties of the light absorber layer are the first step to ensure minimum losses. This can be developed by searching and optimizing the synthesis route, which results in a kesterite layer with fewer secondary phases and higher grain size, which minimize the recombination in the intergrains. Controlling the defects in the crystalline structure and the impact that they have on the PV performance is essential.

On the other hand, the interfaces and the materials used in the junction requires special attention. For the formation p-n junction, CdS is mainly used, which, as we have shown, does not have the optimal properties to be combined with kesterite, and the search of alternative materials that gives optimal properties for its use as buffer/window layer is very limited. There are materials available to substitute that can provide a better affinity with kesterite. We found that C_{60} has potential, but it requires modifications to work alone as an efficient buffer. Alternative deposition methods such as physical vapour deposition can provide better coverage, while modulation of the electron transport properties can be get by dopping[1] or mixing different fullerenes.[2]

If turn the attention to the development of a superstrate structure, we found that the exploration of quaternary I_2-II-IV-VI_4 materials can provide interesting candidates with the required properties for an ideal absorber material composed of abundant materials. Multiple quaternary compounds have been demonstrated to have the potential of overcoming the limitations

of kesterite,[3] such $(Cu,Ag)_2ZnSn(S,Se)_4$,[4] $Cu_2ZnGeSe_4$, $Cu_2CdGe(S,Se)_4$ or $Cu_2CdSn(S,Se)_4$. Moreover, solid solutions between these compounds could offer a large number of combinations to suits a very specific set of electric, optical and crystalline properties, providing specific solutions for the application of interest, although the complexity of these multielement compounds can make them very challenging. Alloys of ternary and quaternary compounds have not been widely explored and can provide new ways of fine-tuning their properties.

Moreover, other chemical compositions lead to semiconductor materials, such as $I–II–III–VI_3$ with a bournonite structure, that is starting to be explored due to its suitable semiconductor properties, as is the case of $CuPbSbS_3$.[5] Some $I–II_2–III–VI_4$ compositions have been explored as thermoelectric semiconductor, which may also be suitable for PV applications.[6,7]

These materials may also represent an opportunity to increase the popularity of superstrate architecture. An ideal material would have a good affinity with TiO_2 and would require a lower temperature for its synthesis and crystallization acquiring high photovoltaic properties and maintaining the advantages in simplicity and low cost that a superstrate architecture offers.

As shown in the last part of this thesis, Cu_2CdSnS_4 and $Cu_2CdSn(S,Se)_4$ show high potential for their use on efficient superstrate PV cells. From the experience obtained from kesterite, direct possibilities to further improve its performance can be applied:

- Substitution of Cu by Ag: Compounds containing Ag instead of Cu have been found to require synthesis temperatures below 500 ºC, which is ideal for the superstrate case. The conductivity shifts from p-type to slightly n-type for a high substitution,[8] along with a progressive increase of the band-gap[9] which can be adapted in a n^+-n-p structure.[10,11] The behaviour of Ag substitution in the case of a $(Ag,Cu)_2CdSn(S,Se)_4$ compound is expected to be similar.

- Substitution of Sn by Ge: Ge was started to be used to partially substitute Sn in kesterite solar cells,[12] and $Cu_2ZnGeSe_4$ has been studied as an alternative.[13] The substitution of Sn by Ge in kesterite results in materials with higher band-gap, from 1.49 eV for $Cu_2ZnGeSe_4$ to 2.25 eV for Cu_2ZnGeS_4, maintaining the same valence band maximum (VBM) and shifting the conduction band minimum.[14] This shift can be advantageous to adjust the band alignment of the junctions. If the absorber is based on $Cu_2CdGeSe_4$, an appropriate band-gap of 1.22 eV is maintained,[15] which allows it use in PV.
- Alkali metal doping: The importance of Na as non-radiative defects passivation agent was found important in CIGS base PV, and it was maintained with kesterites.[16] Superstructure impedes a natural Na diffusion from the glass substrate, so an alternative and more controlled source of Na can be useful as passivation of the grain boundaries. The use of alternative alkali elements is facilitated in this case, where Li has been found to have better passivation than Na. Anyhow, the effects that the alkali have on the absorber properties highly depends on the temperature and methods used to introduce them.[17]
- Activation treatments: A characteristic treatment that can be adopted from CdTe based PV, consisting in a moderate temperature post-treatment with $CdCl_2$ or similar chlorine salts,[18] creating a reactive atmosphere that removes oxygen impurities and passivates the back surface and grain boundaries. This treatment can be expected to result in similar effects when applied to $Cu_2CdSn(S,Se)_4$ compounds.
- Back surface optimization: Beyond the studied materials in this thesis, there are plenty of possibilities for the back contact. A potential option could be a thin-film of NiO[19] or MoO_3[20] among other possibilities,[21] which provides a high work function back contact, an electron blocking behaviour, and creates a transparent surface with low roughness, ideal for the subsequent deposition of a metallic contact such Ag or Al, to provide an increased reflectivity in all the visible spectrum.

As general research scopes in photovoltaics, an improvement of the power conversion efficiency in already known materials is still important to facilitate its transfer to the industry, but the focus on materials with advantages and functionalities is gaining interest. Semi-transparent and bifacial solar cells are of high interest for the building integration PV (BIPV), which can be acquired by ultrathin, selective, or wide bandgap absorbers. Superstrate architectures are more indicated for this application since they already provide a highly transparent substrate. On the other hand, highly flexible solar cells are also of high interest for BIPV, where a substrate architecture can be found more suitable. For this application, thin foils of stable metals, such stainless steel, Mo, or Al, can be used as a substrate for solar cells.

6.3 Beyond PV applications

These emerging chalcogenides studied can have applications in other areas of interest, due to their stability, reduced cost, and variety of optical, optoelectronic and electric properties.

6.3.1 Electronics

As the first application of semiconductor materials, chalcogenides can provide advantages in electronic compounds. Its high stability can make them suitable for diodes or transistors in high power electronics. The modulation of its band-gap can be used to modify the threshold voltage of a diode and adapt it to specific applications. Thin film transistors (TFT) with high performance, field-effect transistors and memristors have been demonstrated in binary chalcogenides,[22,23] and quaternary compounds could be adapted for these devices. Their thin-film nature makes them suitable for printed, flexible and wearable electronics.[24]

6.3.2 Photonics

Photonics is a wide topic with emerging fields requiring very specific optical properties of the materials in function of the specific application. The tunable optical properties, in particular for high band-gap or high IR transparency, can be used as optical fibres, waveguides or optical signal processing.[25] Infrared and light-emitting diodes (LEDs) are probably the most direct application that an already known PV material can be applied since electroluminescence is a reversed photovoltaic effect, based on the principle.[26] Engineering the band-gap by the elemental composition in quaternary chalcogenides could provide a simple way of developing an emitter material with the desired wavelength for a LED device. Another approach to get emission wavelength modulation is by their use in nanoparticles, commonly with a core-shell structure to passivate the non-radiative recombination in the surface.[27]

6.3.3 Electrochemistry and photoelectrochemistry

We can include photoelectrochemical and electrochemical applications, such as photo-catalysis, photo-fuel cells or water splitting. These applications require very chemically stable materials, in combination with high light absorption, and a specific band-gap and fermi-level depending on the particular case. Many quaternary chalcogenides have the stability and absorption required, while the electric properties can be tuned with the composition, making them good candidates for its use as stable photocathodes[28,29] and as an alternative to noble metals such Pt.[30]

6.3.4 Thermoelectricity

Thermoelectric devices take advantage of the Seebeck effect in semiconductors to generate electricity from a temperature difference, or the Peltier effect to do the reverse operation. Thermoelectricity is not comparable in efficiency for heat energy harvesting with classic steam

turbines,[31] but gains interest in small scale applications where turbines have bad scalability or are not practical, such as self-power electronics, or space exploration.[32] In a reverse operation is used as an active cooling or fast response heating-cooling cycler, which is a useful tool in biochemistry applications such as polymerase chain reactions (PCRs).[33]

Semiconductors used in thermoelectricity requires a good majority carrier conductivity to have a high Seebeck coefficient, low thermal conductivity to maintain the temperature gradient, and high thermal stability. Currently, most thermoelectric devices are based on Te chalcogenides such Bi_2Te_3 or PbTe, being Bi and Te very rare elements. Quaternary chalcogenides such as $Cu_2ZnSnSe_4$,[34] $Cu_2ZnGeSe_4$,[35] $Cu_2CdSnSe_4$ [36] among many others[37] have been found to have a thermoelectric figure of merit zT approaching 1, making them comparable with the current thermoelectric devices.

6.3.5 Sensors

Roughly, any material with a sensible property to a change in the environment can be adapted as a sensor device. In general, stimuli that provokes a change in an electric property are especially practical, since facilitates its measurement. By this means, chalcogenide semiconductors offer adaptability to a specific application, which may suppose a better response, sensitivity, stability or cost reduction of the device.

Photoconductivity or photovoltaic effects can be used for photo-detectors, while its band-gap tunability can be adapted for the detection of a specific wavelength. Another interesting sensing application is the detection of specific chemical compounds and gases, which can be detected by the chemical changes or chemisorption in the sensor surface, used to measure the humidity,[38] methane,[39] or reactive and dangerous gasses such as liquefied petroleum gas.[40] Alternatively, visible and NIR detectors can be used to monitor and specific absorption peak of the compound of interest such as CO_2.[41]

6.4 Conclusions

The tunability of the properties by the elemental composition of the quaternary chalcogenides was used to optimize their use in solar cells while maintaining an abundant element composition, with scalable, low-cost and green deposition processes. However, there are further opportunities available for efficiency improvements in the proposed solar cells, as well as the exploration of their use in alternative PV applications.

Overall, we consider successfully our objective of providing an insight into alternative materials and solar cell configurations with high potential of competing with the current PV technologies. Every improvement is a step closer toward a reduction of energy costs and a sustainable future.

Moreover, the knowledge obtained from the properties of the materials studied can be applied in other fields of interest, where the advantages of an abundant element composition can be of interest.

6.5 Chapter references

1. Zhang, J. *et al.* Self-Doping Fullerene Electrolyte-Based Electron Transport Layer for All-Room-Temperature-Processed High-Performance Flexible Polymer Solar Cells. *Adv. Funct. Mater.* **28**, 1705847 (2018).

2. Lin, H. S. *et al.* Achieving High Efficiency in Solution-Processed Perovskite Solar Cells Using C60/C70 Mixed Fullerenes. *ACS Appl. Mater. Interfaces* **10**, 39590–39598 (2018).

3. Li, J., Wang, D., Li, X., Zeng, Y. & Zhang, Y. Cation Substitution in Earth-Abundant Kesterite Photovoltaic Materials. *Adv. Sci.* **5**, 1700744 (2018).

4. Gong, Y. *et al.* Ag Incorporation with Controlled Grain Growth Enables 12.5% Efficient Kesterite Solar Cell with Open Circuit Voltage Reached 64.2% Shockley–Queisser Limit. *Adv. Funct. Mater.*

31, 2101927 (2021).

5. Liu, Y. *et al.* Bournonite CuPbSbS3: An electronically-3D, defect-tolerant, and solution-processable semiconductor for efficient solar cells. *Nano Energy* **71**, 104574 (2020).

6. Nolas, G. S., Hassan, M. S., Dong, Y. & Martin, J. Synthesis, crystal structure and electrical properties of the tetrahedral quaternary chalcogenides CuM2InTe4 (M=Zn, Cd). *J. Solid State Chem.* **242**, 50–54 (2016).

7. Shi, W., Khabibullin, A. R. & Woods, L. M. Exploring Phase Stability and Properties of I-II2-III-VI4 Quaternary Chalcogenides. *Adv. Theory Simulations* **3**, 2000041 (2020).

8. Gershon, T. *et al.* Photovoltaic Device with over 5% Efficiency Based on an n-Type Ag2ZnSnSe4 Absorber. *Adv. Energy Mater.* **6**, 1601182 (2016).

9. Kumar, J. & Ingole, S. Structural and optical properties of (AgxCu1-x)2ZnSnS4 thin films synthesised via solution route. *J. Alloys Compd.* **727**, 1089–1094 (2017).

10. Gershon, T. *et al.* Photovoltaic materials and devices based on the alloyed kesterite absorber (AgxCu1-x)2ZnSnSe4. *Adv. Energy Mater.* **6**, 1502468 (2016).

11. Gershon, T. *et al.* Compositional effects in Ag2ZnSnSe4 thin films and photovoltaic devices. *Acta Mater.* **126**, 383–388 (2017).

12. Collord, A. D. & Hillhouse, H. W. Germanium Alloyed Kesterite Solar Cells with Low Voltage Deficits. *Chem. Mater.* **28**, 2067–2073 (2016).

13. Benhaddou, N. *et al.* Investigation on limiting factors affecting Cu2ZnGeSe4 efficiency: Effect of annealing conditions and surface treatment. *Sol. Energy Mater. Sol. Cells* **216**, 110701 (2020).

14. Tsuji, K., Maeda, T. & Wada, T. Optical properties and electronic

structures of Cu2ZnSnS4, Cu2ZnGeS4, and Cu2Zn(Ge,Sn)S4 and Cu2Zn(Ge,Sn)Se4 solid solutions. *Jpn. J. Appl. Phys.* **57**, 08RC21 (2018).

15. Krustok, J. *et al.* Observation of band gap fluctuations and carrier localization in Cu2CdGeSe4. *J. Phys. D. Appl. Phys.* **52**, 285102 (2019).

16. Gershon, T. *et al.* The role of sodium as a surfactant and suppressor of non-radiative recombination at internal surfaces in Cu2ZnSnS4. *Adv. Energy Mater.* **5**, 1400849 (2015).

17. Mule, A. *et al.* Effect of different alkali (Li, Na, K, Rb, Cs) metals on Cu2ZnSnSe4 solar cells. *Thin Solid Films* **633**, 156–161 (2017).

18. Major, J. D., Treharne, R. E., Phillips, L. J. & Durose, K. A low-cost non-toxic post-growth activation step for CdTe solar cells. *Nature* **511**, 334–337 (2014).

19. Caruge, J. M., Halpert, J. E., Bulović, V. & Bawendi, M. G. NiO as an Inorganic Hole-Transporting Layer in Quantum-Dot Light-Emitting Devices. *Nano Lett.* **6**, 2991–2994 (2006).

20. Larsen, J. K., Simchi, H., Xin, P., Kim, K. & Shafarman, W. N. Backwall superstrate configuration for ultrathin Cu(In,Ga)Se2 solar cells. *Appl. Phys. Lett.* **104**, 033901 (2014).

21. Rajeswari, R., Mrinalini, M., Prasanthkumar, S. & Giribabu, L. Emerging of Inorganic Hole Transporting Materials For Perovskite Solar Cells. *Chem. Rec.* **17**, 681–699 (2017).

22. Mitzi, D. B., Copel, M. & Chey, S. J. Low-voltage transistor employing a high-mobility spin-coated chalcogenide semiconductor. *Adv. Mater.* **17**, 1285–1289 (2005).

23. Gao, X., Bian, G. & Zhu, J. Electronics from solution-processed 2D semiconductors. *J. Mater. Chem. C* **7**, 12835–12861 (2019).

24. Garlapati, S. K. *et al.* Printed Electronics Based on Inorganic Semiconductors: From Processes and Materials to Devices. *Advanced Materials* **30**, 1707600 (2018).

25. Eggleton, B. J., Luther-Davies, B. & Richardson, K. Chalcogenide photonics. *Nature Photonics* **5**, 141–148 (2011).

26. Rau, U. Reciprocity relation between photovoltaic quantum efficiency and electroluminescent emission of solar cells. *Phys. Rev. B - Condens. Matter Mater. Phys.* **76**, (2007).

27. Aldakov, D., Lefrançois, A. & Reiss, P. Ternary and quaternary metal chalcogenide nanocrystals : synthesis, properties and applications. *J. Mater. Chem. C* **1**, 3756–3776 (2013).

28. Ozel, F., Aslan, E., Istanbullu, B., Akay, O. & Hatay Patir, I. Photocatalytic hydrogen evolution based on Cu2ZnSnS4, Cu2NiSnS4 and Cu2CoSnS4 nanocrystals. *Appl. Catal. B Environ.* **198**, 67–73 (2016).

29. Sheebha, I. *et al.* Comparative studies on hierarchical flower like Cu2XSnS4[X= Zn, Ni, Mn & Co] quaternary semiconductor for electrocatalytic and photocatalytic applications. *Int. J. Hydrogen Energy* **45**, 8139–8150 (2020).

30. David Kirubakaran, D., Ravi Dhas, C., Jain, S. M., Marchesi, L. F. & Pitchaimuthu, S. Jet nebulizer-spray coated CZTS film as Pt-free electrocatalyst in photoelectrocatalytic fuel cells. *Appl. Surf. Sci.* **463**, 994–1000 (2019).

31. Vining, C. B. An inconvenient truth about thermoelectrics. *Nature Materials* **8**, 83–85 (2009).

32. Champier, D. Thermoelectric generators: A review of applications. *Energy Conversion and Management* **140**, 167–181 (2017).

33. Xianbo, Q. & Jingqi, Y. Temperature control for PCR thermocyclers based on peltier-effect thermoelectric. in *Annual International*

Conference of the IEEE Engineering in Medicine and Biology - Proceedings **7 VOLS**, 7509–7512 (2005).

34. Dong, Y., Wang, H. & Nolas, G. S. Synthesis and thermoelectric properties of Cu excess Cu2ZnSnSe4. *Phys. Status Solidi - Rapid Res. Lett.* **8**, 61–64 (2014).

35. Mangelis, P., Vaqueiro, P., Smith, R. I. & Powell, A. V. The onset of copper-ion mobility and the electronic transition in the kesterite Cu 2 ZnGeSe 4. *J. Mater. Chem. A* **9**, 27493–27502 (2021).

36. Liu, M. L., Chen, I. W., Huang, F. Q. & Chen, L. D. Improved thermoelectric properties of cu-doped quaternary chalcogenides of Cu2CdSnSe4. *Adv. Mater.* **21**, 3808–3812 (2009).

37. Freer, R. *et al.* Key properties of inorganic thermoelectric materials – tables (version 1). *J. Phys. Energy* (2022). doi:10.1088/2515-7655/ac49dc

38. Maurya, D. K., Sikarwar, S., Chaudhary, P., Angaiah, S. & Yadav, B. C. Synthesis and Characterization of Nanostructured Copper Zinc Tin Sulphide (CZTS) for Humidity Sensing Applications. *IEEE Sens. J.* **19**, 2837–2846 (2019).

39. Han, Z. *et al.* On-chip mid-infrared gas detection using chalcogenide glass waveguide. *Appl. Phys. Lett.* **108**, 141106 (2016).

40. Patil, S. J., Bulakhe, R. N. & Lokhande, C. D. Liquefied petroleum gas (LPG) sensing using spray deposited Cu2ZnSnS4 thin film. *J. Anal. Appl. Pyrolysis* **117**, 310–316 (2016).

41. Starecki, F. *et al.* All-optical carbon dioxide remote sensing using rare earth doped chalcogenide fibers. *Opt. Lasers Eng.* **122**, 328–334 (2019).

Annex: Scientific Contributions

Publications part of the thesis

1. **Payno, D.**, Sánchez, Y., Blázquez, O., Giraldo, S., Salado, M., Kazim, S., Saucedo, E., Ahmad, S., 2020. Partial substitution of the CdS buffer layer with interplay of fullerenes in kesterite solar cells. J. Mater. Chem. C 8, 12533–12542. https://doi.org/10.1039/d0tc02666b

2. **Payno, D.**, Kazim, S., Salado, M., Ahmad, S., 2021a. Sulfurization temperature effects on crystallization and performance of superstrate CZTS solar cells. Sol. Energy 224, 1136–1143. https://doi.org/10.1016/j.solener.2021.06.038

3. **Payno Zarceño, D.**, Kazim, S., Ahmad, S., 2021. Impact of cation substitution in all solution-processed Cu2(Cd,Zn)SnS4 superstrate solar cells. J. Mater. Chem. C. https://doi.org/10.1039/d1tc04527j

Other publications

4. Lopez-Garcia, A.J., Bauer, A., Fonoll Rubio, R., **Payno, D.**, Jehl Li-Kao, Z., Kazim, S., Hariskos, D., Izquierdo-Roca, V., Saucedo, E., Pérez-Rodríguez, A., 2020. UV-Selective Optically Transparent Zn(O,S)-Based Solar Cells. Sol. RRL 2000470. https://doi.org/10.1002/solr.202000470

5. **Payno, D.**, Salado, M., Andresini, M., Gutiérrez-Moreno, D., Huang, P., Ciriaco, F., Kazim, S., Sastre-Santos, Á., Fernández-Lázaro, F., Ahmad, S., 2021b. Substituents interplay in piperidinyl-perylenediimide as dopant-free hole-selective layer for perovskite solar cells fabrication. Emergent Mater. 1, 1–9. https://doi.org/10.1007/s42247-021-00317-z

6. (Submitted) Salado, M., **Payno D.**, Ahmad, S., 2022. Long-term stability improvement of perovskite solar cells through a solvent-free encapsulation method.

7. (Submitted) Valverde, A., **Payno D.**, Lezama, L., Laza, JM., Wuttke, S, Fernández de Luis, R. Multivariate functionalization of UiO-66 for photoreductive water remediation.

Oral presentations

1. *"Partial substitution of CdS buffer layer with interplay of fullerenes in kesterite solar cells."* David Payno, *E-MRS SPRING MEETING 2021, Virtual Conference, June 03, 2021.*

Poster contributions

1. "*Superstrate Type Solar Cells Using Kesterite Semiconductor*"; David Payno, Manuel Salado, Ahmed Shalan, Samrana Kazim, Shahzada Ahmad; International Conference on Materials for Advanced Technologies (ICMAT); Singapore; June 2019

2. "*Electrochemical impedance spectroscopy: A powerful characterization technique for electronic devices*"; David Payno, Manuel Salado, Samrana Kazim, Shahzada Ahmad; BCMaterials bridging day, BCMaterials, September 2020.

3. "*Chalcogenides liquid coating for photovoltaic solar cells*", David Payno, Samrana Kazim, Manuel Salado, Shahzada Ahmad, B&B 2021: BCMaterials – University of Bordeaux, online conference, 22/06/2021..

4. "*Water-ethanol based sprayed photovoltaic solar cells.*", David Payno, Samrana Kazim, Shahzada Ahmad, Workshop: 10th New Materials for a Better Life: Advanced Materials for next-generation Biomedicine, Biotechnology and Bioelectronics, October 2021

Awards

1. *Best poster flash presentation for "Water-ethanol based sprayed photovoltaic solar cells.", in* 10th New Materials for a Better Life, *2021.*

Scientific outreach

1. *OnZietzia*, David Payno, "Blues del electrón*", science divulgation video, 2020.* *https://www.onzientzia.tv/es/concurso/2020-2021-concurso/el-blues-del-foton-azul-2/*